Master's thesis

NTNU
Norwegian University of Science and Technology
Faculty of Engineering
Department of Geoscience and Petroleum

Khayrullaev Jokhongir

Seismic geophysics application for Seafloor Massive Sulfides

Seafloor Massive Sulfide deposits mineral richness estimation using their acoustic impedance or zero-offset seismic

Master's thesis in Petroleum Geosciences
Supervisor: Associate Professor Kenneth Duffaut
Co-supervisor: Dr Ketil Hokstad
June 2022

NTNU
Norwegian University of
Science and Technology

Khayrullaev Jokhongir

Seismic geophysics application for Seafloor Massive Sulfides

Seafloor Massive Sulfide deposits mineral richness estimation using their acoustic impedance or zero-offset seismic

Master's thesis in Petroleum Geosciences
Supervisor: Associate Professor Kenneth Duffaut
Co-supervisor: Dr Ketil Hokstad
June 2022

Norwegian University of Science and Technology
Faculty of Engineering
Department of Geoscience and Petroleum

NTNU
Norwegian University of
Science and Technology

Abstract

Seafloor massive sulfide deposits are generated in tectonically active areas such as the back-arc spreading centre, volcanic arc, and mid-ocean ridges. Seafloor massive sulfide deposits form at or near the seafloor surrounded by host-rocks. Seafloor massive sulfide deposits contain ore bodies consisting of more than 40 % of sulfides, such as Pyrite, Pyrrhotite, Chalcopyrite, Sphalerite, and Galena minerals, containing a significant amount of Copper, Zinc, Iron, Lead, Gold, Silver that are necessary for many purposes, especially for transition to renewable energy sources that creates the need for their assessing their mineral richness nowadays. Seismic geophysics is a lucrative tool for this purpose thanks to big areal coverage and the possibility of deep imaging subsurface with satisfactory resolution at a relatively low cost. Based on previous research work on Seafloor massive sulfides rock physics during the author's specialization project, an assumption that it is not possible to estimate Seafloor massive sulfide mineral richness from its acoustic impedance alone and consequently from zero-offset or near-stack seismic data has been developed.

This assumption is examined on real data from Trans-Atlantic Geotraverse Seafloor massive sulfide field. Trans-Atlantic Geotraverse Seafloor massive sulfide field is located on Mid-Atlantic Ridge at 26°9'N, 44°48'W and it is one of most studied Seafloor massive sulfide fields in the world where 2D reflection seismic profiles are recorded and set of core samples are collected. Core composition analyses, P-wave velocity measurements in the core and core bulk density measurements are performed in the laboratory. Existence of several Seafloor massive sulfide deposits located near seabed at Trans-Atlantic Geotraverse Seafloor massive sulfide field is proved during several scientific expeditions. Active Trans-Atlantic Geotraverse mound is one of those Seafloor massive sulfide deposits.

During this work, firstly, the relation between the acoustic impedance and mineral richness of the Active Trans-Atlantic Geotraverse mound is examined. The acoustic impedance of the Active Trans-Atlantic Geotraverse mound is obtained using model-based inversion and calculated, from P-wave velocity measurements and bulk density measurements of cores from a shallow hole for this purpose. Secondly, the relation between the seismic amplitudes on the seabed and the mineral richness of the Active Trans-Atlantic Geotraverse mound is investigated.

Acknowledgement

I am thankful to NTNU for giving me opportunity to study at Norway's best scientific and technical university. I thank NTNU for providing good conditions for study, such as an excellent academic team who taught me for two years and administrative staff who organized the teaching process and supported me whenever needed.

I thank the lecturers of the courses I took for sincerely sharing their academic knowledge gathered during their life and tediously explaining the answers to all my questions.

I thank my supervisor, Associate Professor at NTNU Kenneth Duffaut, for sharing his knowledge and time and giving his suggestions on my work during this master's thesis.

I thank my co-supervisor Dr Ketil Hokstad for sharing his knowledge on Seafloor Massive Sulfides, giving advises on my research during the meetings and for sharing his finding on Trans-Atlantic Geotraverse Seafloor Massive Sulfide field during this masters thesis.

I thank Dr Joerg Bialas from GEOMAR for providing raw 2D reflection seismic data recorded on the Trans-Atlantic Geotraverse Seafloor Massive Sulfide field that I could use during this masters thesis work.

Table of Contents

List of Figures

List of Tables

Nomenclature

λ	(Predominant) wavelength
$\overset{\circ}{A}$	Atomic mass of material
$\overset{\circ}{Z}$	Atomic number or number of electrons of material
ρ	Bulk density
ρ_{sw}	Sea-water density
τ	Predominant period of the wavelet
A	Metal element
Ag	Silver
$AmFeO$	Amorphous Silica
Anh	Anhydrite
Au	Gold
AUV	Autonomous underwater vehicles
AVO	Amplitude versus offset
Ba	Barite
Ca	Carbon
CMP	Common mid point
Co	Cobalt
Cpy	Chalcopyrite
Cu	Copper
d	Sample thickness
d_F	Fresnel zone diameter
f	Dominant frequency
Fe	Iron
g	Gravitational constant
Gn	Galena
h	Water column height
$h_{sea-bed}$	Vertical distance between sea-surface and sea-bed
h_{sw}	Sea-water depth
Hm	Hematite
L	Core length
m, n	Integers
Mn	Manganese
N_{ava}	Avogadro number
n_e	Electron density

Ni	Nickel
OBS	Ocean bottom refraction seismic
ODP	Ocean drilling program
P	Hydro-static pressure
Pb	Lead
Po	Pyrrhotite
Py	Pyrite
Qtz	Quartz
R_0	Zero angle reflection coefficient
S	Sulfur element
s	Sample cross section for scattering
Si	Silicon
SMS	Seafloor massive sulfide
Sph	Sphalerite
t	P-wave travel-time through a core
t_{min}	Quater of (predominant) wavelength criterion
TAG	Trans-Atlantic Geotraverse
Tlc	Talc
$TotalS$	Total Sulfur
TWT	Two-way traveltime
$TWT_{sea-bed}$	Seismic wave two-way travel time to sea-bed at zero-offset
$V_{p(sw)}$	P-wave velocity in sea-water
V_p	P-wave velocity
$vol.\%$	Volume percent
$wt.\%$	Weight percent
Y_i	Detected gamma ray flux
Y_t	Emitted gamma ray flux
Z	Acoustic impedance
z	Reflecting surface depth
Z_{hr}	Acoustic impedance of host-rock
Z_{sb}	Acoustic impedance of sea-bed
Z_{sd}	Acoustic impedance of massive sulfide deposit
Z_{sw}	Acoustic impedance of sea-water
Zn	Zinc

1 Introduction

1.1 Background

Seafloor Massive Sulfide (SMS) deposits contain Copper (Cu), Zinc (Zn), Iron (Fe), Lead (Pb), Gold (Au), Silver (Ag) that are necessary for making electronics, technologies and other goods used for building renewable energy sources such as wind energy, solar energy and hydro-energy. Mining SMS deposits can increase valuable metal reserves worldwide and decrease prices, accelerating the transition to green energy sources soon.

SMS hosting rocks accompany SMS mineral deposits at SMS fields. SMS mineral deposits have a distinct difference in physical properties compared to hosting rocks; some of them are seismic wave velocities and densities. Subsurface images can be built based on rocks' seismic velocities and densities contrast using seismic geophysics. The seismic geophysics covers larger areas than other geophysical methods (magnetic, electrical, gravity) and provides a good resolution image of the deep subsurface. In Salisbury et al. 1996, it is shown that host-rocks and sulfide minerals have a distinct difference in P-wave velocity (V_p) and bulk density (ρ). Their interface creates a strong seismic wave reflector. According to Salisbury et al. 2000 many sulfide deposits meet or exceed the size requirements for both detection and imaging (for example, a 500 m diameter $\times$ 15 m thick deposit could easily be imaged at a depth of 2 km under subsurface, assuming a peak frequency of 100 Hz and a formation velocity of 6.0 km/s) using seismic geophysics. Considering seismic geophysics's advantages in areal coverage and depth of investigation compared to other geophysical methods, seismic geophysics has a high potential for being applied for SMS deposits exploration.

Seismic geophysics application for SMS mineral deposits exploration and appraisal is a relatively new field. There are many questions to be addressed and engineering tools to be developed. One of the questions to be investigated is "Can one determine SMS deposits mineral richness from its acoustic impedance (Z)?". In order to answer this question, it is decided to employ an analytic rock physics template (Figure 1) for qualitatively differentiating SMS mineral deposits from hosting rocks in Z against the ρ domain.

The author believes it is impossible to determine SMS deposits mineral richness only from its Z, and additional information is needed. This assumption can be proved on a SMS field example by obtaining subsurface rocks' Z from processed seismic data employing a suitable seismic inversion method and then analysing Z with known mineral richness.

Trans-Atlantic Geotraverse (TAG) SMS field at 26°N on the Mid-Atlantic Ridge is one of the most intensively studied fields in the world (Murton et al. 2019). The 2D reflection seismic, ocean bottom refraction seismic (OBS), and sea-bed bathymetry by autonomous underwater vehicles (AUV) were recorded during research expedition M127. Drilling core samples, gravity core samples and sea-bed surface grab samples are collected, consequently performing laboratory studies on samples' physical properties and composition during scientific expeditions M127, JC-138 in 2016, Ocean drilling program (ODP) leg 158 in 1994. One active TAG SMS mound and seven inactive SMS mineral deposits "Shimmering", "New mound 2&3", "Shinkai", "Southern", "Double Rona" and "MIR" were previously been identified in an area of $\approx$ 2.5km^2, Figure 19B (Rona et al. 1993a,b).

This master's thesis work attempts to prove that it is impossible to determine SMS deposit mineral richness from only its Z and that additional information is required.

The thesis is divided into eight chapters to focus on one topic in time.

The first chapter is **introduction**, where thesis content and some necessary terms are introduced, answers to the fundamental questions such as "What are the Sulfide minerals?", "What are the SMSs?", "Why do we need SMSs?", "Can seismic geophysics detect SMS deposits?" are provided.

The second chapter is **Theory**, where theory relative to the thesis is explained.

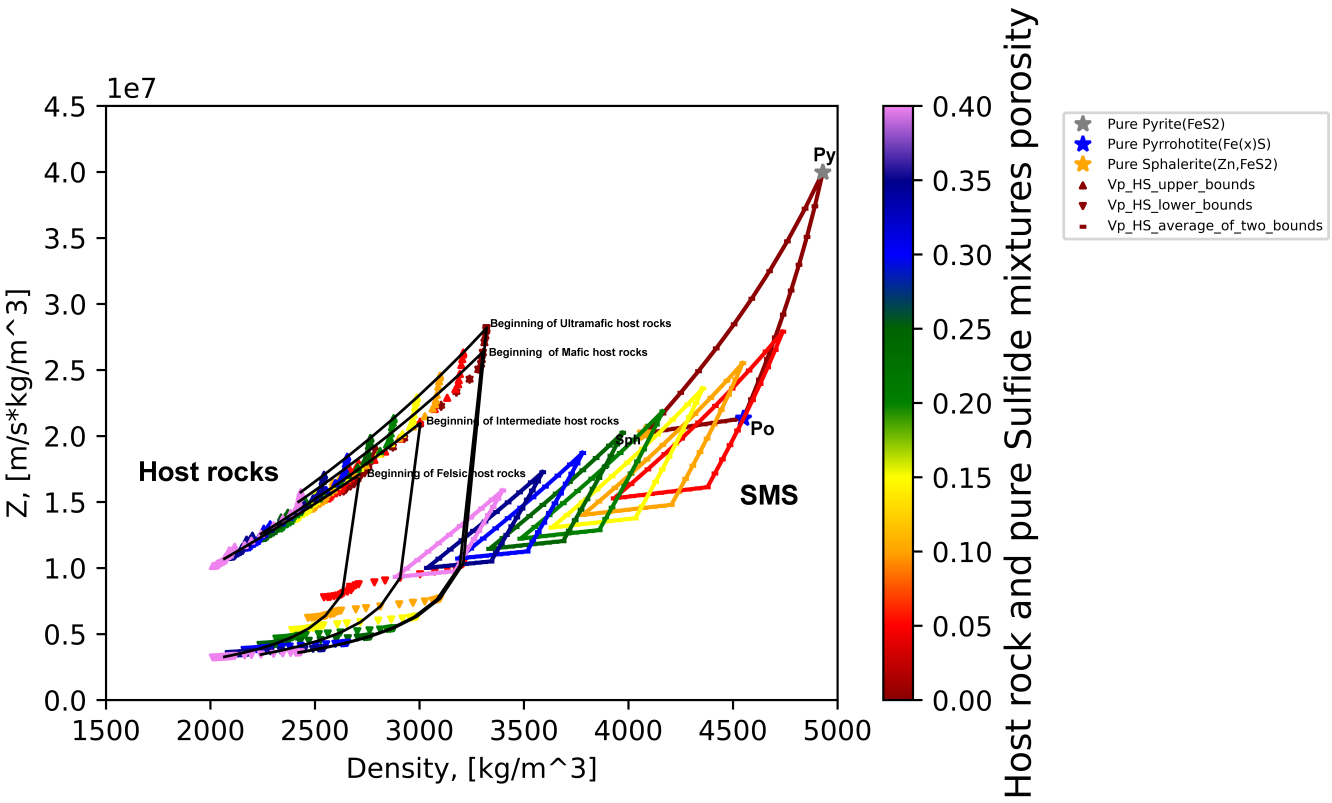

Figure 1: Modified analytical rock physics template for distinguishing SMS from host-rocks in Z versus ρ domain.

The third chapter covers information on TAG SMS **field and database** used for the thesis.

The fourth chapter focus on the **methods** used during this work.

The thesis **results** are shown in the fifth chapter while **discussion and conclusion** are the last sixth and seventh chapters, respectively. The work is finished with some suggestions for **further work** on the eighth chapter.

1.2 Terms and Definitions

Mineral - naturally occurring element or compound of no biological origin, having an ordered atomic structure and characteristic chemical composition, physical properties and crystal form. Minerals are composed of different elements such as O, Si and Al.

Rock - any aggregate of minerals that may consist of a variety of minerals (also only one type). Magmatic, metamorphic and sedimentary rocks define the origin of the rock.

Magmatic rock - has solidified from the molten rock material. The host-rock and Seafloor Massive Sulfides (SMS) are magmatic rocks.

Metamorphic rock - is a result of partial or complete recrystallisation in the solid state of pre-existing rock.

Sedimentary rock - is formed as a result of a consolidation of sediments.

Mineral deposit - Accumulation of minerals and metals of potential economic interest through geological processes. Mineral deposits are the results of geological processes that have led to a higher concentration of specific (or several) elements within the host-rock, the concentration

(grade) of the specific element(s) is/are significantly higher than the background concentration of the same element(s). Mineral deposits are classified in different ways depending on the application. For example:

Relative to the geological formation of the host-rock.

- Magmatic deposits.
- Sedimentary deposits.
- Metamorphic deposits.

Ore - is a deposit of minerals or elements in an amount (tonnage) and grade (concentration) that mining and mineral processing to prepare a sell-able concentrate would be economically feasible. Ore is typically used for deposits of metallic elements but may also be used for industrial minerals, construction raw materials, natural stone, and energy minerals under the same conditions.

Deep-marine mineral deposits - mineral deposits found outside the continental slope. Typically formed by geological processes on the seafloor and in the ocean. Examples: SMS, Polymetallic Manganese Nodules (PMN), Cobolt rich Manganese Crust (CMC).

1.3 What Are Sulfide Minerals

A sulfide mineral, also spelt as sulphide, is any member of a group of compounds of sulfur with one or more metals. Most sulfides are simple structurally, exhibit high symmetry in their crystal forms, and have many metals properties, including metallic lustre and electrical conductivity. They often are strikingly coloured and have a low hardness and high specific gravity.

The composition of the sulfide minerals can be expressed with the general chemical formula.

$$A_m S_n \tag{1}$$

Where:

A - metal element

S - sulfur element

m and n - integers

Sulfide mineral deposits originate in the following principal processes, both of which have reducing conditions: (A) separation of an immiscible sulfide melt during the early stages of crystallization of primary magmas; and (B) deposition from aqueous brine solutions at temperatures in the 300-600° C range and relatively high pressure, such as at the seafloor or several kilometres beneath Earth's surface. Phase relations of sulfides are particularly complex, and many solid-state reactions occur at relatively low temperatures (100-300° C), producing complex intergrowths.

Several hundred sulfide minerals are known, but only five are sufficiently abundant accessory minerals to have been categorized as 'rock-forming (Bowles 2011). These five are Pyrite (Py), Pyrrhotite (Po), Chalcopyrite (Cpy), Galena (Gn) and Sphalerite (Sph). Their chemical composition is presented in Table 1 below.

The Py, Po, and Cpy are mostly formed during the process (A), while Gn and Sph occur due to process (B). The sulfides are the most important group of ore minerals because they are responsible for the concentration of many metals as mineable deposits. The metals that occur most commonly in sulfides are Fe, Cu, nickel (Ni), Pb, cobalt (Co), Ag and Zn though about fifteen others enter sulfide structures (Vaughan and Corkhill 2017).

Mineral	Chemical formula
Pyrite	FeS_2
Pyrohotite	$Fe_{(1-x)}S$
Chalcopyrite	$CuFeS_2$
Galena	PbS
Sphalerite	ZnS

Table 1: Sulfide minerals chemical composition

1.4 What Are The SMSs

SMS deposits, also named volcanic-associated massive sulfide deposits, hydrothermal sulfide deposits, massive polymetallic sulfides on the modern seafloor, and volcanogenic massive sulfide deposits, are generated in tectonically active areas such as back-arc spreading centre, volcanic arc, and mid-ocean ridges, these areas are presented in Figure 2. The tectonic activities lead to the fracturing of crustal rocks and create paths for sea bottom fluids circulation. These fluids reach near magma regions, and magma heats fluids, creating hydrothermal fluid circulation. SMS deposits form at or near the seafloor where circulating hydrothermal fluids driven by magmatic heat are quenched through mixing with seawater or pore-water in near-seafloor lithologies (Shanks III et al. 2012). The fluids reach the sea bottom, cool down, mix with seawater, and precipitate sulfides forming chimneys. The chimneys have up to 40 % porosity thanks to circulating hydrothermal fluids in their genesis process. The chimneys are fragile. They eventually get destroyed and form SMS mounds. Many deposits have stringer or feeder zones beneath the massive zone consisting of crosscutting veins and veinlets of sulfides in a matrix of the pervasively altered host-rock and gangue. SMS deposits contain ore bodies, consisting of more than 40 % of sulfides, such as Py, Po, Cpy, Sph, and Gn minerals, containing a significant amount of Cu, Zn, Fe, Pb, Au, Ag and the remaining part is Quartz (Qtz), Barite (Ba), Anhydrite (Anh), Fe, Chlorite (CiO_2), Talc (Tlc). Cu precipitate early from high temperature hydrothermal circulating fluids while Zn precipitate at a later stage from colder fluids. SMS deposits vary in shape and size. They might be less than 1 ton and super-giant ones even more than 1.5 Bt. Schematic diagram of typical SMS genesis process is presented in Figure 3 (Khayrullaev 2021).

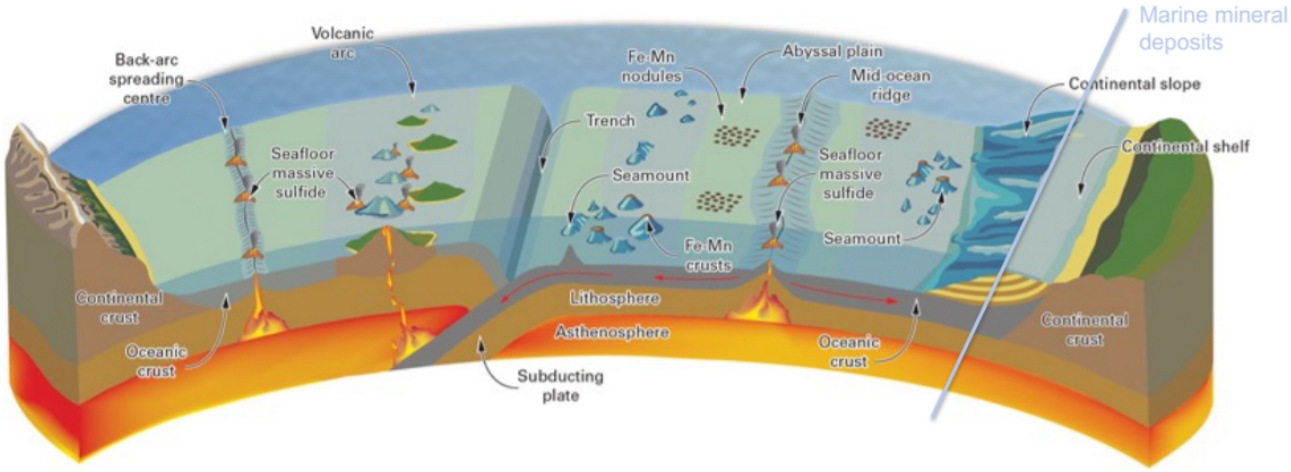

Figure 2: Tectonically active SMS deposition areas.

Source: Image modified after Ian Longhurst (Copyright British Geological Survey © UKRI 2018)

Other rocks always host SMS deposits, and these rocks are named host-rocks. Host-rocks type depends on SMS's deposition area. Alteration zonation in the host-rocks surrounding the SMS are usually well-developed and include advanced argillic (kaolinite, alunite), argillic (illite, sericite),

sericitic (sericite, quartz), chloritic (chlorite, quartz), and propylitic (carbonate, epidote, chlorite) types (Bonnet et al. 2007). Hannington et al. 1997, Galley et al. 2007 proposed to categorize host-rocks in mafic, bimodal mafic, mafic siliciclastic, bimodal felsic, bimodal siliciclastic types. In contrast, Franklin et al. 2005 suggested to group them as bimodal mafic, mafic, pelitic-mafic, bimodal-felsic, and siliciclastic-felsic. These categorizations are not suitable for seismic geophysics, in terms of rocks' V_p and ρ contrast and categorizing host-rocks in ultramafic, mafic, intermediate, felsic was presented in Khayrullaev 2021.

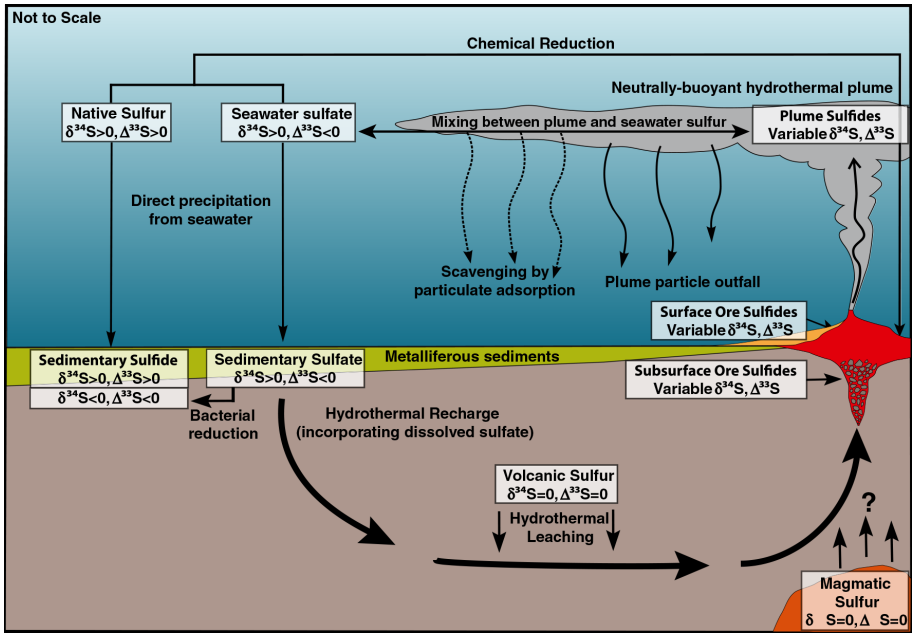

Figure 3: Schematic diagram of an Archean seafloor hydrothermal system and associated volcanogenic massive sulfide deposit, with predicted multiple sulfur isotope signatures.

Source: Figure 1, Sharman et al. 2015

1.5 Why Do We Need SMSs

One knows SMS deposits contain ore bodies, consisting of more than 40 % of sulfides, such as Py, Po, Cpy, Sph, and Gn minerals, containing a significant amount of Cu, Zn, Fe, Pb, Au, Ag. Only modern, hydrothermally active SMS sites globally contain at least 650 million t of massive sulphides containing 10 million t of Cu, 29 million t of Zn, 1 million t of Pb, 33 million kg of Ag and 750 000 kg of Au according to studies in Hannington et al. 2011, 1997. Published bulk geochemical data from 95 of these modern SMS deposits shows a median grade of 3 wt.- % Cu, 9 wt.-% Zn, 2 g/t Au and 100 g/t Ag (Hannington et al. 2011; Monecke et al. 2016).

There are several drivers for SMS mining to extract these valuable elements nowadays. Global economic growth, state securing access to resources, innovative frontier industry, and increasing difficulty and complexity of onshore mining are primary drivers of the global transition to environmentally friendly, sustainable green energy sources. Global economic growth, the complexity of onshore mining and the global transition to environmentally friendly, sustainable green energy sources are considered primary drivers in the thesis and focus is put on them.

Global economic growth - globally, the size of the middle class (defined as those households with daily expenditures between $10 and $100 per person in purchasing power parity terms) is predicted to increase from 1.8 billion people in 2009 to 3.2 billion by 2020 and 4.9 billion by 2030, with the majority of the population growth (85 per cent) located in Asia (Kharas 2010). The purchasing power of this group is forecast to increase from US$21 trillion to US$56 trillion by 2030 (Kharas 2010). Rising incomes lead to changes in consumption, with increased demand for durable goods, such as cars and white goods (household equipment) with high mineral and/or metal

content (Kharas and Gertz 2010). The World Bank identifies China as the chief driver of metal demand over the past decade (Burns and van Rensburg 2012). Between 2000 and 2009, Chinese consumption of the main base metals (Al, Co, Pb, Nc, and Zn) rose 17 percent per-annum, a trend that continued during the recovery from the global financial crisis (Figure 4). Additionally, the world population is growing faster than at any time in history (Figure 5), accompanied by an even more rapid increase in mineral consumption as the global standard of living increases and a growing number of consumers enter the market for minerals (Kesler 2007).

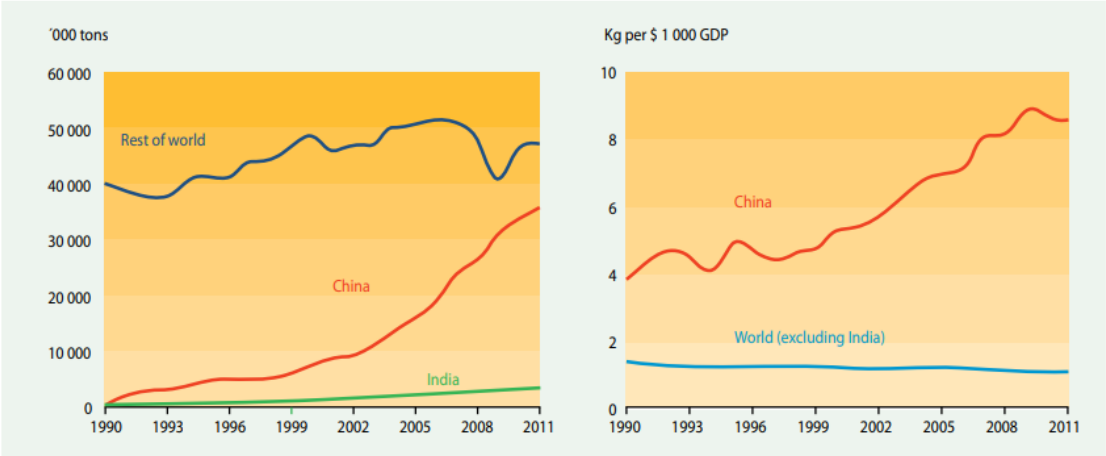

Figure 4: Refined metal consumption and metal consumption intensity.

Source: The-World-Bank 2012

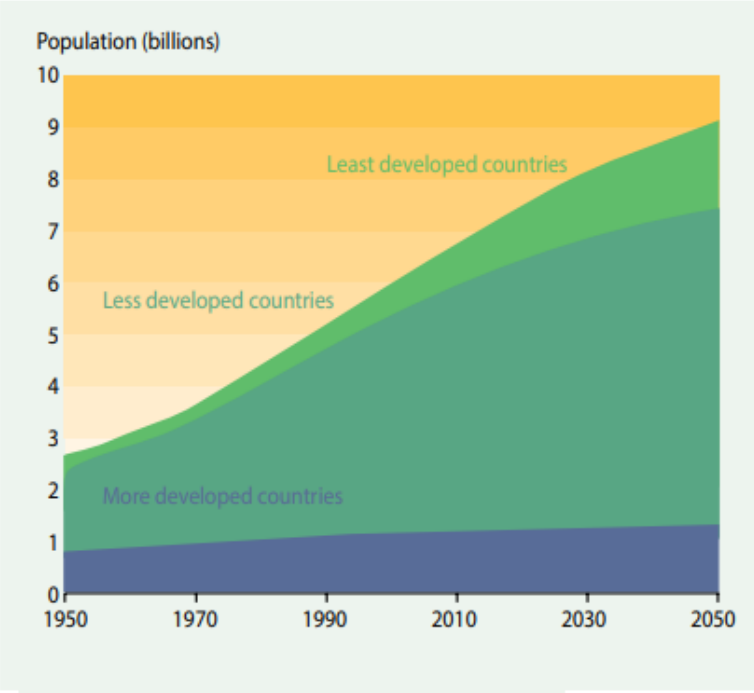

Figure 5: World population growth, 1950-2050.

Source: UNDESA 2011

The complexity of onshore mining - the discovery rate of high-grade onshore ore deposits is declining lately (Figure 6). High-grade ores have been mined, and mining companies are investing more in lower-grade ore deposit development nowadays. This is increasing waste rocks generation while mining, which is represented in the Cu mining example in Figure 7 and the cost of the

production. These factors are making onshore ore extraction economically and environmentally harder.

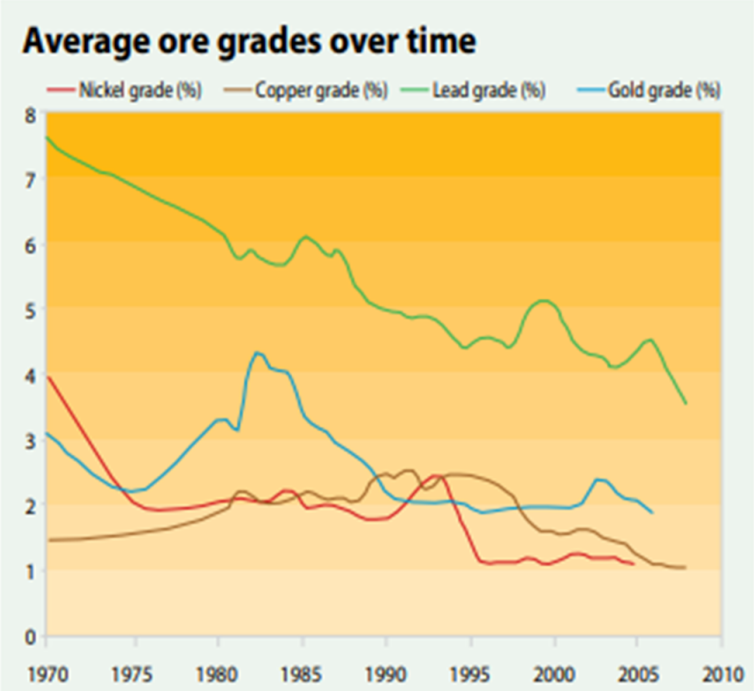

Figure 6: Declining average ore grades.

Source: Figure 3.6, Baker and Beaudoin 2013

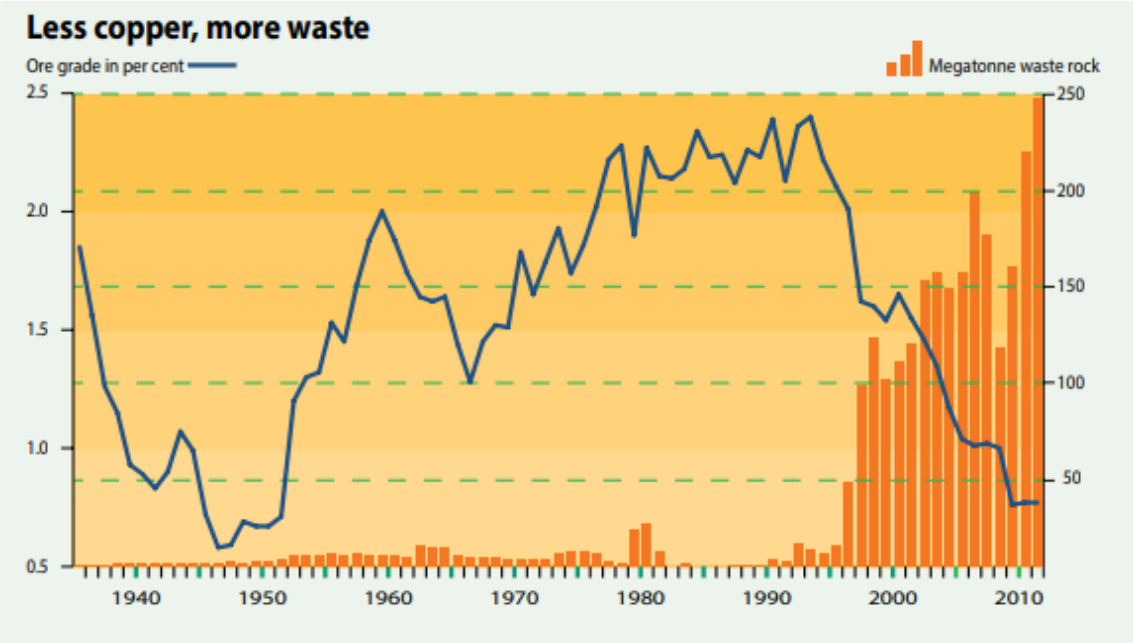

Figure 7: Increase in mine waste associated with lower ore grades.

Source: Figure 3.7, Baker and Beaudoin 2013

The global transition to environmentally friendly, sustainable green energy sources - sustainability issues are tied to, but not wholly concerned with, impacts from existing terrestrial mining. The rising demand for clean-energy infrastructure to replace fossil fuels and reduce carbon emissions will place further demand pressure on metals. Many clean-energy technologies (such as wind

turbines, solar power units, electric cars, etc.) are far more metal-intensive than traditional forms of energy, requiring far greater quantities of metal to produce an equivalent unit of energy output. With its goal of intra- and inter-generational equity, sustainability has become a powerful social driver, able to influence projects, governments, and industries. This is evident in the increasing pressure on the industry to comply with a new community and government expectations and standards, despite the rising costs of complying (Baker and Beaudoin 2013).

1.6 Can Seismic Geophysics Detect SMS Deposits

Research has been done on theoretical aspects of seismic geophysics application for massive sulfide deposits detection and there are successful case examples of onshore seismic geophysics application for massive sulfide deposits imaging. In Salisbury et al. 1996, scientist considered theoretical aspects of seismic geophysics application while field case examples of imaging massive sulfide bodies 900-1500 m and 550-600 m below in sub-surface are presented in Milkereit et al. 1996, Salisbury et al. 2000 correspondingly. Considering the main difference between offshore and onshore seismic geophysics is the presence of water column until the sea-bed, and many seismic geophysics techniques for petroleum exploration and production have been successfully transferred from onshore to offshore and visa-versa during many years. The scientific work has been done for onshore massive sulfide deposits imaging using seismic geophysics is equally valid and applicable for SMS imaging on offshore conditions.

Three general criteria must be satisfied for imaging massive sulfide deposits using seismic geophysics:

1. Difference in Z between host-rock and massive sulfide should be large enough to create a strong reflection. If one denotes Z of host-rock as Z_{hr} and Z of massive sulfide deposit as Z_{sd}. Zero angle reflection coefficient (R_0) is calculated as

$$R_0 = \frac{Z_{sd} - Z_{hr}}{Z_{sd} + Z_{hr}} \tag{2}$$

   Where:

   R_0 - zero angle reflection coefficient;

   Z_{sd} - Z of massive sulfide deposit;

   Z_{hr} - Z of host-rock.

2. Massive sulfide deposit must have a diameter greater than the width of the first Fresnel zone (d_F) to be imaged as a planar reflection surface

$$d_F = \sqrt{\frac{2zV_p}{f}} \tag{3}$$

   Where:

   d_F - Fresnel zone diameter;

   z - reflecting surface depth;

   V_p - formation P-wave velocity;

   f - dominant frequency.

3. The massive sulfide deposits should have thickness greater than a quarter of the (predominant) wavelength (λ) criterion (t_{min})

$$t_{min} = \frac{V_p}{4f} \tag{4}$$

   Where:

t_{min} - quater of (predominant) wavelength criterion;

V_p - formation P-wave velocity;

f - dominant frequency.

Massive sulfide deposits with smaller thicknesses can still be detected. However, their thickness can not be determined, and reflection amplitudes will be decreased by destructive interference (Widess 1973).

Below is an attempt to showcase how massive sulfide deposits satisfy these conditions.

In Salisbury et al. 1996 massive sulfide and host-rock samples' V_p and ρ are measured in the laboratory under high pressures (200 MPa), have shown that massive sulfides and host-rocks have distinct differences compared to silicate rocks. Common sulfide minerals have extremely variable V_p while their ρ are consistently high (Table 2), resulting in ores of even low grade having high Z. Host-rocks encountered in massive sulfide deposition environments can be categorized as felsic (F), intermediate (IM), mafic (M) and ultramafic (UM) rocks according to Khayrullaev 2021. They have varying V_p as massive sulfides while their ρ are relatively lower (Figure 8). Sediments and basement interface create R_0 equal to 0.06, which is sufficient to make a strong reflection (Salisbury et al. 1996), which means R_0=0.06 is sufficient to have a bright reflection from any interface. An example case is shown in Figure 9, as one can see massive sulfides' Z increases with its grade, the difference in massive sulfides' and host-rocks' Z=2.5-5 is enough to create R_0=0.06, and mostly this condition is met even for massive low-grade sulfides, thanks to the difference in their densities.

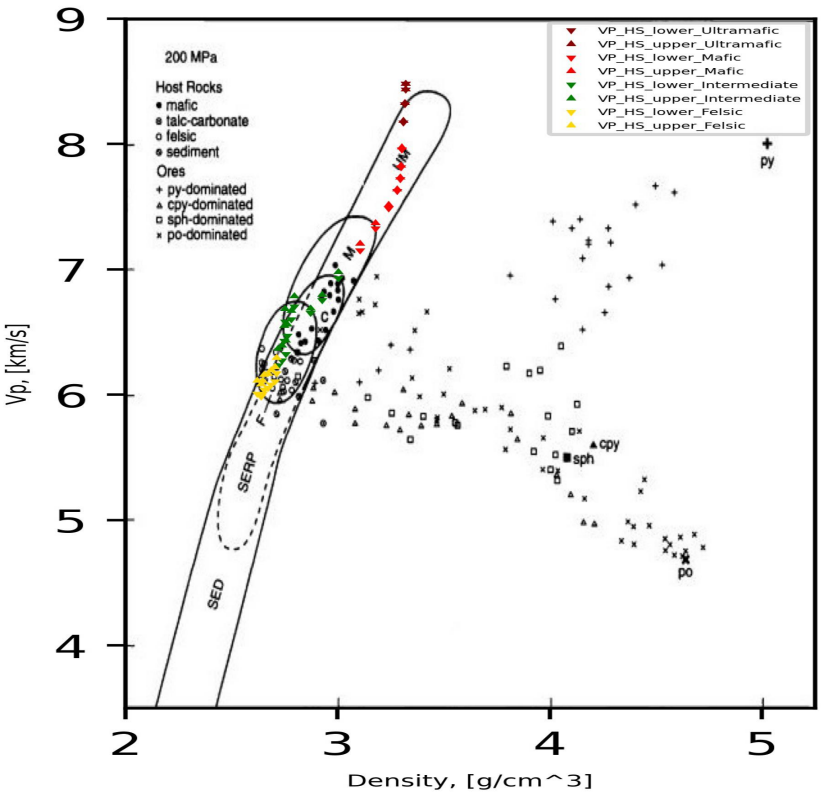

Figure 8: Measured samples in Salisbury et al. 1996 and modeled non-porous host-rocks in V_p versus ρ domain

.

Source: Figure 8 in Khayrullaev 2021

Sulfide mineral	Vp, **[m/s]**	$\rho, [kg/m^3]$	Z, **[(m/s)*(kg/m^3)]**
Pyrite	8 040	5 020	40 360 800
Pyrohotite	4 680	4 630	21 668 400
Chalcopyrite	5 360	4 060	21 761 600
Sphalerite	5 500	4 080	22 440 000

Table 2: Sulfide minerals V_p and ρ laboratory measurements.

Source: Modified Table 1 in Salisbury et al. 1996

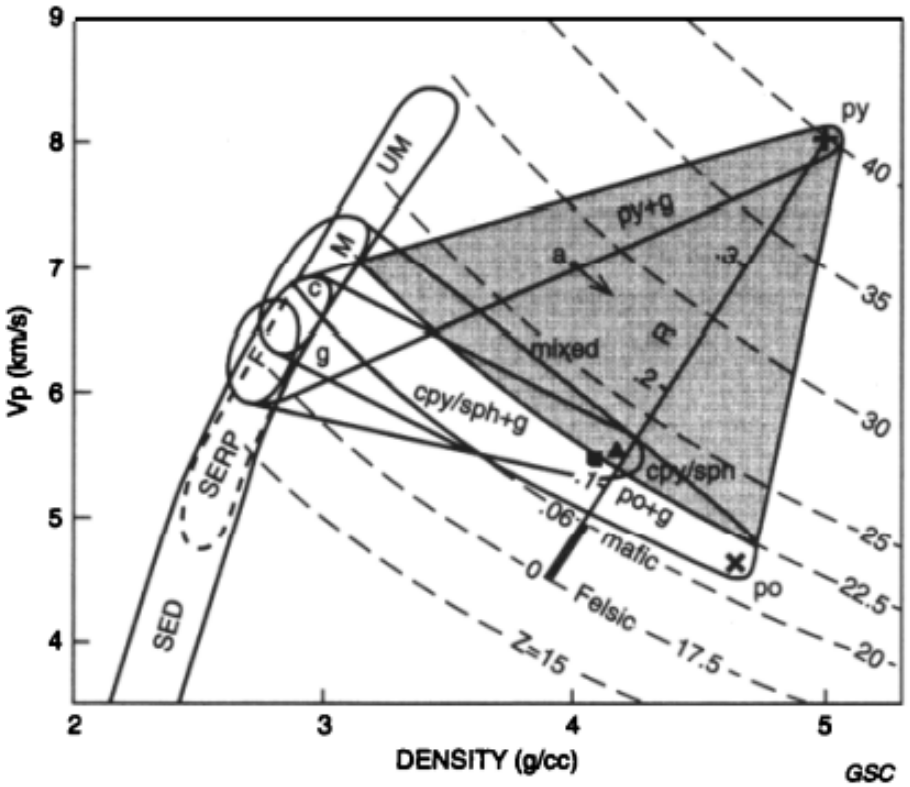

Figure 9: Lines of constant Z superimposed on V_p vs ρ fields for silicate rocks and sulfide ores. Also shown are the reflection coefficient scale for ores versus felsic rocks and the minimum coefficient (R_0= 0.06) required to make a strong reflector. Point "a" corresponds to ore with 50 percent pyrite and 50 percent felsic gangue. "SERP" means Serpentites.

Source: Figure 6 in Salisbury et al. 1996

Usually, massive sulfide deposits have varying dimensions, small deposits may have tens of thousands of square meters, and giant deposits can have dimensions of several square kilometres in plan view. For instance, the Windy Craggy deposit in British Columbia, Canada, is about 200 m wide and 1.6 km long (Peter and Steven 1999), with a dimension of 0.3 km^2. The Kidd Creek orebody in Ontario, Canada, is approximately 500 m wide and at least 2,000 m long (downdip mining extent) and has a minimum dimension, vertically restored, of 1.0 km^2 (Hannington et al. 1997). The Besshi deposit on Shikoku, Japan, is 3,500 m by 1,800 m, thus covering an area (reconstructed prior to deformation) of 6.3 km^2 (Slack 1993). If one assumes massive sulfides with V_p in range from 4500 m/s to 8100 m/s, that its located z=2000-4000 m at or near sea-bed and nowadays seismic geophysics can be recorded at f 40-240 Hz, d_F= 274-1273 m (Please refer to Appendix A.1 for d_F calculation proves) according to equation 3.

Typically massive sulfide deposits have vertical extents (thicknesses) on the order of tens of meters; thicknesses of >250 m occur in a few deposits, such as San Nicolás in Mexico, Tambo

Grande in Peru, and Sibay in Russia (Johnson et al. 2000; Tegart et al. 2000; Herrington et al. 2005). Considering the same massive sulfides' V_p and seismic data f ranges, one can calculate that t_{min} is in range 5-51 m (Please refer to Appendix A.1 for t_{min} calculation proves.) by equation 4.

One can see from the last two paragraphs above that massive sulfides size within a range or extend d_F most of the time, and their thickness is in or above the range of t_{min}, which means they can be imaged by correctly chosen seismic acquisition set up providing required f.

Examples of recording seismic with a suitable set up for massive sulfide deposits imaging laying 900-1500 m and 550-600 m below in sub-surface are presented in Milkereit et al. 1996, Salisbury et al. 2000 correspondingly.

Scientists focused on Sudbury structure in Canada (Figure 10) in Milkereit et al. 1996. A high-frequency seismic (from 30 to 140 Hz) 2D profile shown as line 43 in Figure 10 located across a deep-seated mineral deposit lying below the South Range of the Sudbury structure was recorded. The recorded data was processed in the following steps static corrections, deconvolution, time-variant band-pass filtering, crooked line binning, dip moveout (DMO) processing, detailed stacking velocity analysis, and migration.

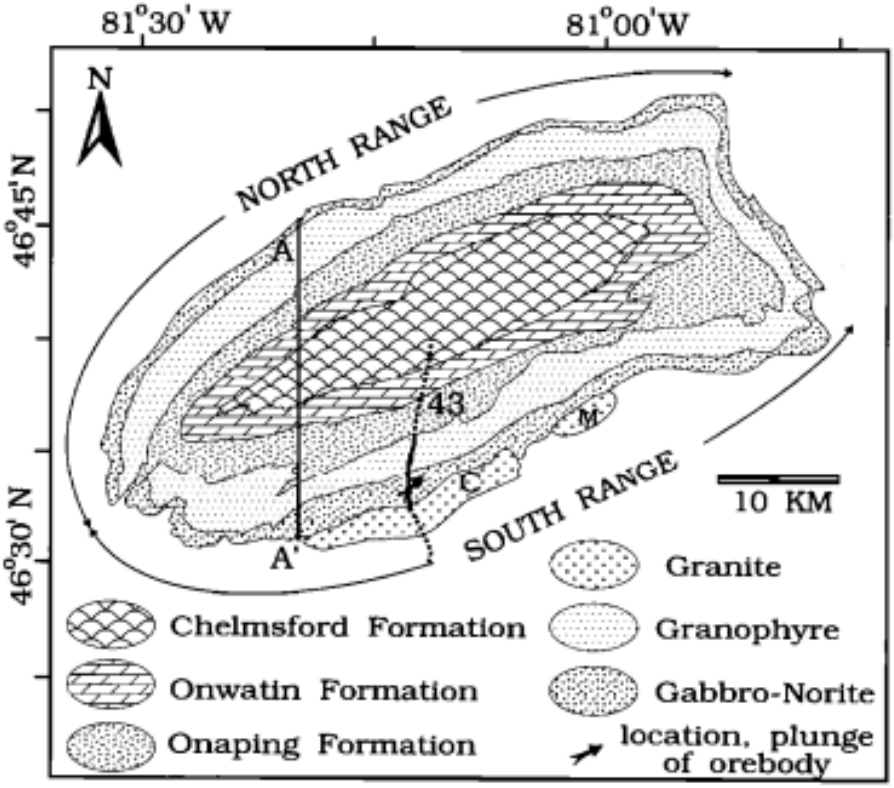

Figure 10: Map showing geology of the Sudbury structure and location of 2D seismic profile discussed in the text. Seismic section shown in the Figure 11 is taken from solid portion of line 43

Source: Figure 1 in Milkereit et al. 1996

Water saturated sediments have V_p higher than 1 500 m/s, and mafic rocks have velocities of about 6 000 m/s as expected according to processing results. For interpreting the resulting seismic synthetic reflection, seismic data was modelled assuming norite, granite-greenstone host-rocks with Z equal to 19 and 18 correspondingly and Zsb set equal to 22, massive sulfide's geometry modelled satisfying above mention criteria, and please refer to Milkereit et al. 1996 for additional details. The resulting processing and modelling results are presented in Figure 11. As one can see, a massive sulfide deposit is imaged successfully.

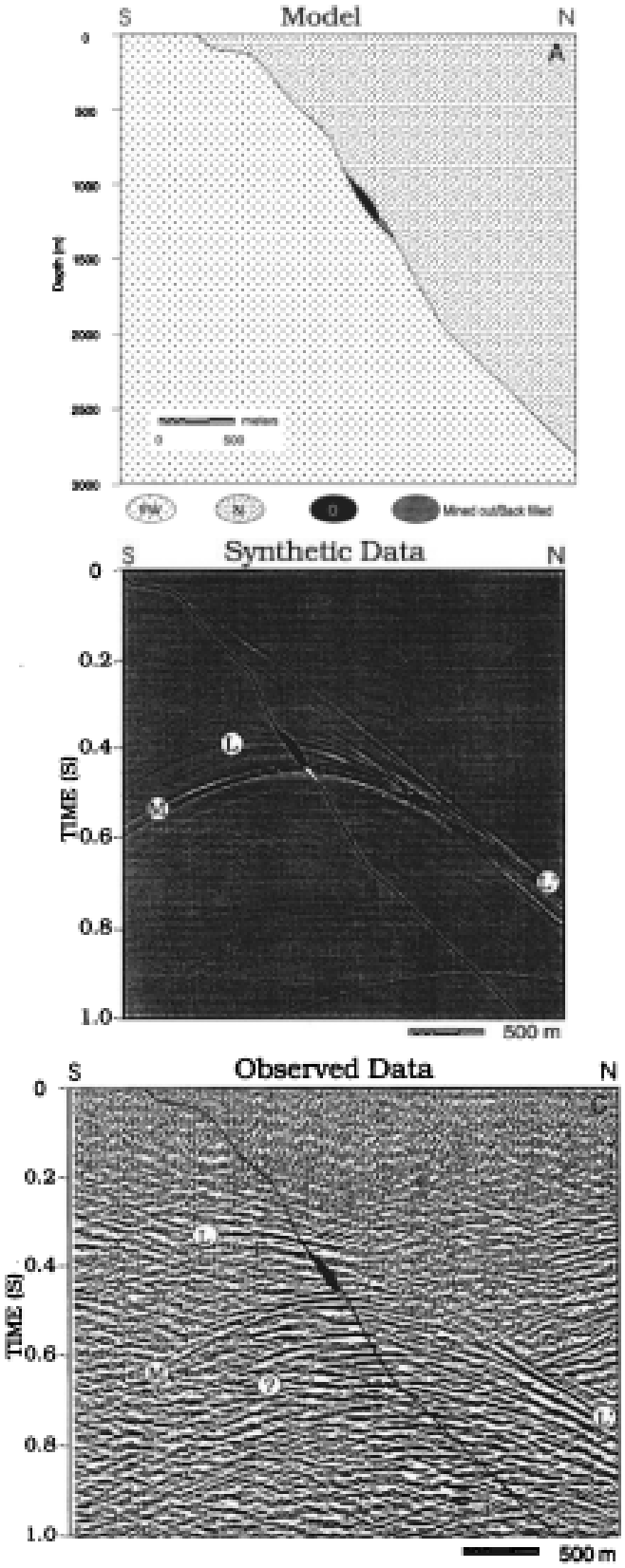

Figure 11: Modelled and observed after processing 2D seismic high frequency profile data. Massive sulfide deposit denoted with "O" and colored in black, located approximately on 0.4 s in time and 1350 m in depth domains.

Source: Figure 5 in Milkereit et al. 1996

For another successful case study of imaging massive sulfide deposits, the 2D seismic profile recorded on the Halfmile Lake deposit (Figure 12) is provided in this work.

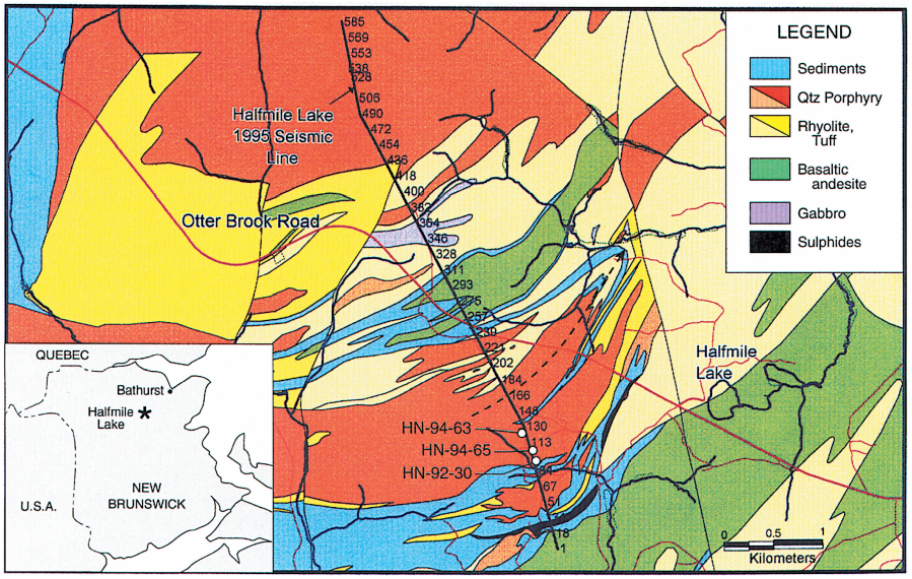

Figure 12: Geological map of Halfmile Lake deposit showing location of 2D seismic line presented in Figure 14

Source: Figure 2 in Salisbury et al. 2000

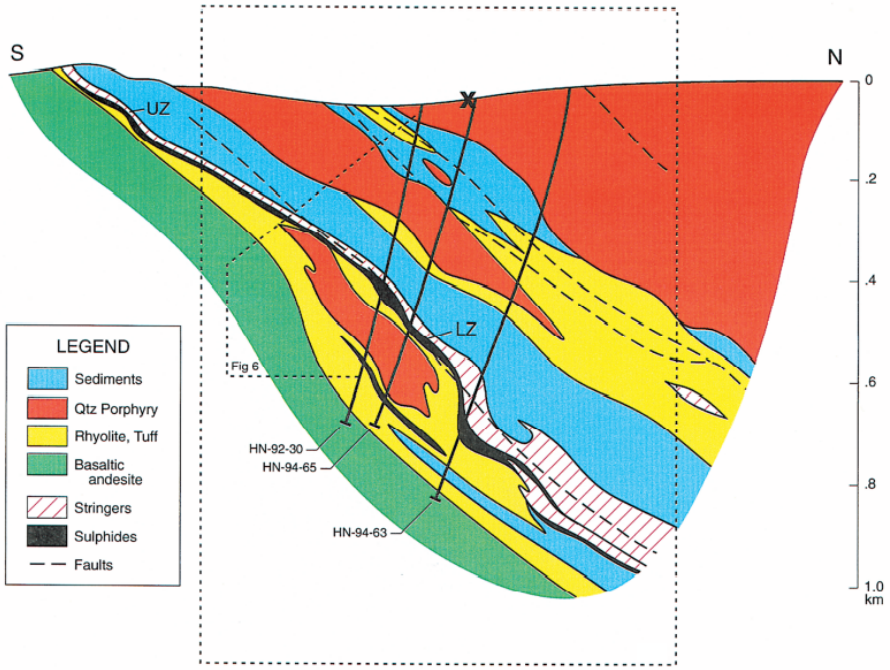

Figure 13: Simplified geological cross-section through Halfmile Lake deposit based on drilling results projected onto seismic line between stations 1 and 166. The box created by dashed line shows location of 2D seismic profile showed in Figure 14

Source: Figure 3 in Salisbury et al. 2000

The massive sulfide deposit in the south limb of a large antiform ranging in thickness from 1 to 45 m and extended 3 km has been studied. The massive sulfide body has a 45 ° dip in a north-

northwest and is overlaid by a stringer zone containing 5 % and 35 % Py and Po. Massive sulfide deposits consist of Py-Po rich, layered sulfides and Po rich breccia matrix sulfides containing variable amounts of Sp, Ga. They are hosted by thick turbidite sequences of felsic volcanic, epiclastic rocks, argillites, and intermediate volcanic rocks. Massive sulfide deposit is separated into two Upper zones (UZ) and Lower zone (LZ). The researchers focused on undeveloped, largest, 6.1 million ton LZ that has 9.7 % Zn, 3.34 % Pb, 0.1 %. Simplified geology of 2D seismic survey area is presented in cross-section in Figure 13.

The 5.85 km long multichannel 2D seismic shown in Figure 12 is conducted over the massive sulfide deposit. The recorded data is processed by applying static correction, scaling, high-pass filter, deconvolution, common mid-point binning, stacking velocity analysis, noise suppression, post-stack scaling and a clear image of massive sulfide deposit is obtained (Figure 14).

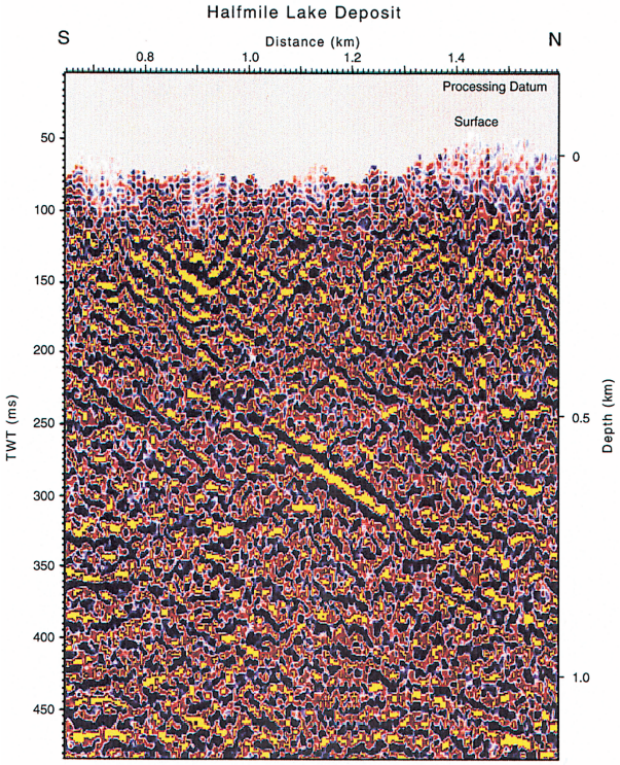

Figure 14: Unmigrated 2D multichannel reflection seismic of the Halfmile lake massive sulfide deposit.

Source: Figure 7 in Salisbury et al. 2000

The author hopes mentioned above brief explanation of the theory and case examples result could explain that seismic geophysics can detect SMS deposits.

2 Theory

2.1 Analytical Rock Physics Template

The main work for developing the rock physics template shown in Figure 1 was performed during the author's specialization project, and one can find the details of this work in Figure Khayrullaev 2021. Figure 1 is nothing but a modified version of a rock physics template in V_p versus ρ domain developed for differentiating host-rocks from SMS deposits that are provided in Figure 22 in Khayrullaev 2021. The modification is performed by converting the rock physics template from V_p versus ρ domain to Z versus ρ domain and deleting actual data in Figure 22 in Khayrullaev 2021. The conversion is made by replacing the vertical V_p axis with Z, which is the multiplication of V_p and ρ. Here the brief theory behind the rock physics template is provided, and the reader is kindly asked to refer to Khayrullaev 2021 for more details. One can see areas for porous host-rocks models and porous SMS deposits models on 1.

The porous host-rock models were generated using the information on bulk modulus, shear modulus, and density of minerals in the mineralogical classification of common magmatic rock types from Schön 2015. It is assumed that porous host-rocks are water-filled. The mineral type and volume fraction vary with silica content in the mineralogical classification of common magmatic rock types in Schön 2015. At first, the non-porous host-rock models are generated for each silica content in the mineralogical classification of common magmatic rock types in Schön 2015. Then they are divided into four Ultromafic host-rock, Mafic host-rock, Intermediate host-rock, and Felsic host-rock categories depending on silica content in the mineralogical classification of common magmatic rock types in Schön 2015. In order to generate one model for certain silica content, bulk modulus, shear modulus and density of that model are calculated by inserting bulk modulus, shear modulus and volume fraction of corresponding minerals at the silica content into equations for Hashin-Shtrikman-Walpole bonds and by taking the weighted average density of minerals in the mixture. After that, several models of the porous host-rock model are calculated by introducing water-saturated pores into the calculations. The model generation process is almost the same as for non-porous host-rock models, except minerals fractions corresponding to silica content, which are decreased depending on porosity and water bulk modulus, water shear modulus, and water density are taken into account in Hashin-Shtrikman-Walpole bounds and in mixture density calculations. Using resulting bulk modulus, shear modulus and density of mixtures, their V_p is calculated.

Porous SMS deposit models are created assuming SMS deposits are made from Py,Po, Sp sulfide minerals and water-filled pores. Firstly as it is with non-porous host-rock models, non-porous SMS deposit models are created. Two of three Py, Po, Sp sulfide minerals are mixed in different ratios to create one leg of a triangle, and three legs of the triangle are created in this way. Bulk modulus, the shear modulus of a mixture, is calculated by taking half of the Hashin-Shtrikman-Walpole bounds, and its density is computed by taking the weighted average density of minerals in the mixture. Further, porous SMS deposit models are created, introducing water-filled pores into the calculation procedure above.

2.2 Fresnel Zone

To understand what is Fresnel zone, it is important to be familiarized with the Huygens-Fresnel principle. The huygens-Fresnel principle states that wave-fronts every point is a source of wavelets. These wavelets propagate in the same direction at the same speed as the source wave. The new wavefront is a line tangent to all of the wavelets, see Figure 15 (Stovas and Hao 2015).

The Fresnel zone is the area from which reflected energy arriving at a detector has phases differing by no more than 180 degrees. The first Fresnel zone is the circular area directly beneath the source where wave energy reflects constructively (see Figure 15). The diameter d_F of the first Fresnel zone is expressed by equation 3. The first Fresnel zone is often taken as a measure of the horizontal resolution of unmigrated seismic data. (Stovas and Hao 2015). Fresnel zone's visual example is provided in Figure 16.

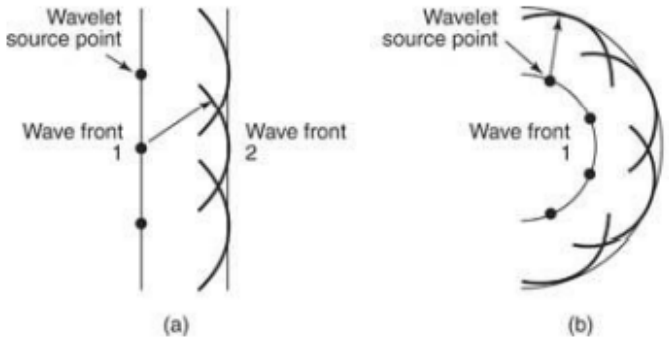

Figure 15: The Huygens-Fresnel principle for a plane wave (a) and a spherical wave (b).

Source: Figure 8.2. in Stovas and Hao 2015

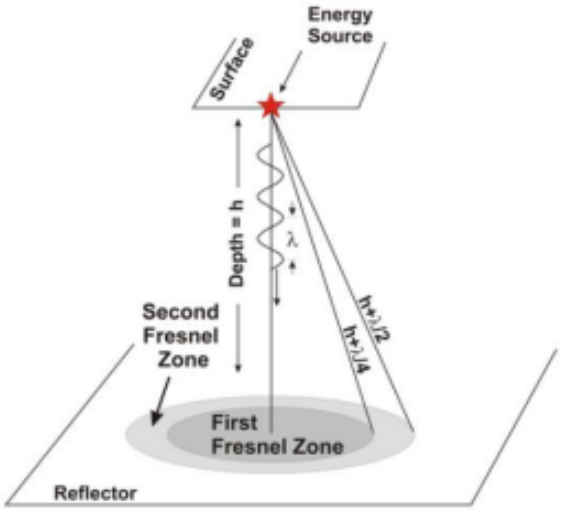

Figure 16: The partition of first and second Fresnel zones. The first Fresnel zone corresponds to the dark gray area in this plot.

Source: Figure 8.3. in Stovas and Hao 2015

2.3 Quarter of The Wavelength Criterion

t_{min} is a simple approach derived based on works of Widess 1973, where in elementary terms, the method for estimating bed thicknesses that cannot be visible on seismic trace recorded with certain f is provided, these beds are named as thin beds. One can use the t_{min} to determine a bed thickness value that would be visible on seismic trace with certain f. Thin beds are defined as beds that have thickness less than $\frac{\lambda}{8}$, that would have two-way traveltime (TWT) through less than about $\frac{\tau}{4}$, where τ is a predominant period of the wavelet.

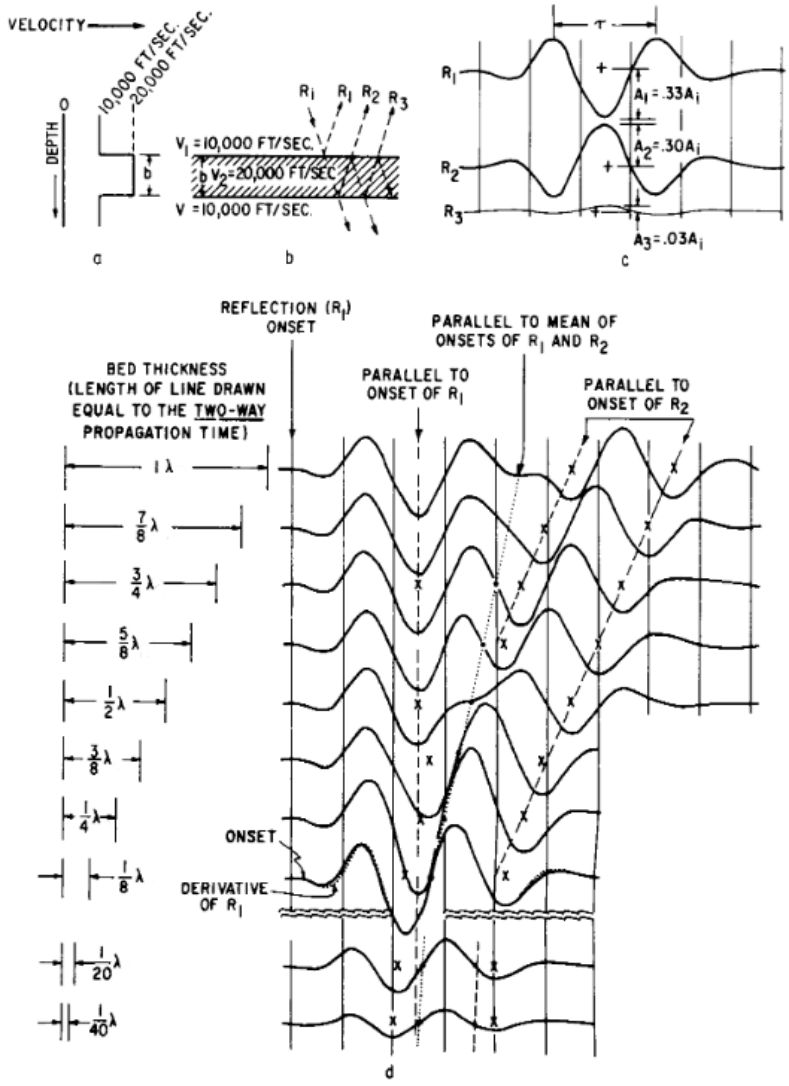

Figure 17: Effect of bed thickness on reflection. a. Velocity graph. b. Reflection ray diagram. c. Individual reflected waves are composited using time delays computed from bed thickness. d. Form and relative timing of composite reflection as a function of bed thickness. X marks through time. 0 marks zero-amplitude time ("centre" of composite reflection). The timing line interval is 0.5 T. b = thickness of the bed. 7 =predominant period of incident wavelet. τ=wavelength within the bed. Amplitudes for composite reflections are all relative to the same incident wavelet Rt.

Source: Figure 2. in Widess 1973

In his works, Widess has shown simulation results of reflection of the same wave from beds with different thicknesses while keeping all other variables constant. One can see part of his simulation results in Figure 17. During the simulations, a bed with higher velocity is located between two beds with lower velocities (Figure 17.a), the separate (Figure 17.c) and composite (Figure 17.d) wave-traces resulted in a wave reflection from the upper reflecting interface and lower reflecting interface have been constructed. One can easily recognize in the composite wave trace for bed with a

thickness equal to 1 λ two events representing the wave reflections from upper and lower reflecting interfaces, as it is shown in Figure 17.c. As bed thickness decreases, two wavelets resulting in reflection from lower and upper reflecting interfaces start to interfere, and they become separately invisible on the composite seismic trace due to their negative interference when bed thickness becomes lower than $\frac{\lambda}{8}$. Hence one cannot see the bed on seismic trace below this threshold $\frac{\lambda}{8}$.

In order to image a reflecting interface on seismic, a good continuous reflection event representing the reflection interface on seismic traces is needed. Taking into account presence of noise during seismic experiments, the threshold is lifted from $\frac{\lambda}{8}$ to $\frac{\lambda}{4}$ as a rule of thumb, which is named as t_{min}. $\frac{\lambda}{4}$ can be rewritten as in equation 4 for convenience by taking into account f and V_p of seismic experiments.

2.4 Model Based Seismic Inversion

Seismic inversion is estimating subsurface layers elastic properties from seismic data. Seismic inversion result has several advantages compared to seismic data. These are increased resolution thanks to removing wavelets from seismic traces and estimated subsurface layers' elastic properties that can be used for quantitative analyses. Seismic inversion can be performed on post-stack seismic data and pre-stack seismic data. Post-stack seismic data inversion results in determining subsurface layers Z.

There are several things to check in post-stack seismic data processing before performing post-stack seismic data inversion. These are:

- Amplitudes are true relative amplitudes
- Amplitudes are zero offset amplitudes
- Seismic wavelet is invariant in the window of interest
- Bandwidth is maximised
- All multiples and noise are removed from seismic data

There are several types of post-stack seismic inversion methods, such as Model-driven inversion, Simple trace integration of seismic traces, Spare spike inversion and Coloured inversion. Model-based inversion gives satisfactory results. No zero-phase wavelets can be utilised even when well control is limited, and the seismic quality is relatively poor (Veeken and Da Silva 2004).

A model-driven inversion creates a simple model representing low-frequency Z change with depth, consisting of Z layers. Seismic wavelet is estimated on the window of interest in seismic data and convolved with reflection coefficients generated from Z layers in the model to produce synthetic seismic traces. The difference between synthetic and real seismic traces is estimated. If the difference is not satisfactory, the model Z is slightly changed in such a way as to improve the fit between synthetic and actual seismic traces. The Z change must be constrained to decrease the effect of noise on seismic data to Z change and prevent the model-based inversion algorithm from generating false results. Figure 18 presents the model-driven inversion's flow-chart.

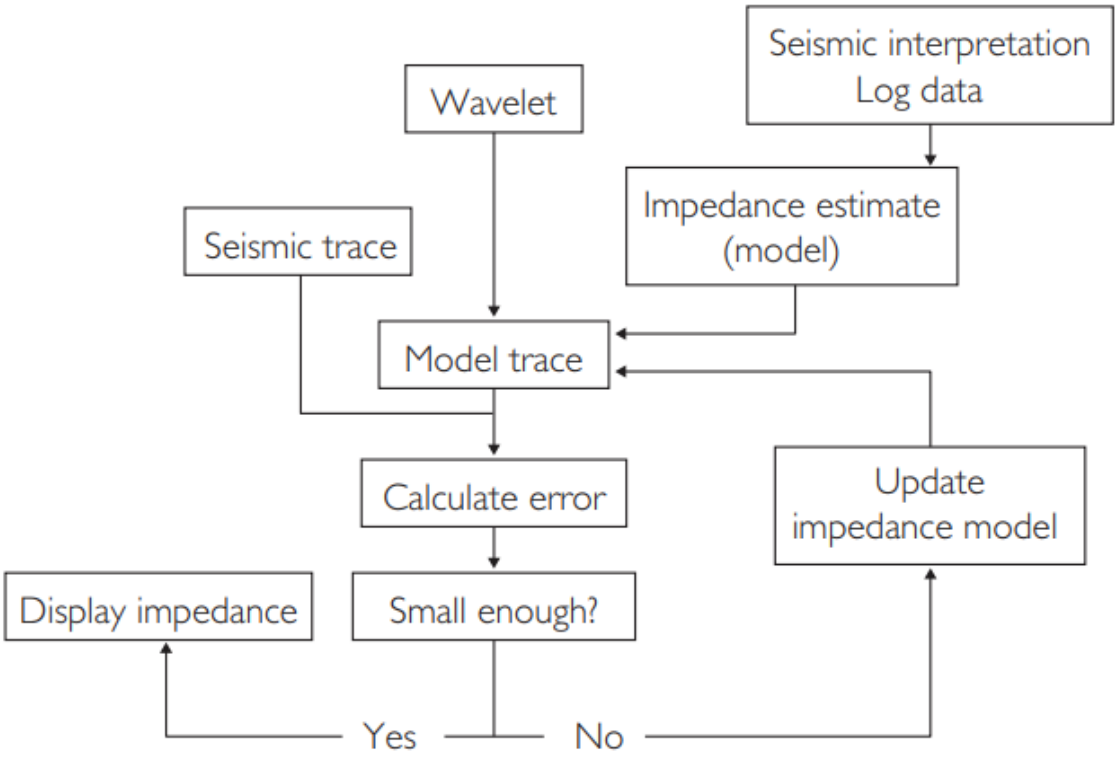

Figure 18: Generalised flow-chart for model driven inversion.

Source: Figure 9.4. in Rob and Bacon 2014.

3 TAG SMS Field and Database

3.1 TAG SMS Field

TAG segment of the Mid-Atlantic Ridge is notable for being the site of one of the largest and best-studied hydro-thermal fields on the deep seafloor(Rona et al. 1986, Rona et al. 1993a, Scott et al. 1974) containing *SMS* deposits. It lies at water depths ranging from 3,430 to 3,670 m on the eastern and shallowest part of a 75 km-long, slow-spreading segment of Mid Atlantic Ridge bounded by two right-lateral non-transform discontinuities at 25°58N and 26°17N (Figure 19. A) (Murton et al. 2019). Slow-spreading ridges characterised by slow magma flux and tectonic extension, often accommodated by long-lived detachment faults creating favourable conditions for hydrothermal activity and *SMS* deposition.

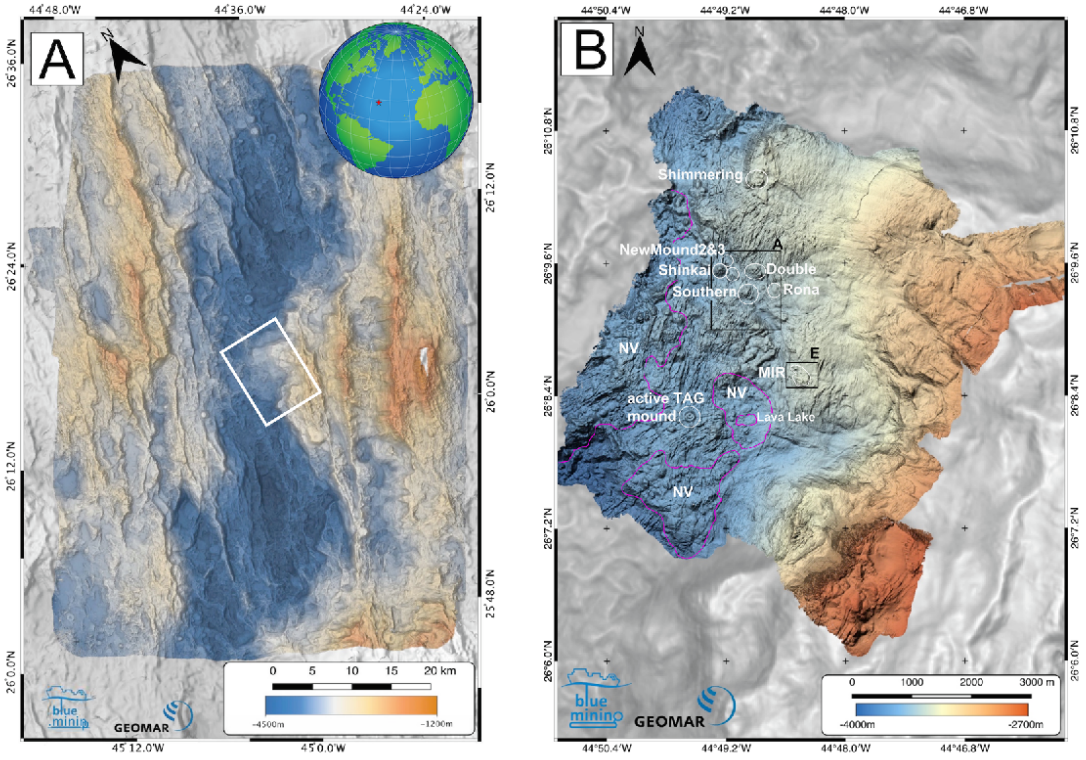

Figure 19: (A) Ship-board multibeam swath bathymetry map (50 m grid) of the axial valley of the Mid-Atlantic Ridge containing the *TAG* hydrothermal field, at 26°08°N on the Mid-Atlantic, and indicated by the location of the red star on the inset globe. Inset white outlined box is the location of Fig. 1B. (B): AUV-derived, near bottom multibeam swath bathymetry map (5 m grid) of the *TAG* hydrothermal field showing the location of the active *TAG* mound and other *SMS* mounds (outlined in white) and young neovolcanic areas (outlined in magenta and denoted NV). Inset black boxes (A) and (E) show the location of the 'Three Mounds' area and the MIR zone, respectively.

Source: Figure 1, Murton et al. 2019

Hydrothermal venting has been active at *TAG* for the past 140 000 years (Lalou et al. 1995) and has generated several *SMS* deposits, mostly in the form of mounds within an 5×5 km area of the Mid-Atlantic Ridge axial valley. The area can be divided into four parts, the *TAG* mound area, the Alvin zone located approximately 1.5 km north-northeast of the *TAG* mound, the MIR zone situated two km to the east-northeast of the *TAG* mound and the Shimmering mound located roughly 2.5 km north north-northeast of *TAG* mound (Figure 19. B).

TAG mound area has only one active *TAG* mound where the *SMS* deposition process is still

active. TAG mound has 200 m diameter, 50 m high circular deposit topped by the number of 12 m black-smokers chimneys according to Humphris et al. 1995. The TAG mound has the following stratigraphy from its top to bottom, massive Py rich breccia, Anh rich breccia, silicified, pyritised, altered basaltic stockwork. Valuable metals such as Cu, Zn, Ag and Au are only found in the enriched upper 5 m part of the mound.

Alvin zone consists of several mounds containing SMS deposits. These are Double, Southern (Figure 20. C), Rona (Figure 20. D), Shinkai and new mound # 2 and new mound # 3 (Figure 20. B). Double, Shinkai, and Southern have a roughly circular shape, their height is about 60 m, and their diameter is 100-300 m. Rona mound is dome-shaped. It is 30 m high and 100 m in diameter. The smallest mounds, new mound # 2 and new mound # 3 approximately with diameters 20-30 m.

The Shimmering mound area is represented by FeO2, and weathered sulfide material resulted in the diffusion of low-temperature fluids. It has about 200 m in diameter.

MIR zone (Figure 20. E) lacks mound-shaped features and represents a raised area of irregular and undulating seafloor 100's m in diameter and 10's m in height. The MIR zone is composed of an accumulation of weathered sulfide material and Fe-rich sediments. Rona et al. 1993a proposed dividing the area into three parts, the western part containing weathered sulfide debris and hydrothermal sediments underlain by hydrothermal breccia. The central part is dominated by toppled and standing, currently inactive hydrothermal chimneys and the eastern part with no sulfides, where FeOOH, Fe-rich clays and MnOOH crusts occur.

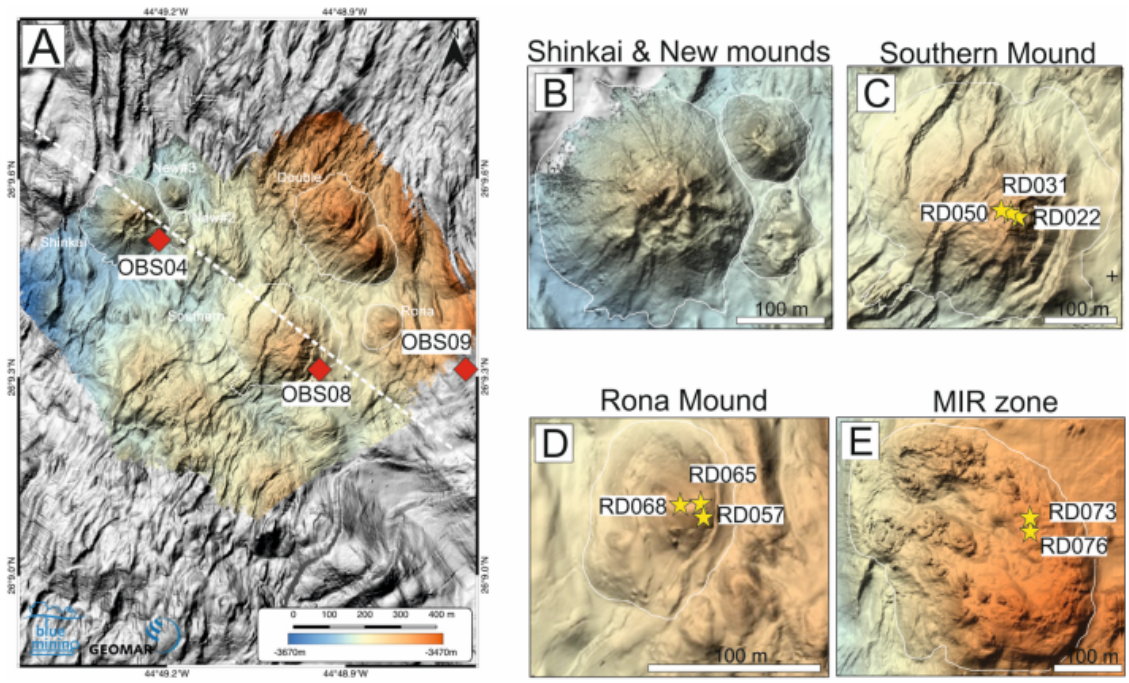

Figure 20: (A) Colour-shaded bathymetry maps (0.5 m resolution) of the area surveyed by the autonomous underwater vehicle during expedition M127, ocean-bottom seismometers positions (red diamonds). Thin white lines depict the base of the mounds. Note depth scale bar (lower right) applies to all panels. (B) Detail showing Shinkai Mound and the smaller New Mound 2 and 3, located NE and SE of main Shinkai Mound, respectively. (C) Detail showing Southern Mound, its fault scarps and drill locations occupied during expedition JC-138 (yellow stars). (D) Detail showing Rona Mound and the location of the drill holes occupied during JC-138. (E) Detail showing MIR Zone and drill locations occupied during JC-138.

Source: Figure 2, Murton et al. 2019

All the zones at TAG SMS field are hosted by basaltic rocks Rona et al. 1993a,b. The reserve

amount in the whole TAG field is not accurately estimated, according to rough estimations in Hannington et al. 1998 based on bulk geochemical data from literature and volumes of mounds in the TAG mound zone, Alvin zone and MIR zone, assuming last two have the same lithology as TAG mound zone, sulfides mass in TAG field is in range of 1-4 million tons. Surface grab or shallow drilled holes core samples taken from the most attractive zones in the field are used for this estimation. Therefore they may not be representing the whole TAG SMS field truly.

3.2 Database

The data used in this work is acquired during scientific expeditions ODP Leg 158, M127, and JC-138 carried out on TAG SMS field at Mid Atlantic Ridge in 1994 and 2016 correspondingly.

ODP Leg 158 is one expedition of the ODP international research program founded by the U.S. National Science Foundation and 22 international partners focused on investigating ocean basins' history and the nature of ocean basins' crust using drill ships. ODP Leg 158 is designed for studying fluid flow, alteration, mineralization, associated geochemical fluxes, microbiological processes and subsurface nature of TAG hydrothermal mound. Both M127 and JC-138 expeditions are part of EU funded Blue mining program aimed at suggesting modern solutions for a sustainable deep-sea mining value chain. The M127 expedition is focused on the nature and resource potential of the TAG SMS field, while JC-138 have two purposes, first demonstrating SMS exploration and SMS assessment technologies application on the field and second to the understanding of the formation, alteration and preservation of the SMS deposits. The three expeditions have collected a broad range of data by geophysical methods and via extracting drilling core, gravity core and sea-bed surface grab samples sequentially by performing a large set of laboratory analyses. The geophysical methods include multi-beam bathymetry, magnetic surveys, 2D streamer seismic, and ocean bottom refraction seismic. The performed laboratory analyses are V_p measurements based on first arrival travel-time, ρ measurements via Gamma-ray densiometry, visual core description, thin section analyses, XRF measurements, Mass spectrometry and other types of a sample composition analyses.

Only marine streamer 2D seismic (both processed and raw data), drilling core, gravity core, and sea-bed surface grab samples V_p, ρ and/or composition laboratory analyses results have been considered most relevant for this thesis objective are used in this work. These data are gathered from the expeditions reports, their public databases, and related articles and organized in a structural manner.

3.2.1 Field Work Data

2D streamer seismic is acquired during the scientific expedition M127. 49 2D marine seismic profiles denoted from P1 to P49 have been acquired in total (Figure 21). A compressor with the capacity of 10 m^3/min, either two 105/105 $inch^3$ GI airguns towed at 2.5 m depth or 380/380 $inch^3$ a G-gun cluster towed at 6 m depth in the sea with the shot rate of 10-12 s and with shot offsets of 16.5-19.8 m are used in order to provide sufficient enough source signal frequency. The profiles P35 to P46 have been shot by two GI airguns, and the rest of the profiles are shot by the G-gun cluster. Airguns are triggered based on a GPS clock timing system to provide a time base for all recording devices. 192 channels surface towed streamer with 1.53 m group offset (292 m active length) has been used for recording the seismic signal. The distance from the source to the first channel is 30 m. The streamer is comprised of 12.7 m long sections. 14 sections closest to the vessel are oil filled and have 3 depth controlling birds ensuring 2 m to 4 m depth in sea, while 10 remaining sections do not have depth control. However, streamer ghost effects observed in the second part of the streamer suggest these sections have been on depth deeper than 3 m during acquisition. The seismic signal recording has been done at a 0.5 ms sample rate with an 8 s record length.

Core samples extracted from 22 shallow holes drilled at TAG area during ODP Leg 158 and JC-138 expeditions are considered in this work since laboratory measurements (V_p, ρ and composition) have been performed on them. During ODP Leg 158, 80 drilling core samples are recovered from

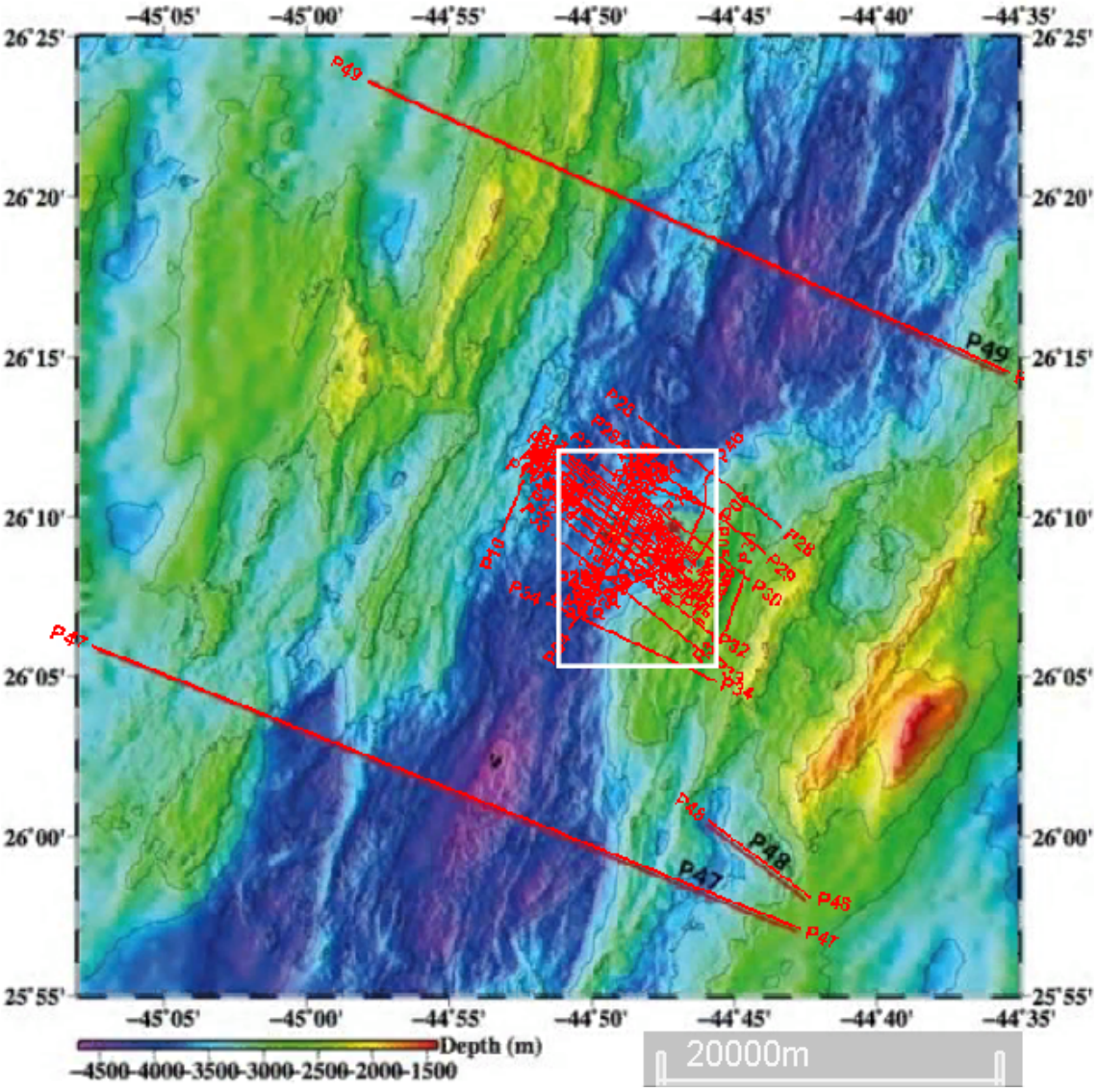

Figure 21: Map of all marine 2D seismic profiles acquired during M127 expedition. White box shows the $TAG\ SMS$ field area shown in the Figure 22

Source: Modified Figure 5.3.4 from Petersen 2016

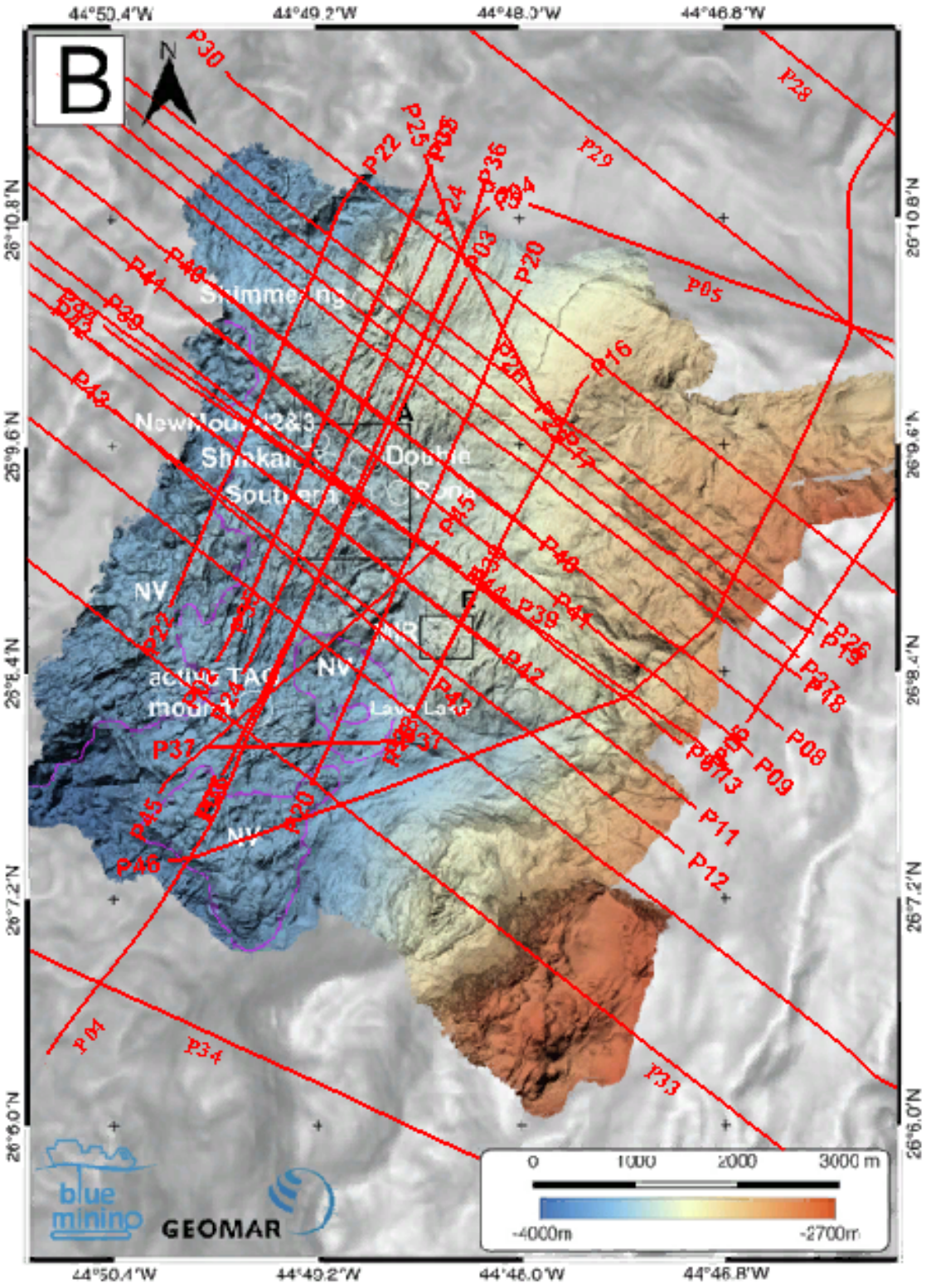

Figure 22: Marine 2D seismic profiles acquired on top of *TAG SMS* field during M127 expedition.

Source: Modified Figure 1.B. from Murton et al. 2019

15 shallow holes drilled in active TAG mound at TAG mound area, coring bits APC/XCB with inner diameters 28 cm ($11^{7/16}$ in), 25 cm $10^{1/8}$ in and coring bits RCB C-7, C-9 with inner diameter 25 cm $10^{1/8}$ are used for coring. The core samples have a length of 0.7 m on average. Their length varied in range from 0.1 m to 5.8 m. While expedition JC-138, 7 shallow holes are drilled using RD2 sub-sea drilling system from Southern mound, Rona mound at Alvin zone and from MIR zone for coring. 30 drilling core samples with 61 mm diameter are collected in total. The cores have 0.035 m in length on average. Their length varied between 0.1 m and 1.8 m. Please refer to Table 9 and Table 10 for detailed information on shallow holes coordinates and recovered cores during these expeditions. All shallow holes locations are shown in the Figures 23, one can see location of shallow holes by zones at TAG field area in Figures 24, 25, 26.

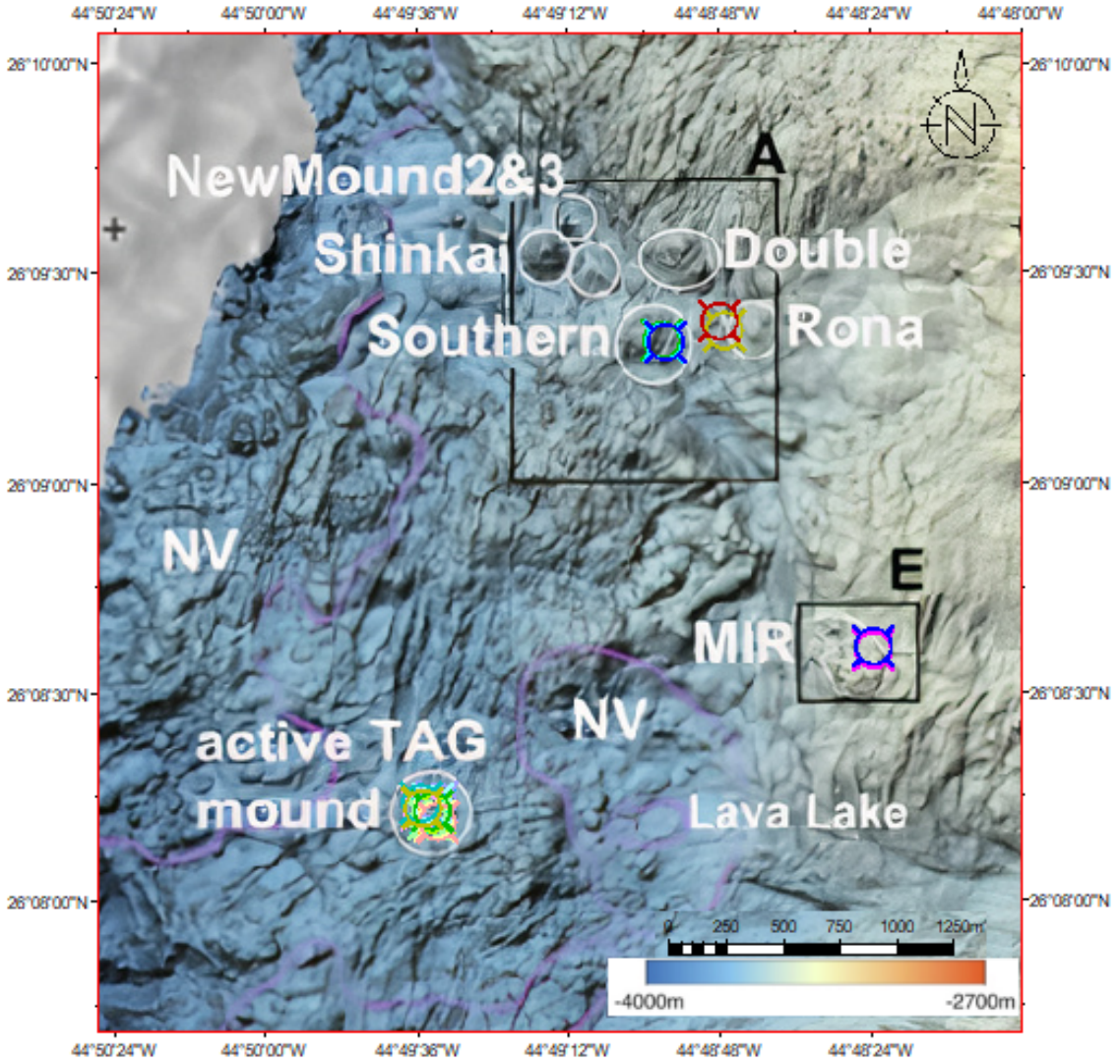

Figure 23: The all shallow holes location at TAG field area.

Source: Modified Figure 1.B. from Murton et al. 2019

Information on 30 gravity core samples taken from the TAG field area by 8 gravity core stations during M127 and JC-138 expeditions are used in this work. 17 gravity core samples with a total length of 5.13 m were recovered by 3 gravity core stations with 3 m length, 125 mm diameter and with top weight from 600 to 900 kg during the M127 expedition. Information on these core stations' location and gravity core recovery is presented in Table 11. 13 gravity cores with a total length of 7.23 m were taken by 5 gravity core stations during the JC-138. There is no information on equipment that has been used for the gravity coring in JC-138's report (Murton 2018). Therefore it is not mentioned here. Please refer to Table 12 for the information on gravity core stations location and gravity core recovery during the JC-138 scientific expedition. One can see the gravity

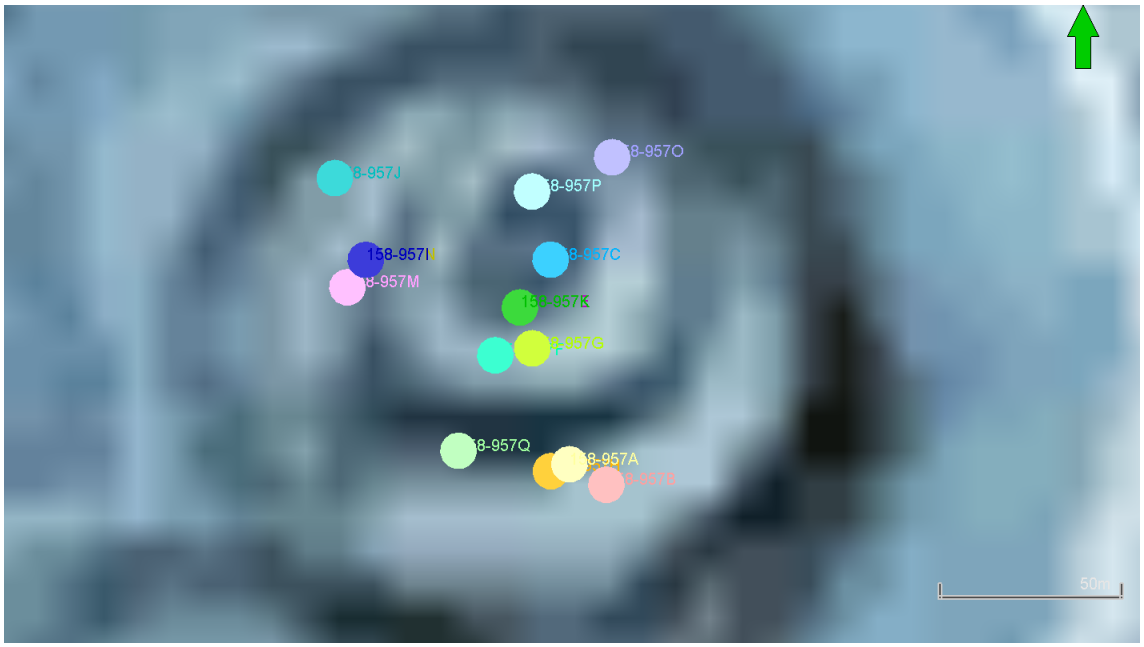

Figure 24: The shallow holes location at TAG mound area, on active TAG mound.

Source: Modified Figure 1.B. from Murton et al. 2019

Figure 25: The shallow holes location at Alvin zone, on Southern mound (left) and Rona mound (right).

Source: Modified Figure 1.B. from Murton et al. 2019

Figure 26: The shallow holes location at MIR zone.

Source: Modified Figure 1.B. from Murton et al. 2019

core stations' location in Figure 27.

Data on 29 sea-bed surface grab samples collected by Hydraulic Benthic Interactive Sampler (HyBIS) robotic underwater vehicle (RUV) during the JC-138 expedition are considered in this work. The samples are taken by HyBIS RUV's sampling arm from the sea-bed. The samples have up to 5 kg weight in the air. Please look at Figure 28 for the sampling process illustration. The summary information on sea-bed surface grab samples is given in Table 13, and one can see where samples are taken from the *TAG* field area in Figure 29.

3.2.2 Laboratory Work Data

The recorded 2D streamer seismic profiles are processed in the M127 expedition. The raw data traces quality checked, 25-55-400-500 Hz band-pass filtered, the resulting data binned in bins with 1.5 m width, stacked in CMPs and time migrated during processing.

V_p in shallow hole core samples extracted during *ODP* Leg 158 program are measured by PWL system from GEOTEK Ltd.(UK) in two modes PWL and PWS3 using ultrasonic waves with 500 kHz frequency on whole core and split (in coring direction) core samples respectively. The measurements on both modes are based on measuring core length (L), detecting P-wave travel-time through the core (t) and calculating V_p by equation 5 with some technical differences in execution. The reader is kindly asked to refer to Chapter 6 in Blum 1997 for measurement modes technical details.

$$V_p = \frac{L}{t} \tag{5}$$

Where:

V_p - P-wave velocity;

L - core length;

t - P-wave travel-time through a core.

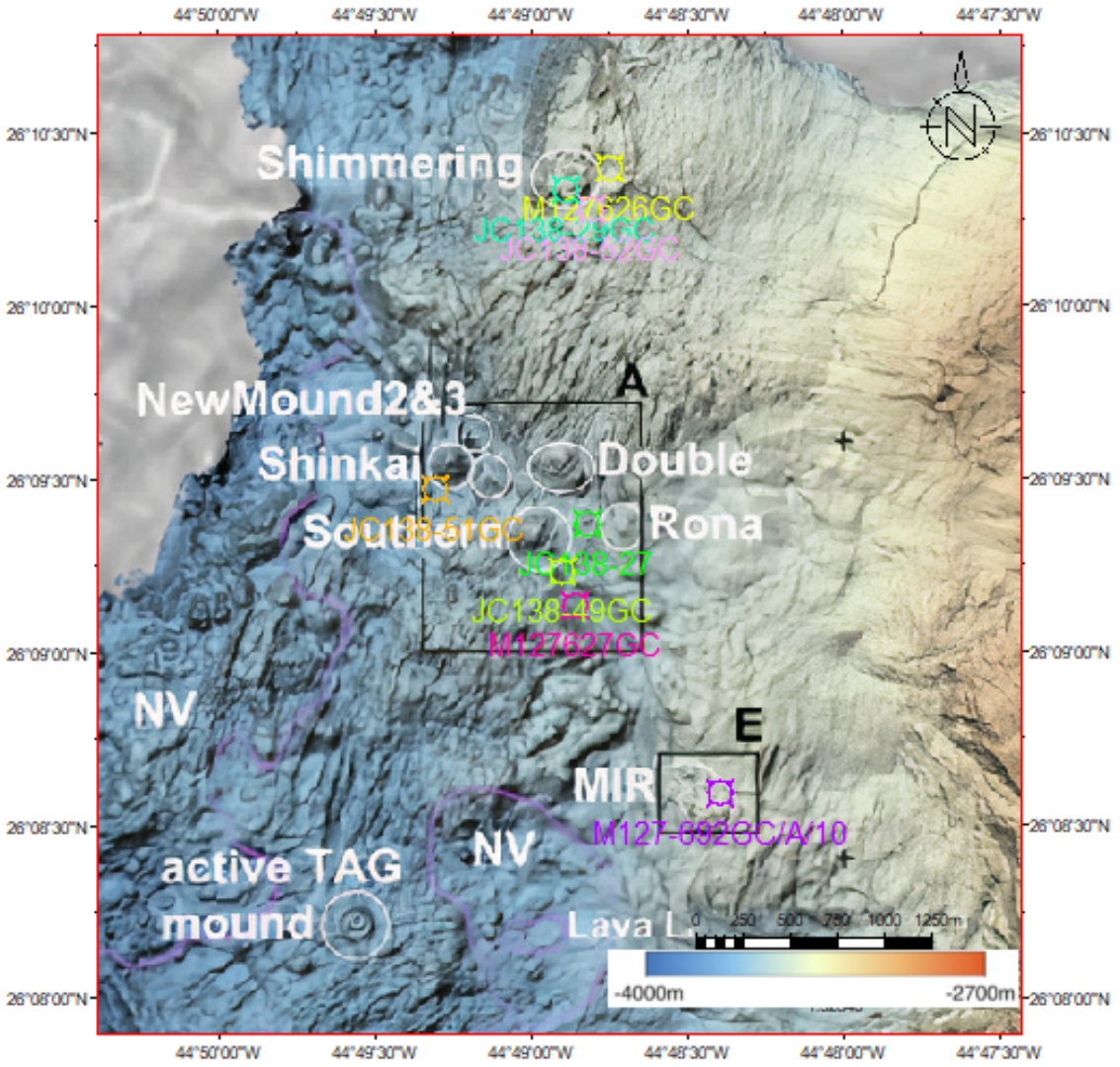

Figure 27: The gravity core stations location at *TAG* field area.

Source: Modified Figure 1.B. from Murton et al. 2019

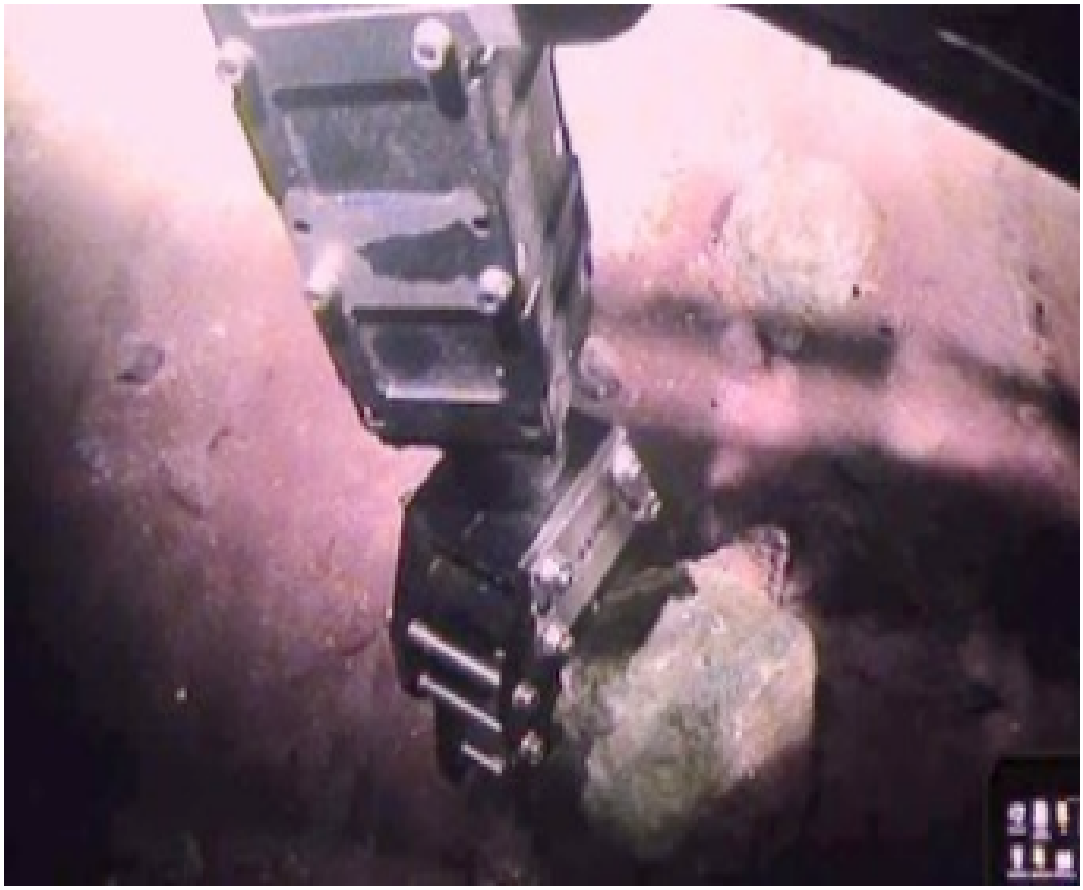

Figure 28: Sea-bed surface grab sampling by HyBIS RUV at *TAG* field area.

Source: Figure on page 40 in Murton 2018

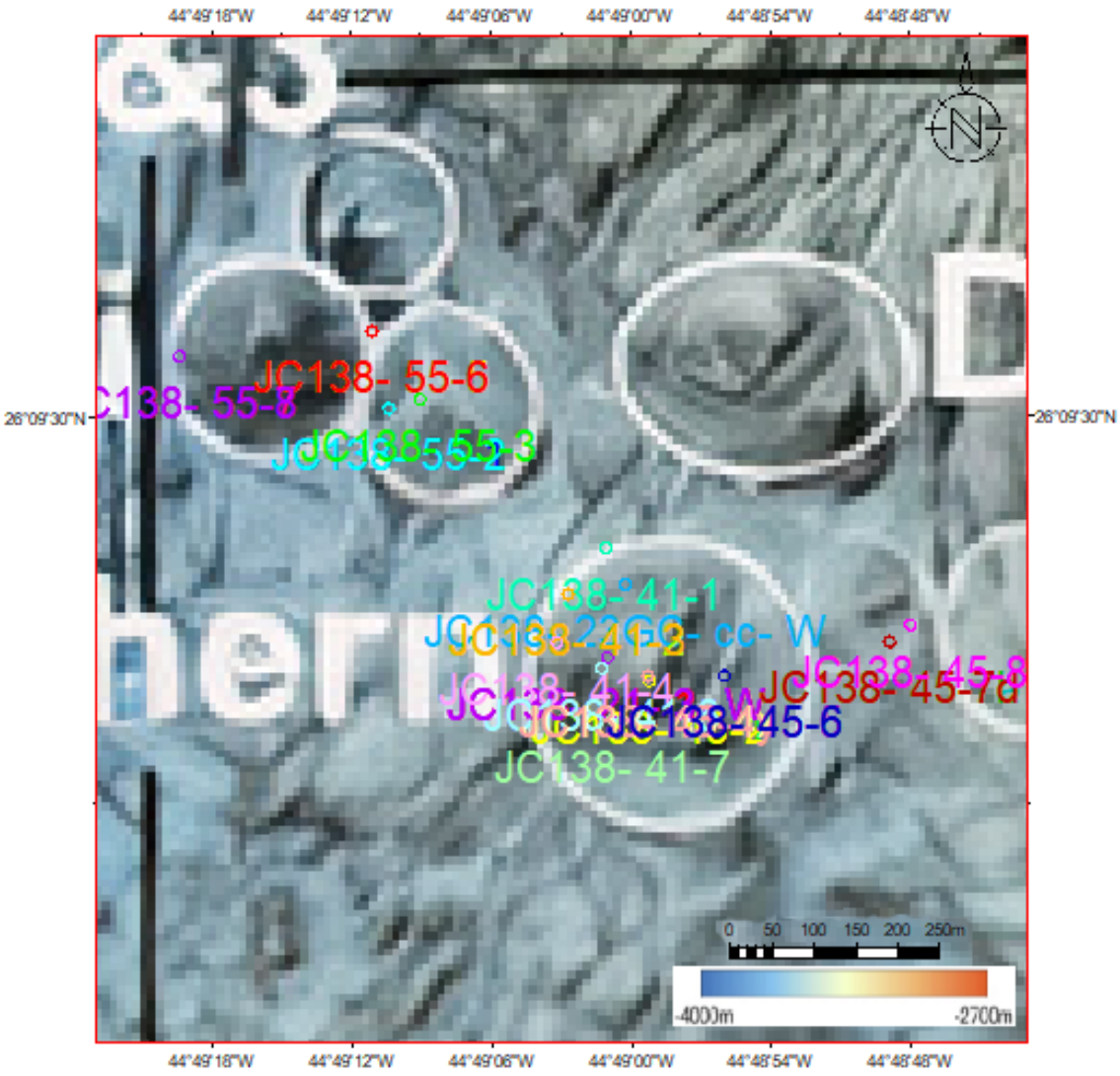

Figure 29: Sea-bed surface grab samples location on *TAG* field area.

Source: Modified Figure 1.B. from Murton et al. 2019

The measurements are performed on water-saturated core samples in room conditions. Measuring V_p by such techniques usually provide results with 5 % error comparing to true V_p values in *In-Situ* conditions according to Blum 1997. The P-wave measurement results are provided in Table 14.

During the *ODP* Leg 158 program, shallow hole core samples ρ are measured by the Gamma-ray densiometry technique that is based on the relation of gamma-ray attenuation by Compton-scattering to the media's electron density. During the measurements, gamma rays with 660 KeV energy were emitted by the Celium-137 source, and the gamma rays interacting with the sample minerals were detected by the NaI scintillation detector. The gamma rays attenuation is calculated by subtracting recorded gamma rays energy from emitted gamma rays energy. The calculated gamma rays attenuation is related to the material's electron density via equation 6.

$$n_e = \frac{1}{sd} \ln \frac{Y_i}{Y_t} \tag{6}$$

Where:

n_e - electron density;

Y_i - detected gamma ray flux;

Y_t - emitted gamma ray flux;

s - sample cross-section for scattering;

d - sample thickness.

Most of the minerals have constant Compton/mass attenuation coefficients depending on their electron density since there is a relationship between a nucleus electrons with its neutrons and protons as $2Electrons = Protons + Neutrons$ which is true for most elements. Material electron density is related to its mass by equation 7 and the sample ρ determined.

$$\rho = \frac{n_e * \overset{\circ}{A}}{\overset{\circ}{Z} * N_{ava}} \tag{7}$$

Where:

ρ - bulk density;

n_e - electron density;

$\overset{\circ}{A}$ - atomic mass of material;

$\overset{\circ}{Z}$ - atomic number or number of electrons of material;

N_{ava} - Avogadro number.

The reader is kindly asked to refer to Chapter 3 in Blum 1997 for details of performed Gamma-ray densiometry technique, and the results of ρ measurements are provided in the Table 15.

The *ODP* Leg 158 expedition's shallow hole core samples composition is represented by *Py*, *Cpy*, *Po*, *Sph*, *Qtz*, *Anh*, Amorphous Silica ($AmFeO$) and Hematite (Hm). Their composition is determined by visual core description using visual core description (VCD) form for igneous and hydro-thermally altered rocks which have been modified for sulfide rocks (see "Igneous Petrology and Geochemistry" and "Hydro-thermal Alteration" sections in Chapter 5 of Humphris et al. 1996). The rock types are defined by the content of principal minerals in them and by hand sample examination of the most distinctive textural attributes. The principal mineral content and distinctive textural attributes have been confirmed via polished thin section analysis results. The data on *ODP* Leg 158 shallow hole core samples composition that has been used for this thesis is

taken from Tables 2, 6, 7 in Chapter 7, Table 2 in Chapter 8, Table 1 in Chapter 9, Table 2 in Chapter 10 and Table 2 in Chapter 11 of Humphris et al. 1996 and provided in Table 16.

Shallow hole core samples, gravity core samples and sea-bed surface grab samples composition is represented by Silicon (Si), Carbon (Ca), Manganese (Mn), Cu, Zn, Fe, total Sulfur $TotalS$ content. Shallow hole drill cores collected during the JC-138 expedition are analyzed only on composition, V_p and ρ measurements are not performed on them. Shallow hole drill core samples' bulk geochemical data is obtained from 10 g crushed, powdered and homogenized individual or composite quarter-core pieces of the same lithology. The 10 g sample is analyzed by using: Instrumental Neutron Activation Analysis (INNA), sodium peroxide fusion with Inductively-Coupled Plasma Optical Emission Spectrometry (ICPOES) and Mass Spectrometry (ICP-MS) analyses, total sulphur infrared spectroscopy, and cold vapour flow-injection atomic absorption spectrometry. The obtained laboratory results on the JC-138 expedition's shallow hole core samples are provided in Table 17.

The gravity core samples collected during the M127 expedition have been analyzed only for composition. Portable XRF instrument (XRF, Niton Ultra XL3t Thermo Finnigan) with a variety of routines and accessories, including light elements (at first with He purge) and a large number of trace elements with variable detection limits and precisions (generally better than 20 % relative to the amount present) is used for the analyses. Analyses have been improved by the use of a stand and sample holders with calibrated polyethylene windows which allowed for longer probe time spans and by a constant distance between the sample and the X-ray source and sensor. The tests are carried out on dry, ground samples. Some of the samples were remounted and reanalyzed without substantial variations in the results. Tests show that the values obtained are free of sampling mistakes. M127 expedition's gravity core samples composition analysis results that have been used in this thesis are provided in Table 19.

The gravity core and sea-bed surface grab samples collected during JC-138 are represented by unconsolidated sediment samples. These samples were analyzed as approximately 100 mg of acid-digested dried and ground material after applying an internal spike of Be, Re and In. Analysis was performed by ICP-OES for major elements (e.g. Ca, Cu, Fe, Mn and Zn) and by ICP-MS for minor elements and trace elements (e.g. Cu for some depths). Precision and accuracy were determined for each analytical run by repeat analysis (n = 3) of the two Certified Reference Materials: (i) marine sediments MESS-1 (National Research Council of Canada) and (ii) sulphide ore mill tailings RTS-1 (National Research Council of Canada). Elemental precision for each run was less than 4 % and 2.7 %, respectively, except for Zn, which was up to 13 % by ICP-OES due to a low concentration in RTS-1 and MESS-1. Silica concentrations in jasper samples were determined by X-Ray Fluorescence (XRF) using approximately 0.5 g of dried, ground and homogenized material, mixed with Lithium Tetraborate flux and fused into a glass bead. These were analyzed on a Philips® MagiX-Pro 4 kW using an Rh X-ray tube. Mineral identification in sediment was performed on homogenized dried powder samples using an X-Ray diffractometer (MiniFlexII, Rigaku, Japan) equipped with MiniFlex2 + goniometer and detector. CuK1 radiation (1.541 Å) was applied at 30 kV, with 15 mA of beam current. The 2 incidence angle spanned from 5° to 60° with a scan speed of 1.2°/min using a continuous scan mode. Quartz standards were also run to ensure calibration. The data were analyzed using the "Panalytical Highscore" software with reference to the ICDD minerals database 2018 (Murton et al. 2019).

The obtained laboratory results on the JC-138 expedition's gravity core samples and sea-bed surface grab samples composition are provided in Table 18 and in Table 20 correspondingly.

4 Methods

4.1 Estimating Phase of Seismic Data

The seismic data is recorded at the $TAG\ SMS$ field using a relatively short maximum offset length of 322 m, and the sea-bed is located at 3500 m depth. Therefore the effect of seismic amplitude changes with offset on full-stack seismic data being used in this work is considered weak and seismic amplitudes are treated as zero-offset seismic amplitudes throughout this work.

Defining seismic data wavelet's phase and polarity is essential before starting the seismic interpretation since wavelet type controls how reflecting interfaces may appear on seismic. For example, the same reflecting interface can appear either as the onset of peak amplitude or peak amplitude on a seismic trace if the reflection coefficient on the reflecting interface convolves by either minimum phase or zero phase normal polarity wavelet, respectively. One can see provided illustrative example in Figure 30.

It is known from the M127 expedition's report that the processing sequence consists of the raw data traces quality check, 25-55-400-500 Hz band-pass filtering, data binning in bins with 1.5 m width, stacking in bins and time migration have been applied on 2D marine streamer seismic lines. There is no information about the seismic wavelet's phase or polarity in the M127 expedition's report.

One of the ways to estimate the wavelet's polarity and phase is to analyze seismic data on the sea-bed. The first and most probably strongest seismic reflector is expected to be on the sea-bed on seismic data. Because seismic data is represented by 2D marine streamer seismic profiles recorded on offshore conditions, where source and receivers have been located near the sea surface during acquisition. Sea-water where the seismic wave starts propagating and sea-bed sediments have a significant difference in Z resulting in a reflecting interface with high R_0. When the seismic wave starts propagating from the source after a shot, Z of seawater (Z_{sw}) where the seismic wave is propagating through does not change sharply with depth. Therefore reflectors are not expected. The first sharp change in Z with depth takes place on the sea-bed. This change creates a boundary with strong positive reflectivity. The shape of the seismic trace representing this strong reflection boundary on the sea-bed depends on the seismic wavelet, for example, as shown in Figure 30. Based on this knowledge, one can investigate distinctively visible first trough, first peak, and second trough on seismic trace, representing sea-bed on seismic data for estimating seismic wavelet polarity and phase. For instance, one can see troughs in blue colour are representing negative amplitudes and peaks in red colour represent positive amplitudes on the processed 2D seismic profile P03 on Figures 31, 32. It is known that seawater and sea-bed create a positive reflection coefficient since the positive reflection coefficient is represented by the trough-peak-trough sequence on the seismic data of seismic profile P03 (Figure 32). One can say seismic data have normal polarity. The wavelet cannot have reverse polarity since, in that case, the sea-bed has to be represented by peak-trough-peak sequence on the seismic profile P03 on Figure 32.

Seismic data Wavelet's phase estimation using sonic log and density log data from a well is generally applied method for determining seismic wavelet's phase in the petroleum industry. Unfortunately, there is no well log data from the $TAG\ SMS$ field in our project. Therefore it is not possible.

The author assumes no processing has been applied for changing recorded raw seismic data's wavelet during processing, and the seismic wavelet is represented by a mixed-phase wavelet generated by the interference of minimum phase seismic wave from the source and shifted phase seismic ghost wave. Since seismic's polarity is known, it is decided that looking at the amplitude of first trough, first peak and second trough of distinctively visible first reflection on seismic profiles, most probably representing reflecting sea-bed, could give a rough estimation of seismic data's phase. 2D seismic profiles P02, P03, P04, P06, P07, P08, P09, P11, P12, P16, P17, P19, P20, P22, P24, P27, P28, P29, P30, P32, P33, P34, P46 are chosen for interpreting horizons picked on the first trough, first peak and on the second trough of the first reflection to acquire their amplitude estimations overall $TAG\ SMS$ field.

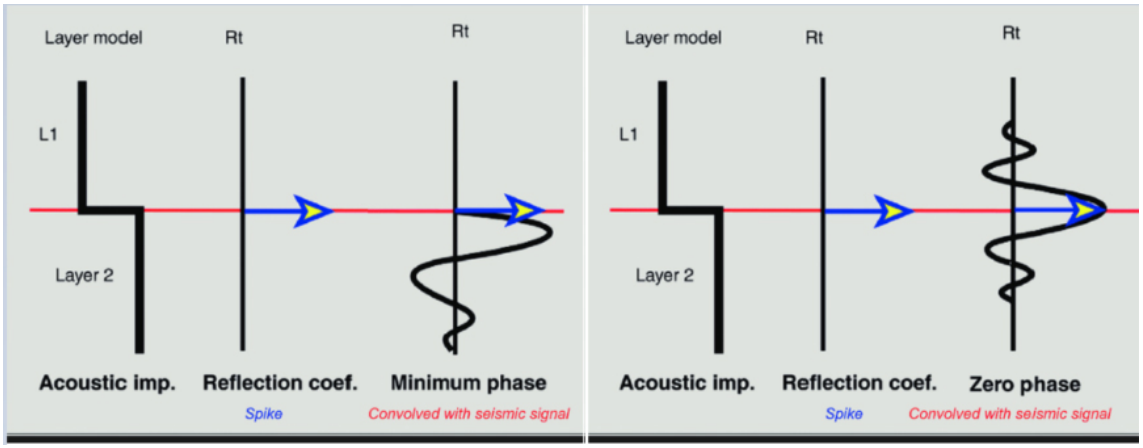

Figure 30: Example of reflection coefficient convolution with different wavelets.

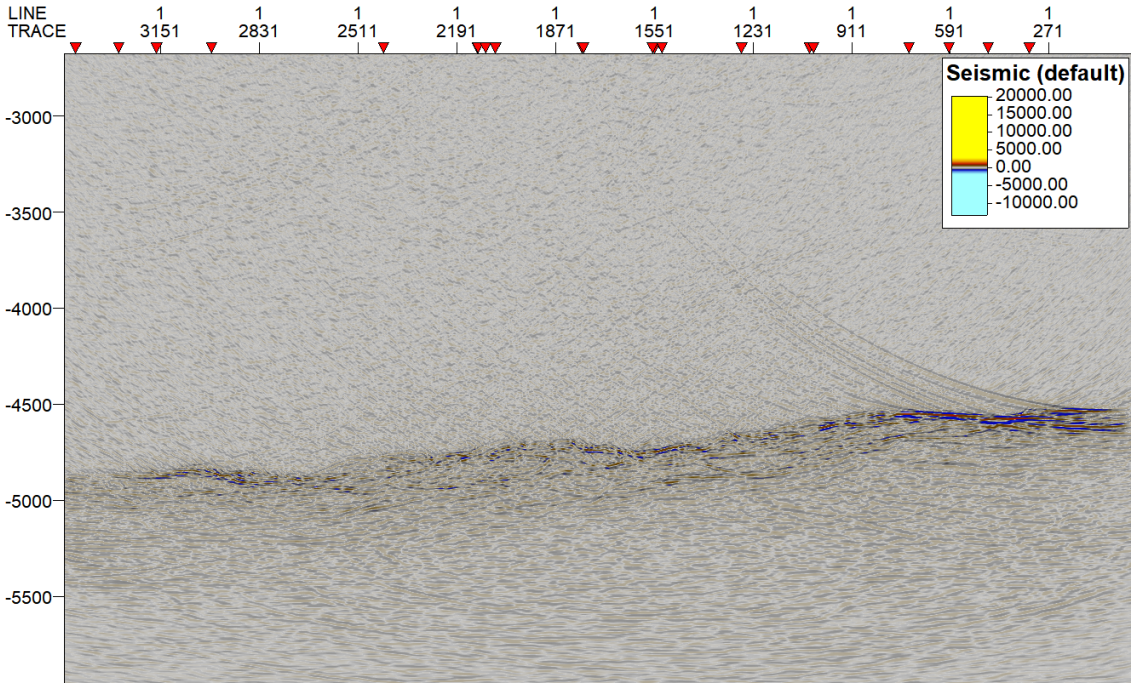

Figure 31: 2D marine streamer seismic profile P03. Sea-bed is distinctively visible between 4500-5000 ms

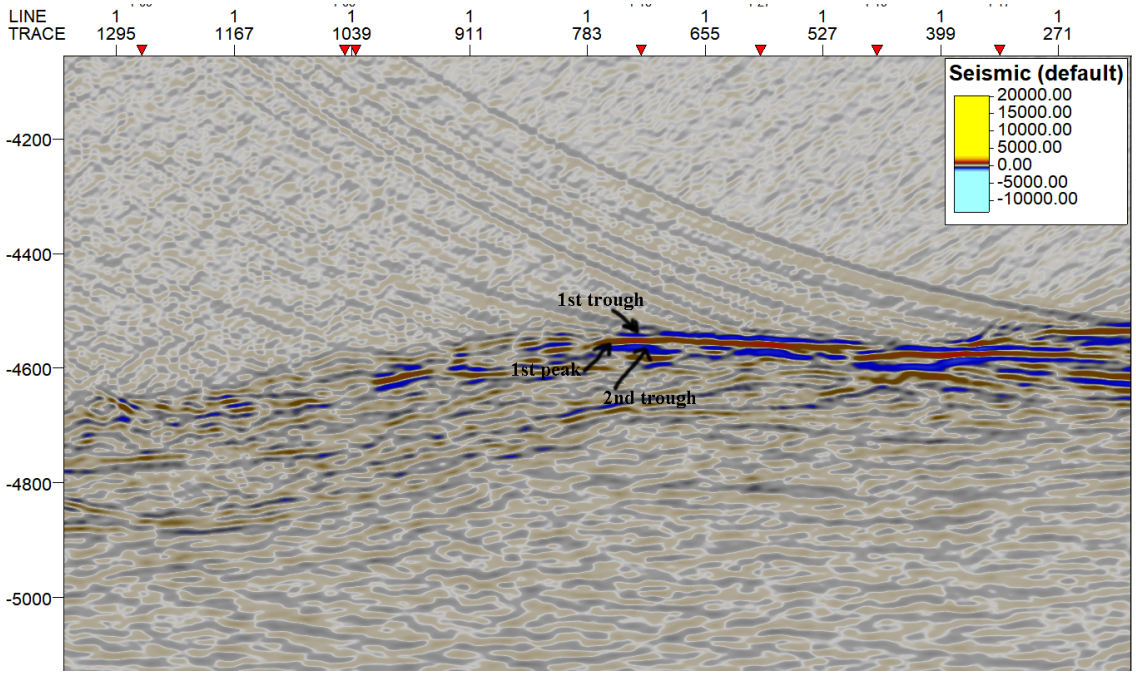

Figure 32: Zoomed in 2D marine streamer seismic profile P03.

The reason for choosing these 2D seismic profiles for interpretation is they cover the whole TAG SMS field. They have better seismic data quality than other 2D seismic profiles overlapping with them. They cross the maximum number of SMS zones at the TAG field. One can see the location of these 2D seismic profiles at the TAG field in Figure 33. Horizons interpretation is made in Petrel software using "Seeded 2D auto-tracking" mode to pick the highest maximum positive amplitudes on the first peak and maximum negative amplitudes on the first trough and second trough. Amplitude values from interpreted horizons are extracted using the "Surface attributes" function in the seismic interpretation pan in Petrel, and mean values are calculated. An average seismic trace with these amplitude values is generated.

As a next step, two statistical wavelets have been extracted from seismic profile P03, where good sea-bed reflection is visible using Geoview software to assess the frequency range of the mixed-phase wavelet. The good sea-bed reflection is visible in two parts of seismic profile P03. The first window is in the 1995-2247 common mid point(CMP)s range and in the 4500-4900 ms two-way travel-time (TWT) interval. The second window is between 2959-3119 CMPs and 4700-5100 ms TWT intervals.

Once the mixed-wavelet's frequency band is known, several synthetic band-pass wavelets with that frequency band but with different phases are created in "Geoview", synthetic band-pass wavelets have been created with a default wavelet length of 100 ms in "Geoview", and for phase degrees from -60 to 60 with 15 phase degree step. Generated synthetic wavelets shape compared to the previously created average seismic trace shape. The idea is synthetic band-pass wavelets with which phase degrees would show the same tendency as the average seismic trace of the TAG field.

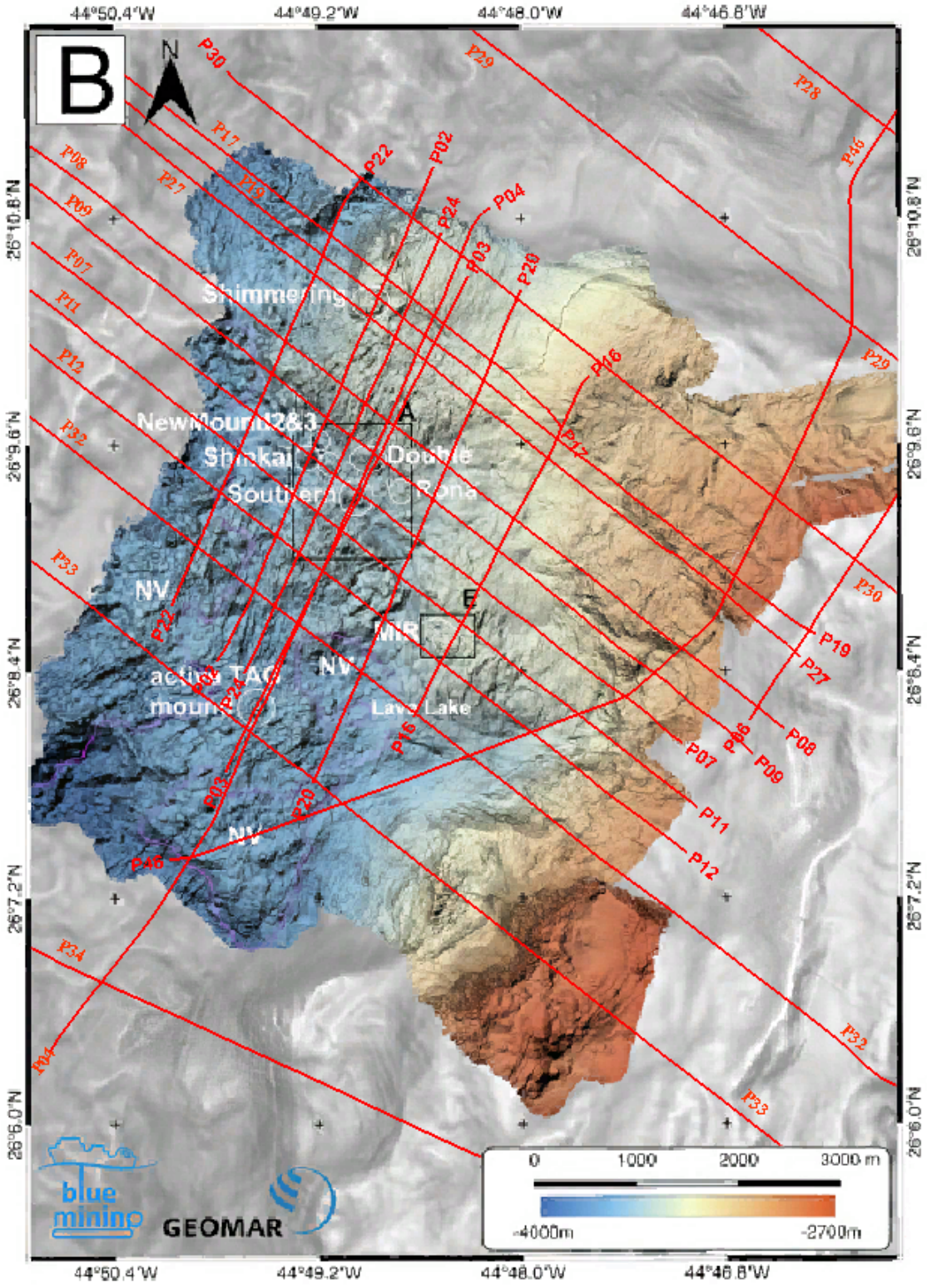

Figure 33: 2D seismic section profiles chosen for first trough, first peak and second trough horizons interpretation on sea-bed at *TAG SMS* field.

4.2 SMS Mineral Richness and Seismic Amplitudes Analyses

SMS deposits in the TAG mound area, Alvin zone, MIR zone and Shimmering mound are located on or near the seafloor at the TAG SMS field. These SMS deposits are hosted by basalt host-rocks. Basal is a mafic host-rock, and based on Figure 1, it is expected that mineral-rich SMS deposits have distinctively different Z than basaltic host-rocks. They consecutively create an interface with different seismic R_0 in contact with sea-water compared to basaltic host-rock. The author had two questions. First, "Can one observe distinctive seismic amplitudes from the sea-bed on mineral-rich SMS deposit zones and surrounding basaltic host-rock zones due to variance in their Z at TAG SMS field?". Second, "If mineral richness affects seismic amplitudes on the sea-bed?".

For the first question, sea-bed reflection's first peak amplitudes are visually examined overall TAG SMS field to find a relation between SMS deposit zones, surrounding host-rock areas and seismic amplitudes.

For the second question, during the ODP Leg 158 expedition, core samples are extracted from six shallow holes 158-957C, 158-957F, 158-957G, 158-957O, 158-957P, 158-957Q at the TAG SMS field and the core samples mineralogical composition, V_p are measured in the laboratory. These six shallow holes are located on or near (within a 10 m lateral radius of) 2D seismic profiles P03, P36, and P45 at the TAG SMS field as shown in Figure 34.

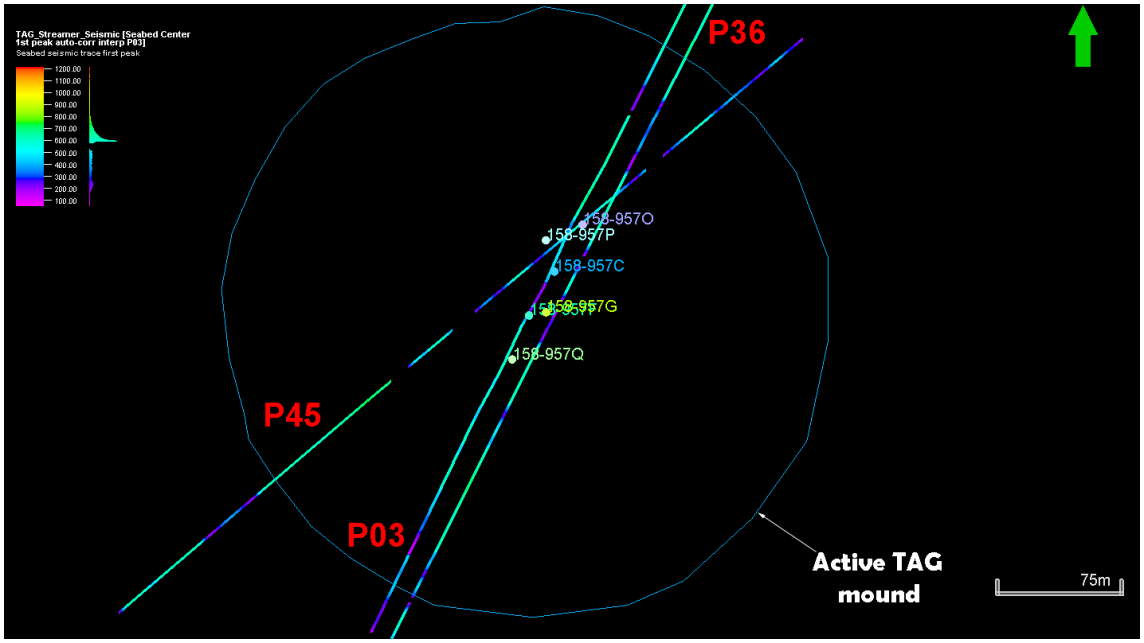

Figure 34: Six shallow holes with mineralogical composition, V_p measurement laboratory analyses at Active TAG mound.

The peak of seismic amplitudes on the sea-bed at these six shallow holes' location is plotted against the major minerals Py, Cpy, Qtz, Anh content in these core samples taken from six shallow holes at the TAG SMS field. The average of seismic amplitudes within a 3ms window on the sea-bed at the location of the shallow holes is considered representative peak seismic amplitude for plotting. The core samples depth have been converted to time domain using $V_{p(sw)}$ provided in Table 6 and V_p laboratory measurement results mentioned in Table 14. To get one representative value for major minerals Py, Cpy, Qtz, Anh content at shallow holes location, the weighted average value of each mineral range from a seismic trace peak representing sea-bed until a point when this seismic trace crosses zero amplitude value has been calculated at a shallow hole location. One can see six shallow holes 158-957C, 158-957F, 158-957G, 158-957O, 158-957P, 158-957Q major minerals Py, Cpy, Qtz, Anh content and sea-bed seismic amplitudes averaged windows in section view on Figures 35, 37, **??**, 38, 39, 40. The idea is, if one considers sea-bed as reflecting interface created

by two spaces represented by sea-water on the top and a minerals composition on the bottom, where peak of seismic amplitude refers to the reflecting interface, the minerals creating the lower space should be within a range when seismic trace amplitude crosses zero amplitude value.

The remaining twenty-one drilled core samples, gravity core samples, and sea-bed surface grab samples were collected during *ODP* Leg 158, JC-138 and M127 scientific expeditions from locations lying on or near (within 10 m lateral radius of) 2D seismic profiles P03, P07, P38, P44 at *TAG SMS* field are not included for the analyses due to several reasons. These are, for drilled core samples and gravity core samples, it is impossible to calculate the representative value of mineralogical composition of elements content since their V_p is not measured in the laboratory, and one cannot set time-depth relation for them below the sea-bed. It might be possible to use the average of measured V_p values in core samples to set time-depth relation for them below the sea-bed; however, measured V_p values in core samples varies from 1077.4 m/s until 6749 m/s and using average V_p 3913.2 m/s could cause an error in calculating the representative value of mineralogical composition of elements content. For sea-bed surface grab samples, they are too sparse, and they can only give generalised information about the area. They cannot truly represent the composition of the area they are taken from; hence, one cannot use them to analyse the mineral richness effect on seismic amplitudes.

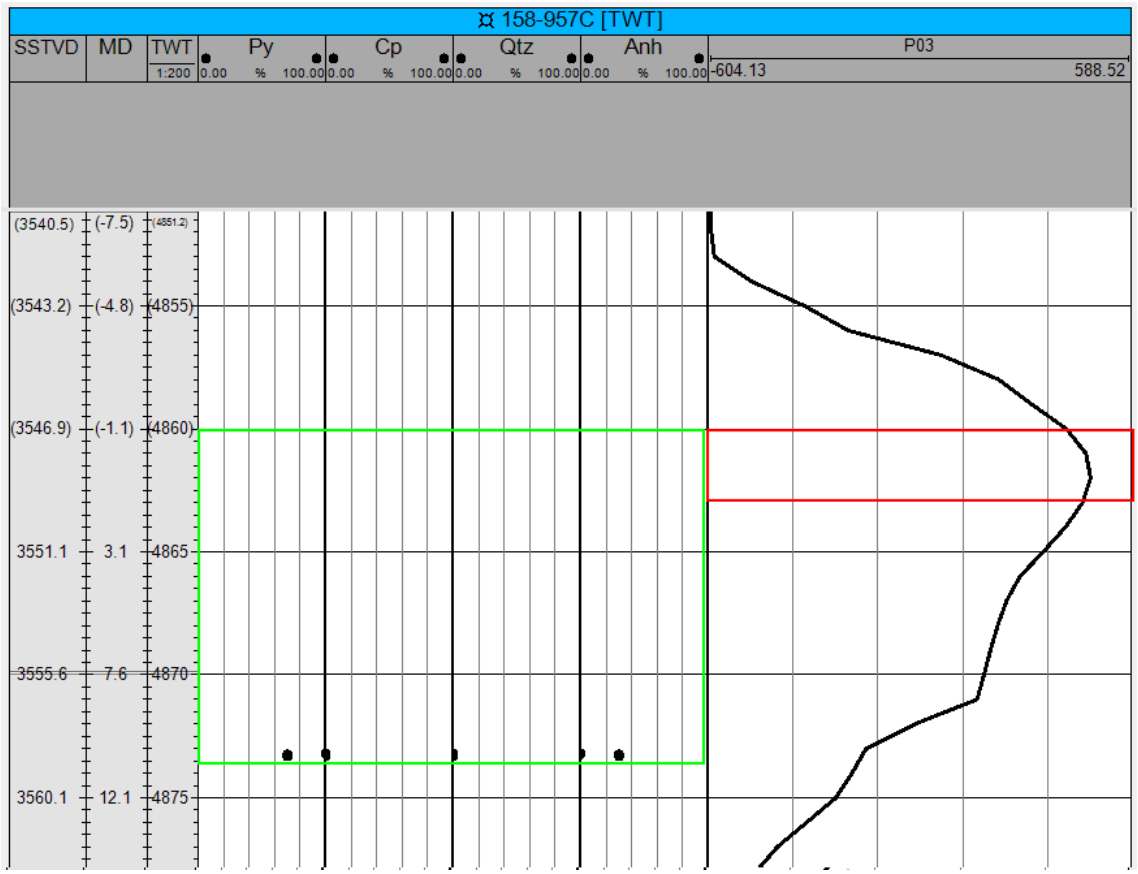

Figure 35: Py, Cpy, Qtz, Anh minerals content and seismic amplitudes at location of shallow hole 158-957C. Each mineral content weighted averaged within window in green. The average of seismic amplitude is calculated within red window.

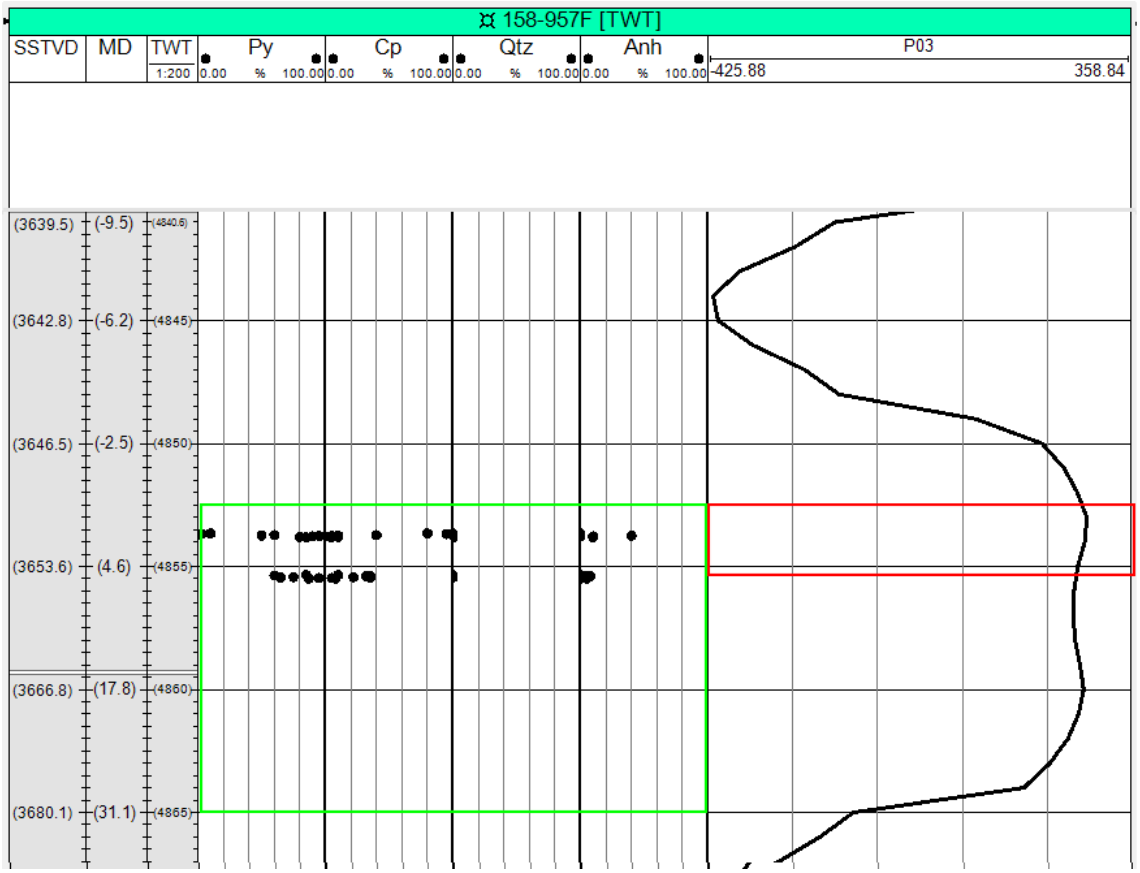

Figure 36: Py, Cpy, Qtz, Anh minerals content and seismic amplitudes at location of shallow hole 158-957F. Each mineral content weighted averaged within window in green. The average of seismic amplitude is calculated within red window.

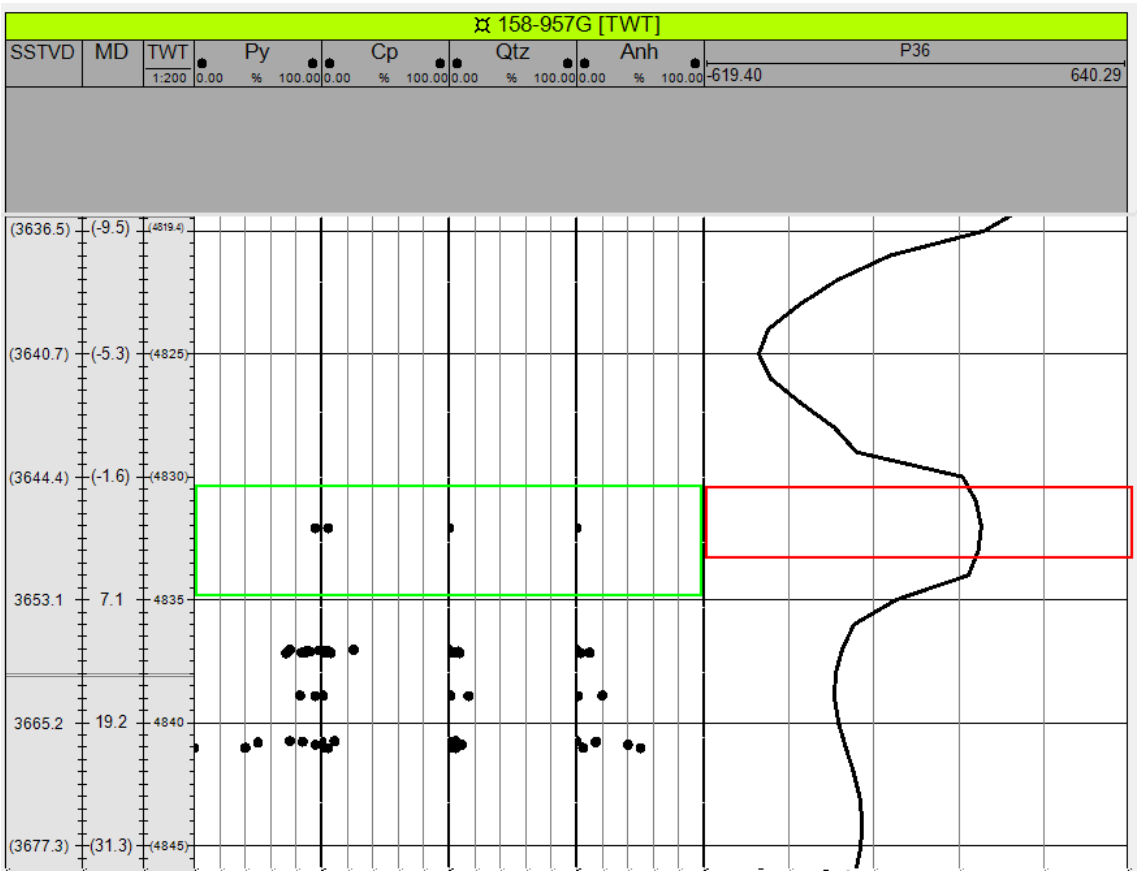

Figure 37: Minerals Py, Cpy, Qtz, Anh and seismic amplitudes at location of shallow hole 158-957G. Each mineral content weighted averaged within window in green. The average of seismic amplitude is calculated within red window.

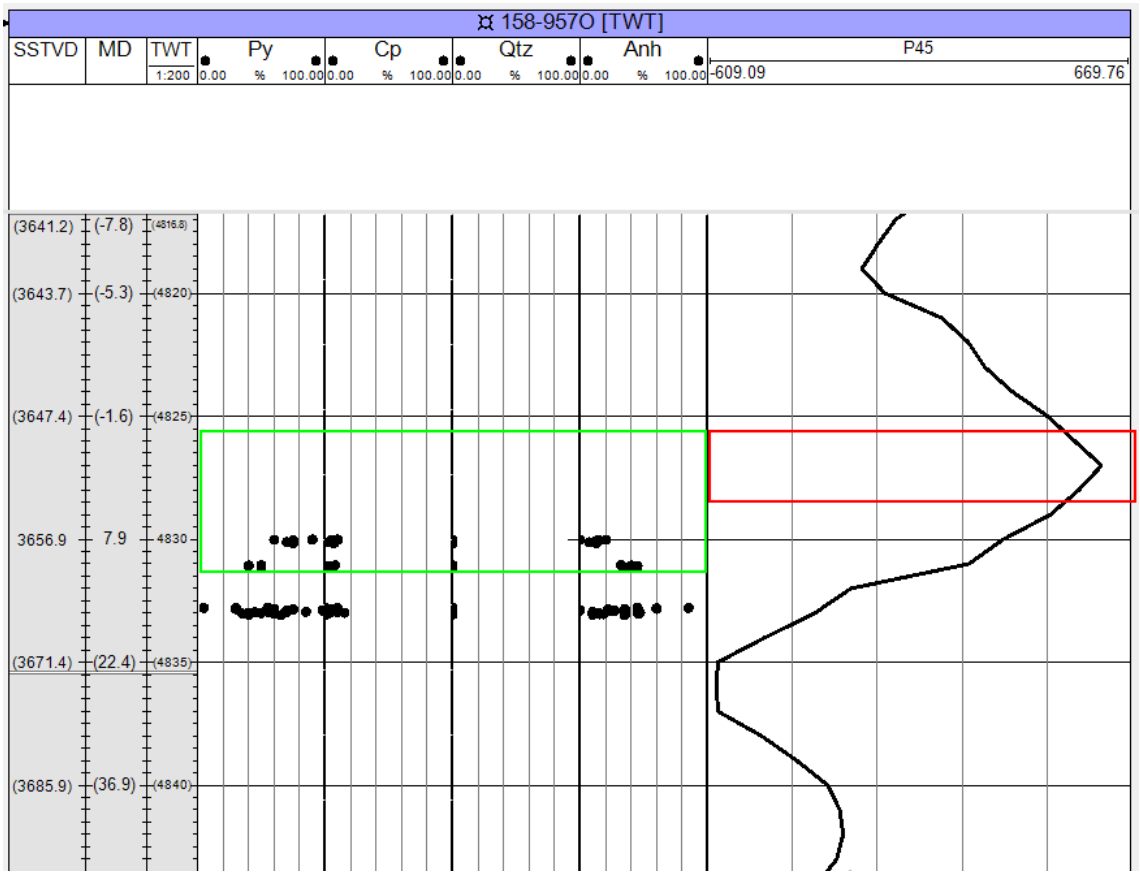

Figure 38: Py, Cpy, Qtz, Anh minerals content and seismic amplitudes at location of shallow hole 158-957O. Each mineral content weighted averaged within window in green. The average of seismic amplitude is calculated within red window.

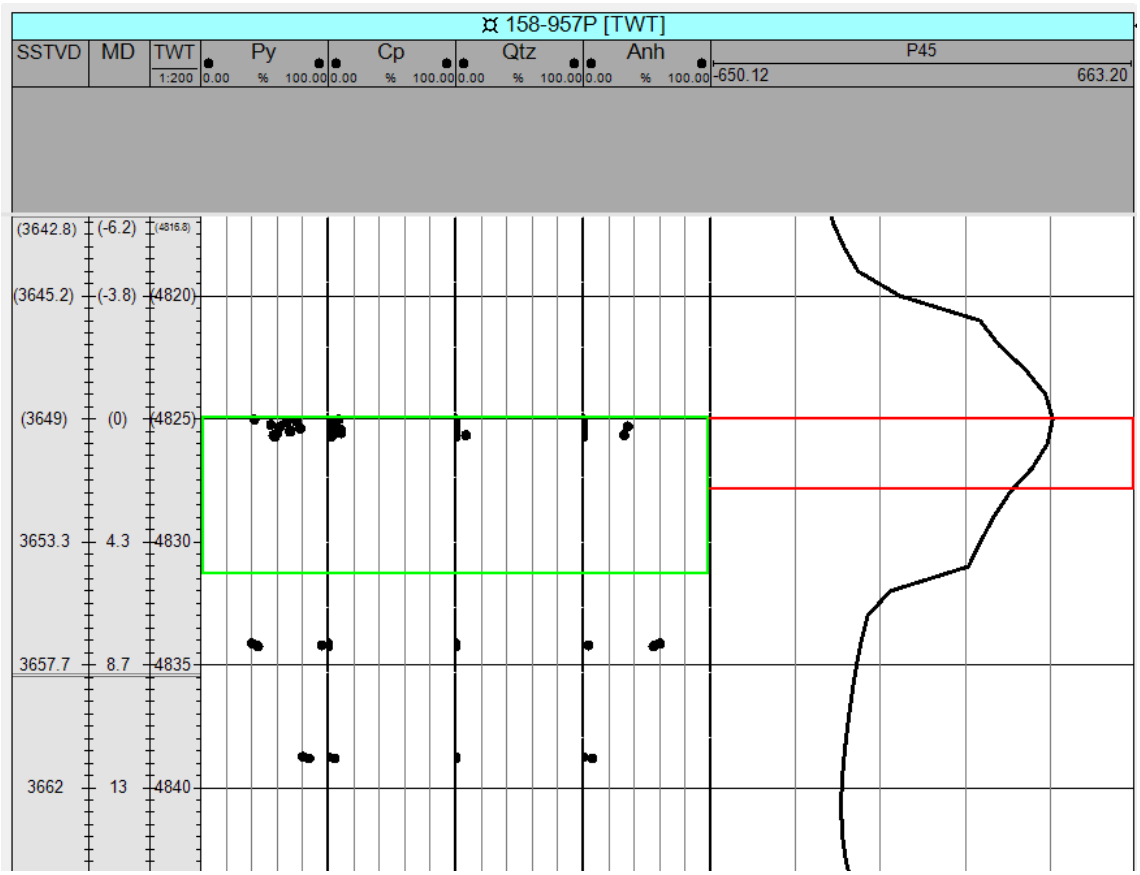

Figure 39: Py, Cpy, Qtz, Anh minerals content and seismic amplitudes at location of shallow hole 158-957P. Each mineral content weighted averaged within window in green. The average of seismic amplitude is calculated within red window.

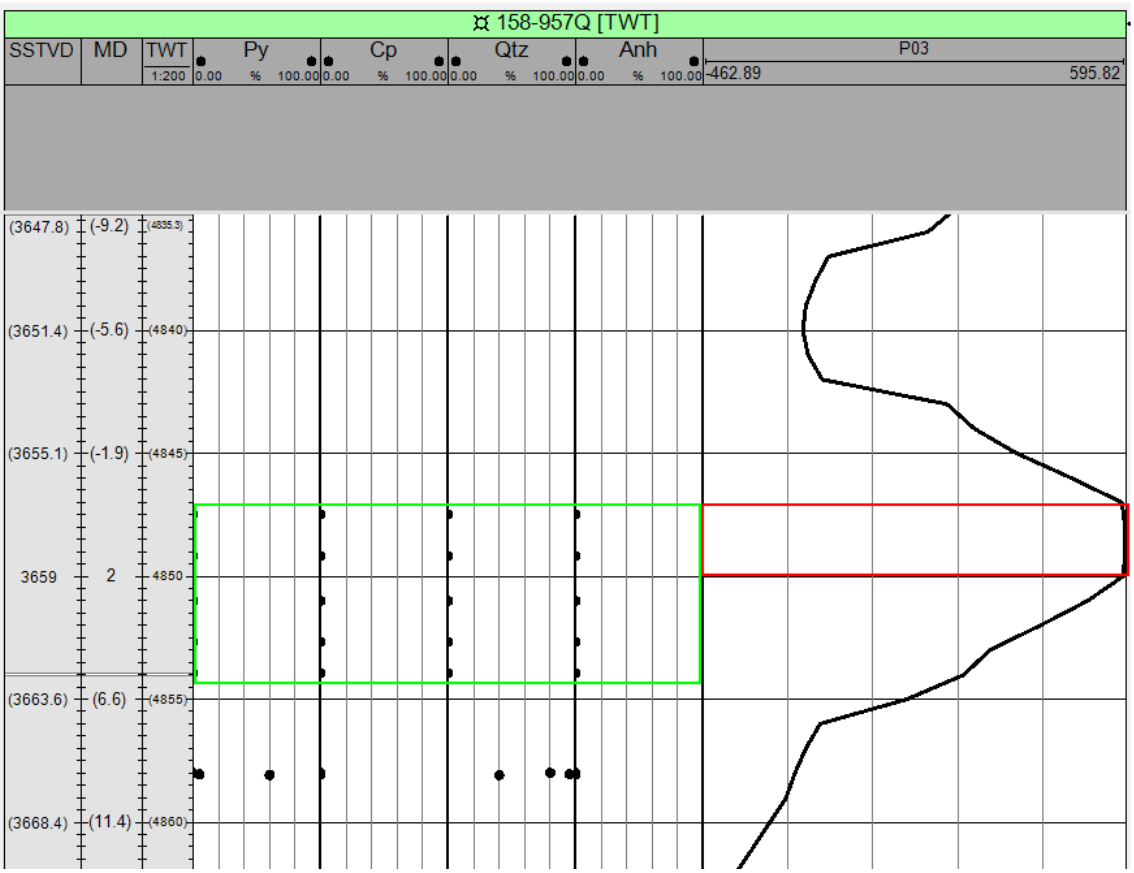

Figure 40: Py, Cpy, Qtz, Anh minerals content and seismic amplitudes at location of shallow hole 158-957Q. Each mineral content weighted averaged within window in green. The average of seismic amplitude is calculated within red window.

4.3 Estimating Acoustic Impedance of Sea-water

Seismic data in use is acquired by source and receivers located near the sea surface in marine conditions at the $TAG\ SMS$ field. The first media where the seismic wave starts propagating is sea-water. Sea water represents the upper space on the sea-water and sea-bed interface. Hence it contributes to R_0 on sea-water and sea-bed interface as shown in equation 8. Z_{sw} is an essential part of the initial model to be submitted into the model-based inversion algorithm.

$$R_0 = \frac{Z_{sb} - Z_{sw}}{Z_{sb} + Z_{sw}} \tag{8}$$

Where:

R_0 - zero angle reflection coefficient;

Z_{sb} - Z of sea-bed;

Z_{sw} - Z of sea-water.

Z_{sw} is a result of sea-water V_p ($V_{p(sw)}$) and sea-water ρ (ρ_{sw}) multiplication. There is no known direct method for estimating Z_{sw} from available data. Therefore it is decided to estimate $V_{p(sw)}$ and ρ_{sw} separately in order to obtain Z_{sw}.

4.3.1 Estimating P-wave Velocity in Sea-water

$V_{p(sw)}$ in sea-water can be estimated by dividing seismic-wave travel distance by seismic-wave travel time.

Seismic data have normal polarity and mixed-phase between 0 and -45 degrees according to seismic data polarity and phase estimation results. Sea-water and sea-bed interface creates positive reflectivity, and its convolution with mixed-phase wavelets between 0 and -45 degrees results in the sea-bed being near peak on the seismic trace. Therefore sea-bed interpretation by the peak of the first reflection event on 2D seismic profiles provides zero-offset two-way travel time of seismic wave to the sea-bed.

There is information on forty eight sampled points (shallow holes, gravity cores and surface-grab samples) location and depth at $TAG\ SMS$ field that is provided in Tables 9, 10, 11, 12, 13. The twenty seven sampled points lie on or near (within 10 m lateral radius of) 2D seismic profiles P03, P07, P36, P38, P44, P45 at $TAG\ SMS$ field, the sample points location are illustrated on Figures 49, 50, 51, 52. Sea-water depth (h_{sw}) that is distance between sea-surface and sea-bed is known at these twenty seven sampled points.

Zero-offset seismic wave two-way travel time to the sea-bed has been interpreted by the peak of the first reflection event on 2D seismic profiles P03, P07, P36, P38, P44, P45. Once zero-offset seismic wave, two-way travel time to the sea-bed and seismic wave travel distance are known at these twenty-seven sampled points. $V_{p(sw)}$ has been calculated using equation 9.

$$V_{p(sw)} = \frac{2h_{sea-bed}}{TWT_{sea-bed}} \tag{9}$$

Where:

$V_{p(sw)}$ - P-wave velocity in sea-water;

TWT_{seabed} - Seismic wave two-way travel time to sea-bed at zero-offset;

h_{seabed} - Vertical distance between sea-surface and sea-bed.

In order to quality-check calculated $V_{p(sw)}$ results by the method mentioned above, P07 2D seismic profile's raw data have been processed and direct seismic wave velocity in the sea-water

surface has been estimated. The 2D seismic profile P07 has been recorded in the southeast to northwest orientation and has a total length of 9 363 m. The 659 shots numbered from 4012 to 4671 and 192 channels surface towed streamer with 1.53 m group offset (292 m active length) have been used for recording the 2D seismic profiles. The raw data is represented by 659 shot files in ".su" format containing only recorded seismic information and by a separate geometry file "geombin2D.ascsubP07" file with source and receiver coordinates during acquisition. The processing has been performed in Shearwater's "Reveal" software in the following steps:

- Loading the shot files
- Loading the geometry file
- Merging shot file with the geometry file
- Computing offset and midpoint coordinates with setting source depth 6 m and receivers depth 4 m
- Create seismic processing grid with bin width 1.4 m, cross-line bin width 155 m, smoothing 268 m
- Calculating bin and CMP coordinates
- Applying 25 - 55 - 400 - 500 band pass-filter for decreasing noise content in seismic data

It is expected that after a shot from a source, a direct seismic wave arrives firstly on receivers before any other seismic waves, it would have strong amplitude, and it would have a slope on a plot receiver against TWT thanks to the difference in receivers offset. The direct seismic wave velocity on the sea-water surface is estimated by the slope of the first distinctive event on recordings of four shots 4015, 4215, 4415, and 4615, evenly distributed by the length of 2D seismic profile P07.

4.3.2 Estimating Sea-water Density

ρ_{sw} at $TAG\ SMS$ field has been estimated based on sea-water pressure measurements recorded at oceanographic station "I", presented in Mackenzie 1981. Station "I" is one of the fifteen world-wide oceanographic stations lettered "A" through "O", where sea-water pressure with depth is measured, and these measurements have been used for developing Mackenzie's nine-term equation for calculating $V_{p(sw)}$ in Mackenzie 1981. Station "I" is located at 30°N and 60°W, and it is the closest station to the $TAG\ SMS$ field out of the fifteen stations. One can see the station's location on Figure 41 for reference.

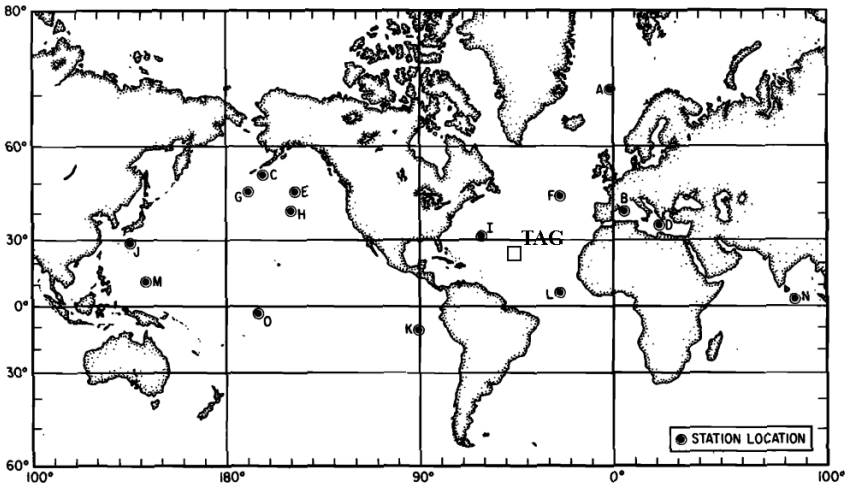

Figure 41: Location of fifteen world-wide ocean properties measuring stations presented in Mackenzie 1981.

Source: Figure 1 in Mackenzie 1981

The measured sea-water pressures by the station "I" and measurement depths are presented in columns number one and number ten of Figure 42 correspondingly, measured sea-water pressures are given in kg/cm^2 and depths in m.

	A	B	C	D	E	F	G	H	I	J	K	L	M	N	O
Surface temperature, °C	4.39	13.30	0.12	22.61	6.66	12.89	5.16	10.25	21.71	21.28	19.65	27.19	29.52	28.48	28.83
Surface salinity, °/₀₀	35.19	37.75	33.18	38.04	32.70	35.71	32.94	33.52	36.83	34.61	35.61	35.48	34.52	34.65	35.65
Pressure[a] kg/cm²	Depth, m														
0	0	0	0	0	0	0	0	0	0	0	0	0	0	0	0
50	484.9	485.7	485.9	485.9	486.3	486.3	486.4	486.8	487.3	487.8	487.8	487.9	488.4	488.4	488.4
100	968.5	970.2	970.5	970.6	971.2	971.4	971.4	972.1	973.2	973.8	974.1	974.2	974.7	974.7	974.7
150	1451.0	1453.7	1454.0	1454.2	1454.9	1455.1	1455.1	1456.1	1457.6	1458.4	1459.1	1459.2	1459.7	1459.8	1459.8
200	...	1936.1	1936.3	1936.7	1937.4	1937.7	1937.7	1938.9	1940.8	1941.7	1942.9	1943.1	1943.6	1943.7	1943.6
250	...	2417.5	2417.4	2418.3	2418.8	2419.2	2419.1	2420.6	2422.9	2423.9	2425.6	2425.8	2426.3	2426.5	2426.4
300	...	...	2897.5	2898.8	2899.1	...	2899.5	2901.3	2903.9	2905.0	2907.3	2907.4	2907.9	2908.2	2908.1
400	...	...	3854.5	3856.9	3856.5	...	3857.0	3859.3	3862.8	3864.0	...	...	3867.9	3868.4	3868.3
500	...	...	4807.4	4811.2	4809.8	...	4810.4	...	...	...	...	...	4823.8	...	...

[a] $g = 9.80665$ m/s².

Figure 42: Fifteen world-wide oceanographic stations location.

Source: Table 1 in Mackenzie 1981

Since the measured sea-water pressure for different depths by station "I" can be calculated using equation 10 for calculating pressure of hydro-static-column. Where variables P, h are known from measurements of station "I" and g has constant value of 9.80665 m/s^2. The ρ_{sw} has been computed by rearranged form of equation 10, for measurement depths from 487.3 m to 3862.8 m of the station "I" using equation 11.

$$P = \rho_{sw} g h \tag{10}$$

$$\rho_{sw} = \frac{P}{gh} \tag{11}$$

Where:

ρ_{sw} - ρ of sea-water;

P - hydro-static pressure;

g - gravitational constant;

h - water column height.

The linear function (equation 12) for h_{sw} versus ρ_{sw} relation has been determined using trend-line function in MS Excel. This linear function has been used for calculating ρ_{sw} versus h_{sw} profile at sampled locations mentioned in Table 6 and the mean value of the ρ_{sw} versus h_{sw} profile has been accepted as representative of ρ_{sw} at sampled locations at $TAG\ SMS$ field.

$$\rho_{sw} = 0.0028 h_{sw} + 1024.9 \tag{12}$$

Where:

ρ_{sw} - ρ of sea-water;

h_{sw} - sea-water depth.

4.4 Model Based Inversion

2D seismic profile P03 is chosen for performing model-based inversion at $TAG\ SMS$ field since there are seven shallow holes 158-957C, 158-957F, 158-957Q, 158-957E, 158-957K, JC138-22, JC138-50 in total located on or near (within 10 m lateral radius of) this profile which is shown in Figures 49, 51. Five of the seven shallow holes 158-957C, 158-957F, 158-957Q, 158-957E, 158-957K have been drilled during the ODP Leg 158 expedition, and two shallow holes are JC138-22, JC138-50 drilled while JC-138 expedition. Mineralogical composition laboratory analyses are performed on core samples from all five shallow holes, V_p laboratory measurement analyses are performed on core samples from three shallow holes 158-957C, 158-957F, 158-957Q, ρ laboratory measurement analyses are performed on core samples from two shallow holes 158-957C, 158-957Q during ODP Leg 158 expedition and hence they have Z of subsurface defined in a laboratory. Only element-wise composition laboratory analyses are performed on core samples from two shallow holes during the JC-138 expedition. One can see the summary of available information on the location of the shallow holes in Table 3.

Name of Shallow hole	Drilled mound	Expedition	Composition	Information on V_p	Information on ρ	Information on Z
[-]	[-]	[-]	[-]	[-]	[-]	[-]
158-957C	Active TAG	ODP Leg 158	Mineralogical composition	Available	Available	Available
158-957F	Active TAG	ODP Leg 158	Mineralogical composition	Available	Not available	Not available
158-957Q	Active TAG	ODP Leg 158	Mineralogical composition	Available	Available	Available
JC138-50	Southern	JC-138	Element-wise composition	Not available	Not available	Not available
JC138-22	Southern	JC-138	Element-wise composition	Not available	Not available	Not available
158-957E	Active TAG	ODP Leg 158	Mineralogical composition	Not available	Not available	Not available
158-957K	Active TAG	ODP Leg 158	Mineralogical composition	Not available	Not available	Not available

Table 3: Available information on core samples from shallow holes located on/near 2D seismic profile P03.

The shallow holes have been divided into Input and Blind categories before performing a model-based inversion. Data from shallow holes in the Input category have been used for performing inversion, and data from shallow holes in the Blind category for analyzing model-based inversion results. Input category include shallow holes 158-957Q, 158-957E, 158-957K, JC138-22, JC138-50 and Blind category consist from shallow holes 158-957C, 158-957F.

As a first step in preparation for model-based inversion synthetic V_p and ρ log files have been generated for shallow holes in Input category using data in Tables 5, 14, 15. Only shallow hole 158-957Q has V_p and ρ log values below sea-bed while shallow holes 158-957E, 158-957K, JC138-22, JC138-50 have V_p and ρ log values only in sea-water. Secondly, it is decided to use the sea-bed interpretation horizon picked by the sea-bed reflection's first peak amplitudes as the input horizon for inversion.

The model-based inversion has been performed using Geoview software. It begins with downloading 2D seismic profile P03, the location of shallow holes from the Input category, the synthetic log files and the sea-bed interpretation in Geoview software. The model-based inversion workflow in the Geoview consists from eight stages:

1. Selecting seismic data
2. Selecting horizons
3. Extracting statistical wavelet
4. Selecting shallow holes
5. Correlating shallow holes
6. Building initial background model
7. Inversion analyses on the location of a shallow hole
8. Applying inversion algorithm to the selected seismic data

2D seismic profile P03 and the sea-bed interpretation are selected in the first and second stages. Zero phase statistical wavelet is extracted from window 1995-2247 CMP and in 4500-4900 ms TWT window where good sea-bed seismic reflection exists as shown in the Figure 32. Shallow holes 158-957Q, 158-957E, 158-957K, JC138-22, and JC138-50 from the Input category have been selected on a fourth stage. The shallow hole 158-957Q is selected on a fifth stage for correlating shallow holes with seismic data. The best correlation is achieved by rotating the phase of the statistical wavelet to -40 degrees. The initial background model has been constructed using all data from shallow holes in the Input category, the sea-bed interpretation horizon and statistical wavelet with the phase of -40 degrees defined in stage three by applying a high-frequency cut of 10-12 Hz on model generation in order to compensate low-frequency component of Z in final model-based inversion result. Inversion analyses are performed on shallow hole 158-957Q location using generated initial background model, the statistical wavelet with the phase of -40 degree, the sea-bed interpretation horizon and by setting 100 to number of iterations in model-based inversion analyses, whereas correlation coefficient 0.99882 is achieved. This correlation coefficient is considered acceptable and using input data for Inversion analyses; the inversion algorithm has been applied to the whole seismic 2D profile P03.

4.5 SMS Mineral Richness and Acoustic Impedance Analyses

Analysing results of applying model-based inversion on 2D seismic profile P03 at $TAG\ SMS$ field is started by comparing Z values acquired from the model-based inversion at shallow hole 158-957C location with Z values determined from V_p and ρ laboratory core measurement results. Z from the two sources are compared in a cross-section view.

Further, Z values from model-based inversion are compared with Py, Cpy, Qtz, Anh minerals content along shallow hole 158-957C to see if there is a relation between mineral richness and Z values from model-based inversion. The synthetic log representing Z values from model-based inversion along shallow hole 158-957C is created in Petrel. The comparison is performed on a two-dimensional plot on the "Function window" in Petrel for each mineral separately by plotting one of Py, Cpy, Qtz, Anh mineral content on the vertical axis and Z values from model-based inversion on the horizontal axis.

In order to cross-check the obtained correlation results between Z values from model-based inversion and Py, Cpy, Qtz, Anh minerals content, Z values determined from V_p and ρ laboratory core measurement results on core samples from shallow hole 158-957C are plotted against Py, Cpy, Qtz, Anh minerals content on "Function window" in Petrel for each mineral separately as well.

5 Results

5.1 Phase of Seismic Data

5.2 SMS Mineral Richness and Seismic Amplitudes

One can see the interpreted peak of seismic amplitudes on the sea-bed and mineral-rich SMS mounds location at the TAG SMS field in Figure 43 below. There are no apparent amplitude anomalies at the SMS mounds compared to surroundings. One can say average amplitudes represent SMS mounds areas within 600-700; however, it is not unique or distinctive over the TAG SMS field.

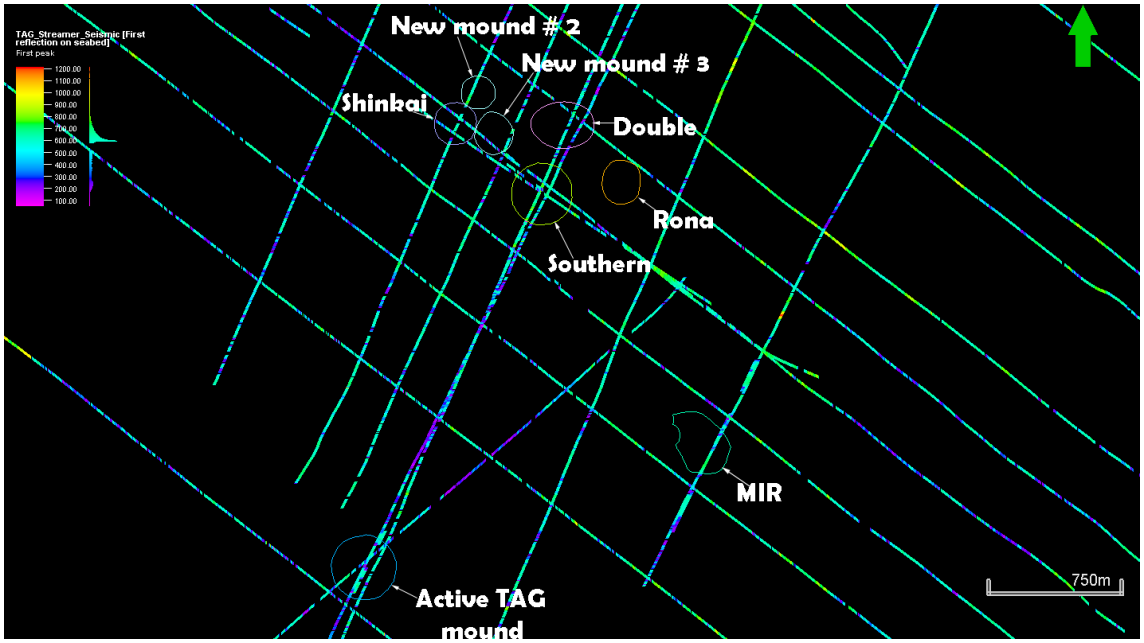

Figure 43: Interpreted peak of seismic amplitudes on sea-bed and SMS mounds location at TAG SMS field.

The calculated peak of seismic amplitudes on the sea-bed averaged over a 3ms window and weighted average content of Py, Cpy, Qtz, Anh minerals at 158-957G, 158-957F, 158-957P, 158-957C, 158-957O, 158-957Q shallow holes location is provided in Table 4.

Shallow hole	Py	Cpy	Qtz	Anh	Seismic amplitude on sea-bed
[-]	[%]	[%]	[%]	[%]	[-]
158-957G	95.0	5.0	0.0	0.0	178.4
158-957F	59.0	37.0	0.0	11.4	280.5
158-957P	63.0	6.0	8.0	33.5	400.5
158-957C	80.0	0.0	0.0	30.0	469.3
158-957O	74.0	7.0	0.0	13.4	541.9
158-957Q	0.0	0.0	0.0	0.0	595.8

Table 4: Calculated peak of seismic amplitudes on the sea-bed and weighted average content of Py, Cpy, Qtz, Anh minerals at 158-957G, 158-957F, 158-957P, 158-957C, 158-957O, 158-957Q shallow holes location of TAG SMS field.

And one can see these Py, Cpy, Qtz, Anh minerals content plotted together against the seismic amplitudes on sea-bed on Figure 44 and plotted separately on Figures 45, 46, 47, 48 below.

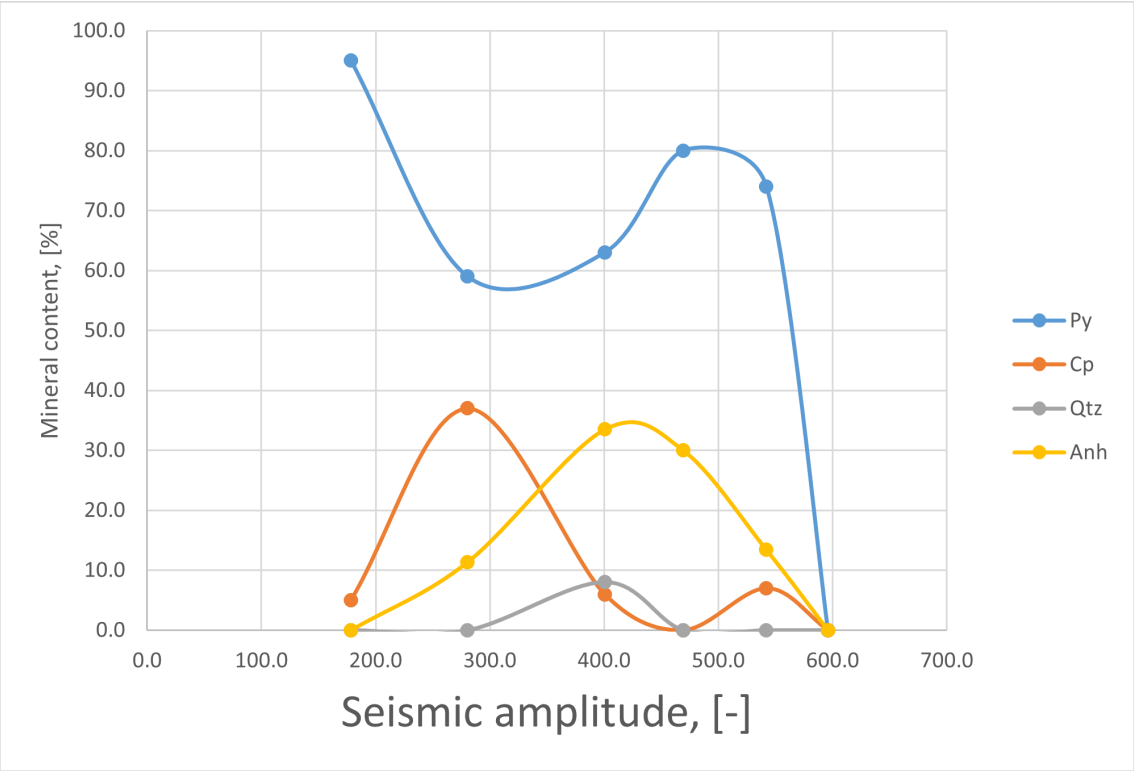

Figure 44: Seismic amplitude on sea-bed against Py, Cpy, Qtz, Anh minerals content at 158-957G, 158-957F, 158-957P, 158-957C, 158-957O, 158-957Q shallow holes location of $TAG\ SMS$ field.

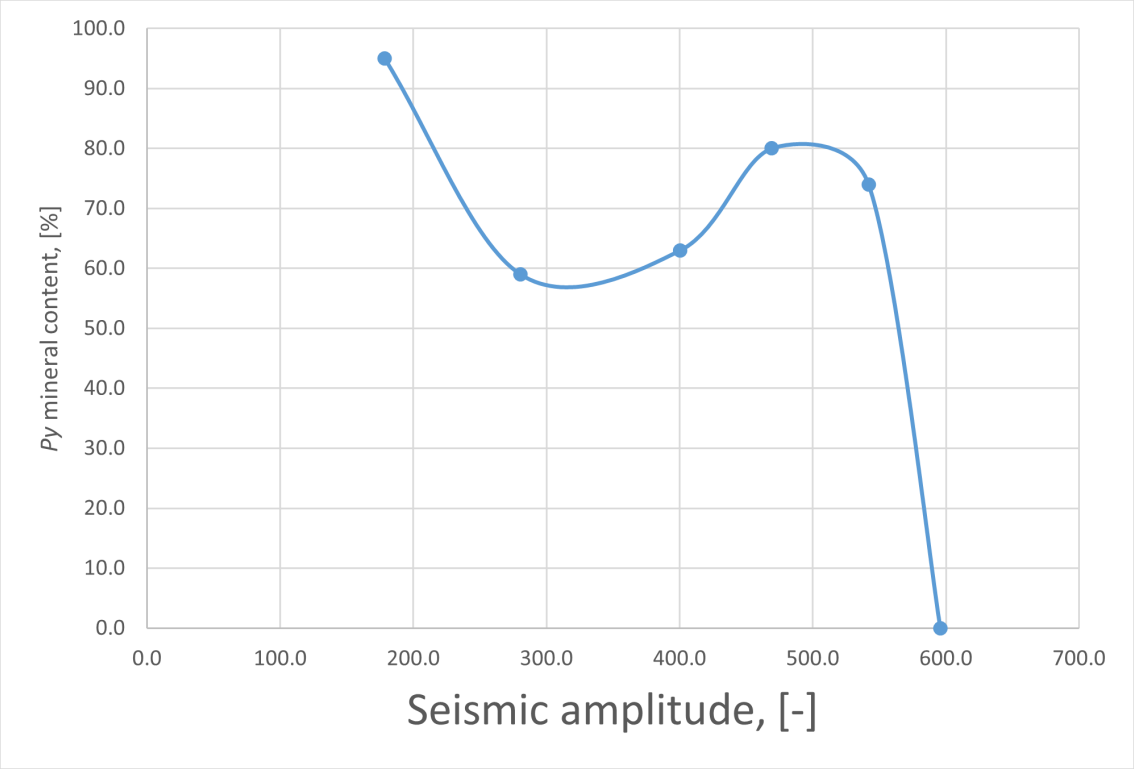

Figure 45: Seismic amplitude on sea-bed against Py content at 158-957G, 158-957F, 158-957P, 158-957C, 158-957O, 158-957Q shallow holes location of $TAG\ SMS$ field.

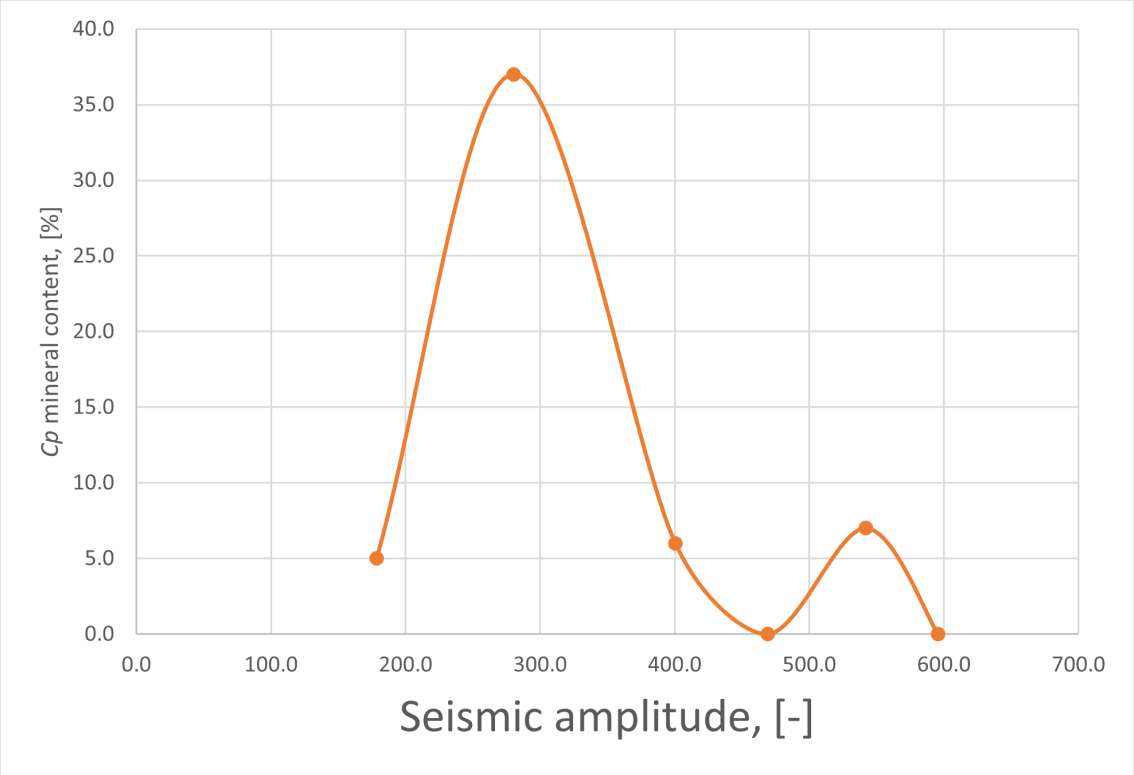

Figure 46: Seismic amplitude on sea-bed against *Cpy* content at 158-957G, 158-957F, 158-957P, 158-957C, 158-957O, 158-957Q shallow holes location of *TAG SMS* field.

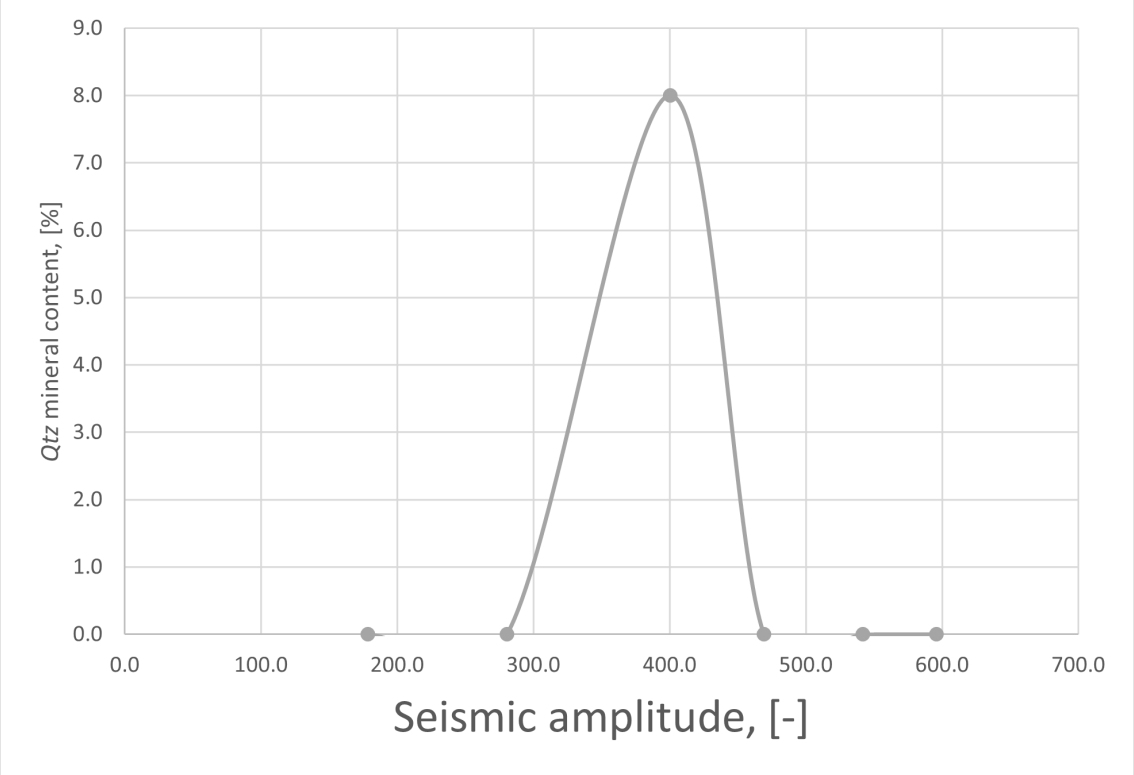

Figure 47: Seismic amplitude on sea-bed against *Qtz* content at 158-957G, 158-957F, 158-957P, 158-957C, 158-957O, 158-957Q shallow holes location of *TAG SMS* field.

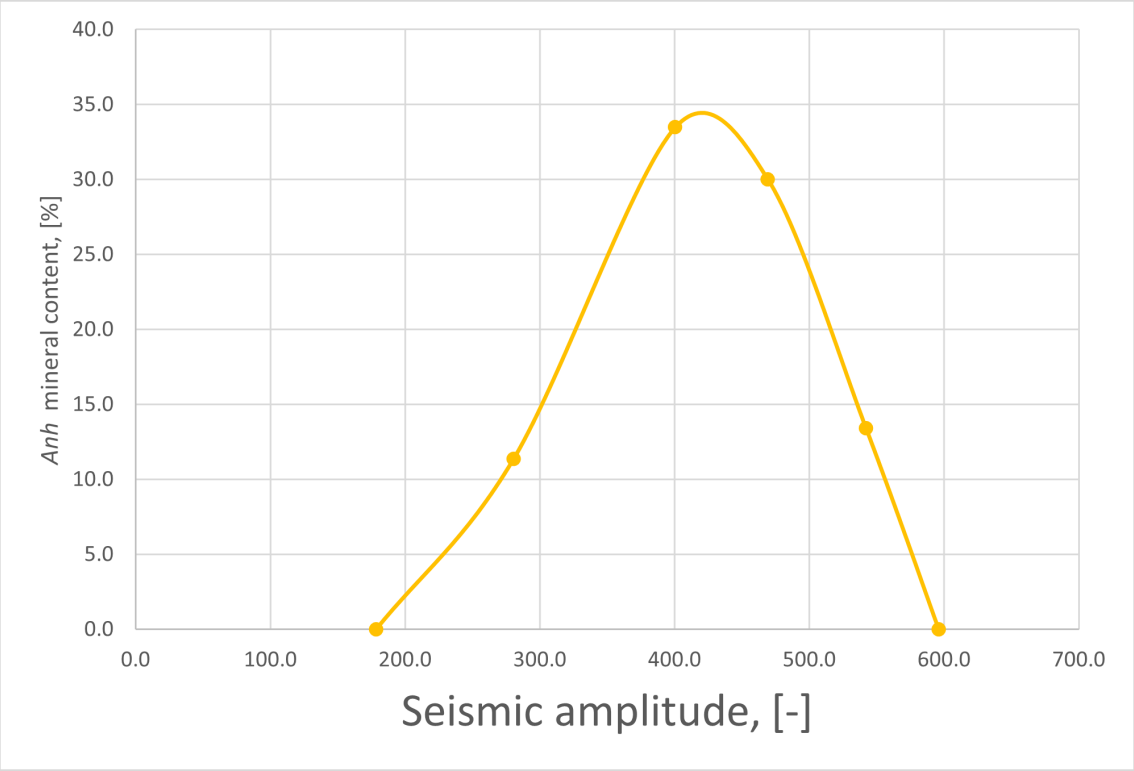

Figure 48: Seismic amplitude on sea-bed against *Anh* content at 158-957G, 158-957F, 158-957P, 158-957C, 158-957O, 158-957Q shallow holes location of $TAG\ SMS$ field.

5.3 Sea-water Acoustic Impedance

Z_{sw} has been calculated from multiplication of $V_{p(sw)}$ and ρ_{sw} values determined at sampled points of $TAG\ SMS$ field shown in Figures 49, 50, 51, 52. One can see the calculated $V_{p(sw)}$, ρ_{sw} and Z_{sw} values in Table 5 below.

Detailed information on how $V_{p(sw)}$ and ρ_{sw} are determined is presented below.

5.3.1 P-wave Velocity in Sea-water Estimation

$V_{p(sw)}$ has been estimated using two methods, first by considering time spent for the seismic wave to reach and reflect from the sea-bed on sampled locations where sea-bed depth and seismic wave TWT are known, and second by looking at direct wave velocity in sea-water on P07 2D seismic profile. For more detailed information, please refer to the "Estimating P-wave Velocity In Sea-water" subsection in Methods.

For the first method, the twenty seven sampled points located on or near (within 10 m lateral radius of) 2D seismic profiles P03, P07, P36, P38, P44, P45 at $TAG\ SMS$ field have been chosen for $V_{p(sw)}$ calculations. One can see these points in the Figures 49, 50, 51, 52 below.

$V_{p(sw)}$ has been calculated using equation 9 at these sampled locations. These calculations provide the results shown in Table 6. Mean $V_{p(sw)}$ at $TAG\ SMS$ field is equal to 1506.61 m/s according to the first method results.

One can see $V_{p(sw)}$ in sea surface obtained by the second method in Figures 53, 54, 55, 56. Mean $V_{p(sw)}$ in sea surface is 1525 m/s according to slope of direct wave on recordings of shots number 4015, 4215, 4415, 4645 of 2D seismic profile P07.

Sample name	Sample type	Mound	2D seismic profile	Sea-bed depth	$V_{p(sw)}$	Mean ρ_{sw}	Z_{sw}
[-]	[-]	[-]	[-]	[m]	[m/s]	[kg/m^3]	[(m/s)(kg/m^3)]
158-957C	Shallow hole	Active TAG	P03	3548	1459.62	1029.87	1503212.50
158-957F	Shallow hole	Active TAG	P03	3649	1503.73	1030.01	1548847.90
158-957G	Shallow hole	Active TAG	P36	3646	1509.08	1030.00	1554354.72
158-957O	Shallow hole	Active TAG	P45	3649	1511.89	1030.01	1557261.05
158-957P	Shallow hole	Active TAG	P45	3649	1512.53	1030.01	1557916.23
158-957Q	Shallow hole	Active TAG	P03	3657	1508.83	1030.02	1554117.72
JC138-45-1	Sea-bed surface grab	Southern	P36	3530	1487.80	1029.84	1532197.32
JC138-45-2	Sea-bed surface grab	Southern	P36	3530	1487.80	1029.84	1532194.09
JC138-23GC-cc-W	Sea-bed surface grab	Southern	P07	3537	1501.93	1029.85	1546759.89
JC138-41-2	Sea-bed surface grab	Southern	P44	3574	1524.71	1029.90	1570303.73
JC138-41-3	Sea-bed surface grab	Southern	P44	3574	1524.71	1029.90	1570303.73
JC138-45-4x	Sea-bed surface grab	Southern	P36	3540	1491.87	1029.85	1536413.01
JC138-45-4y	Sea-bed surface grab	Southern	P36	3540	1491.87	1029.85	1536413.01
JC138-45-5	Sea-bed surface grab	Southern	P07	3552	1515.84	1029.87	1561123.74
JC138-45-6	Sea-bed surface grab	Southern	P07	3552	1515.84	1029.87	1561123.74
JC138-55-1	Sea-bed surface grab	New mound # 3	P07	3589	1535.97	1029.92	1581930.58
JC138-55-2	Sea-bed surface grab	New mound # 3	P07	3589	1535.97	1029.92	1581930.58
JC138-55-7	Sea-bed surface grab	Shinkai	P44	3624	1523.58	1029.97	1569240.61
JC138-55-8	Sea-bed surface grab	Shinkai	P44	3624	1523.58	1029.97	1569240.61
JC138-50	Shallow hole	Southern	P03	3536.8	1490.42	1029.85	1534902.61
JC138-73	Shallow hole	MIR	P38	3437.1	1508.64	1029.71	1553456.93
JC138-76	Shallow hole	MIR	P38	3435.7	1506.49	1029.71	1551243.71
JC138-22	Shallow hole	Southern	P03	3535	1489.64	1029.85	1534106.43
JC138-31	Shallow hole	Southern	P07	3533	1509.50	1029.84	1554550.79
M127-692GC/A/10	Gravity core	MIR	P38	3422	1502.50	1029.69	1547103.19
158-957E	Shallow hole	Active TAG	P03	3646	1502.43	1030.00	1547510.82
158-957K	Shallow hole	Active TAG	P03	3644	1501.60	1030.00	1546644.99

Table 5: Data for calculating Z_{sw} and Z_{sw} calculation results at sampled points of TAG SMS field.

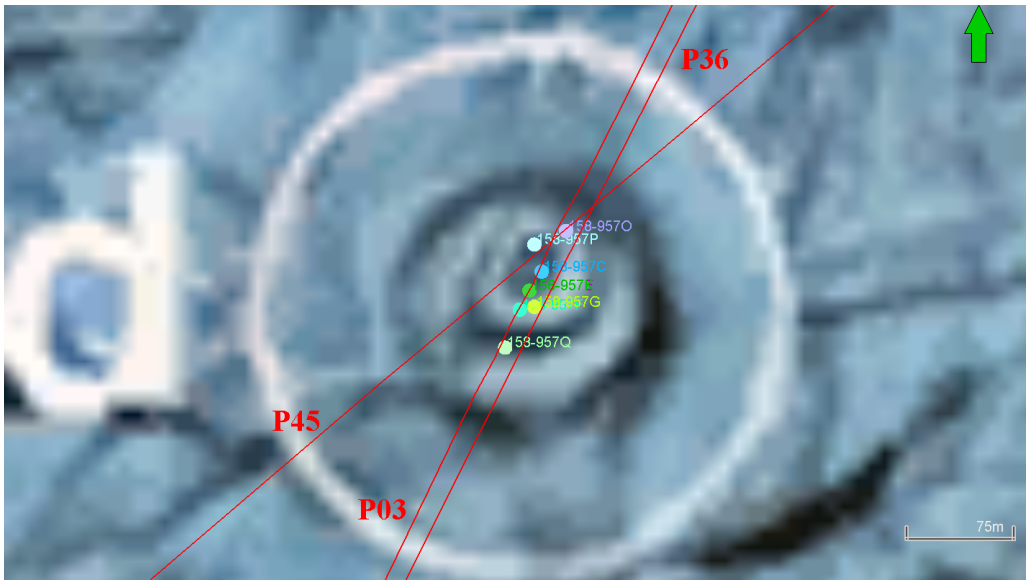

Figure 49: Sampled locations at active TAG mound located on/near P03, P36 and P45 2D seismic profiles.

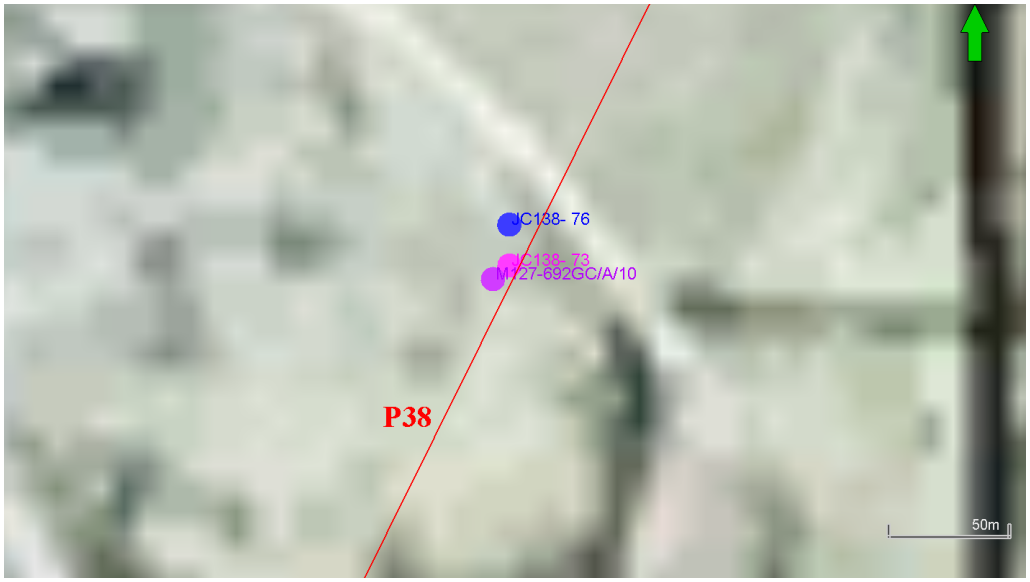

Figure 50: Sampled locations at MIR zone located on/near P38 2D seismic profiles.

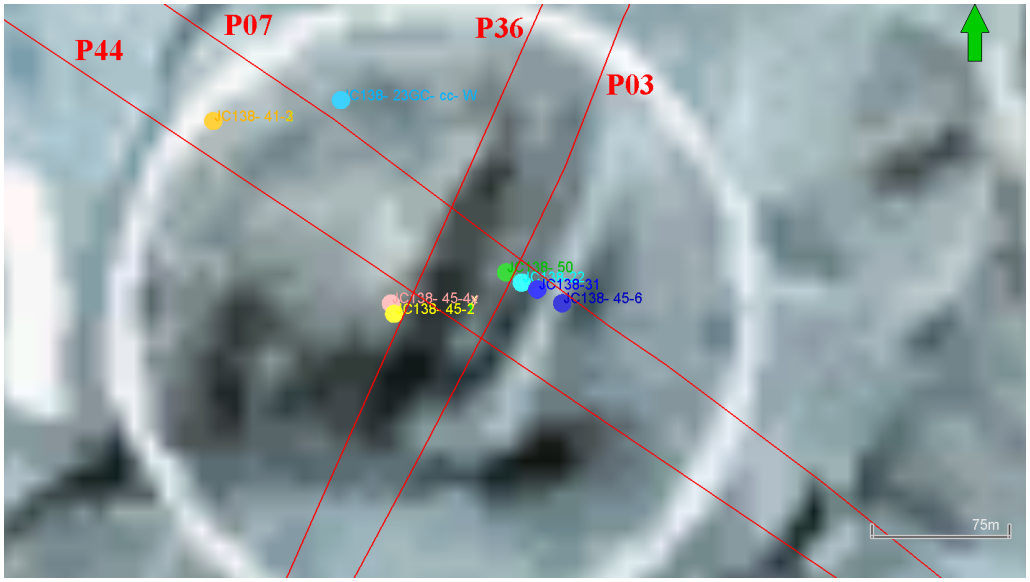

Figure 51: Sampled locations at Southern mound located on/near P03, P07, P36, P44 2D seismic profiles.

Figure 52: Sampled locations at Shinkai mound (left) and New-mound # 3 (right) located on/near P07, P44 2D seismic profiles.

Sample name	Sample type	Mound	The profile	Sea-bed depth	TWT	$V_{p(sw)}$
[-]	[-]	[-]	[-]	[m]	[ms]	[m/s]
158-957C	Shallow hole	Active *TAG*	P03	3548	4861.54	1459.62
158-957F	Shallow hole	Active *TAG*	P03	3649	4853.28	1503.73
158-957G	Shallow hole	Active *TAG*	P36	3646	4832.09	1509.10
158-957O	Shallow hole	Active *TAG*	P45	3649	4827.06	1511.89
158-957P	Shallow hole	Active *TAG*	P45	3649	4825.03	1512.53
158-957Q	Shallow hole	Active *TAG*	P03	3657	4847.48	1508.83
JC138-45-1	Sea-bed surface grab	Southern	P36	3530	4745.26	1487.80
JC138-45-2	Sea-bed surface grab	Southern	P36	3530	4745.27	1487.80
JC138-23GC-cc-W	Sea-bed surface grab	Southern	P07	3537	4709.95	1501.93
JC138-41-2	Sea-bed surface grab	Southern	P44	3574	4688.10	1524.71
JC138-41-3	Sea-bed surface grab	Southern	P44	3574	4688.10	1524.71
JC138-45-4x	Sea-bed surface grab	Southern	P36	3540	4745.71	1491.87
JC138-45-4y	Sea-bed surface grab	Southern	P36	3540	4745.71	1491.87
JC138-45-5	Sea-bed surface grab	Southern	P07	3552	4686.50	1515.84
JC138-45-6	Sea-bed surface grab	Southern	P07	3552	4686.50	1515.84
JC138-55-1	Sea-bed surface grab	New mound # 3	P07	3589	4673.27	1535.97
JC138-55-2	Sea-bed surface grab	New mound # 3	P07	3589	4673.27	1535.97
JC138-55-7	Sea-bed surface grab	Shinkai	P44	3624	4757.23	1523.58
JC138-55-8	Sea-bed surface grab	Shinkai	P44	3624	4757.23	1523.58
JC138-50	Shallow hole	Southern	P03	3537	4746.06	1490.42
JC138-73	Shallow hole	MIR	P38	3437	4556.57	1508.64
JC138-76	Shallow hole	MIR	P38	3436	4561.20	1506.49
JC138-22	Shallow hole	Southern	P03	3535	4746.10	1489.64
JC138-31	Shallow hole	Southern	P07	3533	4681.02	1509.50
M127-692GC/A/10	Gravity core	MIR	P38	3422	4555.09	1502.50
158-957E	Shallow hole	Active *TAG*	P03	3646	4853.46	1502.43
158-957K	Shallow hole	Active *TAG*	P03	3644	4853.50	1501.60
					Mean:	1506.61

Table 6: Data for calculating $V_{p(sw)}$ and $V_{p(sw)}$ calculation results at sampled points of *TAG SMS* field.

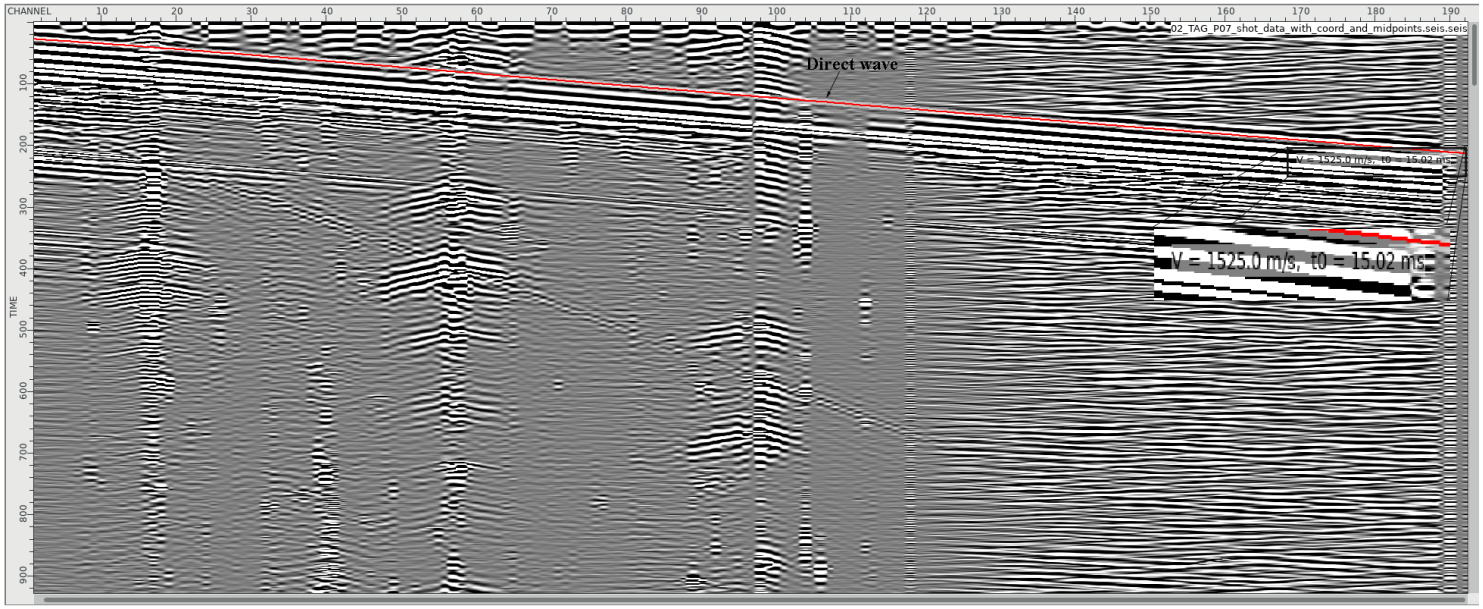

Figure 53: Recordings of shot number 4015 of 2D seismic profile P07.

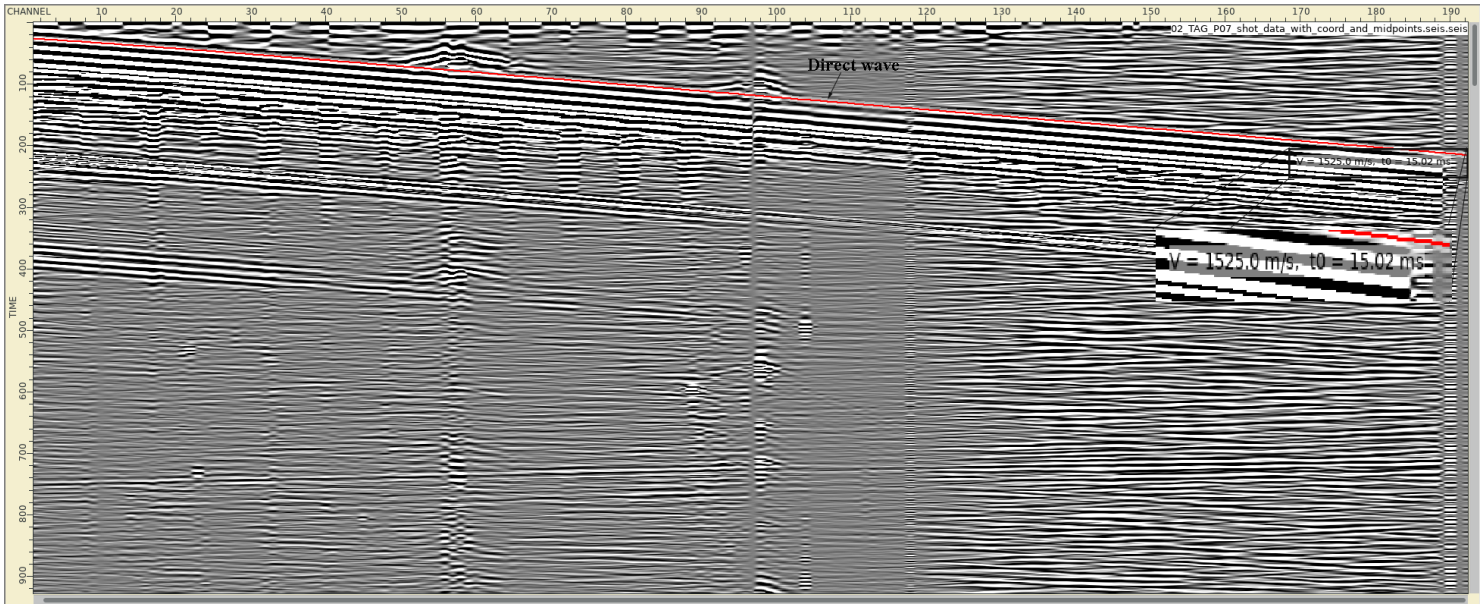

Figure 54: Recordings of shot number 4215 of 2D seismic profile P07.

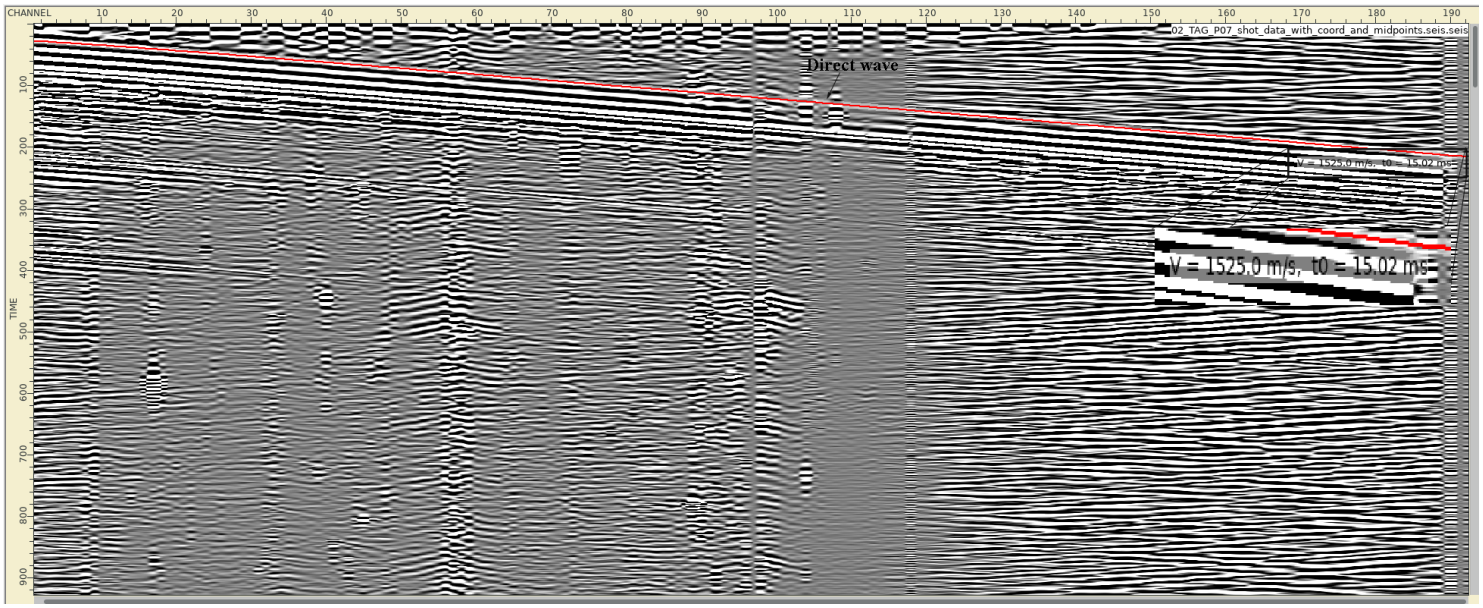

Figure 55: Recordings of shot number 4415 of 2D seismic profile P07.

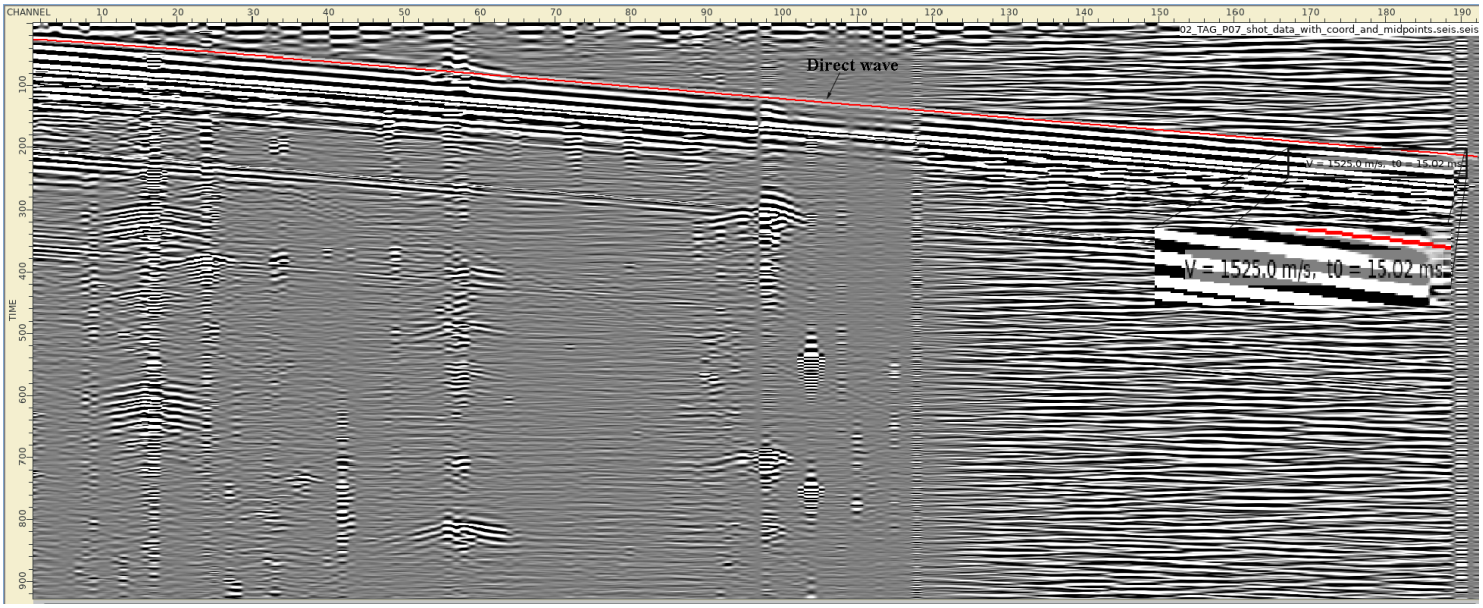

Figure 56: Recordings of shot number 4615 of 2D seismic profile P07.

Two methods provide close results. Mean $V_{p(sw)}$ is 1506.61 m/s and $V_{p(sw)}$ in sea-surface is 1525 m/s. The difference in obtained results can be explained by variance of $V_{p(sw)}$ with depth due to sea-water temperature, pressure and mineralisation change. There is no available information on sea-water temperature, pressure and mineralisation change with depth at the $TAG\ SMS$ field; therefore, it is impossible to estimate $V_{p(sw)}$ change with depth. $V_{p(sw)}$ estimated by the first method is considered more reliable since it is estimated taking into account seismic wave travel-time through the whole thickness of the water column at sampled points. It considers $V_{p(sw)}$ lateral and depth variations depending on a sample location. Therefore $V_{p(sw)}$ results shown in Table 6, estimated by the first method, have been used further.

5.3.2 Sea-water Density Estimation

Oceanographic station "I" is located near $TAG\ SMS$ field as shown in Figure 41 and it is assumed that ρ_{sw} derived from sea-water pressure measurement values at the station's location would give representative value of ρ_{sw} for $TAG\ SMS$ field. One can see ρ_{sw} values calculated by equation 11 along h_{sw} at oceanographic station "I" location in Table 7 below.

h_{sw}	P	P	g	ρ_{sw}
[m]	$[kg/cm^2]$	[Pa]	[N/kg]	$[kg/m^3]$
0	0	0	9.80665	
487.3	50	4903325	9.80665	1026.06
973.2	100	9806650	9.80665	1027.54
1457.6	150	14709975	9.80665	1029.09
1940.8	200	19613300	9.80665	1030.50
2422.9	250	24516625	9.80665	1031.82
2903.9	300	29419950	9.80665	1033.09
3862.8	400	39226600	9.80665	1035.52

Table 7: Data for calculating ρ_{sw} from measurements of oceanographic station "I" and ρ_{sw} calculation results using equation 11.

The linear function in equation 12 has been checked on reliability before implementing it to calculate ρ_{sw} versus h_{sw} profile at $TAG\ SMS$ field's sampled locations, mentioned in Table 6. The ρ_{sw} calculated using the linear function has been compared with ρ_{sw} results in Table 7 and the absolute difference in their values have been observed. One can see obtained results in Figures 57, 58 below.

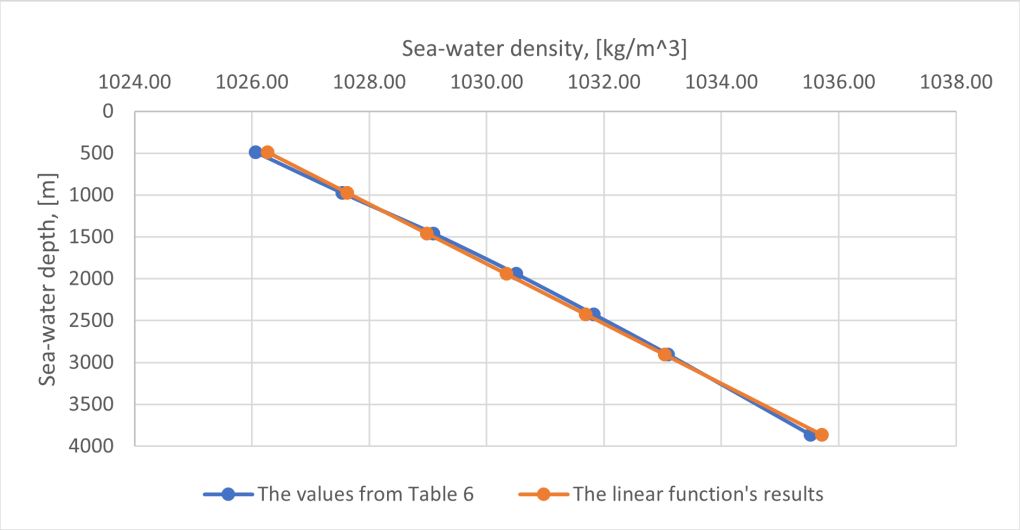

Figure 57: ρ_{sw} versus h_{sw} profile at location of oceanographic station "I".

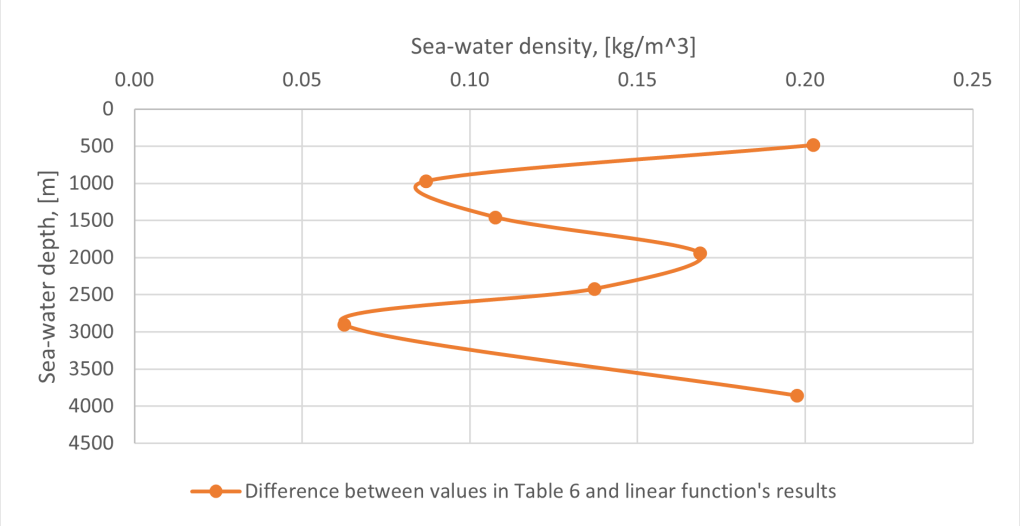

Figure 58: Difference in ρ_{sw} values at location of oceanographic station "I".

As one can see the difference in results is small, therefore the linear function is considered reliable for predicting ρ_{sw} with h_{sw}. The linear function has been applied for calculating ρ_{sw} versus h_{sw} profile at $TAG\ SMS$ field's sampled locations, mentioned in Table 6 and the profile's mean values are accepted as representative ρ_{sw} for that particular location. The ρ_{sw} versus h_{sw} profile's mean values are presented in Table 8.

Sample name	Sample type	Mound	2D seismic profile	Sea-bed depth	Mean ρ_{sw}
[-]	[-]	[-]	[-]	[m]	[kg/m^3]
158-957C	Shallow hole	Active TAG	P03	3548	1029.87
158-957F	Shallow hole	Active TAG	P03	3649	1030.01
158-957G	Shallow hole	Active TAG	P36	3646	1030.00
158-957O	Shallow hole	Active TAG	P45	3649	1030.01
158-957P	Shallow hole	Active TAG	P45	3649	1030.01
158-957Q	Shallow hole	Active TAG	P03	3657	1030.02
JC138-45-1	Sea-bed surface grab	Southern	P36	3530	1029.84
JC138-45-2	Sea-bed surface grab	Southern	P36	3530	1029.84
JC138-23GC-cc-W	Sea-bed surface grab	Southern	P07	3537	1029.85
JC138-41-2	Sea-bed surface grab	Southern	P44	3574	1029.90
JC138-41-3	Sea-bed surface grab	Southern	P44	3574	1029.90
JC138-45-4x	Sea-bed surface grab	Southern	P36	3540	1029.85
JC138-45-4y	Sea-bed surface grab	Southern	P36	3540	1029.85
JC138-45-5	Sea-bed surface grab	Southern	P07	3552	1029.87
JC138-45-6	Sea-bed surface grab	Southern	P07	3552	1029.87
JC138-55-1	Sea-bed surface grab	New mound # 3	P07	3589	1029.92
JC138-55-2	Sea-bed surface grab	New mound # 3	P07	3589	1029.92
JC138-55-7	Sea-bed surface grab	Shinkai	P44	3624	1029.97
JC138-55-8	Sea-bed surface grab	Shinkai	P44	3624	1029.97
JC138-50	Shallow hole	Southern	P03	3537	1029.85
JC138-73	Shallow hole	MIR	P38	3437	1029.71
JC138-76	Shallow hole	MIR	P38	3436	1029.71
JC138-22	Shallow hole	Southern	P03	3535	1029.85
JC138-31	Shallow hole	Southern	P07	3533	1029.84
M127-692GC/A/10	Gravity core	MIR	P38	3422	1029.69
158-957E	Shallow hole	Active TAG	P03	3646	1030.00
158-957K	Shallow hole	Active TAG	P03	3644	1030.00

Table 8: Data for calculating mean ρ_{sw} and mean ρ_{sw} calculation results at sampled points of $TAG\ SMS$ field.

5.4 Model Based Inversion

In this section, the results of four stages of model-based inversion are presented. The stages are Extracting statistical wavelet, Correlating shallow holes, Building an initial background model, conducting Inversion analyses on a shallow hole location, and Applying an inversion algorithm to the selected seismic data.

The resulting statistical wavelet extracted from 1995-2247 CMP and in 4500-4900 ms TWT window on 2D seismic profile P03 is presented in Figure 59 below. As one can see, the frequencies below 10 Hz are absent, which means Z below these frequencies are lost; this will be taken into account and compensated by generating an initial background model.

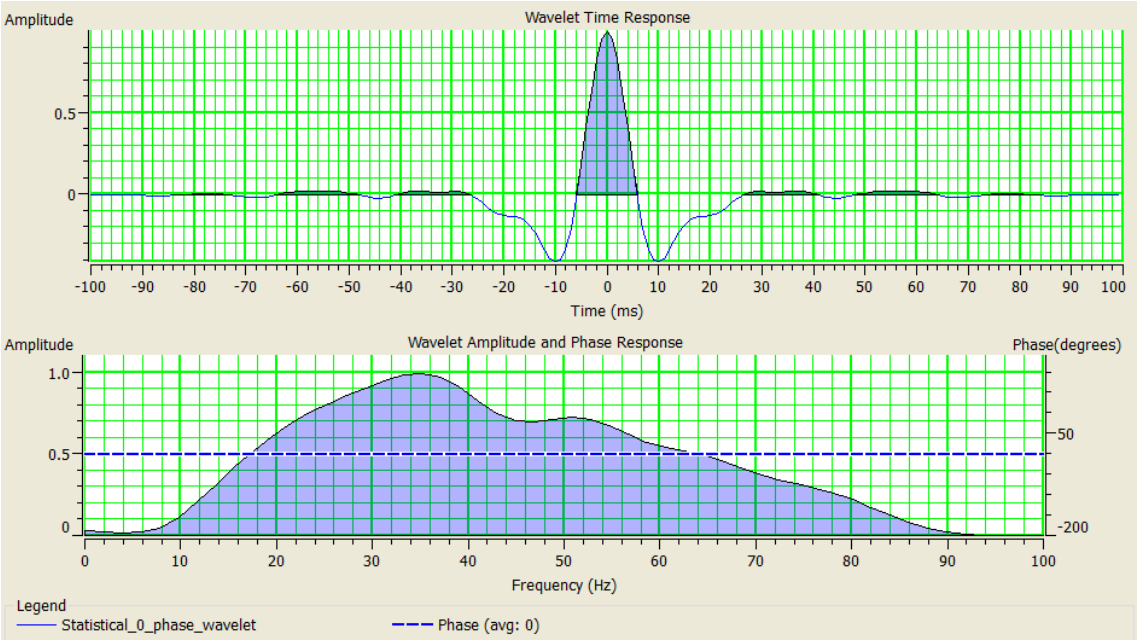

Figure 59: Zero phase statistical wavelet extracted from 1995-2247 CMP and in 4500-4900 ms TWT window on P03 2D seismic profile.

Correlating shallow holes with 2D seismic profile P03 is performed using shallow hole 158-957Q. The initial correlation is performed using the zero phase statistical wavelet extracted in the previous stage; a small mismatch between synthetic seismic trace and actual seismic trace on the shallow hole location equal to 2ms is observed after correlation, as shown in Figure 60. It is assumed this mismatch could be due to the zero phase statistical wavelet since the seismic data has a mixed-phase wavelet according to seismic data phase estimation results. The statistical wavelet's phase has been rotated until -40 degrees, and the mismatch between synthetic seismic trace and actual seismic has been eliminated. One can see the resulted correlation in the Figure 61.

The initial background model was generated using data from shallow holes 158-957Q, 158-957E and JC138-22, JC138-50 by applying a high-frequency cut of 10-12 Hz to compensate for the lost low-frequency component of Z mentioned above. One can see resulting initial background model on Figures 62, 63 below. As one can see, Z increases with depth and the sharpest Z change is observed on the sea-bed. Z is changing with a relatively large scale with time as it is expected from 10-12 Hz high-frequency cut applied for the modelling.

Before applying the model-based inversion algorithm on the 2D seismic profile P03, its algorithm was applied only on shallow hole 158-957Q location to analyze the outcome. Synthetic seismic trace generated from statistical wavelet with -40 phase degree and resulting in Z from model-based inversion algorithm is compared with actual seismic trace at the location of shallow hole 158-957Q. The comparison gave an outcome with a correlation coefficient equal to 0.9882 between synthetic and actual seismic traces. An error between synthetic seismic traces and actual seismic

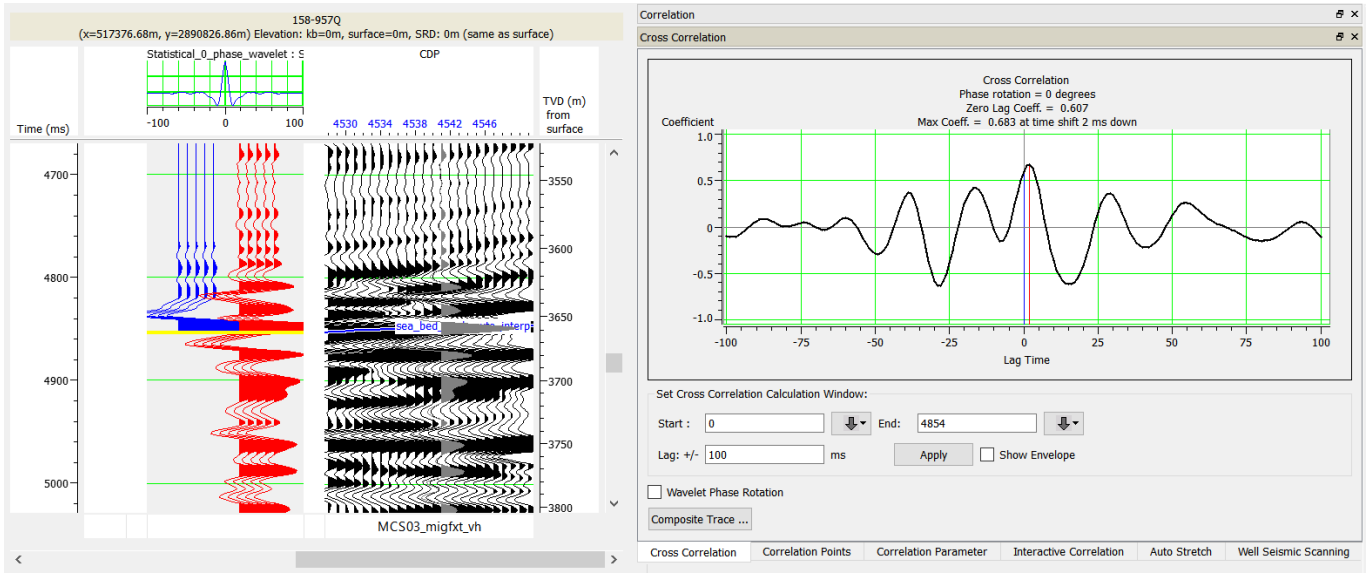

Figure 60: Correlating shallow hole 158-957Q to P03 2D seismic profile using the zero phase statistical wavelet.

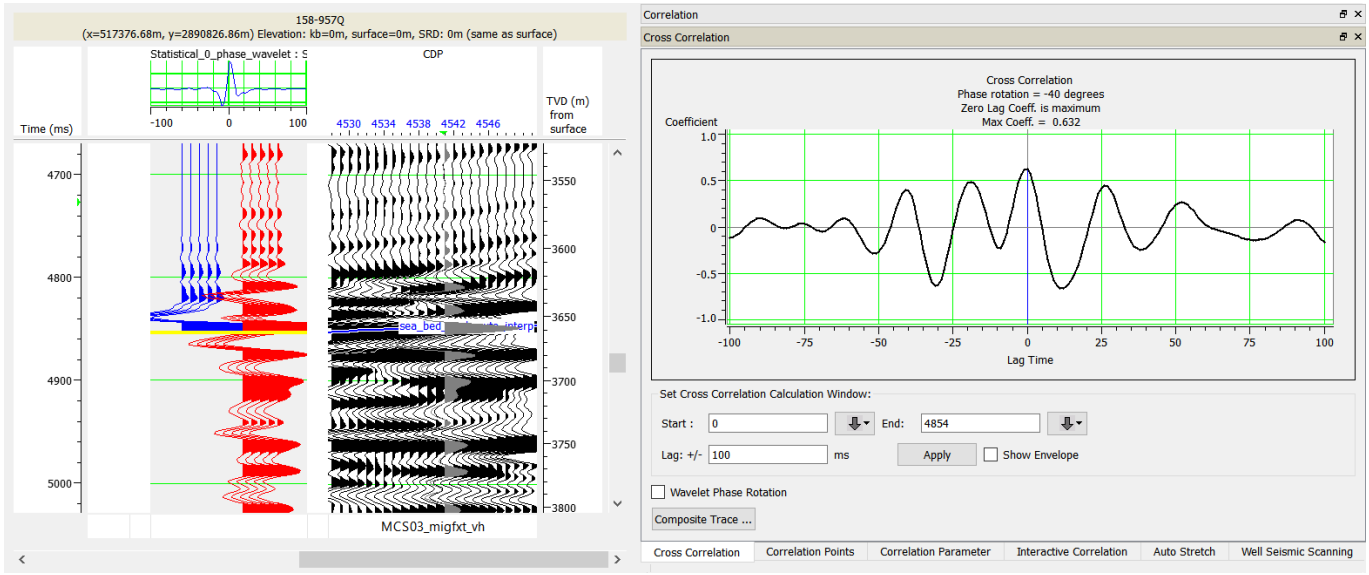

Figure 61: Correlating shallow hole 158-957Q to P03 2D seismic profile using the statistical wavelet with -40 degrees phase.

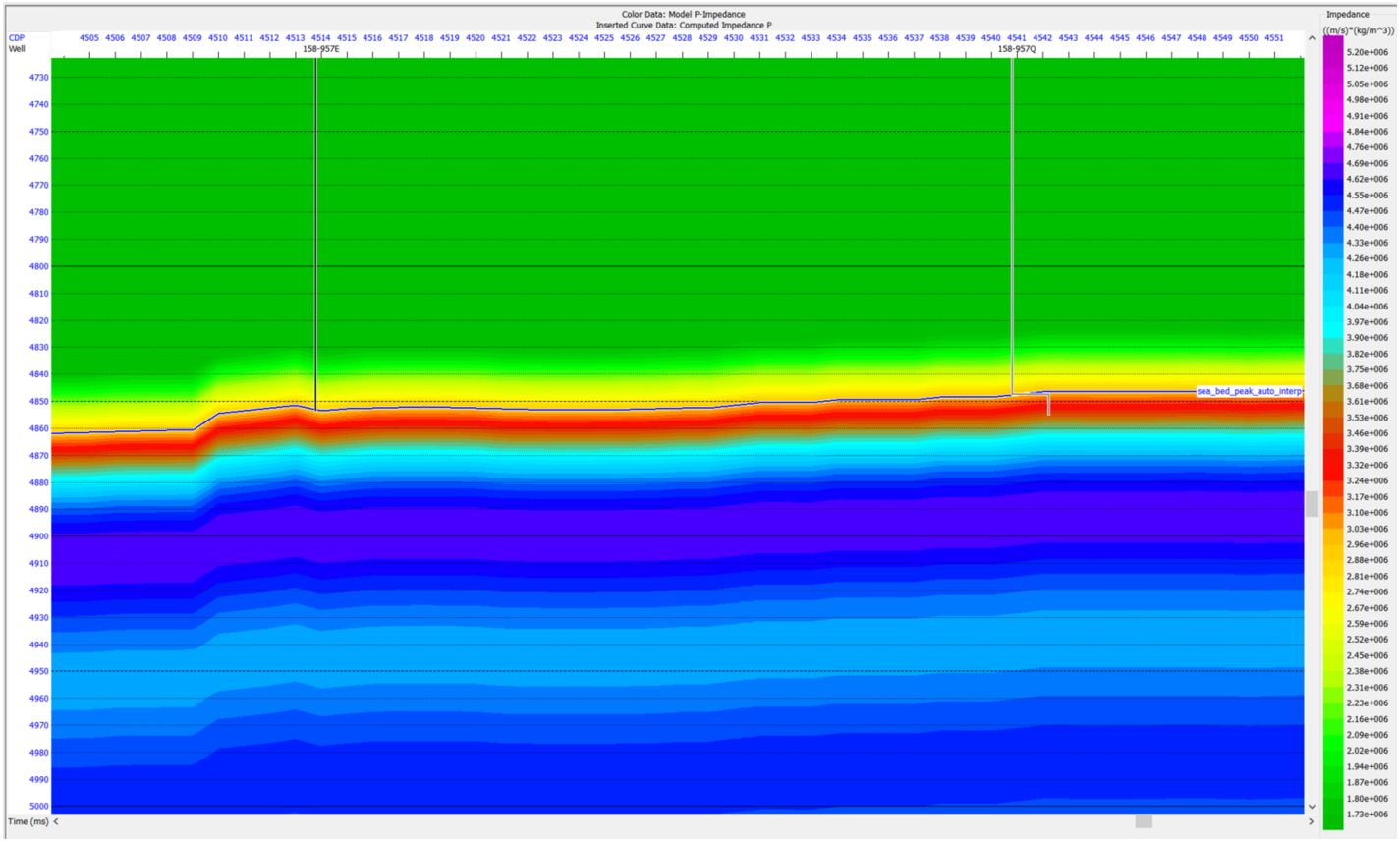

Figure 62: Initial background model on shallow holes 158-957Q and 158-957E location.

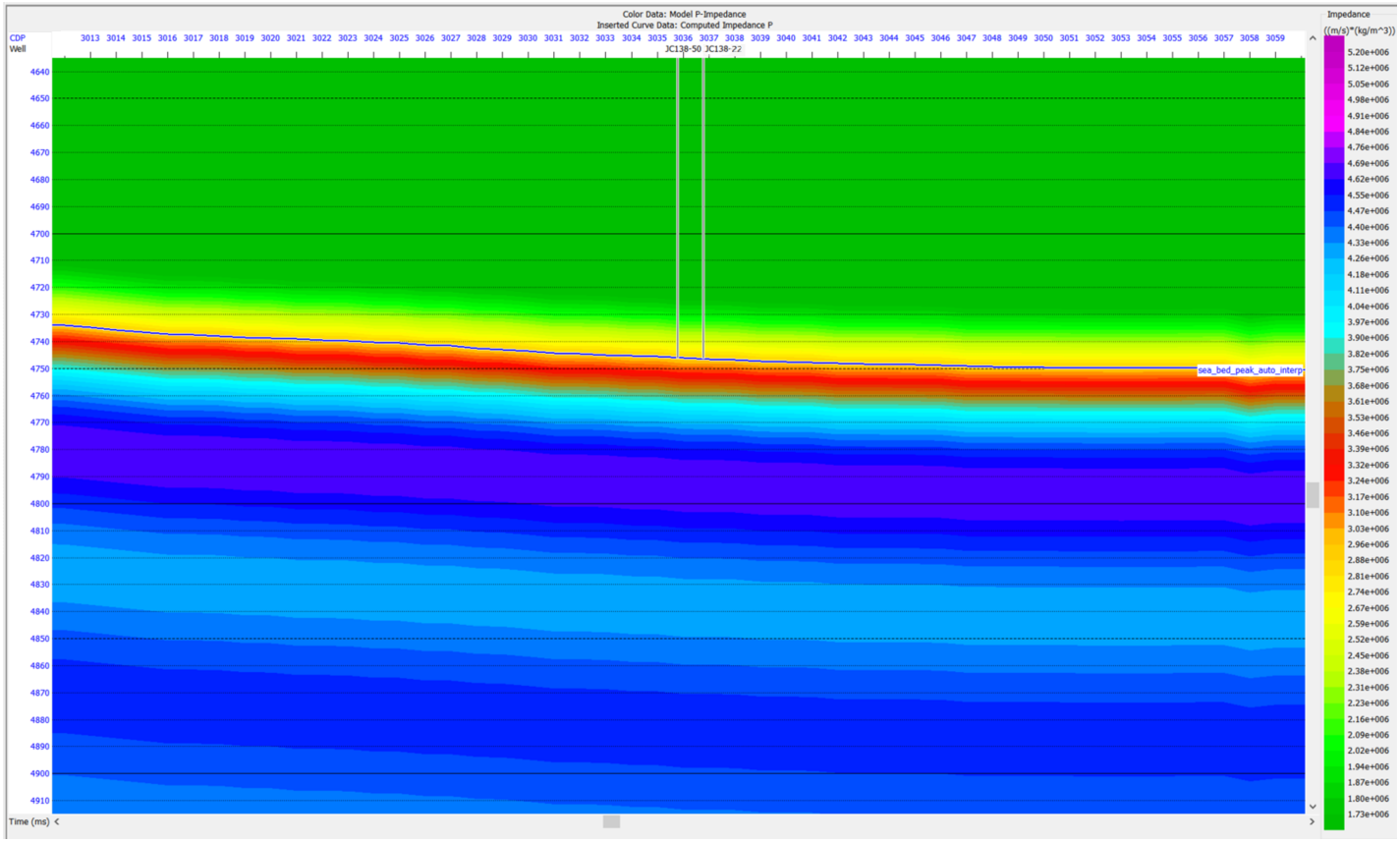

Figure 63: Initial background model on shallow holes JC138-22 and JC138-50 location.

traces is 0.0486. Figure 64 presents the picture showing inversion analysis results on the shallow hole location. The correlation coefficient equals 0.9882, the error of 0.0486 is considered acceptable, and the model-based inversion has been applied to the whole 2D seismic profile P03.

The results of applying model-based inversion on 2D seismic profile P03 are provided on shallow holes 158-957Q, 158-957E and JC138-22, JC138-50 location on Figures 65, 66 below. One can see some zones with elevated Z above sea-bed interpretation on the sides of shallow hole 158-957E. They are generated as a result of noise on seismic data; therefore, it is believed they are artificial.

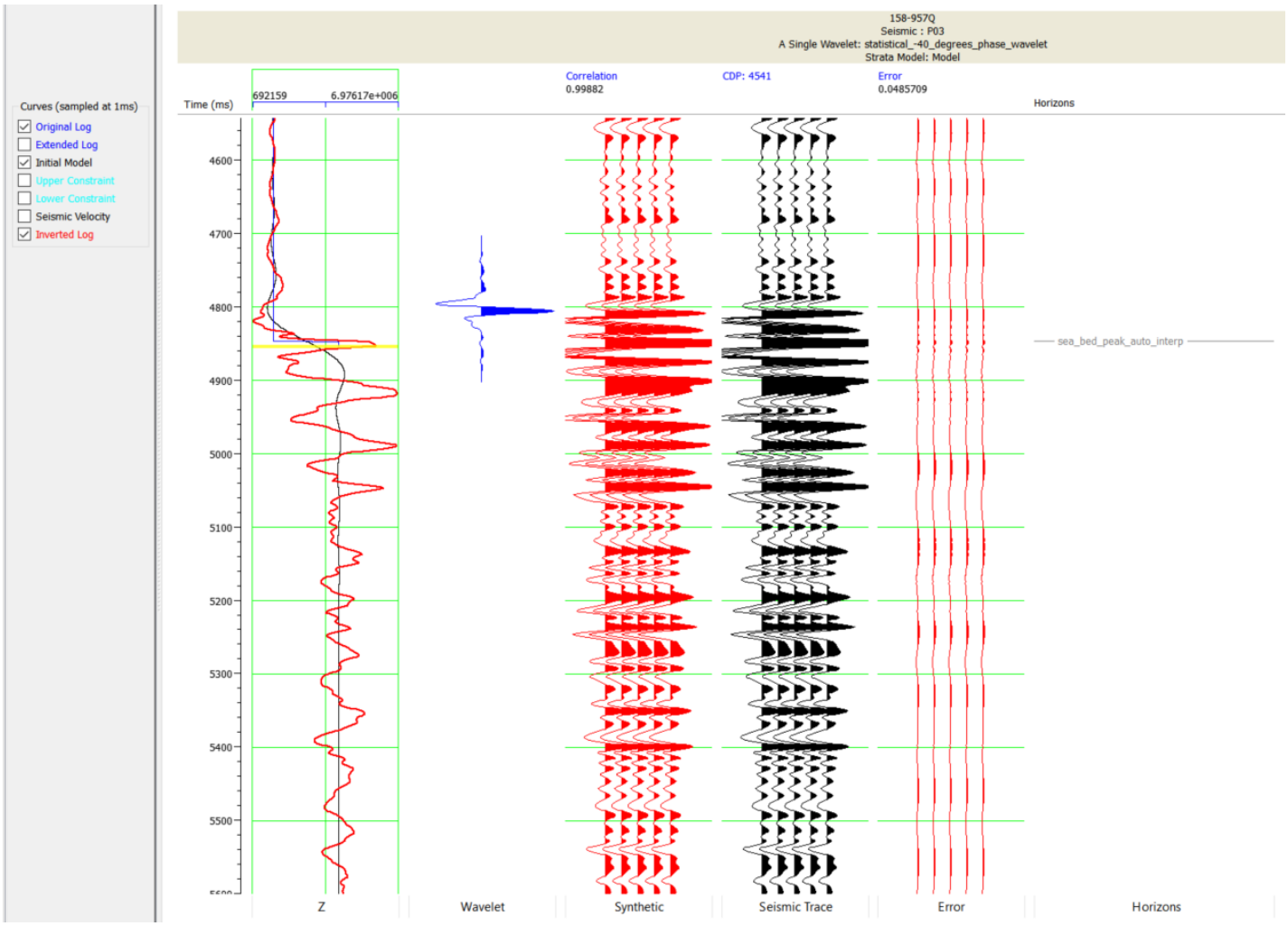

Figure 64: Model based inversion analyses results on a shallow hole 158-957Q location.

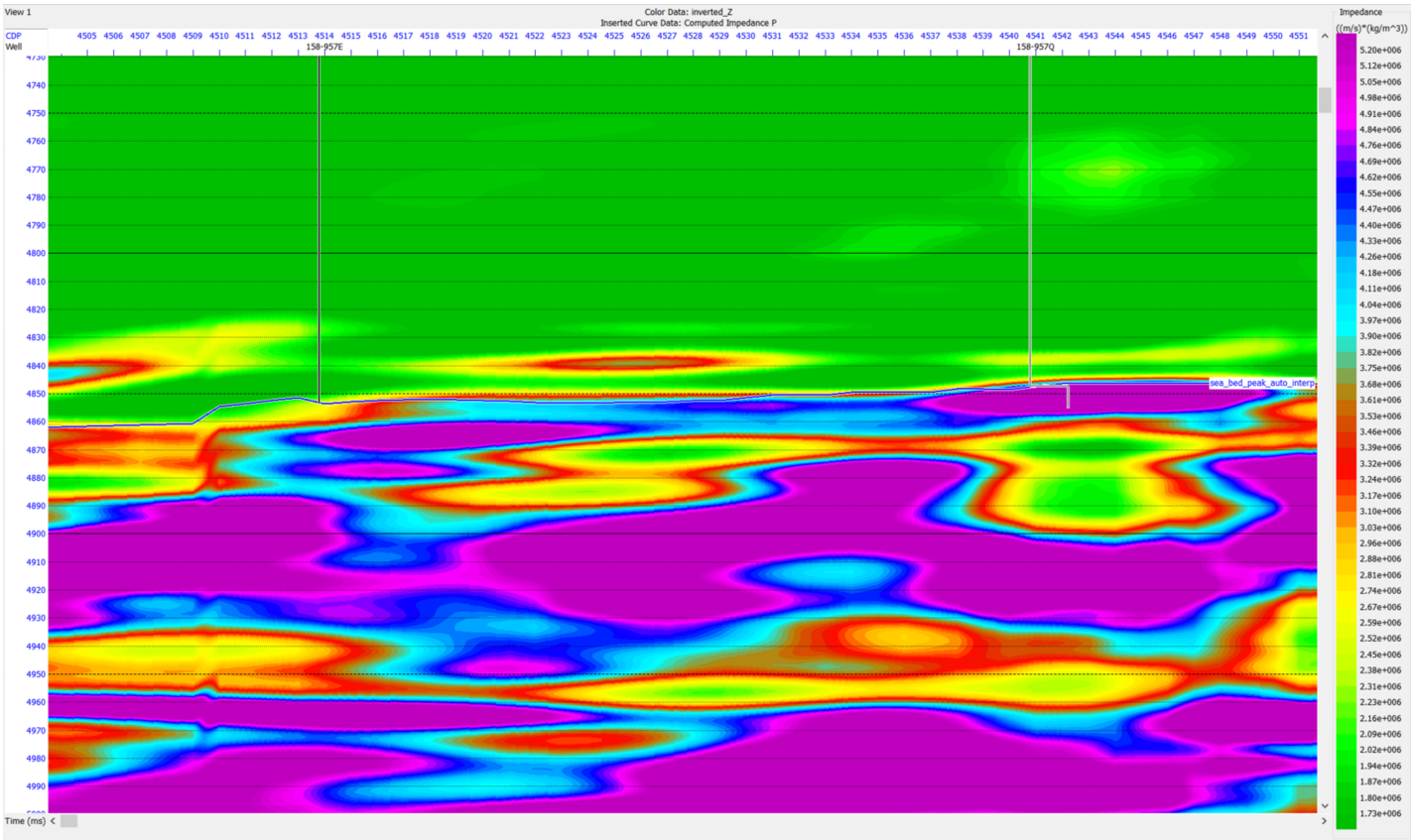

Figure 65: Applying model based inversion on 2D seismic profile P03 result on shallow holes 158-957Q and 158-957E location.

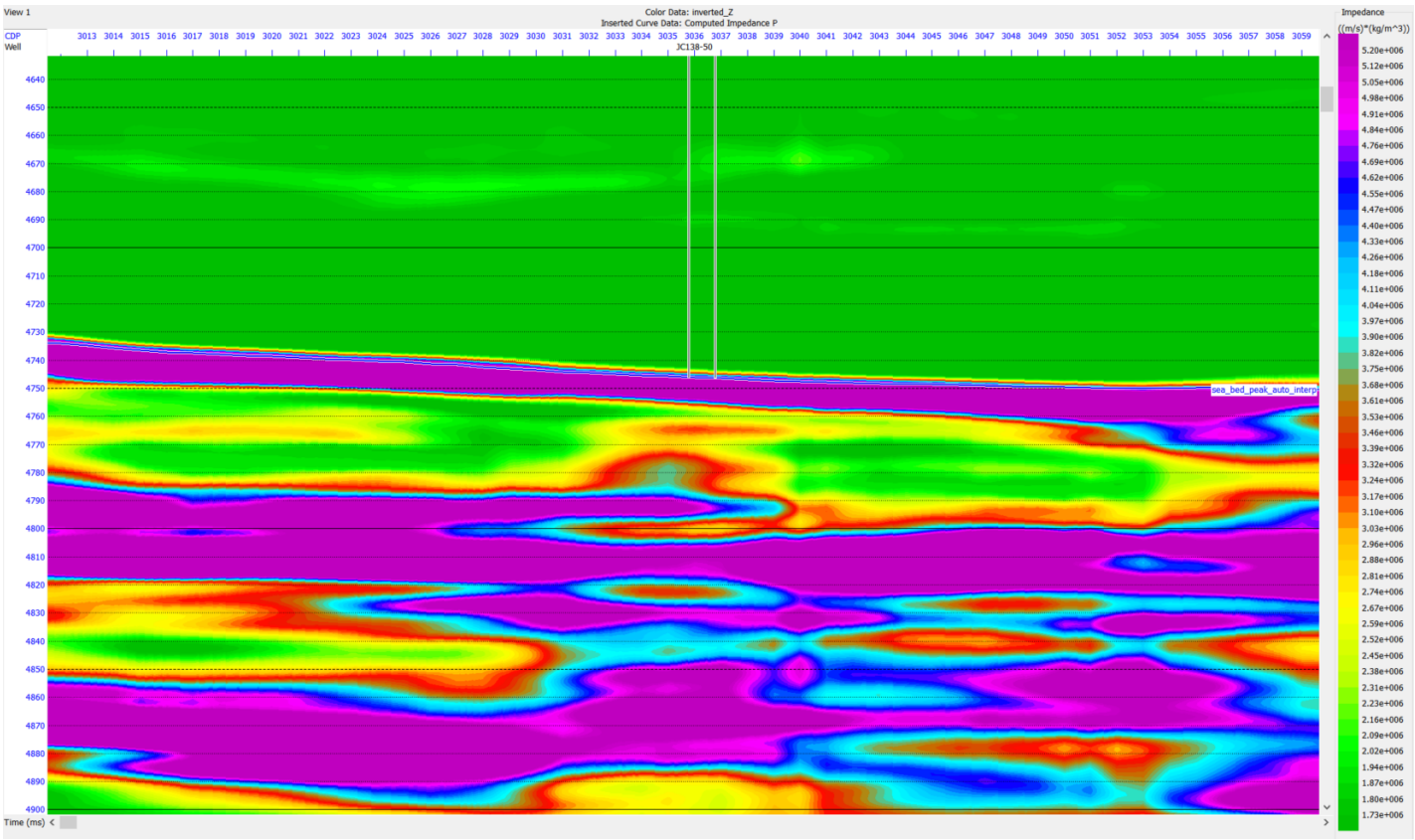

Figure 66: Applying model based inversion on 2D seismic profile P03 result on shallow holes JC138-22 and JC138-50 location.

5.5 SMS Mineral Richness and Acoustic Impedance

One can see the comparison of resulting Z from applying model-based inversion on 2D seismic profile P03 with Z values determined from core analyses at blind shallow hole 158-957C location on Figure 67.

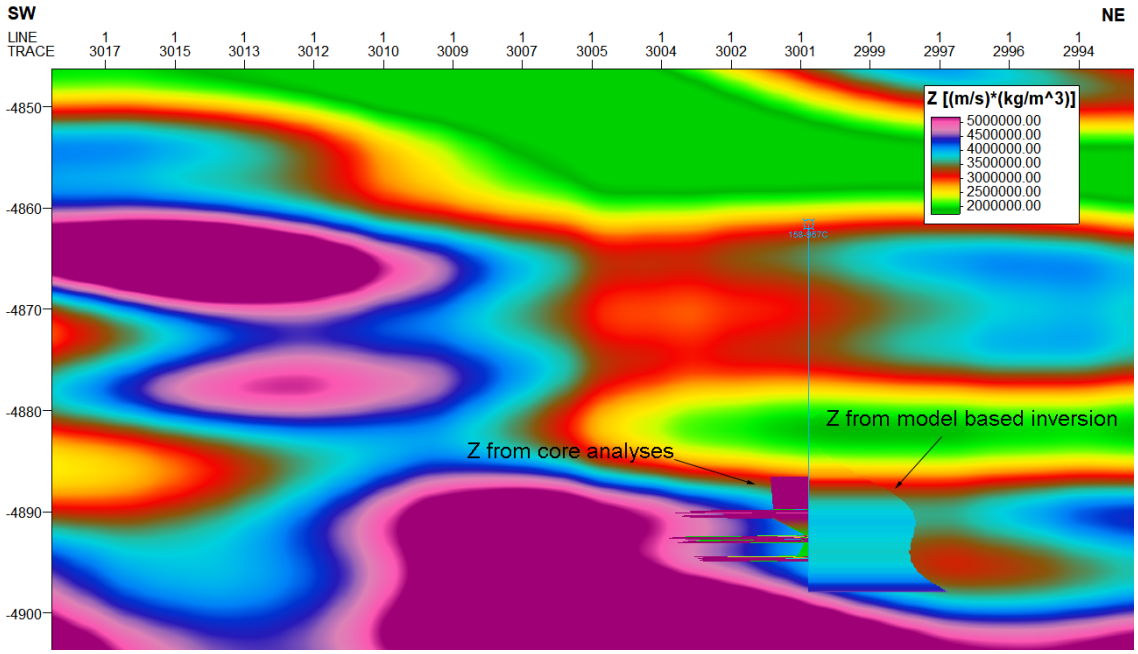

Figure 67: Comparing model based inversion result at blind shallow hole 158-957C location.

As one can see, Z change with depth is in a similar tendency on Z from core analyses and Z from model-based inversion.

Plots showing relation between Z from model based inversion and Py, Cpy, Qtz, Anh minerals content along shallow hole 158-957C are shown in Figures 68, 69, 70, 71 below.

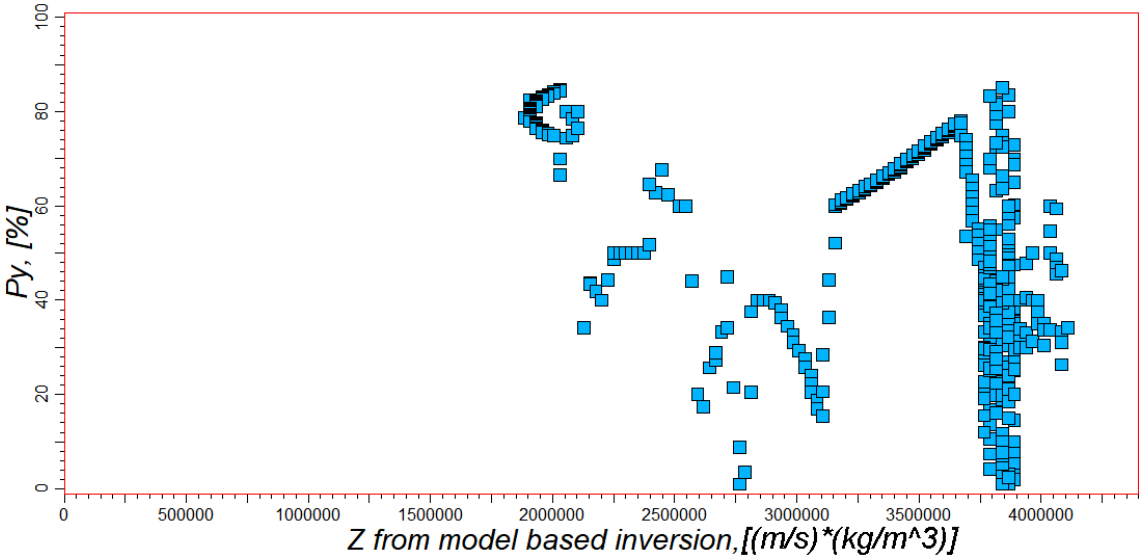

Figure 68: Comparing Z from model based inversion with Py content along shallow hole 158-957C.

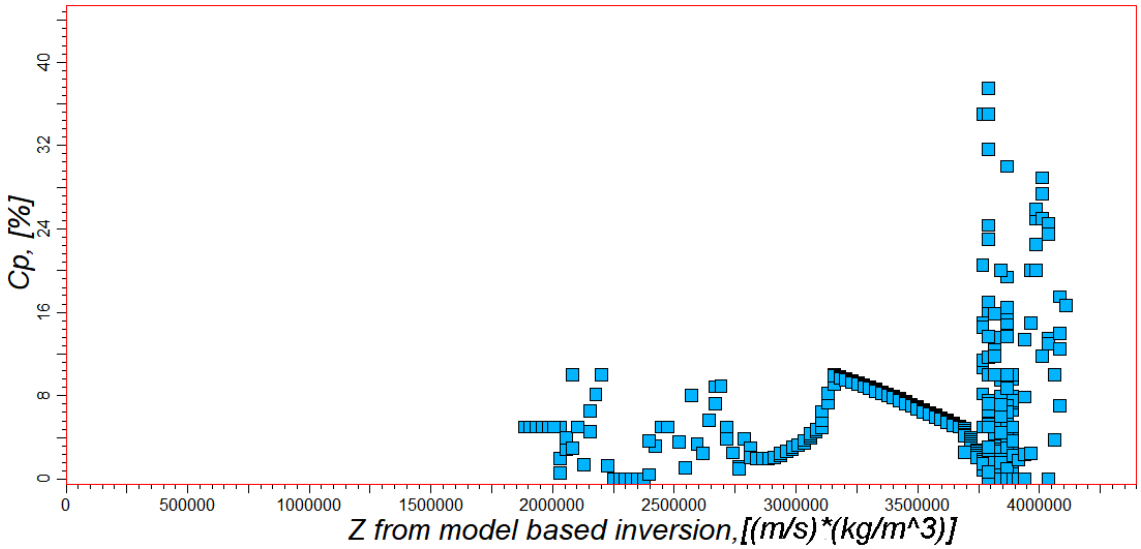

Figure 69: Comparing Z from model based inversion with Cpy content along shallow hole 158-957C.

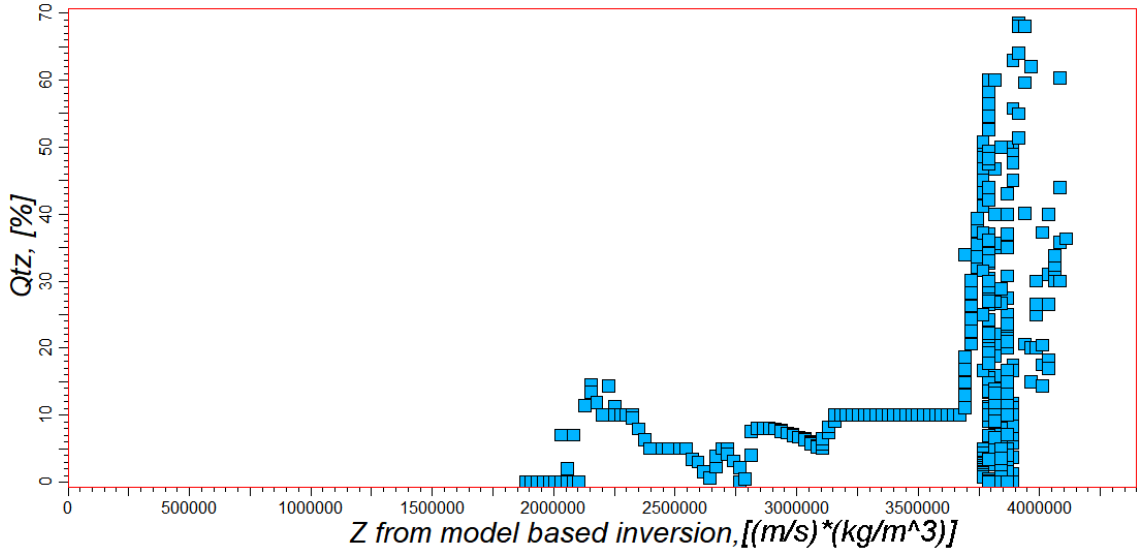

Figure 70: Comparing Z from model based inversion with Qtz content along shallow hole 158-957C.

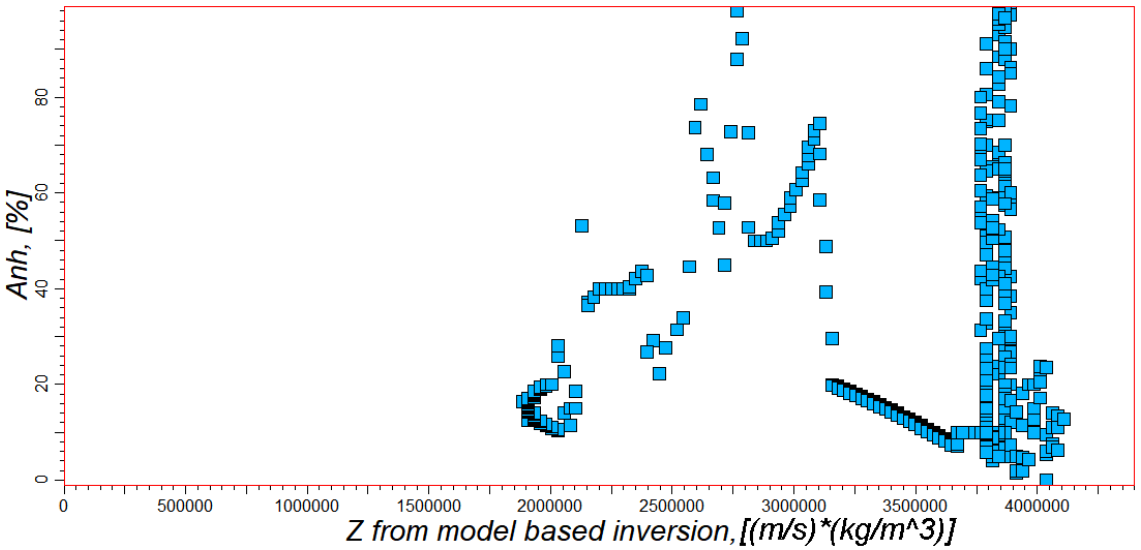

Figure 71: Comparing Z from model based inversion with Anh content along shallow hole 158-957C.

Plots showing relation between Z from V_p and ρ laboratory core measurement results and Py, Cpy, Qtz, Anh minerals content along shallow hole 158-957C are shown in Figures 72, 73, 74, 75 below.

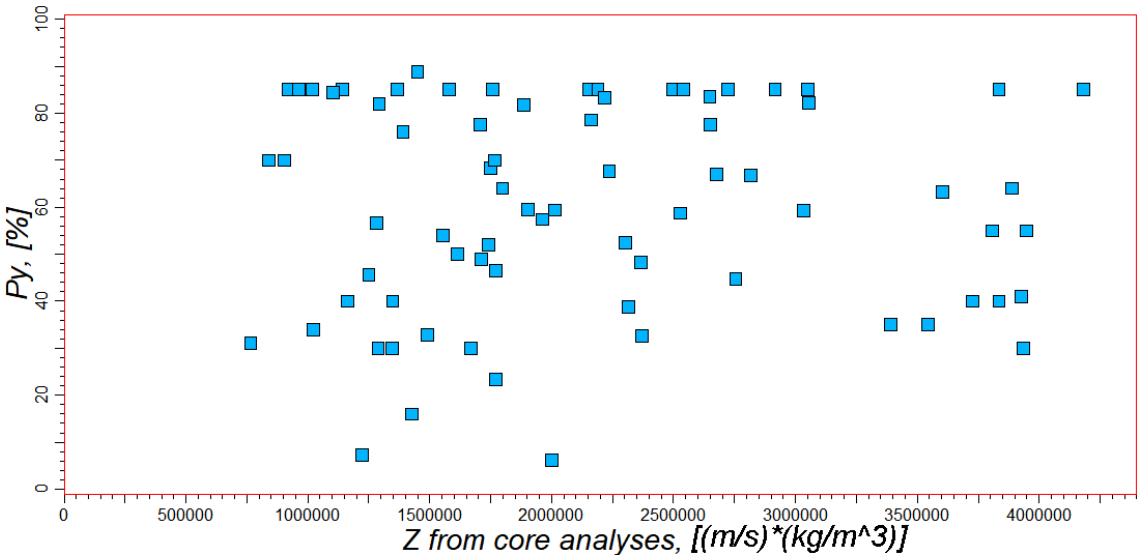

Figure 72: Comparing Z from V_p and ρ laboratory core measurement results with Py content along shallow hole 158-957C.

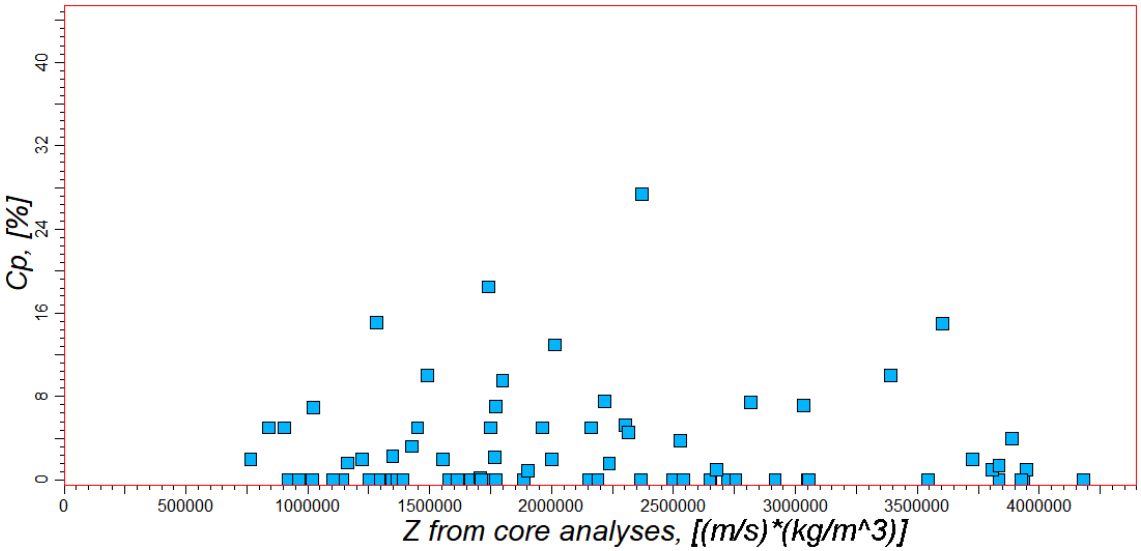

Figure 73: Comparing Z from V_p and ρ laboratory core measurement results with Cpy content along shallow hole 158-957C.

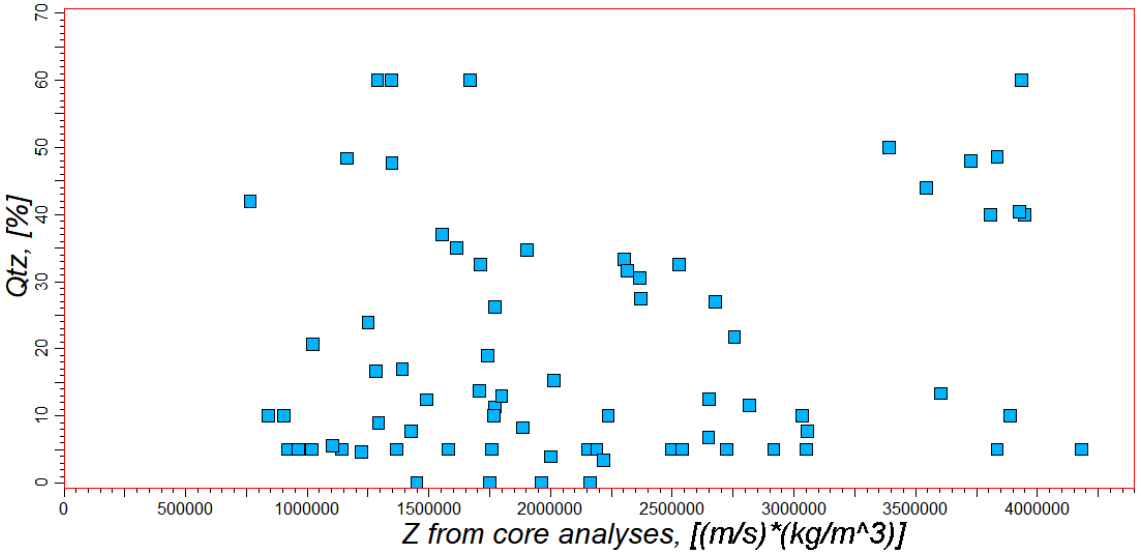

Figure 74: Comparing Z from V_p and ρ laboratory core measurement results with Qtz content along shallow hole 158-957C.

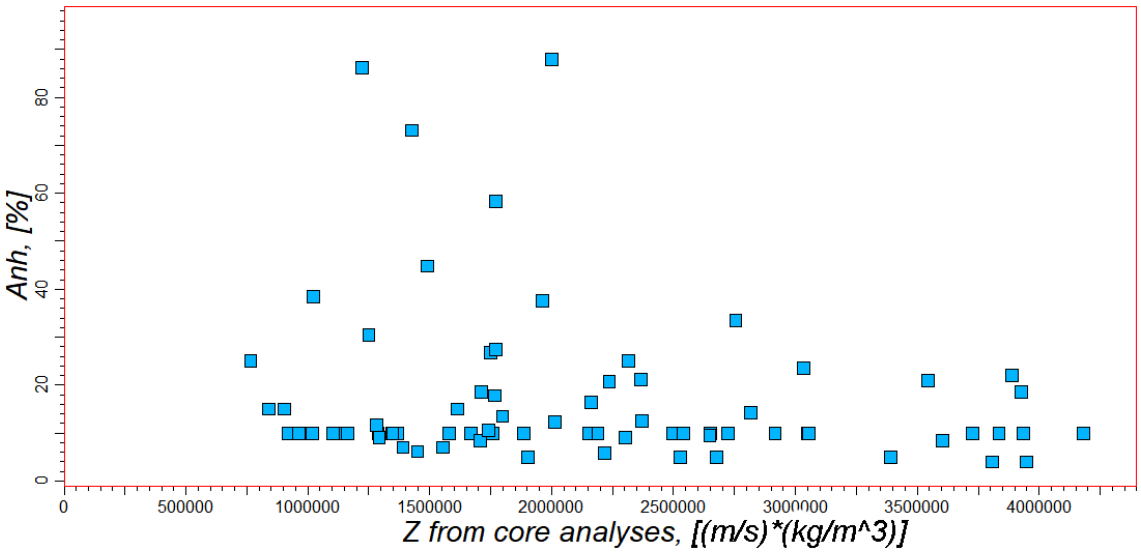

Figure 75: Comparing Z from V_p and ρ laboratory core measurement results with Anh content along shallow hole 158-957C.

6 Discussion

6.1 Analytical Rock Physics Template

One can see on Figure 1 that pure Py has highest Z comparing to pure Po, Sph and host-rocks. Pure Sph with Z similar to Cpy (please refer to Table 2) has Z lower than pure Py, Po and zero porosity Mafic host-rocks which may represent basalt host-rock at $TAG\ SMS$ field. It is expected that an increase in Py content should increase, and a decrease in Py content should decrease Z of SMS deposit. And increase in Sph or Cpy content should decrease, and a decrease in Sph or Cpy content should increase Z of SMS deposit. Although these observations are generally true, it is not so simple, and there is an interplay between minerals content, host-rock content, and porosity in a real SMS deposit; therefore increase in a mineral content does not mean a definite increase or decrease of Z. SMS deposit is never represented with only one mineral and is always a mixture of several minerals, hosting rocks. For instance, SMS deposit with certain Py content may have a range of Z values depending on variations in minerals content, host-rock content, and porosity. This is also true for any other mineral encountered at the SMS field. Hence it is believed Z alone is not a good indicator for determining the SMS deposit's mineral richness, and additional information such as SMS deposit's ρ is needed to determine SMS deposit's mineral richness.

6.2 SMS Mineral Richness and Seismic Amplitudes

The sea-bed is a seismic reflector created by sea-water on upper space and SMS deposit on lower space at $TAG\ SMS$ field. An amplitude of seismic wave reflected from the sea-bed at zero-offset depends on R_0 of the sea-bed, which can be explained by equation 8. One should expect a change in seismic amplitude of seismic wave reflected from this reflector in direct proportion with a change of Z of SMS deposit. If Z of SMS deposit increases, R_0 of sea-bed increases and visa-versa. One can see Py, Cpy, Qtz, Anh minerals richness and sea-bed seismic amplitudes relationship at Active TAG mound area of $TAG\ SMS$ field shown in Figures 44, 45, 46, 47, 48. One thing to be noted before going deeper into the discussion is that plotted minerals content at one amplitude value represents rock composition at the same location. Change in one mineral's content affecting to other minerals' content. Please refer to Methods for a more detailed explanation. One can note on Figure 45 that generally seismic amplitude is increasing with decrease of Py content and there is no distinct relationship between Cpy, Qtz, Anh richness and seismic amplitude on Figures 46, 47, 48. The reverse relationship between Py content and seismic amplitude is not true for all amplitude intervals. One can see periodic Py content increase within 300-450 seismic amplitude window and Py content decrease in ranges of 180-280, 500-600 seismic amplitudes. It is believed this is happening due to the complex interplay between minerals richness at sampled points as it is expected from Figure 1 analyses above and the absence of any relationship between seismic amplitudes and Cpy, Qtz, Anh minerals richness on Figures 46, 47, 48 proves this assumption. Therefore, zero-offset seismic amplitudes are not a good indicator for determining SMS deposits minerals richness. Additional research on the possibility of employing amplitude versus offset (AVO) analyses for determining SMS deposits mineral richness is needed.

6.3 Model Based Inversion

Before discussing the SMS deposit mineral richness and Z relationship, the methods and results for Z_{sw} estimation should be analysed. Z_{sw} is determined by estimating $V_{p(sw)}$ and ρ_{sw} separately. Obtained $V_{p(sw)}$ results in sea-water column at sampled locations of $TAG\ SMS$ field provided in Table 6 are considered reliable since the method for their estimation takes into account lateral and vertical variations of $V_{p(sw)}$ depending on location and depth of sea-water at $TAG\ SMS$ field. They have a reasonable agreement with $V_{p(sw)}$ in sea-surface estimated from direct-wave velocities. It should be accepted that method has been used for ρ_{sw} estimation at sampled points of $TAG\ SMS$ field is robust and has several assumptions, such as recorded sea-water P at the oceanographic station "I" is representative for whole $TAG\ SMS$ field, calculated ρ_{sw} values change only with depth and ρ_{sw} does not vary laterally. These assumptions are hardly completely

true since oceanographic station "I" is located near but not at $TAG\ SMS$ field and sea-water salinity, temperature change laterally from one place to another, for example, as shown on Figure 42. However, sea-water salinity and temperature changes are small; hence ρ_{sw} does not vary much and considering that there is no data on sea-water salinity, temperature variations laterally and with depth at $TAG\ SMS$ field for taking them into account in order to calculate more exact results. Taking these factors into account simple approach for ρ_{sw} estimation has been used. Regardless robustness of the approach used for ρ_{sw} estimation, obtained ρ_{sw} results are considered reasonable and errors in their estimation negligible. Model-based inversion method has been used on 2D seismic profile P03 for determining Z of sea-bed. Z_{sw} at shallow holes 158-957E, 158-957K, JC138-22, and JC138-50 locations have been used as input for model-based inversion together with synthetic low frequency Z curve constructed from Z_{sw} and Z of sea-bed core samples at shallow hole 158-957Q location. Z of sea-bed core samples from shallow hole 158-957Q calculated from V_p and ρ laboratory measurement results provided in Tables 14 and 15, It should be noted that constructed synthetic low frequency Z curve has information only for depths up-to 2.95 m below sea-bed since V_p and ρ laboratory measurement are performed on core samples only from these depths. In order to analyse the obtained Z results from model-based inversion, subsurface Z from blind shallow hole 158-957C core samples have been used, which were calculated in the same way as for core samples from shallow hole 158-957Q. One can see Z from core samples and Z from model-based inversion comparison in Figure 67. Two Z have the same trend with depth; however, they are different in absolute values. It is believed that the main reason for the difference in Z absolute values is the comparison being performed on depth interval 22.5-43.872 m of shallow hole 158-957C, and the low frequency Z which is used as input for model-based inversion is up-to 2.95 m. High likely Z of subsurface below 2.95 m varies differently than Z of subsurface above 2.95 m, and therefore, the low input frequency Z curve is not valid for depths 22.5-43.872 m.

6.4 SMS Mineral Richness and Acoustic Impedance

It is decided to use Z values from both models based on inversion and laboratory core analyses to perform Z and Py, Cpy, Qtz, Anh mineral richness analyses due to the difference in the absolute Z values from the two sources discussed in the previous section. Py, Cpy, Qtz, Anh mineral richness values have been used from 22.5-43.872 m of shallow hole 158-957C. Analyses are performed on 2D plots, whereas Z is plotted on the horizontal axis and a mineral richness on the vertical axis.

Z from model based inversion is plotted against Py, Cpy, Qtz, Anh minerals richness on four separate plots, one for ech mineral, provided in Figures 68, 69, 70, 71. As it is with seismic amplitude and mineral richness analyses results above, there is no clear relationship between Z from model based inversion and a mineral richness. If one would analyze Py richness and Z relation on Figure 68, one could see the Z is increasing with decrease of Py content in the interval of 1 750 000 $(m/s) * (kg/m^3)$ - 3 150 000 $(m/s)(kg/m^3)$ which is opposite to what is expected from Figure 1 analyses above. However in the interval of 3 150 000 $(m/s)(kg/m^3)$ - 3 700 000 $(m/s)(kg/m^3)$ trend is changing and Z is increasing with raise of Py content. This trend is breaking when Z is above 3 700 000 $(m/s)(kg/m^3)$ where none of trend exist, and one can see only vertical column of points on Figure 68. Relation between Z from model based inversion and Cpy content is provided on Figure 69. Z is increasing with raise of Cpy richness in the interval of 2 750 000 $(m/s)(kg/m^3)$ - 3 150 000 $(m/s)(kg/m^3)$ and the Z is increasing with decrease in Cpy richness in the interval of 3 150 000 $(m/s)(kg/m^3)$ - 3 750 000 $(m/s)(kg/m^3)$. There is no clear trend below 2 750 000 $(m/s)(kg/m^3)$ and above 3 750 000 $(m/s)(kg/m^3)$. From Z and Anh relation on Figure 71 one can see that Z is increasing with increase of Anh content in the interval of 1 750 000 $(m/s)(kg/m^3)$ - 3 050 000 $(m/s)(kg/m^3)$ and that Z is increasing with decrease of Anh content within 3 050 000 $(m/s)(kg/m^3)$ - 3 650 000 $(m/s)(kg/m^3)$, no any trend is above 3 650 000 $(m/s)(kg/m^3)$. On Z and Qtz relation on Figure 70 we can see no trend.

Z from core analyses results is plotted against Py, Cpy, Qtz, Anh minerals richness on four separate plots provided in Figures 72, 73, 74, 75. Although one could previously see some relationship between minerals richness and Z from model based inversion, there is no any trend on these plots on Figures 72, 73, 74, 75. These observations agrees with what is expected from Figure 1 analyses above.

Considering analytical rock physics template, seismic amplitude on sea-bed versus mineral richness analyses, and Z versus mineral richness analyses result above, one can say Z and seismic amplitude (near-stack or zero-offset) alone are not sufficient indicators for determining SMS deposit richness.

7 Conclusions

This master's thesis work attempts to prove an assumption that it is not possible to determine SMS deposit mineral richness from only its Z. This assumption is based on the author's observations regarding the existence of different host-rock models and/or SMS deposit models with different sulfide mineral ratios, porosity at the same Z values on rock physics template in Figure 1, for instance, Z at 2.5e7 $m/s * kg/m^3$ may represent 5 percent porosity Ultramafic host-rock, non-porous Mafic-host rock or Sulfide deposit with various mineralization and porosity from 0 to 15 percent.

In order to prove the assumption of 2D marine seismic, core V_p and ρ laboratory measurements, core composition analysis results and other data from the TAG SMS field have been used. Firstly seismic amplitudes on the sea-bed of Active TAG mound deposit at TAG SMS field and its Py, Cpy, Qtz, Anh richness relation have been analyzed. Secondly, Z from 2D seismic profile P03 has been extracted using model-based inversion, and the relation between Active TAG mound deposit's Py, Cpy, Qtz, Anh richness and Z from model-based inversion is investigated. Thirdly relation between Py, Cpy, Qtz, Anh richness and Z determined from V_p and ρ laboratory measurements of core samples from shallow hole 158-957C at Active TAG mound deposit at TAG SMS field have been examined. The main conclusions from the work done are the followings.

It is impossible to determine an SMS deposit mineral richness from its Z alone. It is supported by a lack of clear relationship between Py, Cpy, Qtz, Anh richness and Z of core samples from shallow hole 158-957C at Active TAG mound deposit at TAG SMS field. And by the absence of clear relation between Py, Cpy, Qtz, Anh richness and Z from model-based inversion of Active TAG mound deposit at TAG SMS field.

It is also impossible to determine a SMS deposit's mineral richness from zero-offset or near-stack seismic amplitudes. Zero-offset or near-stack seismic amplitudes are mostly controlled by Z. Since it is not possible to determine an SMS deposit's mineral richness from its Z alone, one can not determine the SMS deposit's mineral richness from zero-offset or near-stack seismic amplitudes. No clear relationship observed between sea-bed seismic amplitudes and Py, Cpy, Qtz, Anh richness of Active TAG mound at TAG SMS field supports this conclusion.

SMS deposits are usually located at or near the sea-bed and composed of hard rocks where it is difficult to drill wells and subsequently have deep well-log recordings. Therefore one common source of low frequency Z change with depth used for seismic inversion in the petroleum industry usually exists for shallow depths or does not exist. Therefore extra care while acquiring and processing raw seismic data should be taken to ensure that it is possible to get low frequency Z change with depth from seismic data itself and use it for seismic inversion algorithms later.

8 Further Work

It is recommended to investigate if it is possible to determine the SMS deposit's mineral richness from AVO analyses. Considering that SMS are located at or near the sea-bed and $V_{p(sw)}$, S-wave velocity in sea-water, ρ_{sw} are known or can be reasonably estimated. One can perform AVO inversion on the sea-bed and extract V_p, S-wave velocity, ρ of SMS deposit. Extracted V_p and ρ of SMS deposit can be used in the rock-physics template in Figure 1 for estimating the Active TAG mound SMS deposit's mineral richness.

It should be noted that seismic data recorded at the TAG SMS field is not high quality, and significant noise exists. It is also recorded using a short maximum offset length of 322 m while the sea-bed is located at 3500 m depth which makes it hard to perform research on employing AVO methods for SMS richness analyses. Therefore seismic data with higher quality and recorded with larger offsets at an SMS field should be searched.

References

Baker, E. and Y. Beaudoin (2013). *Deep Sea Minerals: Deep Sea Minerals and the Green Economy*. URL: https://www.researchgate.net/profile/Yannick-Beaudoin/publication/260596769_Deep_Sea_Minerals_and_the_Green_Economy/links/0c960531b6bbdc4095000000/Deep-Sea-Minerals-and-the-Green-Economy.pdf.

Blum, P. (1997). 'Physical properties handbook: a guide to the shipboard measurement of physical properties of deep-sea cores'. In.

Bonnet, A., L. Corriveau and W. Goodfellow (2007). 'Alteration vectors to metamorphosed hydrothermal systems in gneissic terranes'. In: *Mineral deposits of Canada: a synthesis of major deposit-types, district metallogeny, the evolution of geological provinces, and exploration methods. Edited by WD Goodfellow* 5, pp. 1035–1049.

Bowles, J. (2011). *Rock-forming Minerals: Non-silicates: Oxides, Hydroxides and Sulphides. V. 5A*. Geological Society.

Burns, A. and T. van Rensburg (2012). 'Global economic prospects'. In: *The World Bank, Washington, DC*. URL: https://openknowledge.worldbank.org/bitstream/handle/10986/12106/GEP-June-2012.pdf?sequence=16.

Franklin, J., H. Gibson, A. Galley and I. Jonasson (2005). 'Volcanogenic massive sulfide deposits'. In: *Econ Geol* 100th Anniversary, pp. 523–560. URL: https://doi.org/10.5382/AV100.17.

Galley, A., M. Hannington and I. Jonasson (2007). 'Volcanogenic massive sulphide deposits'. In: *Geological Association of Canada, Mineral Deposits Division*, pp. 141–161. URL: https://silverspruceresources.com/site/assets/files/5585/vms-deposits-canada-review.pdf.

Hannington, M., A. Galley, P. Herzig and S. Petersen (1998). 'Comparison of the TAG mound and stockwork complex with Cyprus-type massive sulfide deposits'. In: *Proceedings of the Ocean Drilling Program: Scientific Results*. Vol. 158. Texas A & M University, pp. 389–415. URL: https://doi.org/10.2973/odp.proc.sr.158.217.1998.

Hannington, M., J. Jamieson, T. Monecke, S. Petersen and S. Beaulieu (2011). 'The abundance of seafloor massive sulfide deposits'. In: *Geology* 39.12, pp. 1155–1158. URL: https://doi.org/10.1130/G32468.1.

Hannington, M., K. Poulsen, J. Thompson and R. Sillitoe (1997). 'Volcanogenic gold in the massive sulfide environment'. In: URL: https://doi.org/10.5382/Rev.08.14.

Herrington, R., V. Maslennikov, V. Zaykov, I. Seravkin, A. Kosarev, B. Buschmann, J. Orgeval, N. Holland, S. Tesalina, P. Nimis et al. (2005). '6: Classification of VMS deposits: lessons from the South Uralides'. In: *Ore Geology Reviews* 27.1-4, pp. 203–237. URL: https://doi.org/10.1016/j.oregeorev.2005.07.014.

Humphris, S., P. Herzig, D. Miller, J. Alt, K. Becker, D. Brown, G. Brügmann, H. Chiba, Y. Fouquet, J. Gemmell et al. (1995). 'The internal structure of an active sea-floor massive sulphide deposit'. In: *Nature* 377.6551, pp. 713–716. URL: https://doi.org/10.1038/377713a0.

Humphris, S., P. Herzig, J. Miller and et al (1996). 'Proc. ODP, Init. Repts., 158: College Station, TX (Ocean Drilling Program)'. In: *Oceanographic Literature Review*. URL: http://dx.doi.org/10.2973/odp.proc.ir.158.1996.

Humphris, S., P. Herzig, J. Miller, P. Rabinowitz, J. Baldauf and T. Francis (1994). 'Ocean Drilling Program: Leg 158 Preliminary Report, TAG: Drilling an Active Hydrothermal System on a Sediment-Free Slow-Spreading Ridge'. In: *Ocean Drilling program*. Citeseer. URL: http://citeseerx.ist.psu.edu/viewdoc/download?doi=10.1.1.224.233&rep=rep1&type=pdf.

Johnson, B., A. Montante-Martinez, M. Canela-Barboza and T. Danielson (2000). 'Geology of the san Nicolas deposit, Zacatecas, Mexico'. In: *VMS Deposits of Latin America: Geological Association of Canada, Mineral Deposits Division Special Publication* 2, pp. 71–85.

Kesler, S. (2007). *Mineral supply and demand into the 21st century*. Vol. 1294, pp. 55–62.

Kharas, H. (2010). 'The emerging middle class in developing countries'. In: URL: https://doi.org/10.1787/18151949.

Kharas, H. and G. Gertz (2010). 'The new global middle class: A cross-over from West to East'. In: *Wolfensohn Center for Development at Brookings*, pp. 1–14. URL: https://www.almendron.com/tribuna/wp-content/uploads/2016/08/03_china_middle_class_kharas.pdf.

Khayrullaev, J. (2021). *Sea Floor Massive Sulfides Rock Physics. Specialization project.* URL: https://drive.google.com/file/d/1SUK0O2SS58cB6g0zTzlVV_oQTHiO27ns/view?usp=sharing.

Lalou, C., J. Reyss, E. Brichet, P. Rona and G. Thompson (1995). 'Hydrothermal activity on a 105-year scale at a slow-spreading ridge, TAG hydrothermal field, Mid-Atlantic Ridge 26° N'. In: *Journal of Geophysical Research: Solid Earth* 100.B9, pp. 17855–17862. URL: https://doi.org/10.1029/95JB01858.

Mackenzie, K. (1981). 'Nine-term equation for sound speed in the oceans'. In: *The Journal of the Acoustical Society of America* 70.3, pp. 807–812. URL: https://doi.org/10.1121/1.386920.

Milkereit, B., D. Eaton, J. Wu, G. Perron, M. Salisbury, E. Berrer and G. Morrison (1996). 'Seismic imaging of massive sulfide deposits; Part II, Reflection seismic profiling'. In: *Economic Geology* 91.5, pp. 829–834. URL: https://doi.org/10.2113/gsecongeo.91.5.829.

Monecke, T., S. Petersen, M. Hannington, H. Grant and I. Samson (2016). 'The minor element endowment of modern sea-floor massive sulfides and comparison with deposits hosted in ancient volcanic successions'. In: URL: https://doi.org/10.5382/Rev.18.11.

Murton, B. (2018). 'Cruise report: Expedition JC 138: 29th June–8th August 2016, Mid Atlantic Ridge, 26 8.38'N; 44 49.92'W'. In: *Nat. Oceanogr. Centre, Southampton, UK*. URL: https://www.bodc.ac.uk/resources/inventories/cruise_inventory/reports/jc138.pdf.

Murton, B., B. Lehrmann, A. Dutrieux, S. Martins, A. de la Iglesia, I. Stobbs, F. Barriga, J. Bialas, A. Dannowski, M. Vardy et al. (2019). 'Geological fate of seafloor massive sulphides at the TAG hydrothermal field (Mid-Atlantic Ridge)'. In: *Ore Geology Reviews* 107, pp. 903–925. URL: https://doi.org/10.1016/j.oregeorev.2019.03.005.

Peter, J. and S. Steven (1999). 'Windy Craggy, northwestern British Columbia; the world's largest besshi-type deposit'. In: *Reviews in Economic Geology* 8, pp. 261–295. URL: https://www.academia.edu/download/33537947/Peter___Scott_1999_SEG_Revs_Geol_150dpi.pdf.

Petersen, S. (2016). 'RV METEOR Fahrtbericht/Cruise Report M127 Metal fluxes and Resource Potential at the Slow-spreading TAG Midocean Ridge Segment (26° N, MAR)–Blue Mining@ Sea, Bridgetown (Barbados)–Ponta Delgada (Portugal), 25.05.-28.06. 2016 (Extended Version)'. In: URL: http://oceanrep.geomar.de/34777/1/geomar_rep_ns_32_2016.pdf.

Rob, S. and M. Bacon (2014). *Seismic Amplitude: An interpreter's handbook*. Cambridge University Press.

Rona, P., Y. Bogdanov, E. Gurvich, N. Rimski-Korsakov, A. Sagalevitch, M. Hannington and G. Thompson (1993a). 'Relict hydrothermal zones in the TAG hydrothermal field, Mid-Atlantic Ridge 26° N, 45° W'. In: *Journal of Geophysical Research: Solid Earth* 98.B6, pp. 9715–9730. URL: https://doi.org/10.1029/93JB00552.

Rona, P., M. Hannington, C. Raman, G. Thompson, M. Tivey, S. Humphris, C. Lalou and S. Petersen (1993b). 'Active and relict sea-floor hydrothermal mineralization at the TAG hydrothermal field, Mid-Atlantic Ridge'. In: *Economic Geology (plus the Bulletin of the Society of Economic Geologists);(United States)* 88.8. URL: https://doi.org/10.2113/gsecongeo.88.8.1989.

Rona, P., R. Pockalny and G. Thompson (1986). 'Geologic setting and heat transfer of black smokers at TAG hydrothermal field'. In: *Mid-Atlantic Ridge* 26, p. 1021.

Salisbury, M., B. Milkereit, G. Ascough, R. Adair, L. Matthews, D. Schmitt, J. Mwenifumbo, D. Eaton and J. Wu (2000). 'Physical properties and seismic imaging of massive sulfides'. In: *Geophysics* 65.6, pp. 1882–1889. URL: https://doi.org/10.1190/1.1444872.

Salisbury, M., B. Milkereit and W. Bleeker (1996). 'Seismic imaging of massive sulfide deposits; Part I, Rock properties'. In: *Economic Geology* 91.5, pp. 821–828. URL: https://doi.org/10.2113/gsecongeo.91.5.821.

Schön, J. (2015). *Physical properties of rocks: Fundamentals and principles of petrophysics*. Elsevier.

Scott, R., P. Rona, B. McGregor and M. Scott (1974). 'The TAG hydrothermal field'. In: *Nature* 251.5473, pp. 301–302. URL: https://doi.org/10.1038/251301a0.

Shanks III, W., R. Koski, D. Mosier, K. Schulz, L. Morgan, J. Slack, I. Ridley, C. Dusel-Bacon, R. II Seal and N. Piatak (2012). *Volcanogenic massive sulfide occurrence model*. Tech. rep. US Geological Survey. URL: https://doi.org/10.3133/sir20105070C.

Sharman, E., B. Taylor, W. Minarik, B. Dubé and B. Wing (2015). 'Sulfur isotope and trace element data from ore sulfides in the Noranda district (Abitibi, Canada): implications for volcanogenic massive sulfide deposit genesis'. In: *Mineralium Deposita* 50.5, pp. 591–606. URL: https://doi.org/10.1007/s00126-014-0559-7.

Slack, J. (1993). 'Descriptive and grade-tonnage models for Besshi-type massive sulfide deposit'. In: *MINERAL DEPOSIT MODELING, Geol. Assoc. Canada, Special Paper* 40, pp. 343–371.

Stovas, A. and Q. Hao (2015). *Lecture notes on the course TPG4125*. Norwegian University of Science and Technology.

Tegart, P., G. Allen and A. Carstensen (2000). *Regional setting, stratigraphy, alteration and mineralization of the Tambo Grande VMS district, Piura Department, northern Peru*, pp. 375–405.

The-World-Bank (2012). *Uncertainties and Vulnerabilities*. URL: https://openknowledge.worldbank.org/handle/10986/12105.

UNDESA (2011). *World population prospects*.

Vaughan, David J and Claire L Corkhill (2017). 'Mineralogy of sulfides'. In: *Elements* 13.2, pp. 81–87. URL: https://doi.org/10.2113/gselements.13.2.81.

Veeken, P. and M. Da Silva (2004). 'Seismic inversion methods and some of their constraints'. In: *First break* 22.6. URL: https://doi.org/10.3997/1365-2397.2004011.

Widess, M. (1973). 'How thin is a thin bed?' In: *Geophysics* 38.6, pp. 1176–1180. URL: https://doi.org/10.1190/1.1440403.

Appendix

A Project Set-up in Petrel

The Petrel project for organising and handling available data on $TAG\ SMS$ field has been created with "PowerPlan:UTM8423" metric coordinate reference system, please refer to Figure 76 for details. The processed 49 2D marine seismic profiles are imported into the Petrel project firstly. The shallow holes, gravity cores and sea-bed grab samples location coordinate units are transformed from Geographic coordinate system units to Projected coordinate system units and loaded into the project. The V_p, ρ and Po, Cpy, Sp, Qtz, $Anhdy$, Am, Hm, Cly content log files for ODP Leg 158 shallow holes and Si, Ca, Mn, Cu, Zn, Fe, $Total\_Sulfur$ content log files for drilled core, gravity core and sea-bed grab samples from M127 and JC-138 expeditions are created and loaded into the project.

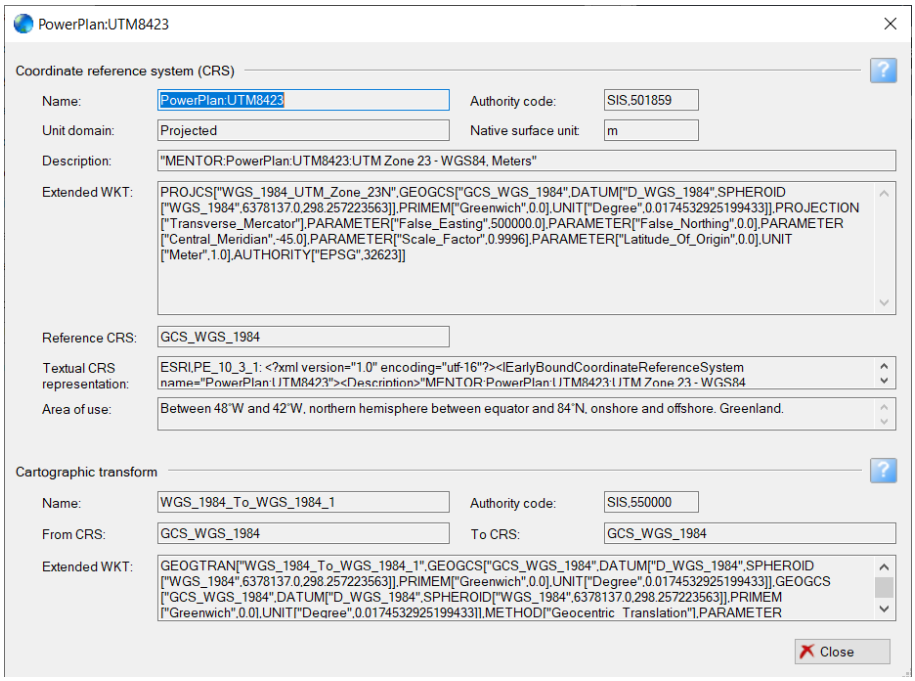

Figure 76: The information on the Petrel project coordinate system.

B Proves

d_F calculations on page number 10.

Given:

V_{p1} =4500 m/s, V_{p2}=8100 m/s;

z_1=2000 m, z_2=4000 m;

f_1=240 Hz, f_2=40 Hz;

Equation:

$$d_F = \sqrt{\frac{2zV_p}{f}}$$

Calculations:

$$d_{F(minimum)} = \sqrt{\frac{2z_1V_{p1}}{f_1}} = \sqrt{\frac{2*2000*4500}{240}} = 274 \text{ m}.$$

$d_{F(maximum)} = \sqrt{\frac{2z_2V_{p2}}{f_2}} = \sqrt{\frac{2*4000*8100}{40}}$ =1273 m.

t_{min} calculations on page number 10.

Given:

V_{p1} =4500 m/s, V_{p2}=8100 m/s;

f_1=240 Hz, f_2=40 Hz;

Equation:

$t_{min} = \frac{V_p}{4f}$

Calculations:

$t_{min(minimum)} = \frac{V_{p1}}{4f_1} = \frac{4500}{4*240}$ =5 m

$t_{min(maximum)} = \frac{V_{p2}}{4f_2} = \frac{8100}{4*40}$ =51 m

C Tables

Hole	Latitude	Longtitude	sea-bed depth	Start depth	End depth	Recovery
[-]	[Degree. min]	[Degree. min]	TVDSS [m]	[mbsf]	[mbsf]	[m]
JC138-022	26°09.339'N	44°48.946'W	-3535	0.000	1.885	0.000
JC138-022	26°09.339'N	44°48.946'W	-3535	1.885	3.506	1.786
JCI38-031	26°09.337'N	44°48.941'W	-3533	0.000	2.190	1.510
JCI38-031	26°09.337'N	44°48.941'W	-3533	2.190	2.607	0.382
JCI38-031	26°09.337'N	44°48.941'W	-3533	2.607	2.739	0.095
JC138-050	26°09.342'N	44°48.951'W	-3536.8	0.000	2.220	0.000
JC138-050	26°09.342'N	44°48.951'W	-3536.8	2.220	2.413	0.000
JC138-050	26°09.342'N	44°48.951'W	-3536.8	2.413	4.268	0.260
JC138-050	26°09.342'N	44°48.951'W	-3536.8	4.268	6.123	0.225
JC138-050	26°09.342'N	44°48.951'W	-3536.8	6.123	6.726	0.230
JC138-057	26°09.365'N	44°48.786'W	-3533.8	0.000	0.172	0.000
JC138-057	26°09.365'N	44°48.786'W	-3533.8	1.720	0.344	0.080
JC138-057	26°09.365'N	44°48.786'W	-3533.8	3.440	5.160	0.180
JC138-057	26°09.365'N	44°48.786'W	-3533.8	5.160	6.880	0.280
JC138-057	26°09.365'N	44°48.786'W	-3533.8	6.880	7.258	0.378
JC138-057	26°09.365'N	44°48.786'W	-3533.8	7.258	9.098	0.170
JC138-057	26°09.365'N	44°48.786'W	-3533.8	9.098	10.829	0.090
JC138-065	26°09.387'N	44°48.799'W	-3539.4	0.000	2.173	0.000
JC138-065	26°09.387'N	44°48.799'W	-3539.4	2.173	4.027	0.000
JC138-065	26°09.387'N	44°48.799'W	-3539.4	4.027	5.883	0.000
JC138-065	26°09.387'N	44°48.799'W	-3539.4	5.883	7.738	0.000
JC138-065	26°09.387'N	44°48.799'W	-3539.4	7.738	9.593	0.108
JC138-065	26°09.387'N	44°48.799'W	-3539.4	9.593	9.872	0.160
JC138-065	26°09.387'N	44°48.799'W	-3539.4	9.872	11.053	0.245
JC138-065	26°09.387'N	44°48.799'W	-3539.4	11.053	11.428	0.225
JC138-065	26°09.387'N	44°48.799'W	-3539.4	11.428	11.909	0.335
JC138-065	26°09.387'N	44°48.799'W	-3539.4	11.909	12.325	0.295
JC138-065	26°09.387'N	44°48.799'W	-3539.4	12.325	12.487	0.162
JC138-073	26°08.602'N	44°48.393'W	-3437.1	0.000	1.510	0.355
JC138-073	26°08.602'N	44°48.393'W	-3437.1	1.510	3.230	0.505
JC138-073	26°08.602'N	44°48.393'W	-3437.1	3.230	4.952	0.135
JC138-073	26°08.602'N	44°48.393'W	-3437.1	4.952	5.767	0.420
JC138-073	26°08.602'N	44°48.393'W	-3437.1	5.787	7.622	0.470
JC138-076	26°08.611'N	44°48.393'W	-3435.7	0.000	1.745	0.425
					Total Recovered	9.506

Table 9: Summary information of 7 shallow drill holes drilled during JC-138 expedition.

Source: Table 11.3.1.2. Petersen 2016

Hole	Latitude	Longtitude	Sea-bed depth	Start depth	End depth	Recovery
[-]	[Degree. min]	[Degree. min]	TVDSS [m]	[mbsf]	[mbsf]	[m]
158-957C	26°08.226'N	44°49.555'W	-3548	0.000	49.200	21.880
158-957F	26°08.212'N	44°49.564'W	-3649	0.000	9.000	0.950
158-957G	26°08.213'N	44°49.558'W	-3646	0.000	13.500	1.120
158-957H	26°08.195'N	44°49.555'W	-3655	0.000	45.800	5.010
158-957M	26°08.222'N	44°49.588'W	-3648	0.000	51.200	6.950
158-957O	26°08.241'N	44°49.545'W	-3649	0.000	20.900	1.270
158-957P	26°08.236'N	44°49.558'W	-3649	0.000	59.400	7.210
158-957Q	26°08.198'N	44°49.570'W	-3657	0.000	14.500	5.910
158-957A	26°08.196'N	44°49.552'W	-3653	0.000	15.000	0.250
158-957B	26°08.193'N	44°49.546'W	-3655	0.000	30.000	1.620
158-957E	26°08.219'N	44°49.560'W	-3646	0.000	126.00	4.030
158-957I	26°08.226'N	44°49.585'W	-3645	0.000	14.000	0.770
158-957J	26°08.238'N	44°49.590'W	-3647	0.000	9.000	0.080
158-957K	26°08.239'N	44°49.583'W	-3644	0.000	20.000	0.990
158-957N	26°08.197'N	44°49.553'W	-3652	0.000	42.200	0.50
					Total Recovered	58.5

Table 10: Summary information of 15 shallow drill holes drilled during OPD Leg158 expedition.

Source: Site summary table. page 70 in Humphris et al. 1994

Station	Latitude	Longtitude	Sea-bed depth	Recovery
[-]	[Degree, min]	[Degree, min]	TVDSS [m]	[m]
M127/626GC	26°10.401'N	44°48.747'W	-3407	1.200
M127/627GC	26°09.139'N	44°48.860'W	-3519	3.140
M127/692GC	26°08.559'N	44°48.397'W	-3422	0.790
			Total Recovered	5.13

Table 11: Information of 3 gravity core stations of M127 expedition.

Source: Table 5.4.1. Petersen 2016

Station	Latitude	Longtitude	Sea-bed depth	Recovery
[-]	[Degree. min]	[Degree. min]	TVDSS [m]	[m]
JC138-27GC	26°09.375'N	44°48.820'W	-3524	0.410
JC138-29GC	26°10.339'N	44°48.888'W	-3430	1.320
JC138-49GC	26°09.237'N	44°48.902'W	-3490	2.300
JC138-51GC	26°09.477'N	44°49.306'W	-3570	1.300
JC138-52GC	26°10.283'N	44°48.806'W	-3397	1.900
			Total Recovered	7.23

Table 12: Information of 5 gravity core stations used in JC-138 expedition.

Source: Table 7.1. Murton 2018

Sample	Latitude	Longtitude	Sea-bed depth
[-]	[Degree, min]	[Degree, min]	TVDSS [m]
JC138-45-1	26°09.330'N	44°48.987'W	-3530
JC138-45-2	26°09.330'N	44°48.987'W	-3530
JC138-21-1-W	26°09.345'N	44°49.017'W	-3550
JC138-21-2-W	26°09.345'N	44°49.017'W	-3550
JC138-21-3-W	26°09.345'N	44°49.017'W	-3550
JC138-23GC-cc-W	26°09.392'N	44°49.004'W	-3537
JC138-41-1	26°09.416'N	44°49.018'W	-3583
JC138-41-2	26°09.386'N	44°49.045'W	-3574
JC138-41-3	26°09.386'N	44°49.045'W	-3574
JC138-41-4	26°09.355'N	44°49.053'W	-3564
JC138-41-5	26°09.338'N	44°49.021'W	-3549
JC138-41-6	26°09.338'N	44°49.021'W	-3549
JC138-41-7	26°09.305'N	44°49.013'W	-3574
JC138-45-4x	26°09.333'N	44°48.988'W	-3540
JC138-45-4y	26°09.333'N	44°48.988'W	-3540
JC138-45-5	26°09.333'N	44°48.933'W	-3552
JC138-45-6	26°09.333'N	44°48.933'W	-3552
JC138-45-7a	26°09.355'N	44°48.815'W	-3535
JC138-45-7b	26°09.355'N	44°48.815'W	-3535
JC138-45-7c	26°09.355'N	44°48.815'W	-3535
JC138-45-7d	26°09.355'N	44°48.815'W	-3535
JC138-45-8	26°09.366'N	44°48.800'W	-3530
JC138-55-1	26°09.506'N	44°49.173'W	-3589
JC138-55-2	26°09.506'N	44°49.173'W	-3589
JC138-55-3	26°09.512'N	44°49.151'W	-3577
JC138-55-5	26°09.556'N	44°49.185'W	-3598
JC138-55-6	26°09.556'N	44°49.185'W	-3598
JC138-55-7	26°09.540'N	44°49.323'W	-3624
JC138-55-8	26°09.540'N	44°49.323'W	-3624

Table 13: Information of 29 sea-bed grab samples collected during JC-138 expedition.

Source: Appendix 1 in Murton 2018

Hole	Cor	Mode	Depth	P-wave velocity
[-]	[-]	[-]	[mbsf]	[m/s]
158-957P	12	PWL	54.461	1735.2
158-957P	12	PWL	54.506	2002.8
158-957P	12	PWL	54.555	2014.6
158-957P	12	PWL	54.611	2012.2
158-957P	12	PWL	54.655	2012.2
158-957P	12	PWL	54.705	2016.9
158-957P	12	PWL	54.761	2016.9
158-957P	12	PWL	54.805	2014.6
158-957P	12	PWL	54.855	2014.6
158-957P	12	PWL	54.91	2009.1
158-957P	12	PWL	55.005	1977
158-957P	12	PWL	55.11	1984
158-957P	12	PWL	55.155	1991.1
158-957P	12	PWL	55.206	1530.2
158-957P	12	PWL	55.26	1519.4
158-957P	12	PWL	55.306	1528.3
158-957P	12	PWL	55.355	1588.1
158-957P	12	PWL	55.41	1915.5
158-957P	12	PWL	55.455	1530.2
158-957P	12	PWL	55.505	1693.7
158-957P	12	PWL	55.56	1077.4
158-957P	12	PWL	55.606	1848.8
158-957P	12	PWL	55.699	1735.2
158-957P	12	PWL	55.745	1735.2
158-957P	12	PWL	55.795	1999.3
158-957P	12	PWL	55.845	2011.5
158-957P	12	PWL	55.895	2011.5
158-957P	12	PWL	55.945	2014.6
158-957P	12	PWL	55.995	1735.2
158-957P	12	PWL	56.045	1735.2
158-957P	12	PWL	56.095	1732.5
158-957P	12	PWL	56.145	1732.5
158-957P	12	PWL	56.195	1735.2
158-957P	12	PWL	56.245	1735.2
158-957P	12	PWL	56.295	1735.2
158-957P	12	PWL	56.345	1735.2
158-957Q	1	PWL	0.061	1997.4
158-957Q	1	PWL	0.106	1643.1
158-957Q	1	PWL	0.155	1693.1
158-957Q	1	PWL	0.211	1697
158-957Q	1	PWL	0.255	1647.3
158-957Q	1	PWL	0.305	1626.7
158-957Q	1	PWL	0.361	1735.2
158-957Q	1	PWL	0.407	1735.2
158-957Q	1	PWL	0.455	1557.5
158-957Q	1	PWL	0.51	1735.2
158-957Q	1	PWL	0.56	1553.8
158-957Q	1	PWL	0.607	1566.8
158-957Q	1	PWL	0.661	1559.3
158-957Q	1	PWL	0.705	1566.7
158-957Q	1	PWL	0.755	1559.2
158-957Q	1	PWL	0.805	1735.2
158-957Q	1	PWL	0.905	1735.2

Continued on next page...

Hole	Cor	Mode	Depth	P-wave velocity
[-]	[-]	[-]	[mbsf]	[m/s]
158-957Q	1	PWL	0.955	1564.8
158-957Q	1	PWL	1.006	1735.2
158-957Q	1	PWL	1.057	1487
158-957Q	1	PWL	1.105	1735.2
158-957Q	1	PWL	1.206	1495.5
158-957Q	1	PWL	1.255	1483.7
158-957Q	1	PWL	1.305	1487
158-957Q	1	PWL	1.357	1735.2
158-957Q	1	PWL	1.561	1542.8
158-957Q	1	PWL	1.605	1478.7
158-957Q	1	PWL	1.655	1879.5
158-957Q	1	PWL	1.711	1487
158-957Q	1	PWL	1.755	1488.7
158-957Q	1	PWL	1.805	1497.3
158-957Q	1	PWL	1.861	1490.4
158-957Q	1	PWL	1.905	1735.2
158-957Q	1	PWL	1.955	1735.2
158-957Q	1	PWL	2.01	1729.9
158-957Q	1	PWL	2.061	1735.2
158-957Q	1	PWL	2.105	1735.2
158-957Q	1	PWL	2.161	1735.2
158-957Q	1	PWL	2.205	1735.2
158-957Q	1	PWL	2.255	1732.5
158-957Q	1	PWL	2.36	1485.4
158-957Q	1	PWL	2.406	1915
158-957Q	1	PWL	2.455	1487
158-957Q	1	PWL	2.505	1732.5
158-957Q	1	PWL	2.556	1735.2
158-957Q	1	PWL	2.607	1722
158-957Q	1	PWL	2.705	1729.9
158-957Q	1	PWL	2.757	1724.6
158-957Q	1	PWL	2.806	1729.9
158-957Q	1	PWL	2.857	1602.8
158-957Q	1	PWL	2.905	1716.8
158-957Q	1	PWL	3.061	1998.1
158-957Q	1	PWL	3.107	2004.5
158-957Q	1	PWL	3.155	2009.9
158-957Q	1	PWL	3.211	2006.8
158-957Q	1	PWL	3.257	2009.9
158-957Q	1	PWL	3.305	2012.2
158-957Q	1	PWL	3.361	2003
158-957Q	1	PWL	3.405	2009.1
158-957Q	1	PWL	3.456	2006.8
158-957Q	1	PWL	3.511	2012.2
158-957Q	1	PWL	3.605	2012.2
158-957Q	1	PWL	3.71	2009.9
158-957Q	1	PWL	3.755	2014.6
158-957Q	1	PWL	3.81	2014.6
158-957Q	1	PWL	3.905	2009.1
158-957Q	1	PWL	3.955	1273
158-957Q	1	PWL	4.011	1581.7
158-957Q	1	PWL	4.055	1156.7

Continued on next page...

Hole	Cor	Mode	Depth	P-wave velocity
[-]	[-]	[-]	[mbsf]	[m/s]
158-957Q	1	PWL	4.105	1655.2
158-957Q	1	PWL	4.16	1669.9
158-957Q	1	PWL	4.205	1735.9
158-957Q	1	PWL	4.257	1918.3
158-957Q	1	PWL	4.311	1117.4
158-957Q	1	PWL	4.357	1625.2
158-957Q	1	PWL	4.405	1265
158-957Q	1	PWL	4.46	1978.3
158-957Q	1	PWL	4.561	1992.7
158-957Q	1	PWL	4.606	1961.2
158-957Q	1	PWL	4.657	2011.5
158-957Q	1	PWL	4.711	1978.3
158-957Q	1	PWL	4.755	1447.8
158-957Q	1	PWL	4.807	2011.5
158-957Q	1	PWL	4.861	2016.9
158-957Q	1	PWL	4.906	2013.8
158-957Q	1	PWL	4.957	2014.6
158-957Q	1	PWL	5.01	1732.5
158-957Q	1	PWL	5.06	1735.2
158-957Q	1	PWL	5.105	1735.2
158-957Q	1	PWL	5.157	2006.8
158-957Q	1	PWL	5.205	2012.2
158-957Q	1	PWL	5.255	2014.6
158-957Q	1	PWL	5.305	2012.2
158-957Q	1	PWL	5.406	1969.4
158-957Q	1	PWL	5.456	1996.2
158-957C	7	PWS3	22.5	1798
158-957C	7	PWS3	22.5	1626
158-957C	7	PWS3	22.52	2263
158-957C	11	PWS3	32.33	5112
158-957C	11	PWS3	34.79	5088
158-957C	14	PWS3	40.38	5198
158-957C	15	PWS3	43.35	4859
158-957C	16	PWS3	46.28	5095
158-957C	16	PWS3	47.69	5661
158-957F	1	PWS3	1	5308
158-957G	1	PWS3	12	4850
158-957H	5	PWS3	27.03	5402
158-957H	5	PWS3	27.89	6749
158-957M	9	PWS3	42.91	6085
158-957M	10	PWS3	46.55	6132
158-957O	2	PWS3	8.24	5356
158-957O	4	PWS3	16.19	5807

Table 14: V_p mesurement results on *ODP* Leg 158 shallow hole core samples.

Hole	Cor	Depth	Density
[-]	[-]	[mbsf]	[g/cc]
158-957C	7	19.515	0.936
158-957C	7	19.544	0.608
158-957C	7	19.568	1.342

Continued on next page...

Hole	Cor	Depth	Density
[-]	[-]	[mbsf]	[g/cc]
158-957C	7	19.591	0.382
158-957C	7	19.614	0.688
158-957C	7	19.638	0.446
158-957C	7	19.662	1.221
158-957C	7	19.685	2.963
158-957C	7	19.707	2.854
158-957C	7	19.731	0.388
158-957C	7	19.756	0.444
158-957C	7	19.779	2.883
158-957C	7	19.8	3.165
158-957C	7	19.822	2.801
158-957C	7	19.848	2.809
158-957C	7	19.872	3.203
158-957C	7	19.894	2.519
158-957C	7	19.917	2.541
158-957C	7	19.942	1.844
158-957C	7	19.964	2.628
158-957C	7	19.987	2.998
158-957C	7	20.012	2.728
158-957C	7	20.033	2.98
158-957C	7	20.056	2.76
158-957C	7	20.079	2.94
158-957C	7	20.105	3.031
158-957C	7	20.128	3.029
158-957C	7	20.149	1.724
158-957C	7	20.174	0.537
158-957C	7	20.199	0.864
158-957C	7	20.22	0.286
158-957C	7	20.242	1.425
158-957C	7	20.267	2.292
158-957C	7	20.291	2.516
158-957C	7	20.313	2.21
158-957C	7	20.337	2.574
158-957C	7	20.36	2.667
158-957C	7	20.385	2.787
158-957C	7	20.408	2.72
158-957C	7	20.429	2.455
158-957C	7	20.454	2.59
158-957C	7	20.478	2.579
158-957C	7	20.5	2.509
158-957C	7	20.522	2.82
158-957C	7	20.547	2.815
158-957C	7	20.572	2.723
158-957C	7	20.594	2.521
158-957C	7	20.617	2.888
158-957C	7	20.64	2.954
158-957C	7	20.665	2.546
158-957C	7	20.687	2.614
158-957C	7	20.71	2.75
158-957C	7	20.735	2.61
158-957C	7	20.757	2.864
158-957C	7	20.78	2.842

Continued on next page...

Hole	Cor	Depth	Density
[-]	[-]	[mbsf]	[g/cc]
158-957C	7	20.802	0.513
158-957C	7	20.87	2.927
158-957C	7	20.884	2.974
158-957C	7	20.9	2.952
158-957C	7	20.923	2.818
158-957C	7	20.93	2.845
158-957C	7	20.94	3.019
158-957C	7	20.96	3.01
158-957C	7	20.974	3.064
158-957C	7	20.99	2.943
158-957C	7	21.004	2.582
158-957C	7	21.023	3.09
158-957C	7	21.05	3.181
158-957C	7	21.06	3.149
158-957C	7	21.08	2.916
158-957C	7	21.096	2.708
158-957C	7	21.11	2.752
158-957C	7	21.14	2.834
158-957C	7	21.156	2.703
158-957C	7	21.17	2.702
158-957C	7	21.19	2.653
158-957C	7	21.2	2.406
158-957C	7	21.215	1.229
158-957C	7	21.233	2.849
158-957C	7	21.26	2.843
158-957C	7	21.267	3.042
158-957C	7	21.29	3.165
158-957C	7	21.309	3.571
158-957C	7	21.32	3.376
158-957C	7	21.339	3.44
158-957C	7	21.355	3.106
158-957C	7	21.38	3.051
158-957C	7	21.39	3.159
158-957C	7	21.41	3.135
158-957C	7	21.428	3.003
158-957C	7	21.443	2.861
158-957C	7	21.47	3.247
158-957C	7	21.478	3.08
158-957C	7	21.5	2.996
158-957C	7	21.519	3.108
158-957C	7	21.53	3.085
158-957C	7	21.536	3.092
158-957C	7	21.56	3.194
158-957C	7	21.572	2.858
158-957C	7	21.59	2.527
158-957C	7	21.613	3.148
158-957C	7	21.62	3.319
158-957C	7	21.627	2.651
158-957C	7	21.65	2.762
158-957C	7	21.665	2.645
158-957C	7	21.681	2.568
158-957C	7	21.69	2.582

Continued on next page...

Hole	Cor	Depth	Density
[-]	[-]	[mbsf]	[g/cc]
158-957C	7	21.702	2.308
158-957C	7	21.71	2.199
158-957C	7	21.715	2.178
158-957C	7	21.74	2.378
158-957C	7	21.754	2.355
158-957C	7	21.77	2.378
158-957C	7	21.8	2.307
158-957C	7	21.808	2.102
158-957C	7	21.83	2.3
158-957C	7	21.847	2.273
158-957C	7	21.86	2.239
158-957C	7	21.871	2.318
158-957C	7	21.895	2.314
158-957C	7	21.919	2.628
158-957C	7	21.942	2.902
158-957C	7	21.966	2.831
158-957C	7	21.99	2.695
158-957C	7	22.007	2.302
158-957C	7	22.029	2.319
158-957C	7	22.056	2.411
158-957C	7	22.101	2.633
158-957C	7	22.124	2.782
158-957C	7	22.146	2.697
158-957C	7	22.171	2.774
158-957C	7	22.194	2.856
158-957C	7	22.217	2.969
158-957C	7	22.239	2.774
158-957C	7	22.264	2.551
158-957C	7	22.29	2.502
158-957C	11	30.714	1.123
158-957C	11	30.72	1.153
158-957C	11	30.721	1.069
158-957C	11	30.744	0.277
158-957C	11	30.75	0.255
158-957C	11	30.758	0.289
158-957C	11	30.78	0.844
158-957C	11	30.797	2.691
158-957C	11	30.81	2.794
158-957C	11	30.83	2.705
158-957C	11	30.84	2.806
158-957C	11	30.843	2.688
158-957C	11	30.87	0.356
158-957C	11	30.881	1.852
158-957C	11	30.9	2.95
158-957C	11	30.919	2.695
158-957C	11	30.93	2.6
158-957C	11	30.933	2.555
158-957C	11	30.96	2.092
158-957C	11	30.973	2.657
158-957C	11	30.99	2.933
158-957C	11	31.01	2.61
158-957C	11	31.02	3.225

Continued on next page...

Hole	Cor	Depth	Density
[-]	[-]	[mbsf]	[g/cc]
158-957C	11	31.025	3.224
158-957C	11	31.05	3.31
158-957C	11	31.06	3.291
158-957C	11	31.08	3.321
158-957C	11	31.099	2.721
158-957C	11	31.11	2.612
158-957C	11	31.115	3.191
158-957C	11	31.14	3.027
158-957C	11	31.145	3.067
158-957C	11	31.17	3.053
158-957C	11	31.173	2.933
158-957C	11	31.194	3.305
158-957C	11	31.2	3.276
158-957C	11	31.205	3.171
158-957C	11	31.23	3.027
158-957C	11	31.242	3.041
158-957C	11	31.26	3.025
158-957C	11	31.281	2.96
158-957C	11	31.29	3.097
158-957C	11	31.295	3.029
158-957C	11	31.32	3.247
158-957C	11	31.331	3.095
158-957C	11	31.35	3.145
158-957C	11	31.365	3.165
158-957C	11	31.38	3.105
158-957C	11	31.401	3.165
158-957C	11	31.41	3.318
158-957C	11	31.417	2.741
158-957C	11	31.44	3.189
158-957C	11	31.452	3.193
158-957C	11	31.47	3.402
158-957C	11	31.491	3.72
158-957C	11	31.5	3.688
158-957C	11	31.502	3.506
158-957C	11	31.53	3.088
158-957C	11	31.54	3.31
158-957C	11	31.56	3.311
158-957C	11	31.577	3.536
158-957C	11	31.59	3.609
158-957C	11	31.62	3.44
158-957C	11	31.629	2.835
158-957C	11	31.65	1.029
158-957C	11	31.66	2.202
158-957C	11	31.681	2.029
158-957C	11	31.705	2.041
158-957C	11	31.729	2.282
158-957C	11	31.752	1.986
158-957C	11	31.775	2.287
158-957C	11	31.797	2.296
158-957C	11	31.823	2.3
158-957C	11	31.84	2.354
158-957C	11	31.842	2.297

Continued on next page...

Hole	Cor	Depth	Density
[-]	[-]	[mbsf]	[g/cc]
158-957C	11	31.865	1.775
158-957C	11	31.886	2.305
158-957C	11	31.911	2.29
158-957C	11	31.935	2.268
158-957C	11	31.957	2.044
158-957C	11	31.981	1.935
158-957C	11	32.003	2.139
158-957C	11	32.028	2.211
158-957C	11	32.051	2.177
158-957C	11	32.13	1.521
158-957C	11	32.146	3.199
158-957C	11	32.16	3.22
158-957C	11	32.179	3.133
158-957C	11	32.19	3.159
158-957C	11	32.193	3.048
158-957C	11	32.214	2.078
158-957C	11	32.22	1.735
158-957C	11	32.232	3.094
158-957C	11	32.25	3.141
158-957C	11	32.269	2.959
158-957C	11	32.28	3.256
158-957C	11	32.31	3.179
158-957C	11	32.324	3.05
158-957C	11	32.34	3.215
158-957C	11	32.362	3.285
158-957C	11	32.37	3.062
158-957C	11	32.378	2.96
158-957C	11	32.4	2.945
158-957C	11	32.419	3.239
158-957C	11	32.441	2.931
158-957C	11	32.465	2.733
158-957C	11	32.487	2.855
158-957C	11	32.51	2.817
158-957C	11	32.534	2.534
158-957C	11	32.557	2.796
158-957C	11	32.582	2.314
158-957C	11	32.605	2.956
158-957C	11	32.627	2.893
158-957C	11	32.65	2.154
158-957C	11	32.674	2.306
158-957C	11	32.698	3.087
158-957C	11	32.721	3.093
158-957C	11	32.744	2.24
158-957C	11	32.767	1.254
158-957C	11	32.79	1.01
158-957C	11	32.815	1.048
158-957C	13	37.212	0.198
158-957C	13	37.22	0.186
158-957C	13	37.234	0.594
158-957C	13	37.25	1.035
158-957C	13	37.272	0.53
158-957C	13	37.28	0.671

Continued on next page...

Hole	Cor	Depth	Density
[-]	[-]	[mbsf]	[g/cc]
158-957C	13	37.288	1.181
158-957C	13	37.31	0.419
158-957C	13	37.324	0.814
158-957C	13	37.34	1.101
158-957C	13	37.341	1.157
158-957C	13	37.363	1.023
158-957C	13	37.37	0.969
158-957C	13	37.379	1.399
158-957C	13	37.4	0.426
158-957C	13	37.408	0.46
158-957C	13	37.43	0.179
158-957C	13	37.445	0.307
158-957C	13	37.46	0.187
158-957C	13	37.463	0.24
158-957C	13	37.49	3.182
158-957C	13	37.499	1.727
158-957C	13	37.52	0.342
158-957C	13	37.539	0.486
158-957C	13	37.55	0.187
158-957C	13	37.556	0.307
158-957C	13	37.58	1.679
158-957C	13	37.592	0.494
158-957C	13	37.61	0.567
158-957C	13	37.629	0.266
158-957C	13	37.64	0.928
158-957C	13	37.67	2.662
158-957C	13	37.68	2.58
158-957C	13	37.7	2.613
158-957C	13	37.713	3.507
158-957C	13	37.73	3.458
158-957C	13	37.742	1.966
158-957C	13	37.76	1.449
158-957C	13	37.778	1.378
158-957C	13	37.79	0.745
158-957C	13	37.793	0.21
158-957C	13	37.82	0.222
158-957C	13	37.833	0.366
158-957C	13	37.85	0.515
158-957C	13	37.871	3.184
158-957C	13	37.88	3.468
158-957C	13	37.887	3.472
158-957C	13	37.91	3.379
158-957C	13	37.926	1.44
158-957C	13	37.94	0.593
158-957C	13	37.964	0.214
158-957C	13	37.97	0.254
158-957C	13	37.98	0.251
158-957C	13	38	0.27
158-957C	13	38.013	2.142
158-957C	13	38.03	2.595
158-957C	13	38.04	2.908
158-957C	13	38.051	3.577

Continued on next page...

Hole	Cor	Depth	Density
[-]	[-]	[mbsf]	[g/cc]
158-957C	13	38.06	3.456
158-957C	13	38.065	3.081
158-957C	13	38.09	3.032
158-957C	13	38.099	3.159
158-957C	13	38.119	3.139
158-957C	13	38.138	0.514
158-957C	13	38.16	0.331
158-957C	13	38.184	0.369
158-957C	13	38.208	0.766
158-957C	13	38.231	2.802
158-957C	13	38.254	3.169
158-957C	13	38.278	2.688
158-957C	13	38.301	1.463
158-957C	13	38.324	2.044
158-957C	13	38.34	2.039
158-957C	13	38.341	2.056
158-957C	13	38.344	1.03
158-957C	13	38.367	0.922
158-957C	13	38.391	0.738
158-957C	13	38.415	1.001
158-957C	13	38.438	0.519
158-957C	13	38.46	0.49
158-957C	13	38.485	0.446
158-957C	13	38.508	2.823
158-957C	13	38.594	0.198
158-957C	13	38.6	0.205
158-957C	13	38.615	1.358
158-957C	13	38.63	3.111
158-957C	13	38.634	3.119
158-957C	13	38.66	2.917
158-957C	13	38.668	2.694
158-957C	13	38.69	1.37
158-957C	13	38.704	0.276
158-957C	13	38.72	0.343
158-957C	13	38.75	2.304
158-957C	13	38.762	2.039
158-957C	13	38.785	2.171
158-957C	13	38.806	2.272
158-957C	13	38.83	2.924
158-957C	13	38.854	2.645
158-957C	13	38.878	3.164
158-957C	13	38.9	3.134
158-957C	13	38.923	3.016
158-957C	13	38.947	2.708
158-957C	13	38.97	3.226
158-957C	13	38.992	1.951
158-957C	13	39.017	2.968
158-957C	13	39.041	3.067
158-957C	13	39.064	3.364
158-957C	13	39.087	1.828
158-957C	13	39.111	1.573
158-957C	13	39.134	0.387

Continued on next page...

Hole	Cor	Depth	Density
[-]	[-]	[mbsf]	[g/cc]
158-957C	13	39.156	0.236
158-957C	15	42.213	0.393
158-957C	15	42.22	0.405
158-957C	15	42.232	0.351
158-957C	15	42.25	0.434
158-957C	15	42.268	0.291
158-957C	15	42.28	0.445
158-957C	15	42.283	0.422
158-957C	15	42.31	0.724
158-957C	15	42.324	0.905
158-957C	15	42.34	0.35
158-957C	15	42.363	0.258
158-957C	15	42.37	0.213
158-957C	15	42.377	0.405
158-957C	15	42.4	0.362
158-957C	15	42.414	0.567
158-957C	15	42.43	0.169
158-957C	15	42.452	0.182
158-957C	15	42.46	0.22
158-957C	15	42.461	0.849
158-957C	15	42.483	3.081
158-957C	15	42.49	3.173
158-957C	15	42.497	1.677
158-957C	15	42.52	1.563
158-957C	15	42.534	0.357
158-957C	15	42.55	0.967
158-957C	15	42.571	0.452
158-957C	15	42.58	0.315
158-957C	15	42.588	0.786
158-957C	15	42.61	0.614
158-957C	15	42.628	2.002
158-957C	15	42.64	2.227
158-957C	15	42.657	0.469
158-957C	15	42.67	0.155
158-957C	15	42.673	0.31
158-957C	15	42.7	0.718
158-957C	15	42.712	0.796
158-957C	15	42.73	0.327
158-957C	15	42.747	0.347
158-957C	15	42.76	0.48
158-957C	15	42.766	0.938
158-957C	15	42.79	0.36
158-957C	15	42.805	0.254
158-957C	15	42.82	0.56
158-957C	15	42.841	2.585
158-957C	15	42.85	2.647
158-957C	15	42.857	2.868
158-957C	15	42.88	2.884
158-957C	15	42.894	3.015
158-957C	15	42.91	2.707
158-957C	15	42.933	2.877
158-957C	15	42.94	2.805

Continued on next page...

Hole	Cor	Depth	Density
[-]	[-]	[mbsf]	[g/cc]
158-957C	15	42.945	2.851
158-957C	15	42.97	1.466
158-957C	15	42.993	0.275
158-957C	15	43.015	0.761
158-957C	15	43.04	0.238
158-957C	15	43.061	0.784
158-957C	15	43.084	2.305
158-957C	15	43.107	2.48
158-957C	15	43.132	2.259
158-957C	15	43.155	2.003
158-957C	15	43.177	2.279
158-957C	15	43.202	2.671
158-957C	15	43.225	2.473
158-957C	15	43.247	2.146
158-957C	15	43.269	2.848
158-957C	15	43.294	2.994
158-957C	15	43.318	2.935
158-957C	15	43.34	2.98
158-957C	15	43.413	0.487
158-957C	15	43.42	0.694
158-957C	15	43.436	2.726
158-957C	15	43.451	2.842
158-957C	15	43.473	2.236
158-957C	15	43.499	2.697
158-957C	15	43.522	2.909
158-957C	15	43.544	2.719
158-957C	15	43.567	2.597
158-957C	15	43.592	2.611
158-957C	15	43.615	1.86
158-957C	15	43.637	2.786
158-957C	15	43.66	2.559
158-957C	15	43.685	2.373
158-957C	15	43.707	1.657
158-957C	15	43.73	0.305
158-957C	15	43.753	1.806
158-957C	15	43.778	2.909
158-957C	15	43.801	2.927
158-957C	15	43.823	2.375
158-957C	15	43.847	2.378
158-957C	15	43.872	1.578
158-957F	1	1.02	1.854
158-957F	1	1.037	0.531
158-957F	1	1.054	0.511
158-957F	1	1.08	0.395
158-957F	1	1.091	0.28
158-957F	1	1.11	0.193
158-957F	1	1.125	0.277
158-957F	1	1.143	0.218
158-957F	1	1.17	0.196
158-957F	1	1.182	0.194
158-957F	1	1.2	0.178
158-957F	1	1.22	0.264

Continued on next page...

Hole	Cor	Depth	Density
[-]	[-]	[mbsf]	[g/cc]
158-957F	1	1.245	0.181
158-957F	1	1.267	0.245
158-957F	1	1.289	0.351
158-957F	1	1.315	2.27
158-957F	1	1.337	1.564
158-957F	1	1.361	0.254
158-957F	1	1.383	0.338
158-957F	1	1.408	2.085
158-957F	1	1.43	2.944
158-957F	1	1.452	2.49
158-957F	1	1.477	2.317
158-957F	1	1.501	2.868
158-957F	1	1.525	2.888
158-957F	1	1.548	2.865
158-957F	1	1.571	3.064
158-957F	1	1.595	3.066
158-957H	5	26.7	3.845
158-957H	5	26.72	3.926
158-957H	5	26.73	3.972
158-957H	5	26.75	2.618
158-957H	5	26.771	0.625
158-957H	5	26.78	0.886
158-957H	5	26.787	0.753
158-957H	5	26.809	0.29
158-957H	5	26.832	1.411
158-957H	5	26.857	2.908
158-957H	5	26.881	2.812
158-957H	5	26.904	1.271
158-957H	5	26.927	0.357
158-957H	5	26.951	1.663
158-957H	5	26.974	0.497
158-957H	5	26.996	2.442
158-957H	5	27.019	3.258
158-957H	5	27.044	3.2
158-957H	5	27.067	3.238
158-957H	5	27.089	2.376
158-957H	5	27.114	3.046
158-957H	5	27.138	3.074
158-957H	5	27.159	2.746
158-957H	5	27.182	2.643
158-957H	5	27.62	2.357
158-957H	5	27.636	2.557
158-957H	5	27.653	2.481
158-957H	5	27.68	2.457
158-957H	5	27.694	2.534
158-957H	5	27.71	2.576
158-957H	5	27.731	2.565
158-957H	5	27.74	2.552
158-957H	5	27.745	2.219
158-957H	5	27.77	1.424
158-957H	5	27.782	1.929
158-957H	5	27.8	2.285

Continued on next page...

Hole	Cor	Depth	Density
[-]	[-]	[mbsf]	[g/cc]
158-957H	5	27.821	1.548
158-957H	5	27.83	1.043
158-957H	5	27.835	1.539
158-957H	5	27.86	2.821
158-957H	5	27.874	3.583
158-957H	5	27.897	3.572
158-957H	5	27.922	3.272
158-957H	5	27.944	2.875
158-957H	5	27.968	2.403
158-957H	5	27.99	3.232
158-957H	5	28.015	2.625
158-957H	5	28.039	1.207
158-957H	5	28.061	0.441
158-957H	5	28.083	0.177
158-957H	5	28.11	0.349
158-957H	5	28.132	0.28
158-957H	5	28.155	0.182
158-957H	5	28.177	0.375
158-957H	5	28.203	2.824
158-957H	5	28.225	3.204
158-957H	5	28.246	2.977
158-957H	5	28.27	3.065
158-957H	5	28.291	2.953
158-957H	5	28.3	3.034
158-957P	12	54.42	2.324
158-957P	12	54.436	2.536
158-957P	12	54.45	2.682
158-957P	12	54.455	2.821
158-957P	12	54.48	2.837
158-957P	12	54.493	2.858
158-957P	12	54.51	2.838
158-957P	12	54.529	2.856
158-957P	12	54.54	2.841
158-957P	12	54.545	2.879
158-957P	12	54.57	2.847
158-957P	12	54.583	2.762
158-957P	12	54.6	2.773
158-957P	12	54.614	2.784
158-957P	12	54.63	2.849
158-957P	12	54.652	2.981
158-957P	12	54.66	2.979
158-957P	12	54.668	2.988
158-957P	12	54.69	3.023
158-957P	12	54.705	2.943
158-957P	12	54.72	2.946
158-957P	12	54.73	3.004
158-957P	12	54.75	2.983
158-957P	12	54.76	2.942
158-957P	12	54.78	2.942
158-957P	12	54.8	2.939
158-957P	12	54.81	2.898
158-957P	12	54.84	2.962

Continued on next page...

Hole	Cor	Depth	Density
[-]	[-]	[mbsf]	[g/cc]
158-957P	12	54.854	2.99
158-957P	12	54.87	2.953
158-957P	12	54.888	2.967
158-957P	12	54.903	2.971
158-957P	12	54.93	2.983
158-957P	12	54.941	2.996
158-957P	12	54.96	2.967
158-957P	12	54.98	2.934
158-957P	12	54.99	2.972
158-957P	12	54.995	2.966
158-957P	12	55.02	3.019
158-957P	12	55.034	3.048
158-957P	12	55.05	3.102
158-957P	12	55.071	3.129
158-957P	12	55.08	3.094
158-957P	12	55.1	3.141
158-957P	12	55.11	2.979
158-957P	12	55.13	3.072
158-957P	12	55.14	3.116
158-957P	12	55.16	3.052
158-957P	12	55.17	3.22
158-957P	12	55.19	3.097
158-957P	12	55.2	3.175
158-957P	12	55.22	3.2
158-957P	12	55.23	3.15
158-957P	12	55.25	3.08
158-957P	12	55.26	3.012
158-957P	12	55.28	2.96
158-957P	12	55.29	2.926
158-957P	12	55.31	3.004
158-957P	12	55.32	3.012
158-957P	12	55.34	2.945
158-957P	12	55.35	3.108
158-957P	12	55.37	3.179
158-957P	12	55.4	3.094
158-957P	12	55.412	3.085
158-957P	12	55.43	3.19
158-957P	12	55.46	3.458
158-957P	12	55.465	3.372
158-957P	12	55.49	3.343
158-957P	12	55.509	3.07
158-957P	12	55.52	3.117
158-957P	12	55.526	3.531
158-957P	12	55.55	3.463
158-957P	12	55.57	3.506
158-957P	12	55.58	3.506
158-957P	12	55.587	3.476
158-957P	12	55.61	3.311
158-957P	12	55.628	3.355
158-957P	12	55.64	3.331
158-957P	12	55.66	3.159
158-957P	12	55.675	3.146

Continued on next page...

Hole	Cor	Depth	Density
[-]	[-]	[mbsf]	[g/cc]
158-957P	12	55.69	3.167
158-957P	12	55.708	3.248
158-957P	12	55.721	3.237
158-957P	12	55.75	3.258
158-957P	12	55.762	3.188
158-957P	12	55.78	3.258
158-957P	12	55.802	3.127
158-957P	12	55.81	3.147
158-957P	12	55.817	3.1
158-957P	12	55.84	3.228
158-957P	12	55.851	3.263
158-957P	12	55.871	3.155
158-957P	12	55.891	3.218
158-957P	12	55.905	3.189
158-957P	12	55.93	3.22
158-957P	12	55.941	3.219
158-957P	12	55.96	3.257
158-957P	12	55.979	3.202
158-957P	12	55.99	3.289
158-957P	12	56.013	3.188
158-957P	12	56.024	3.181
158-957P	12	56.05	3.153
158-957P	12	56.062	3.176
158-957P	12	56.08	3.239
158-957P	12	56.099	3.072
158-957P	12	56.113	3.136
158-957P	12	56.14	3.712
158-957P	12	56.147	3.903
158-957P	12	56.171	3.868
158-957P	12	56.187	3.914
158-957P	12	56.2	3.895
158-957P	12	56.227	3.884
158-957P	12	56.251	3.582
158-957P	12	56.273	2.985
158-957P	12	56.299	3.083
158-957P	12	56.309	3.051
158-957P	12	56.34	3.148
158-957Q	1	0.02	2.587
158-957Q	1	0.037	2.65
158-957Q	1	0.05	2.278
158-957Q	1	0.072	2.365
158-957Q	1	0.08	2.366
158-957Q	1	0.091	2.446
158-957Q	1	0.11	2.264
158-957Q	1	0.129	2.129
158-957Q	1	0.14	2.169
158-957Q	1	0.17	2.171
158-957Q	1	0.182	2.284
158-957Q	1	0.2	2.257
158-957Q	1	0.21	2.305
158-957Q	1	0.23	2.387
158-957Q	1	0.25	2.519

Continued on next page...

Hole	Cor	Depth	Density
[-]	[-]	[mbsf]	[g/cc]
158-957Q	1	0.26	2.533
158-957Q	1	0.268	2.581
158-957Q	1	0.29	2.779
158-957Q	1	0.304	2.797
158-957Q	1	0.32	2.839
158-957Q	1	0.34	2.934
158-957Q	1	0.35	2.891
158-957Q	1	0.381	3.039
158-957Q	1	0.395	3.064
158-957Q	1	0.41	3.086
158-957Q	1	0.431	3.073
158-957Q	1	0.44	3.079
158-957Q	1	0.45	3.098
158-957Q	1	0.47	3.1
158-957Q	1	0.488	3.088
158-957Q	1	0.5	2.995
158-957Q	1	0.522	3.084
158-957Q	1	0.531	3.08
158-957Q	1	0.539	3.106
158-957Q	1	0.56	3.108
158-957Q	1	0.579	3.167
158-957Q	1	0.591	3.017
158-957Q	1	0.62	2.356
158-957Q	1	0.629	2.177
158-957Q	1	0.65	2.868
158-957Q	1	0.67	1.837
158-957Q	1	0.683	2.323
158-957Q	1	0.71	3.02
158-957Q	1	0.72	3.066
158-957Q	1	0.73	3.072
158-957Q	1	0.74	2.817
158-957Q	1	0.751	3.112
158-957Q	1	0.77	3.014
158-957Q	1	0.79	2.974
158-957Q	1	0.8	3.07
158-957Q	1	0.82	2.981
158-957Q	1	0.831	3.056
158-957Q	1	0.836	2.979
158-957Q	1	0.85	3.057
158-957Q	1	0.86	3
158-957Q	1	0.867	3.031
158-957Q	1	0.89	3.109
158-957Q	1	0.904	3.111
158-957Q	1	0.91	3.106
158-957Q	1	0.92	3.039
158-957Q	1	0.948	3.084
158-957Q	1	0.97	3.031
158-957Q	1	0.978	3.01
158-957Q	1	1.003	3
158-957Q	1	1.023	2.977
158-957Q	1	1.03	2.949
158-957Q	1	1.045	2.984

Continued on next page...

Hole	Cor	Depth	Density
[-]	[-]	[mbsf]	[g/cc]
158-957Q	1	1.066	2.955
158-957Q	1	1.089	2.944
158-957Q	1	1.104	2.951
158-957Q	1	1.125	2.954
158-957Q	1	1.151	2.935
158-957Q	1	1.164	3
158-957Q	1	1.187	2.929
158-957Q	1	1.21	3.001
158-957Q	1	1.229	2.916
158-957Q	1	1.255	2.787
158-957Q	1	1.27	2.838
158-957Q	1	1.294	2.797
158-957Q	1	1.318	2.782
158-957Q	1	1.331	2.951
158-957Q	1	1.338	2.9
158-957Q	1	1.52	3.014
158-957Q	1	1.536	2.936
158-957Q	1	1.55	2.967
158-957Q	1	1.554	2.924
158-957Q	1	1.58	2.941
158-957Q	1	1.594	2.917
158-957Q	1	1.61	2.927
158-957Q	1	1.631	2.879
158-957Q	1	1.64	2.908
158-957Q	1	1.648	2.917
158-957Q	1	1.67	2.829
158-957Q	1	1.69	2.909
158-957Q	1	1.7	2.902
158-957Q	1	1.704	2.874
158-957Q	1	1.73	2.839
158-957Q	1	1.742	2.88
158-957Q	1	1.76	2.879
158-957Q	1	1.78	2.903
158-957Q	1	1.79	2.875
158-957Q	1	1.795	2.835
158-957Q	1	1.82	2.769
158-957Q	1	1.834	2.835
158-957Q	1	1.85	2.666
158-957Q	1	1.873	2.877
158-957Q	1	1.88	2.884
158-957Q	1	1.886	2.823
158-957Q	1	1.91	2.866
158-957Q	1	1.925	2.837
158-957Q	1	1.94	2.801
158-957Q	1	1.941	2.896
158-957Q	1	1.963	2.894
158-957Q	1	1.97	2.869
158-957Q	1	1.976	2.87
158-957Q	1	2	2.919
158-957Q	1	2.013	2.884
158-957Q	1	2.03	2.906
158-957Q	1	2.031	2.82

Continued on next page...

Hole	Cor	Depth	Density
[-]	[-]	[mbsf]	[g/cc]
158-957Q	1	2.06	2.868
158-957Q	1	2.069	2.896
158-957Q	1	2.09	2.87
158-957Q	1	2.098	2.858
158-957Q	1	2.12	2.906
158-957Q	1	2.136	2.928
158-957Q	1	2.15	2.874
158-957Q	1	2.171	2.894
158-957Q	1	2.18	2.863
158-957Q	1	2.186	2.931
158-957Q	1	2.21	2.928
158-957Q	1	2.23	2.901
158-957Q	1	2.24	2.864
158-957Q	1	2.26	2.887
158-957Q	1	2.27	2.916
158-957Q	1	2.273	2.929
158-957Q	1	2.29	2.93
158-957Q	1	2.3	2.918
158-957Q	1	2.319	2.897
158-957Q	1	2.331	2.901
158-957Q	1	2.334	2.925
158-957Q	1	2.35	2.874
158-957Q	1	2.36	2.875
158-957Q	1	2.368	2.894
158-957Q	1	2.389	2.902
158-957Q	1	2.41	2.738
158-957Q	1	2.42	2.924
158-957Q	1	2.439	2.877
158-957Q	1	2.45	2.901
158-957Q	1	2.453	2.906
158-957Q	1	2.47	2.867
158-957Q	1	2.48	2.865
158-957Q	1	2.503	2.78
158-957Q	1	2.51	2.92
158-957Q	1	2.518	2.615
158-957Q	1	2.53	2.752
158-957Q	1	2.54	2.865
158-957Q	1	2.554	2.841
158-957Q	1	2.578	2.803
158-957Q	1	2.589	2.868
158-957Q	1	2.597	2.815
158-957Q	1	2.619	2.895
158-957Q	1	2.644	2.894
158-957Q	1	2.651	2.889
158-957Q	1	2.663	2.809
158-957Q	1	2.684	2.864
158-957Q	1	2.71	2.831
158-957Q	1	2.715	2.787
158-957Q	1	2.741	2.738
158-957Q	1	2.762	2.807
158-957Q	1	2.769	2.886
158-957Q	1	2.783	2.72

Continued on next page...

Hole	Cor	Depth	Density
[-]	[-]	[mbsf]	[g/cc]
158-957Q	1	2.807	2.849
158-957Q	1	2.831	2.869
158-957Q	1	2.848	2.876
158-957Q	1	2.872	2.681
158-957Q	1	2.89	2.728
158-957Q	1	2.905	2.664
158-957Q	1	2.927	2.714
158-957Q	1	2.95	2.708

Table 15: ρ mesurement results on ODP Leg 158 shallow hole core samples.

Hole	Depth	Py	Po	Cpy	Sph	Qtz	Anh	$AmFeO$	Hm	Clays
[-]	MD [m]	[%]	[%]	[%]	[%]	[%]	[%]	[%]	[%]	[%]
158-957C	10.5	100	0	0	0	0	0	0	0	0
158-957C	10.52	70	0	0	0	0	30	0	0	0
158-957C	10.58	70	0	0	0	0	30	0	0	0
158-957C	15	75	0	5	0	0	20	0	0	0
158-957C	15.07	70	0	5	0	0	25	0	0	0
158-957C	15.15	95	0	0	0	0	5	0	0	0
158-957C	15.21	90	0	5	0	0	5	0	0	0
158-957C	15.25	95	0	0	0	0	5	0	0	0
158-957C	15.39	85	0	5	0	5	5	0	0	0
158-957C	15.49	90	0	5	0	0	5	0	0	0
158-957C	15	50	0	0	0	0	50	0	0	0
158-957C	15.03	95	0	0	0	0	5	0	0	0
158-957C	15.07	95	0	0	0	0	5	0	0	0
158-957C	19.5	75	0	5	0	0	20	0	0	0
158-957C	19.57	75	0	5	0	0	20	0	0	0
158-957C	19.6	75	0	5	0	0	20	0	0	0
158-957C	19.63	75	0	5	0	0	20	0	0	0
158-957C	19.66	65	0	0	0	10	25	0	0	0
158-957C	19.76	70	0	2	0	0	28	0	0	0
158-957C	19.84	75	0	3	0	0	22	0	0	0
158-957C	19.89	80	0	5	0	0	15	0	0	0
158-957C	19.89	50	0	0	0	0	50	0	0	0
158-957C	19.94	80	0	0	0	10	10	0	0	0
158-957C	20.04	75	0	10	0	0	15	0	0	0
158-957C	20.08	75	0	5	0	0	20	0	0	0
158-957C	20.18	80	0	5	0	0	15	0	0	0
158-957C	20.22	30	0	0	0	10	60	0	0	0
158-957C	20.33	45	0	5	0	15	35	0	0	0
158-957C	20.52	40	0	10	0	10	40	0	0	0
158-957C	20.6	45	0	0	0	15	40	0	0	0
158-957C	20.68	50	0	0	0	10	40	0	0	0
158-957C	20.83	50	0	0	0	10	40	0	0	0
158-957C	20.99	50	0	0	0	10	40	0	0	0
158-957C	21.21	50	0	0	0	5	45	0	0	0
158-957C	21.32	70	0	5	0	5	20	0	0	0
158-957C	21.45	60	0	5	0	5	30	0	0	0
158-957C	21.59	60	0	0	0	5	35	0	0	0
158-957C	21.64	40	0	10	0	3	47	0	0	0

Continued on next page...

Hole	Depth	*Py*	*Po*	*Cpy*	*Sph*	*Qtz*	*Anh*	*AmFeO*	*Hm*	Clays
[-]	MD [m]	[%]	[%]	[%]	[%]	[%]	[%]	[%]	[%]	[%]
158-957C	21.73	10	0	0	0	3	87	0	0	0
158-957C	21.81	25	0	5	0	0	70	0	0	0
158-957C	22.03	30	0	10	0	5	55	0	0	0
158-957C	22.12	45	0	5	0	5	45	0	0	0
158-957C	22.33	7	0	1	0	2	90	0	0	0
158-957C	22.38	1	0	1	0	0	98	0	0	0
158-957C	22.4	1	0	1	0	0	98	0	0	0
158-957C	22.45	1	0	4	0	0	95	0	0	0
158-957C	22.61	40	0	2	0	8	50	0	0	0
158-957C	22.83	40	0	2	0	8	50	0	0	0
158-957C	22.89	40	0	2	0	8	50	0	0	0
158-957C	23	40	0	2	0	8	50	0	0	0
158-957C	19.5	45	0	1	0	4	50	0	0	0
158-957C	24	15	0	5	0	5	75	0	0	0
158-957C	24.4	60	0	10	0	10	20	0	0	0
158-957C	28.7	78	0	5	0	10	7	0	0	0
158-957C	28.75	78	0	5	0	10	7	0	0	0
158-957C	28.81	75	0	5	0	10	10	0	0	0
158-957C	28.86	75	0	5	0	10	10	0	0	0
158-957C	30.7	30	0	0	0	60	10	0	0	0
158-957C	30.78	30	0	0	0	60	10	0	0	0
158-957C	30.88	30	0	0	0	60	10	0	0	0
158-957C	31	70	0	15	0	7	8	0	0	0
158-957C	31.1	75	0	10	0	5	10	0	0	0
158-957C	31.18	75	0	10	0	5	10	0	0	0
158-957C	31.3	75	0	10	0	10	5	0	0	0
158-957C	31.39	75	0	10	0	10	5	0	0	0
158-957C	31.42	70	0	10	0	10	10	0	0	0
158-957C	31.52	75	0	10	0	5	10	0	0	0
158-957C	31.65	2	0	7	0	0	91	0	0	0
158-957C	31.71	2	0	3	0	0	95	0	0	0
158-957C	31.88	2	0	1	0	0	96	0	1	0
158-957C	32	15	0	2	0	0	83	0	0	0
158-957C	32.1	35	0	15	0	40	10	0	0	0
158-957C	32.19	35	0	15	0	40	10	0	0	0
158-957C	32.32	60	0	15	0	10	15	0	0	0
158-957C	32.35	45	0	5	0	40	10	0	0	0
158-957C	32.46	50	0	0	0	40	10	0	0	0
158-957C	32.55	50	0	0	0	40	10	0	0	0
158-957C	32.6	50	0	0	0	35	15	0	0	0
158-957C	32.68	50	0	0	0	15	35	0	0	0
158-957C	32.73	40	0	20	0	0	40	0	0	0
158-957C	32.8	10	0	15	0	5	70	0	0	0
158-957C	32.87	5	0	0	0	0	95	0	0	0
158-957C	32.95	50	0	10	0	5	35	0	0	0
158-957C	33.02	5	0	5	0	0	90	0	0	0
158-957C	33.14	5	0	0	0	0	95	0	0	0
158-957C	33.2	2	0	0	0	0	98	0	0	0
158-957C	33.44	45	0	5	0	20	30	0	0	0
158-957C	33.53	0	0	10	0	0	90	0	0	0
158-957C	33.59	10	0	0	0	0	90	0	0	0
158-957C	33.63	10	0	5	0	0	85	0	0	0

Continued on next page...

Hole	Depth	*Py*	*Po*	*Cpy*	*Sph*	*Qtz*	*Anh*	*AmFeO*	*Hm*	Clays
[-]	MD [m]	[%]	[%]	[%]	[%]	[%]	[%]	[%]	[%]	[%]
158-957C	33.76	5	0	10	0	0	85	0	0	0
158-957C	33.82	10	0	0	0	0	90	0	0	0
158-957C	33.93	50	0	5	0	2	43	0	0	0
158-957C	33.97	60	0	5	0	10	25	0	0	0
158-957C	34.09	70	0	5	0	10	15	0	0	0
158-957C	34.16	2	0	0	0	0	98	0	0	0
158-957C	34.29	2	0	0	0	0	98	0	0	0
158-957C	34.34	2	0	2	0	0	96	0	0	0
158-957C	34.38	70	0	5	0	10	15	0	0	0
158-957C	34.5	75	0	10	0	5	10	0	0	0
158-957C	34.58	50	0	0	0	0	50	0	0	0
158-957C	34.64	35	0	10	0	50	5	0	0	0
158-957C	34.8	35	0	10	0	50	5	0	0	0
158-957C	34.89	40	0	10	0	0	50	0	0	0
158-957C	35.2	60	0	0	0	20	20	0	0	0
158-957C	35.27	49	0	1	0	30	20	0	0	0
158-957C	35.33	65	0	0	0	15	20	0	0	0
158-957C	35.35	80	0	0	0	5	15	0	0	0
158-957C	35.45	85	0	0	0	0	15	0	0	0
158-957C	35.55	3	0	7	0	0	90	0	0	0
158-957C	35.58	3	0	7	0	0	90	0	0	0
158-957C	35.7	3	0	7	0	0	90	0	0	0
158-957C	35.83	60	0	30	0	0	10	0	0	0
158-957C	35.84	3	0	7	0	0	90	0	0	0
158-957C	35.88	3	0	7	0	0	90	0	0	0
158-957C	35.93	58	0	7	0	10	25	0	0	0
158-957C	35.97	15	0	5	0	10	70	0	0	0
158-957C	36.02	27	0	3	0	0	70	0	0	0
158-957C	36.05	20	0	3	0	15	62	0	0	0
158-957C	36.09	27	0	3	0	0	70	0	0	0
158-957C	36.12	53	0	7	0	25	15	0	0	0
158-957C	36.16	27	0	3	0	0	70	0	0	0
158-957C	36.21	50	0	2	0	33	15	0	0	0
158-957C	36.23	53	0	7	0	25	15	0	0	0
158-957C	36.3	53	0	7	0	25	15	0	0	0
158-957C	36.35	27	0	3	0	0	70	0	0	0
158-957C	36.37	27	0	3	0	0	70	0	0	0
158-957C	36.42	53	0	0	0	25	22	0	0	0
158-957C	36.46	27	0	3	0	0	70	0	0	0
158-957C	36.5	53	0	0	0	25	22	0	0	0
158-957C	36.51	20	0	5	0	25	50	0	0	0
158-957C	36.58	40	0	10	0	20	30	0	0	0
158-957C	36.64	40	0	10	0	20	30	0	0	0
158-957C	36.67	1	0	1	0	0	98	0	0	0
158-957C	36.75	45	0	2	0	40	13	0	0	0
158-957C	36.8	45	0	0	0	40	15	0	0	0
158-957C	36.83	1	0	1	0	0	98	0	0	0
158-957C	36.92	25	0	0	0	65	10	0	0	0
158-957C	36.94	1	0	1	0	0	98	0	0	0
158-957C	37.21	85	0	0	0	5	10	0	0	0
158-957C	37.24	85	0	0	0	5	10	0	0	0
158-957C	37.27	85	0	0	0	5	10	0	0	0

Continued on next page...

Hole	Depth	*Py*	*Po*	*Cpy*	*Sph*	*Qtz*	*Anh*	*AmFeO*	*Hm*	Clays
[-]	MD [m]	[%]	[%]	[%]	[%]	[%]	[%]	[%]	[%]	[%]
158-957C	37.31	85	0	0	0	5	10	0	0	0
158-957C	37.4	85	0	0	0	5	10	0	0	0
158-957C	37.48	85	0	0	0	5	10	0	0	0
158-957C	37.52	85	0	0	0	5	10	0	0	0
158-957C	37.57	85	0	0	0	5	10	0	0	0
158-957C	37.6	85	0	0	0	5	10	0	0	0
158-957C	37.63	85	0	0	0	5	10	0	0	0
158-957C	37.79	85	0	0	0	5	10	0	0	0
158-957C	37.82	85	0	0	0	5	10	0	0	0
158-957C	37.86	75	0	0	0	15	10	0	0	0
158-957C	37.97	85	0	0	0	5	10	0	0	0
158-957C	38.02	70	0	0	0	25	5	0	0	0
158-957C	38.15	85	0	0	0	5	10	0	0	0
158-957C	38.19	55	0	1	0	40	4	0	0	0
158-957C	38.34	55	0	1	0	40	4	0	0	0
158-957C	38.37	55	0	1	0	40	4	0	0	0
158-957C	38.4	55	0	1	0	40	4	0	0	0
158-957C	38.43	70	0	0	0	25	5	0	0	0
158-957C	38.47	55	0	5	0	35	5	0	0	0
158-957C	38.6	33	0	7	0	20	40	0	0	0
158-957C	38.71	15	0	3	0	7	75	0	0	0
158-957C	38.74	40	0	15	0	20	25	0	0	0
158-957C	38.81	55	0	5	0	35	5	0	0	0
158-957C	38.89	55	0	0	0	40	5	0	0	0
158-957C	38.95	55	0	0	0	40	5	0	0	0
158-957C	39.04	2	0	2	0	1	95	0	0	0
158-957C	40.2	54	0	2	0	37	7	0	0	0
158-957C	40.25	54	0	2	0	37	7	0	0	0
158-957C	40.43	54	0	2	0	37	7	0	0	0
158-957C	40.48	54	0	2	0	37	7	0	0	0
158-957C	40.53	54	0	2	0	37	7	0	0	0
158-957C	40.61	45	0	15	0	33	7	0	0	0
158-957C	40.71	35	0	25	0	33	7	0	0	0
158-957C	40.79	25	0	45	0	15	15	0	0	0
158-957C	40.85	35	0	25	0	33	7	0	0	0
158-957C	40.9	30	0	35	0	25	10	0	0	0
158-957C	40.9	48	0	2	0	40	10	0	0	0
158-957C	41.06	48	0	2	0	40	10	0	0	0
158-957C	41.12	38	0	15	0	5	42	0	0	0
158-957C	41.23	38	0	15	0	5	42	0	0	0
158-957C	41.45	12	0	5	0	3	80	0	0	0
158-957C	42.2	50	0	5	0	0	45	0	0	0
158-957C	42.27	90	0	5	0	0	5	0	0	0
158-957C	42.33	50	0	20	0	20	10	0	0	0
158-957C	42.43	70	0	5	0	10	15	0	0	0
158-957C	42.5	70	0	5	0	10	15	0	0	0
158-957C	42.56	70	0	0	0	10	20	0	0	0
158-957C	42.63	55	0	10	0	10	25	0	0	0
158-957C	42.68	25	0	0	0	50	25	0	0	0
158-957C	42.73	50	0	0	0	35	15	0	0	0
158-957C	42.9	40	0	0	0	10	50	0	0	0
158-957C	42.94	40	0	3	0	47	10	0	0	0

Continued on next page...

Hole	Depth	*Py*	*Po*	*Cpy*	*Sph*	*Qtz*	*Anh*	*AmFeO*	*Hm*	Clays
[-]	MD [m]	[%]	[%]	[%]	[%]	[%]	[%]	[%]	[%]	[%]
158-957C	43.16	40	0	0	0	50	10	0	0	0
158-957C	43.39	25	0	35	0	30	10	0	0	0
158-957C	43.48	55	0	5	0	20	20	0	0	0
158-957C	43.59	25	0	10	0	15	50	0	0	0
158-957C	43.86	40	0	10	0	10	40	0	0	0
158-957C	43.93	25	0	10	0	15	50	0	0	0
158-957C	44.11	30	0	10	0	5	55	0	0	0
158-957C	44.19	25	0	10	0	15	50	0	0	0
158-957C	44.36	10	0	20	0	5	65	0	0	0
158-957C	44.46	10	0	0	0	5	85	0	0	0
158-957C	44.55	5	0	10	0	5	80	0	0	0
158-957C	44.62	5	0	0	0	0	95	0	0	0
158-957C	44.82	0	0	2	0	0	98	0	0	0
158-957C	44.88	5	0	0	0	0	95	0	0	0
158-957C	44.98	30	0	0	0	50	20	0	0	0
158-957C	45.05	45	0	0	0	50	5	0	0	0
158-957C	45.11	45	0	0	0	50	5	0	0	0
158-957C	45.16	20	0	0	0	15	65	0	0	0
158-957C	45.41	30	0	0	0	65	5	0	0	0
158-957C	45.54	20	0	5	0	45	30	0	0	0
158-957C	45.7	20	0	5	0	45	30	0	0	0
158-957C	45.89	40	0	0	0	55	5	0	0	0
158-957C	45.96	40	0	0	0	55	5	0	0	0
158-957C	46.1	40	0	0	0	55	5	0	0	0
158-957C	46.2	30	0	0	0	70	0	0	0	0
158-957C	46.24	30	0	0	0	68	2	0	0	0
158-957C	46.33	30	0	0	0	68	2	0	0	0
158-957C	46.43	30	0	0	0	68	2	0	0	0
158-957C	46.48	30	0	0	0	68	2	0	0	0
158-957C	46.67	50	0	15	0	15	20	0	0	0
158-957C	46.72	50	0	15	0	15	20	0	0	0
158-957C	46.78	30	0	0	0	68	2	0	0	0
158-957C	46.86	40	0	20	0	20	20	0	0	0
158-957C	46.92	40	0	20	0	20	20	0	0	0
158-957C	46.98	40	0	20	0	20	20	0	0	0
158-957C	47.02	40	0	20	0	20	20	0	0	0
158-957C	47.1	35	0	25	0	30	10	0	0	0
158-957C	47.16	35	0	25	0	30	10	0	0	0
158-957C	47.39	35	0	30	0	10	25	0	0	0
158-957C	47.47	30	0	10	0	40	20	0	0	0
158-957C	47.58	35	0	30	0	10	25	0	0	0
158-957C	47.62	60	0	0	0	40	0	0	0	0
158-957C	47.75	50	0	25	0	15	10	0	0	0
158-957C	47.85	50	0	10	0	35	5	0	0	0
158-957C	48.05	45	0	10	0	30	15	0	0	0
158-957C	48.07	65	0	0	0	30	5	0	0	0
158-957C	48.23	35	0	20	0	30	15	0	0	0
158-957C	48.29	25	0	5	0	65	5	0	0	0
158-957C	48.44	35	0	20	0	30	15	0	0	0
158-957C	48.5	30	0	0	0	68	2	0	0	0
158-957E	31.5	40	0	0	0	55	5	0	0	0
158-957E	31.57	45	0	5	0	45	5	0	0	0

Continued on next page...

Hole	Depth	*Py*	*Po*	*Cpy*	*Sph*	*Qtz*	*Anh*	*AmFeO*	*Hm*	Clays
[-]	MD [m]	[%]	[%]	[%]	[%]	[%]	[%]	[%]	[%]	[%]
158-957E	31.65	70	0	20	0	5	5	0	0	0
158-957E	31.7	35	0	0	0	65	0	0	0	0
158-957E	37	45	0	5	0	45	5	0	0	0
158-957E	37.05	60	0	40	0	0	0	0	0	0
158-957E	37.1	40	0	0	0	55	5	0	0	0
158-957E	37.14	40	0	0	0	55	5	0	0	0
158-957E	37.23	45	0	0	0	55	0	0	0	0
158-957E	37.29	40	0	0	0	55	5	0	0	0
158-957E	37.36	40	0	0	0	55	5	0	0	0
158-957E	41.7	40	0	10	0	40	10	0	0	0
158-957E	41.76	45	0	0	0	50	5	0	0	0
158-957E	41.8	50	0	0	0	45	5	0	0	0
158-957E	41.86	35	0	5	0	55	5	0	0	0
158-957E	49	35	0	8	0	47	10	0	0	0
158-957E	49.08	50	0	0	0	45	5	0	0	0
158-957E	49.11	25	0	0	0	70	5	0	0	0
158-957E	49.18	25	0	0	0	75	0	0	0	0
158-957E	58.6	32	0	0	0	65	3	0	0	0
158-957E	58.64	41	0	0	0	56	3	0	0	0
158-957E	58.68	40	0	3	0	54	3	0	0	0
158-957E	58.76	35	0	0	0	65	0	0	0	0
158-957E	58.81	40	0	2	0	55	3	0	0	0
158-957E	58.87	32	0	0	0	65	3	0	0	0
158-957E	58.92	40	0	0	0	57	3	0	0	0
158-957E	58.99	32	0	0	0	65	3	0	0	0
158-957E	63.3	25	0	4	0	66	5	0	0	0
158-957E	63.34	61	0	6	0	30	3	0	0	0
158-957E	63.41	15	0	5	0	70	0	0	0	10
158-957E	63.48	67	0	0	0	30	3	0	0	0
158-957E	63.52	85	0	7	0	5	3	0	0	0
158-957E	63.55	10	0	5	0	75	0	0	0	10
158-957E	63.58	90	0	3	0	5	2	0	0	0
158-957E	63.63	90	0	3	0	7	0	0	0	0
158-957E	68.3	25	0	4	0	71	0	0	0	0
158-957E	68.39	25	0	2	0	73	0	0	0	0
158-957E	68.42	15	0	0	0	85	0	0	0	0
158-957E	68.49	25	0	2	0	73	0	0	0	0
158-957E	68.53	25	0	2	0	73	0	0	0	0
158-957E	68.59	25	0	2	0	73	0	0	0	0
158-957E	72.8	93	0	7	0	0	0	0	0	0
158-957E	72.88	30	0	0	0	70	0	0	0	0
158-957E	72.95	20	0	3	0	77	0	0	0	0
158-957E	77.8	83	0	2	0	15	0	0	0	0
158-957E	77.88	83	0	2	0	15	0	0	0	0
158-957E	78	70	0	8	0	20	2	0	0	0
158-957E	78.16	70	0	8	0	20	2	0	0	0
158-957E	78.2	30	0	0	0	70	0	0	0	0
158-957E	82.1	20	0	0	0	80	0	0	0	0
158-957E	82.18	90	0	6	0	0	4	0	0	0
158-957E	87.1	20	0	0	0	80	0	0	0	0
158-957E	87.15	80	0	0	0	15	5	0	0	0
158-957E	87.2	20	0	0	0	80	0	0	0	0

Continued on next page...

Hole	Depth	*Py*	*Po*	*Cpy*	*Sph*	*Qtz*	*Anh*	*AmFeO*	*Hm*	Clays
[-]	MD [m]	[%]	[%]	[%]	[%]	[%]	[%]	[%]	[%]	[%]
158-957E	87.23	88	0	0	0	10	2	0	0	0
158-957E	87.28	25	0	0	0	75	0	0	0	0
158-957E	87.34	25	0	0	0	75	0	0	0	0
158-957E	87.39	40	0	5	0	53	2	0	0	0
158-957E	87.45	30	0	2	0	68	0	0	0	0
158-957E	87.52	40	0	2	0	53	5	0	0	0
158-957E	87.59	40	0	0	0	60	0	0	0	0
158-957E	91.8	40	0	0	0	55	5	0	0	0
158-957E	91.89	30	0	5	0	63	2	0	0	0
158-957E	91.95	35	0	0	0	65	0	0	0	0
158-957E	92	30	0	0	0	70	0	0	0	0
158-957E	92.08	30	0	0	0	70	0	0	0	0
158-957E	92.16	25	0	0	0	75	0	0	0	0
158-957E	92.22	35	0	0	0	65	0	0	0	0
158-957E	101.5	28	0	0	0	60	2	0	0	10
158-957E	101.54	0	0	0	0	0	0	0	0	0
158-957E	101.58	28	0	0	0	65	2	0	0	5
158-957E	101.62	27	1	0	0	60	2	0	0	10
158-957E	101.67	20	1	0	0	49	2	0	0	28
158-957E	101.73	0	0	0	0	0	0	0	0	0
158-957E	101.77	20	0	0	0	65	0	0	10	5
158-957E	101.8	50	1	0	0	40	2	0	0	7
158-957E	101.86	40	1	0	0	47	2	0	0	10
158-957E	101.91	15	0	5	0	55	5	0	0	20
158-957E	101.97	15	0	0	0	60	0	0	0	25
158-957E	106.5	25	7	3	0	60	5	0	0	0
158-957E	106.54	15	0	0	0	48	7	0	0	30
158-957E	106.59	63	0	25	0	10	2	0	0	0
158-957E	106.64	30	0	0	0	65	0	0	0	5
158-957E	106.7	0	0	0	0	0	0	0	0	0
158-957E	106.77	40	0	0	0	57	0	0	0	3
158-957E	106.84	40	0	0	0	53	2	0	0	5
158-957E	106.89	40	0	0	0	55	5	0	0	0
158-957E	106.93	40	0	2	0	54	2	0	0	2
158-957E	111.1	24	0	1	0	50	2	0	0	23
158-957E	111.16	10	0	2	0	30	4	0	0	54
158-957E	111.23	68	0	3	0	20	1	0	0	8
158-957E	116.1	30	0	2	0	68	0	0	0	0
158-957E	116.15	60	0	0	0	38	2	0	0	0
158-957E	116.19	10	0	0	0	70	0	0	0	20
158-957E	116.25	20	0	0	0	65	0	0	0	15
158-957E	116.3	40	0	0	0	55	0	0	0	5
158-957E	116.33	60	0	2	0	33	0	0	0	5
158-957E	116.37	15	0	0	0	63	2	0	0	20
158-957E	120.7	15	0	0	0	5	0	0	0	80
158-957F	1	10	0	80	0	0	0	0	0	0
158-957F	1.05	3	0	95	0	0	0	0	0	0
158-957F	1.1	1	0	99	0	0	0	0	0	0
158-957F	1.13	1	0	99	0	0	0	0	0	0
158-957F	1.17	60	0	40	0	0	0	0	0	0
158-957F	1.23	50	0	10	0	0	40	0	0	0
158-957F	1.27	95	0	5	0	0	0	0	0	0

Continued on next page...

Hole	Depth	*Py*	*Po*	*Cpy*	*Sph*	*Qtz*	*Anh*	*AmFeO*	*Hm*	Clays
[-]	MD [m]	[%]	[%]	[%]	[%]	[%]	[%]	[%]	[%]	[%]
158-957F	1.31	90	0	0	0	0	10	0	0	0
158-957F	1.37	80	0	10	0	0	10	0	0	0
158-957F	1.41	85	0	5	0	0	10	0	0	0
158-957F	5.5	85	0	10	5	0	0	0	0	0
158-957F	5.54	60	0	35	0	0	5	0	0	0
158-957F	5.6	60	0	32	0	0	8	0	0	0
158-957F	5.7	75	0	22	0	0	3	0	0	0
158-957F	5.76	65	0	35	0	0	0	0	0	0
158-957F	5.8	95	0	5	0	0	0	0	0	0
158-957F	5.86	87	0	8	0	0	5	0	0	0
158-957G	0	95	0	5	0	0	0	0	0	0
158-957G	12	75	0	25	0	0	0	0	0	0
158-957G	12.05	98	0	2	0	0	0	0	0	0
158-957G	12.1	88	0	5	0	0	0	0	0	0
158-957G	12.17	91	0	5	0	7	0	0	0	0
158-957G	12.21	88	0	2	0	4	0	0	0	0
158-957G	12.27	84	0	5	7	0	10	0	0	0
158-957G	12.32	72	0	7	4	8	3	0	0	0
158-957G	16.5	83	0	1	0	1	20	0	0	0
158-957G	16.55	95	0	0	8	15	1	0	0	0
158-957G	21	75	0	10	1	5	0	0	0	0
158-957G	21.05	85	0	0	15	0	15	0	0	0
158-957G	21.13	50	0	0	5	0	15	0	0	0
158-957G	21.35	95	0	0	0	10	40	0	0	0
158-957G	21.65	40	0	0	10	0	5	0	0	0
158-957G	21.68	0	0	5	5	5	50	0	0	0
158-957A	0	100	0	0	0	0	0	0	0	0
158-957A	0.04	90	0	0	0	0	0	0	0	0
158-957A	0.09	10	0	0	0	45	0	45	0	0
158-957A	5	5	0	0	0	50	0	45	0	0
158-957A	10	50	0	0	0	35	0	15	0	0
158-957A	10.08	45	0	0	0	40	2	10	0	0
158-957A	10.13	45	0	0	0	40	2	10	0	0
158-957A	10.19	80	0	0	2	15	0	3	0	0
158-957A	10.24	98	0	0	2	0	0	0	0	0
158-957A	10.29	80	0	0	2	15	0	3	0	0
158-957A	10.34	98	0	0	2	0	0	0	0	0
158-957A	10.39	5	0	0	0	0	0	0	0	0
158-957A	10.43	20	0	0	2	0	0	0	0	0
158-957A	10.46	7	0	0	0	0	0	3	0	0
158-957A	10.5	60	1	0	0	0	0	0	0	0
158-957B	0	20	0	0	0	20	0	60	0	0
158-957B	1.03	5	0	0	0	30	1	65	1	0
158-957B	1.13	10	0	0	55	30	2	5	2	0
158-957B	1.17	95	0	0	0	0	3	0	3	0
158-957B	14.9	95	0	0	0	3	4	0	4	0
158-957B	19.9	0	0	0	0	0	5	0	5	100
158-957B	20.06	0	0	0	0	0	6	0	6	100
158-957B	20.15	0	0	0	0	0	7	0	7	100
158-957B	20.29	10	0	0	0	0	8	0	8	90
158-957B	20.33	2	0	0	0	0	9	0	9	3
158-957H	8.7	25	0	0	0	0	0	0	0	0

Continued on next page...

Hole	Depth	*Py*	*Po*	*Cpy*	*Sph*	*Qtz*	*Anh*	*AmFeO*	*Hm*	Clays
[-]	MD [m]	[%]	[%]	[%]	[%]	[%]	[%]	[%]	[%]	[%]
158-957H	8.73	100	0	0	0	0	0	0	0	0
158-957H	8.76	100	0	0	0	0	0	0	0	0
158-957H	8.8	83	0	7	0	0	10	0	0	0
158-957H	8.84	83	0	7	0	0	10	0	0	0
158-957H	8.89	83	0	7	0	0	10	0	0	0
158-957H	8.95	83	0	7	0	0	10	0	0	0
158-957H	9.01	83	0	7	0	0	10	0	0	0
158-957H	9.07	75	0	I()	0	0	15	0	0	0
158-957H	9.17	0	0	0	0	0	0	30	0	0
158-957H	9.2	3	0	0	0	0	0	27	0	0
158-957H	9.23	83	0	7	0	0	10	0	0	0
158-957H	9.3	83	0	7	0	0	10	0	0	0
158-957H	9.44	83	0	7	0	0	10	0	0	0
158-957H	9.5	86	0	4	0	0	10	0	0	0
158-957H	13.2	90	0	0	0	0	10	0	0	0
158-957H	13.26	83	0	2	0	0	15	0	0	0
158-957H	13.31	90	0	0	0	0	10	0	0	0
158-957H	13.37	90	0	5	0	0	5	0	0	0
158-957H	17.7	75	0	0	10	0	5	0	0	0
158-957H	17.78	90	0	0	0	0	I 0	0	0	0
158-957H	17.83	90	0	0	0	0	10	0	0	0
158-957H	17.87	90	0	0	0	0	I 0	0	0	0
158-957H	17.92	90	0	0	0	0	10	0	0	0
158-957H	17.97	90	0	0	0	0	10	0	0	0
158-957H	18.02	90	0	0	0	0	I 0	0	0	0
158-957H	18.06	90	0	0	0	0	10	0	0	0
158-957H	18.1	85	0	5	0	0	10	0	0	0
158-957H	18.14	90	0	0	0	0	10	0	0	0
158-957H	18.18	90	0	0	0	0	10	0	0	0
158-957H	18.23	90	0	0	0	0	10	0	0	0
158-957H	18.4	90	0	0	0	0	10	0	0	0
158-957H	18.44	90	0	0	0	0	10	0	0	0
158-957H	26.7	100	0	0	0	0	0	0	0	0
158-957H	26.78	45	0	0	0	50	5	0	0	0
158-957H	26.83	45	0	0	0	50	5	0	0	0
158-957H	26.94	45	0	0	0	50	5	0	0	0
158-957H	26.98	43	0	0	0	50	7	0	0	0
158-957H	27.3	43	0	0	0	50	7	0	0	0
158-957H	27.35	38	0	0	0	55	7	0	0	0
158-957H	27.52	38	0	0	0	55	7	0	0	0
158-957H	27.6	15	0	0	0	67	5	8	0	5
158-957H	27.68	10	0	0	0	70	0	5	0	15
158-957H	27.79	15	0	0	0	75	0	0	0	10
158-957H	27.85	60	0	0	0	35	0	2	0	3
158-957H	27.98	44	0	0	0	50	0	3	0	3
158-957H	28.07	44	0	0	0	50	0	3	0	3
158-957H	28.17	45	0	0	0	45	0	5	0	5
158-957H	31.2	47	0	0	0	47	3	0	0	0
158-957H	31.26	47	0	3	0	47	3	0	0	0
158-957H	31.34	47	0	3	0	47	3	0	0	0
158-957H	31.4	47	0	3	0	47	3	0	0	0
158-957H	31.46	47	0	3	0	47	3	0	0	0

Continued on next page...

Hole	Depth	*Py*	*Po*	*Cpy*	*Sph*	*Qtz*	*Anh*	*AmFeO*	*Hm*	Clays
[-]	MD [m]	[%]	[%]	[%]	[%]	[%]	[%]	[%]	[%]	[%]
158-957H	31.55	47	0	0	0	47	3	0	0	0
158-957H	35.7	60	0	0	0	40	0	0	0	0
158-957H	35.76	60	0	0	0	40	0	0	0	0
158-957H	40.2	67	0	0	0	0	3	0	0	0
158-957H	40.27	67	0	0	0	0	3	0	0	0
158-957H	40.34	67	0	0	0	0	3	0	0	0
158-957H	40.4	67	0	0	0	0	3	0	0	0
158-957H	40.47	30	0	0	0	0	0	0	0	0
158-957H	40.51	30	0	0	0	0	0	0	0	0
158-957H	40.56	50	0	0	0	0	0	0	0	0
158-957H	40.65	20	0	0	0	75	0	0	0	0
158-957H	40.86	95	0	0	0	0	0	0	0	0
158-957H	40.92	45	0	2	0	48	0	0	0	0
158-957H	40.98	50	0	5	0	38	0	0	2	0
158-957H	41.03	45	0	2	0	35	0	0	2	0
158-957H	41.1	55	0	2	0	38	0	0	0	0
158-957H	41.18	60	0	0	0	35	0	0	0	0
158-957H	41.28	55	0	2	0	38	0	0	0	0
158-957H	44.7	20	0	0	0	70	0	0	0	0
158-957H	44.75	20	0	0	0	70	0	0	0	0
158-957H	44.8	72	0	5	0	0	3	0	0	0
158-957H	44.84	72	0	5	0	0	3	0	0	0
158-957N	0	0	0	0	0	0	0	0	0	0
158-957N	0.05	10	0	0	0	0	0	0	0	0
158-957N	0.14	15	0	0	0	75	10	0	0	0
158-957N	0.23	45	0	2	0	30	23	0	0	0
158-957N	0.28	20	0	2	0	68	10	0	0	0
158-957N	0.33	30	0	0	0	65	5	0	0	0
158-957N	0.38	30	0	0	0	68	2	0	0	0
158-957N	0.44	30	0	0	0	68	2	0	0	0
158-957N	0.49	30	0	0	0	68	2	0	0	0
158-957N	0.57	30	0	0	0	68	2	0	0	0
158-957O	7.9	90	0	10	0	0	0	0	0	0
158-957O	7.93	60	0	10	0	0	20	0	0	0
158-957O	7.98	75	0	5	0	0	15	0	0	0
158-957O	8.03	75	0	7	0	0	13	0	0	0
158-957O	8.1	75	0	7	0	0	13	0	0	0
158-957O	8.15	75	0	7	0	0	13	0	0	0
158-957O	8.19	70	0	3	0	0	7	0	0	0
158-957O	8.3	75	0	7	0	0	13	0	0	0
158-957O	10.9	50	0	8	0	0	32	0	0	0
158-957O	10.95	40	0	0	0	0	40	0	0	0
158-957O	11.02	40	0	5	0	0	45	0	0	0
158-957O	11.09	50	0	2	0	0	43	0	0	0
158-957O	11.14	50	0	2	0	0	38	0	0	0
158-957O	15.9	55	0	0	0	0	45	0	0	0
158-957O	15.95	5	0	10	0	0	85	0	0	0
158-957O	15.99	30	0	10	0	0	60	0	0	0
158-957O	16.02	30	0	10	0	0	60	0	0	0
158-957O	16.06	60	0	5	0	0	35	0	0	0
158-957O	16.13	75	0	3	0	0	22	0	0	0
158-957O	16.25	98	0	2	0	0	0	0	0	0

Continued on next page...

Hole	Depth	*Py*	*Po*	*Cpy*	*Sph*	*Qtz*	*Anh*	*AmFeO*	*Hm*	Clays
[-]	MD [m]	[%]	[%]	[%]	[%]	[%]	[%]	[%]	[%]	[%]
158-957O	16.28	70	0	3	0	0	27	0	0	0
158-957O	16.35	70	0	5	0	0	25	0	0	0
158-957O	16.4	85	0	5	0	0	10	0	0	0
158-957O	16.43	55	0	10	0	0	35	0	0	0
158-957O	16.46	45	0	10	0	0	45	0	0	0
158-957O	16.51	40	0	15	0	0	45	0	0	0
158-957O	16.54	50	0	3	0	0	47	0	0	0
158-957O	16.59	60	0	2	0	0	15	0	0	0
158-957O	16.63	35	0	0	0	0	15	0	0	0
158-957O	16.68	40	0	2	0	0	18	0	0	0
158-957O	16.74	40	0	0	0	0	10	0	0	0
158-957O	16.8	65	0	0	0	0	35	0	0	0
158-957P	0	42	0	8	0	0	0	0	0	0
158-957P	0.06	75	0	5	0	0	0	0	0	0
158-957P	0.11	67	0	3	0	0	0	0	0	0
158-957P	0.18	55	0	5	0	0	0	0	0	0
158-957P	0.24	62	0	3	0	0	35	0	0	0
158-957P	0.32	78	0	2	0	0	0	0	0	0
158-957P	0.37	70	0	10	0	0	0	0	0	0
158-957P	0.43	70	0	10	0	0	0	0	0	0
158-957P	0.48	60	0	10	0	0	0	0	0	0
158-957P	0.55	57	0	3	0	8	32	0	0	0
158-957P	0.6	58	0	2	0	0	0	0	0	0
158-957P	7.9	40	0	0	0	0	60	0	0	0
158-957P	7.96	95	0	0	0	0	4	0	0	0
158-957P	7.99	45	0	0	0	0	55	0	0	0
158-957P	11.9	80	0	0	0	0	0	0	0	0
158-957P	11.95	85	0	5	0	0	7	0	0	0
158-957P	16.9	85	0	5	0	0	10	0	0	0
158-957P	16.95	80	0	10	0	0	10	0	0	0
158-957P	21.5	85	0	0	0	0	15	0	0	0
158-957P	21.57	85	0	0	0	0	15	0	0	0
158-957P	26.5	100	0		0	0	0	0	0	0
158-957P	26.54	40	0	0	0	0	0	0	0	0
158-957P	26.59	90	0	0	0	0	10	0	0	0
158-957P	26.65	93	0	2	0	0	5	0	0	0
158-957P	26.72	95	0	5	0	0	0	0	0	0
158-957P	35.1	30	0	5	0	0	0	0	0	0
158-957P	35.15	95	0	5	0	0	0	0	0	0
158-957P	35.1	100	0	0	0	0	0	0	0	0
158-957P	35.14	10	0	0	0	0	0	0	0	0
158-957P	35.18	80	0	5	0	0	15	0	0	0
158-957P	35.23	40	0	0	0	0	0	0	0	0
158-957P	35.28	90	0	0	0	0	10	0	0	0
158-957P	35.32	93	0	2	0	0	0	0	0	0
158-957P	35.37	95	0	0	0	0	0	0	0	0
158-957P	40.1	25	0	0	0	0	0	0	0	0
158-957P	40.19	60	0	0	0	0	0	0	0	0
158-957P	40.26	80	0	0	0	0	0	0	0	0
158-957P	40.32	91	0	2	0	0	2	0	0	0
158-957P	45.1	85	0	5	0	0	0	0	0	0
158-957P	45.16	75	0	0	0	0	0	0	0	0

Continued on next page...

Hole	Depth	*Py*	*Po*	*Cpy*	*Sph*	*Qtz*	*Anh*	*AmFeO*	*Hm*	Clays
[-]	MD [m]	[%]	[%]	[%]	[%]	[%]	[%]	[%]	[%]	[%]
158-957P	45.2	77	0	2	0	0	0	0	0	0
158-957P	45.24	91	0	5	0	0	0	0	0	0
158-957P	45.29	40	0	2	0	0	0	0	0	0
158-957P	45.34	50	0	0	0	0	0	0	0	0
158-957P	50.1	90	0	5	0	0	5	0	0	0
158-957P	50.17	38	0	0	0	0	2	0	0	0
158-957P	50.21	40	0	0	0	0	2	0	0	0
158-957P	50.28	25	0	0	0	0	0	0	0	0
158-957P	50.32	10	0	0	0	0	0	0	0	0
158-957P	50.36	30	0	0	0	0	2	0	0	0
158-957P	50.4	30	0	0	0	0	3	0	0	0
158-957P	50.45	84	0	3	0	0	3	0	0	0
158-957P	50.51	50	0	5	0	0	2	0	0	0
158-957P	50.58	93	0	2	0	0	0	0	0	0
158-957P	50.63	50	0	0	0	0	2	0	0	0
158-957P	50.66	85	0	5	0	0	10	0	0	0
158-957P	54.4	0	0	0	0	0	0	0	0	0
158-957P	55.64	65	0	5	0	0	0	0	0	0
158-957P	55.69	50	0	0	0	0	5	0	0	0
158-957P	55.74	40	0	0	0	0	3	0	0	0
158-957P	55.78	30	0	0	0	0	0	0	0	0
158-957P	55.85	10	0	0	0	0	0	0	0	0
158-957P	55.89	30	0	0	0	0	0	0	0	0
158-957P	55.96	25	0	0	0	0	0	0	0	0
158-957P	56.02	22	0	0	0	0	0	0	0	0
158-957P	56.06	47	0	3	0	0	0	0	0	0
158-957P	56.13	90	0	0	0	0	10	0	0	0
158-957P	56.21	70	0	0	0	0	0	0	0	0
158-957P	56.28	35	0	0	0	0	0	0	0	0
158-957P	56.89	80	0	0	0	0	3	0	0	0
158-957P	56.93	60	0	0	0	0	3	0	0	0
158-957P	57.03	70	0	0	0	0	2	0	0	0
158-957P	57.06	70	0	0	0	0	3	0	0	0
158-957P	57.1	0	0	0	0	0	0	0	0	0
158-957P	57.39	50	0	2	0	0	0	0	0	0
158-957P	57.44	15	0	0	0	0	0	0	0	0
158-957P	57.51	88	0	2	0	0	0	0	0	0
158-957P	57.55	30	0	0	0	0	5	0	0	0
158-957P	57.61	65	0	5	0	0	0	0	0	0
158-957P	57.68	60	0	0	0	0	2	0	0	0
158-957P	57.74	0	0	0	0	0	0	0	0	0
158-957P	57.8	50	0	0	0	0	0	0	0	0
158-957P	57.84	93	0	0	0	0	2	0	0	0
158-957P	57.89	85	0	0	0	0	0	0	0	0
158-957P	57.96	78	0	0	0	0	2	0	0	0
158-957Q	0	0	0	0	0	0	0	0	0	0
158-957Q	1.39	0	0	0	0	0	0	0	0	0
158-957Q	2.9	0	0	0	0	0	0	0	0	0
158-957Q	4.41	0	0	0	0	0	0	0	0	0
158-957Q	5.59	0	0	0	0	0	0	0	0	0
158-957Q	9.5	0	0	0	0	80	0	20	0	0
158-957Q	9.55	5	0	0	0	95	0	0	0	0

Continued on next page...

Hole	Depth	*Py*	*Po*	*Cpy*	*Sph*	*Qtz*	*Anh*	*AmFeO*	*Hm*	Clays
[-]	MD [m]	[%]	[%]	[%]	[%]	[%]	[%]	[%]	[%]	[%]
158-957Q	9.58	60	0	0	0	40	0	0	0	0
158-957I	9	100	0	0	0	0	0	0	0	0
158-957I	9.06	100	0	0	0	0	0	0	0	0
158-957I	9.12	100	0	0	0	0	0	0	0	0
158-957I	9.17	100	0	0	0	0	0	0	0	0
158-957I	9.25	100	0	0	0	0	0	0	0	0
158-957I	9.33	100	0	0	0	0	0	0	0	0
158-957I	9.41	100	0	0	0	0	0	0	0	0
158-957I	9.47	100	0	0	0	0	0	0	0	0
158-957I	9.53	100	0	0	0	0	0	0	0	0
158-957I	9.6	100	0	0	0	0	0	0	0	0
158-957I	9.69	50	0	0	0	50	0	0	0	0
158-957I	9.75	48	0	2	0	50	0	0	0	0
158-957J	0	5	0	0	0	80	0	15	0	0
158-957J	0.06	20	0	0	1	65	0	5	0	0
158-957J	0.15	10	0	0	2	70	0	20	0	0
158-957K	0	95	0	0	0	0	0	0	0	0
158-957K	0.07	30	0	0	0	0	0	2	0	0
158-957K	0.14	92	0	3	0	0	0	2	0	0
158-957K	0.21	90	0	0	0	0	0	0	0	0
158-957K	0.3	93	0	7	0	0	0	0	0	0
158-957K	0.39	93	0	7	0	0	0	0	0	0
158-957K	0.45	87	0	0	0	0	0	0	0	0
158-957K	10	97	0	3	0	0	0	0	0	0
158-957K	10.04	100	0	0	0	0	0	0	0	0
158-957K	10.08	98	0	2	0	0	0	0	0	0
158-957K	10.14	100	0	0	0	0	0	0	0	0
158-957K	10.17	97	0	0	0	0	0	0	0	0
158-957K	10.22	100	0	0	0	0	0	0	0	0
158-957K	10.24	100	0	0	0	0	0	0	0	0
158-957K	10.33	100	0	0	0	0	0	0	0	0
158-957K	10.37	100	0	0	0	0	0	0	0	0
158-957K	10.42	98	0	2	0	0	0	0	0	0
158-957K	10.46	100	0	0	0	0	0	0	0	0
158-957K	14.5	80	0	0	0	0	0	0	0	0
158-957K	14.58	80	0	0	0	0	0	0	0	0
158-957K	14.61	90	0	0	0	0	0	0	0	0
158-957K	14.66	95	0	0	0	0	0	0	0	0
158-957K	14.71	80	0	0	0	0	0	0	0	0
158-957K	14.76	80	0	0	0	0	0	0	0	0
158-957K	14.82	70	0	0	0	0	0	2	0	0
158-957M	0	0	0	0	0	0	0	100	0	0
158-957M	0.55	5	0	0	0	0	0	30	0	0
158-957M	0.58	100	0	0	0	0	0	0	0	0
158-957M	0.63	5	0	0	0	0	0	30	0	0
158-957M	0.68	0	0	0	0	0	0	100	0	0
158-957M	0.74	20	0	5	0	75	0	0	0	0
158-957M	0.79	20	0	7	0	68	0	0	0	5
158-957M	0.85	20	0	5	0	70	0	0	0	5
158-957M	9.3	98	0	2	0	0	0	0	0	0
158-957M	9.35	50	0	0	0	0	0	0	0	0
158-957M	9.4	25	0	5	0	60	0	0	0	0

Continued on next page...

Hole	Depth	*Py*	*Po*	*Cpy*	*Sph*	*Qtz*	*Anh*	*AmFeO*	*Hm*	Clays
[-]	MD [m]	[%]	[%]	[%]	[%]	[%]	[%]	[%]	[%]	[%]
158-957M	9.44	47	0	3	0	30	0	0	0	0
158-957M	9.51	37	0	3	0	25	0	0	0	0
158-957M	9.55	37	0	3	0	25	0	0	0	0
158-957M	9.59	30	0	0	0	70	0	0	0	0
158-957M	9.65	30	0	0	0	70	0	0	0	0
158-957M	9.7	30	0	0	0	70	0	0	0	0
158-957M	9.73	40	0	5	0	55	0	0	0	0
158-957M	14.3	75	0	0	0	25	0	0	0	0
158-957M	14.34	25	0	2	0	68	0	0	0	0
158-957M	14.37	30	0	2	0	66	0	0	0	0
158-957M	14.45	50	0	0	0	50	0	0	0	0
158-957M	14.49	30	0	0	0	70	0	0	0	0
158-957M	14.52	80	0	0	0	15	0	0	0	0
158-957M	14.57	30	0	0	0	0	0	0	0	0
158-957M	14.6	30	0	0	0	0	0	0	0	0
158-957M	14.65	30	0	0	0	70	0	0	0	0
158-957M	14.68	70	0	0	0	20	0	0	0	0
158-957M	14.71	85	0	0	0	10	0	0	0	0
158-957M	14.75	38	0	0	0	2	0	0	0	0
158-957M	14.83	45	0	0	0	10	0	0	0	0
158-957M	14.87	48	0	0	0	40	0	0	0	0
158-957M	14.9	25	0	3	0	72	0	0	0	0
158-957M	14.97	30	0	10	0	60	0	0	0	0
158-957M	15.01	30	0	10	0	60	0	0	0	0
158-957M	15.05	50	0	0	0	0	0	0	0	0
158-957M	15.08	30	0	0	0	70	0	0	0	0
158-957M	15.13	40	0	0	0	60	0	0	0	0
158-957M	15.18	32	0	0	0	68	0	0	0	0
158-957M	15.22	20	0	0	0	10	0	0	0	0
158-957M	15.28	40	0	0	0	60	0	0	0	0
158-957M	15.31	40	0	5	0	55	0	0	0	0
158-957M	15.36	30	0	0	0	70	0	0	0	0
158-957M	15.39	40	0	2	0	60	0	0	0	0
158-957M	15.42	38	0	2	0	55	0	0	0	0
158-957M	15.49	38	0	2	0	60	0	0	0	0
158-957M	15.55	40	0	2	0	58	0	0	0	0
158-957M	15.6	30	0	3	0	62	0	0	0	0
158-957M	15.67	38	0	0	0	60	0	0	2	0
158-957M	15.73	20	0	2	0	76	0	0	2	0
158-957M	15.8	60	0	2	0	38	0	0	0	0
158-957M	15.85	60	0	0	0	30	0	0	0	0
158-957M	15.91	20	0	0	0	80	0	0	0	0
158-957M	19.3	40	0	0	0	50	0	0	0	0
158-957M	19.35	75	0	0	0	20	0	0	0	0
158-957M	19.4	20	0	0	0	80	0	0	0	0
158-957M	19.44	45	0	2	0	53	0	0	0	0
158-957M	19.48	45	0	2	0	51	0	2	0	0
158-957M	19.53	90	0	0	0	0	0	0	0	0
158-957M	19.57	85	0	0	0	5	0	0	0	0
158-957M	19.61	550	0	0	0	50	0	0	0	0
158-957M	19.66	95	0	0	0	5	0	0	0	0
158-957M	19.7	88	0	2	0	5	0	0	0	0

Continued on next page...

Hole	Depth	*Py*	*Po*	*Cpy*	*Sph*	*Qtz*	*Anh*	*AmFeO*	*Hm*	Clays
[-]	MD [m]	[%]	[%]	[%]	[%]	[%]	[%]	[%]	[%]	[%]
158-957M	19.78	60	0	5	0	35	0	0	0	0
158-957M	19.84	30	0	0	0	70	0	0	0	0
158-957M	24.3	28	0	4	0	68	0	0	0	0
158-957M	24.35	48	0	2	0	50	0	0	0	0
158-957M	24.41	95	0	0	0	5	0	0	0	0
158-957M	24.46	95	0	0	0	5	0	0	0	0
158-957M	24.49	20	0	0	0	73	0	0	7	0
158-957M	24.53	20	0	0	0	73	0	0	7	0
158-957M	24.62	20	0	0	0	65	0	0	15	0
158-957M	24.68	25	0	0	0	65	0	0	10	0
158-957M	24.79	25	0	0	0	55	0	0	20	0
158-957M	24.85	40	0	0	0	55	0	0	5	0
158-957M	24.93	40	0	0	0	60	0	0	0	0
158-957M	24.97	40	0	0	0	60	0	0	0	0
158-957M	25.03	20	0	0	0	65	0	0	15	0
158-957M	25.11	20	0	0	0	72	0	0	8	0
158-957M	25.18	27	0	3	0	70	0	0	0	0
158-957M	25.28	30	0	5	0	65	0	0	0	0
158-957M	25.33	30	0	0	0	69	0	0	0	0
158-957M	25.37	48	0	2	0	50	0	0	0	0
158-957M	29.3	77	0	3	0	20	0	0	0	0
158-957M	29.35	65	0	0	0	35	0	0	0	0
158-957M	29.4	15	0	0	0	80	0	0	5	0
158-957M	29.45	15	0	0	0	80	0	0	5	0
158-957M	29.53	89	0	1	0	7	0	0	3	0
158-957M	29.6	15	0	0	0	75	0	0	10	0
158-957M	34.3	5	0	0	0	90	0	5	0	0
158-957M	34.35	94	0	0	0	3	0	0	3	0
158-957M	34.43	15	0	0	0	75	0	0	10	0
158-957M	34.48	15	0	0	0	75	0	0	10	0
158-957M	34.53	20	0	0	0	60	0	0	20	0
158-957M	34.58	10	0	0	0	70	0	0	20	0
158-957M	38.3	85	0	0	0	15	0	0	0	0
158-957M	38.38	95	0	0	0	5	0	0	0	0
158-957M	38.44	20	0	0	0	60	0	0	20	0
158-957M	38.47	30	0	0	0	60	0	0	10	0
158-957M	38.51	20	0	0	0	65	0	5	10	0
158-957M	38.58	17	0	3	0	80	0	0	0	0
158-957M	38.62	30	0	2	0	63	0	0	5	0
158-957M	38.66	39	0	1	0	40	0	0	20	0
158-957M	42.3	5	0	0	0	80	0	15	0	0
158-957M	42.35	60	0	0	0	40	0	0	0	0
158-957M	42.12	20	0	0	0	75	0	0	5	0
158-957M	42.17	30	0	0	0	60	0	0	10	0
158-957M	47.22	5	0	0	0	91	0	2	2	0

Table 16: *ODP* Leg 158 shallow hole core samples visual description based composition.

Hole	Depth	Si	Ca	Mn	Cu	Zn	Fe	Total S
[-]	[mbsf]	[%]	[%]	[ppm]	[ppm]	[ppm]	[%]	[%]
JC138-22	1.9	0.00	0.50	13881	245	584	46.56	0.00

Continued on next page...

Hole	Depth	Si	Ca	Mn	Cu	Zn	Fe	Total S
[-]	[mbsf]	[%]	[%]	[ppm]	[ppm]	[ppm]	[%]	[%]
JC138-22	2.1	0.00	0.12	1010	119	616	41.80	0.00
JC138-22	2.3	0.00	0.14	1307	271	962	47.22	0.00
JC138-22	2.6	0.00	0.08	895	120	970	37.83	0.00
JC138-22	2.7	0.00	0.13	1140	96	1290	46.30	0.00
JC138-22	2.8	0.00	0.12	918	90	1096	41.81	0.00
JC138-22	2.9	0.00	0.19	1270	53	634	51.66	0.00
JC138-22	3.1	0.00	0.30	968	113	252	42.66	0.00
JC138-22	3.1	33.42	0.07	70	37	30	9.50	0.07
JC138-31	0.2	0.00	1.18	119276	1243	357	11.07	0.00
JC138-31	0.3	0.00	0.61	148964	1049	347	23.68	0.00
JC138-31	0.5	0.00	0.30	11492	187	300	31.01	0.00
JC138-31	0.7	0.00	0.22	1322	236	281	27.76	0.00
JC138-31	0.9	0.00	0.17	710	59	416	31.35	0.00
JC138-31	1.2	0.00	0.17	828	81	392	33.07	0.00
JC138-31	1.3	0.00	0.14	1212	160	596	38.69	0.00
JC138-31	1.5	0.00	0.09	2028	338	657	39.82	0.00
JC138-31	2.3	0.00	0.32	2194	58	331	49.35	0.00
JC138-31	2.4	0.00	0.36	3883	79	393	52.69	0.00
JC138-31	2.5	44.21	0.09	44	32	70	6.16	0.05
JC138-31	2.6	43.65	0.18	67	38	60	6.22	0.06
JC138-50	0.0	29.80	0.03	260	33	550	15.60	0.13
JC138-50	1.9	33.52	0.05	245	38	610	13.90	0.08
JC138-50	2.1	0.00	0.06	195	122	470	19.20	0.03
JC138-50	2.9	44.84	0.03	14	21	680	3.30	1.59
JC138-50	3.4	43.78	0.05	0	1790	3650	4.30	3.97
JC138-50	3.7	44.52	0.05	10	1480	30	3.10	0.84
JC138-50	3.9	1.40	0.03	0	9810	280	35.00	52.00
JC138-57	0.1	0.00	0.07	12	19	80	5.00	0.14
JC138-57	1.5	42.03	0.09	8	17	60	5.30	0.11
JC138-57	2.8	38.23	0.06	8	57	9440	7.90	3.70
JC138-57	3.0	38.45	0.004	44	5274	36	12.32	0
JC138-57	3.6	0.12	0.06	0	182	2350	37.70	52.50
JC138-57	4.4	0.11	0.07	0	279	84100	30.10	47.20
JC138-57	6.0	0.12	0.04	0	58300	5400	34.60	49.90
JC138-57	7.4	0.55	0.04	0	12800	480	37.10	52.90
JC138-65	0.1	0.37	0.04	0	20600	490	35.10	52.10
JC138-65	0.3	0.81	0.06	0	4750	1200	36.20	53.00
JC138-65	1.0	0.31	0.07	0	7080	560	37.30	54.90
JC138-65	1.9	0.32	0.03	0	5720	820	41.10	53.40
JC138-65	2.2	0.19	0.05	0	6210	1210	40.90	53.50
JC138-65	2.4	0.28	0.05	0	12900	1920	40.10	54.00
JC138-65	2.8	0.26	0.06	0	32000	1690	37.50	52.00
JC138-65	3.0	0.20	0.02	0	2330	2050	40.60	53.20
JC138-73	0.1	43.66	0.13	22	122	50	7.80	0.08
JC138-73	0.2	44.18	0.11	13	0	60	2.80	0.04
JC138-73	0.5	38.26	0.14	23	0	100	7.60	0.05
JC138-73	1.2	35.40	0.05	31	0	180	10.80	0.02
JC138-73	1.4	35.62	0.04	67	7	390	13.90	0.03
JC138-73	1.6	38.99	0.03	55	0	260	11.30	0.03
JC138-73	3.4	0.27	0.02	0	161000	410	33.90	44.90
JC138-73	4.2	0.29	0.00	0	12700	360	40.50	54.60
JC138-73	4.3	0.31	0.00	0	204000	320	37.30	43.10

Continued on next page...

Hole	Depth	Si	Ca	Mn	Cu	Zn	Fe	Total S
[-]	[mbsf]	[%]	[%]	[ppm]	[ppm]	[ppm]	[%]	[%]
JC138-73	5.5	0.27	0.02	0	897	170	41.30	55.70
JC138-76	0.1	15.00	0.35	33800	5080	730	26.90	0.11
JC138-76	0.4	39.34	0.06	48	9	50	12.80	0.06
JC138-76	0.8	42.49	0.06	21	104	40	5.00	0.20

Table 17: JC-138 expeditions' shallow hole core samples composition.

Station	Depth	Si	Ca	Mn	Cu	Zn	Fe	Total S
[-]	[mbsf]	[%]	[%]	[ppm]	[ppm]	[ppm]	[%]	[%]
JC138-27GC	0.0	0.00	24.30	3114	1367	772	8.54	0.00
JC138-27GC	0.1	0.00	26.38	1875	930	321	6.82	0.00
JC138-27GC	0.2	0.00	0.89	195775	14219	7107	14.69	0.00
JC138-27GC	0.2	0.00	0.40	1228	1701	2447	31.71	0.00
JC138-27GC	0.4	0.00	0.15	2509	146	2064	36.43	0.00
JC138-29GC	1.0	0.00	0.58	0.00	900	2000	24.97	0.29
JC138-29GC	1.1	0.00	7.73	0.00	1700	2300	15.89	0.27
JC138-49GC	0.0	0.00	26.61	0.00	5200	600	12.36	0.35
JC138-49GC	0.2	0.00	32.15	0.00	2000	400	6.18	0.25
JC138-49GC	0.8	0.00	0.26	0.00	48000	15300	32.33	3.41
JC138-51GC	0.9	0.00	0.12	0.00	48300	10200	34.37	28.42
JC138-51GC	1.0	0.00	0.09	0.00	53400	10800	35.68	30.93
JC138-52GC	1.9	0.00	15.00	0.00	200	100	5.08	0.25

Table 18: JC-138 expeditions's gravity core samples composition.

Source: Appendix 1 in Murton 2018

Station	Depth	Si	Ca	Mn	Cu	Zn	Fe	Total S
[-]	[mbsf]	[%]	[%]	[ppm]	[ppm]	[ppm]	[%]	[%]
M127/626GC	0.6	0	30.25	6441	816	191	5.65	0.32
M127/626GC	1.0	0	0.57	>100000	8160	682	21.01	0.26
M127/626GC	1.1	0	0.77	>100000	5146	255	14.65	0.20
M127/627GC	0.6	0	0.70	17011	33634	2806	32.35	0.34
M127/627GC	1.2	0	0.49	3113	44975	5852	37.11	3.22
M127/627GC	2.4	0	0.23	851	82873	5976	36.60	10.04
M127/627GC	2.6	0	0.36	1071	10131	2110	40.11	0.68
M127/627GC	2.8	0	0.27	611	54697	2783	39.88	4.35
M127/627GC	2.8	0	0.13	891	>100000	7114	34.28	29.02
M127/627GC	2.8	0	0.26	1259	30663	3242	39.56	7.91
M127/627GC	3.0	0	0.25	927	19106	2523	42.90	1.26
M127/627GC	3.1	0	0.19	0	>100000	5737	27.81	13.95
M127-692GC	0.1	0.14	31.2	2620	1230	355	3.81	2.60
M127-692GC	0.3	0.19	0.79	24700	3040	3500	33.2	5.38
M127-692GC	0.4	0.22	0.77	2460	1220	2380	30.9	12.20
M127-692GC	0.6	0.16	0.34	1200	1190	3540	33.4	11.50
M127-692GC	0.8	0.10	0.22	1460	1020	4230	44.3	6.15

Table 19: M127 expeditions's gravity core samples composition.

Source: Tabel 5.4.2 in Petersen 2016 and Appendix A. supplementary data in Murton et al. 2019.

Sample	Depth	Si	Ca	Mn	Cu	Zn	Fe	Total S
[-]	TVDSS [m]	[%]	[%]	[ppm]	[ppm]	[ppm]	[%]	[%]
JC138-45-1	3530	44.13	0.11	195	32	380	3.00	0.99
JC138-45-2	3530	45.56	0.03	10	19	130	2.90	0.12
JC138-21- 1- W	3550	0.14	0.19	0	5230	90	35.40	52.50
JC138-21- 2- W	3550	0.18	0.02	0	29900	50	35.30	52.30
JC138-21- 3- W	3550	0.37	0.02	0	13000	150	34.70	53.80
JC138-23GC- cc- W	3537	0.3	1.45	0	4200	340	34.80	49.40
JC138-41-1	3583	0.23	0.04	0	825	160	36.90	52.90
JC138-41-2	3574	0.15	0.01	0	1640	960	36.50	54.50
JC138-41-3	3574	0.21	0.02	0	1740	2390	37.40	51.20
JC138-41-4	3564	0.19	6.96	0	3810	180	30.80	42.90
JC138-41-5	3549	0.17	0.02	0	2360	110	38.70	54.40
JC138-41-6	3549	0.17	0.02	0	17700	170	35.90	52.30
JC138-41-7	3574	0.19	0.02	0	840	530	38.10	53.00
JC138-45-4x	3540	0.17	0.01	0	119	2020	36.10	51.10
JC138-45-4y	3540	0.29	0.03	0	92	3130	38.10	51.10
JC138-45-5	3552	0.27	0	0	5230	1830	38.20	50.10
JC138-45-6	3552	0.17	0.03	0	4940	1240	38.50	53.30
JC138-45-7a	3535	5.58	0.75	679	6220	2600	34.30	0.50
JC138-45-7b	3535	3.79	1.64	2560	109000	1400	26.50	2.97
JC138-45-7c	3535	0.19	0.02	0	422000	190	21.00	31.40
JC138-45-7d	3535	2.06	9.36	377	288000	1350	12.20	10.60
JC138-45-8	3530	6.16	1.19	181000	3550	5000	19.20	0.13
JC138-55-1	3589	1.65	0.03	27	119000	1840	31.00	43.30
JC138-55-2	3589	1.7	1.08	231	303000	90	25.80	30.60
JC138-55-3	3577	0.78	0.12	373	913	4300	37.30	37.90
JC138-55-5	3598	7.2	0	5	16000	1520	29.90	44.60
JC138-55-6	3598	11.1	0.02	0	48400	1130	28.80	36.40
JC138-55-7	3624	28.8	0.04	7	75	2520	13.30	19.20
JC138-55-8	3624	23.7	0.05	13	58	1030	16.90	24.00

Table 20: JC-138 expeditions's sea-bed surface grab samples composition.

Source: Appendix A. supplementary data in Murton et al. 2019.

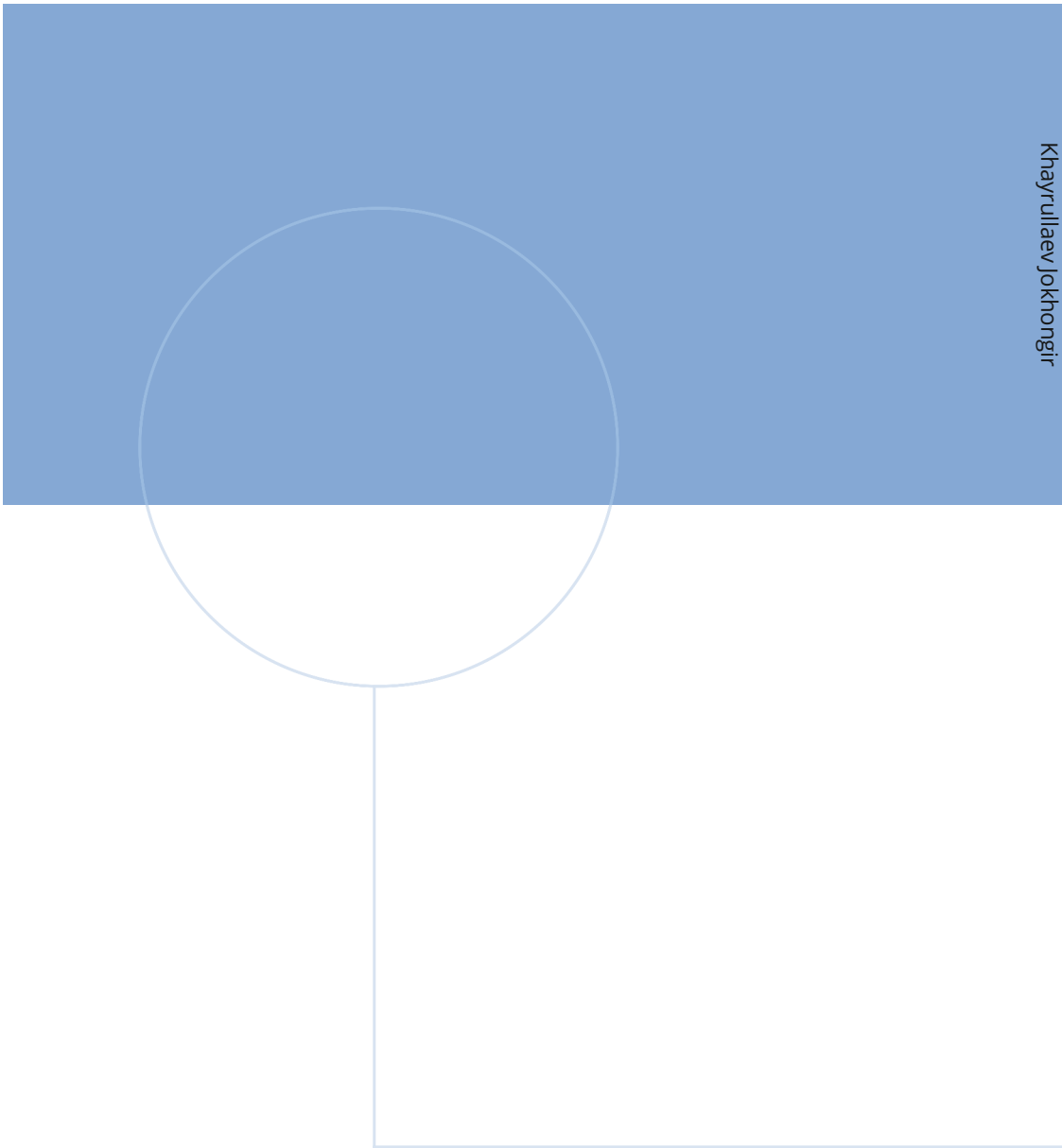

Khayruillaev Jokhongir

NTNU
Norwegian University of
Science and Technology